

**SURFACE FORM MEMORY BY  
INDENTATION-PLANARIZATION TRAINING OF NITI SHAPE  
MEMORY ALLOYS**

By

Xueling Fei

A DISSERTATION

Submitted to  
Michigan State University  
in partial fulfillment of the requirements  
for the degree of

DOCTOR OF PHILOSOPHY

Chemical Engineering and Materials Science

2011

## ABSTRACT

### **SURFACE FORM MEMORY BY INDENTATION-PLANARIZATION TRAINING OF NITI SHAPE MEMORY ALLOYS**

By

Xueling Fei

Shape memory alloys respond to deformation by indentation with strong two-way cyclic displacements on heating and cooling. Shallow indents can vanish on heating, and deeper indents will change depth when thermally cycled. In the present work, following indentation by an added step of surface planarization can furthermore produce what has been termed “Surface Form Memory” or SFM. The term SFM describes an effect that causes one surface form to reversibly transform to another, under thermal excitation. The term surface form is meant to distinguish between say, flat and “bumpy” surfaces, on a scale much larger than the intrinsic surface roughness. Surface protrusions, or ‘exdents’ may reach an amplitude near 20% of the initial indent depth, and may be created on nano to macroscopic size scales. The surface form memory effect may have special applications into novel optical, microelectromechanical, and tribological systems.

Surface deformation of a NiTi shape memory alloy (SMA) was accomplished using spherical, cylindrical, pyramidal, and flat punch indenters. Single indents and indent arrays have been made. The amplitude of SFM after planarization

was found to be related to the size of the subsurface deformation zone and can be maximized by thermal cycling, multiple indentations, by changing indent depth and spacing, and by varying indentation temperature parameters. The spatial extent of the subsurface deformation zone was studied by both experimental methods and finite element modeling. Methods such as successive front and back thinning probed the size of the deformation zone directly, while finite element modeling provided stress-strain information supporting the conclusion that the deformation zone responsible for the two-way effect was a slip zone that had plastic strains larger than 7%.

NiTi SFM, when studied in constrained recovery experiments, showed an energy density up to  $10 \text{ MJ/m}^3$ , which is about the same as that of a conventional NiTi actuator. This proves SFM's potential to be used in high energy density actuation devices.

Finally, Laser Shock Peening (LSP) was demonstrated to make indents in bulk NiTi alloys efficiently. These dynamically made indents have larger two-way response ratio than the quasi-static indents made by conventional indenters. Combining the high energy density and high efficiency of the LSP process, LSP SFM may see special applications into thin film actuators and MEMS devices.

This dissertation is dedicated  
to my dear parents and beloved friends

## ACKNOWLEDGEMENTS

I would like to thank my dear advisor and friend, Professor David S. Grummon, for his guidance in teaching, research, and life. Professor Grummon has taught me how to conduct research, trained me to be a professional engineer, given me opportunities to develop my communication and leadership skills through team management and conference organization.

I would also like to express my gratitude towards Professor Yang-Tse Cheng at University of Kentucky for his guidance in research and career development. His encouragement motivated me to pursue further in research and to develop myself as a competent researcher.

I am also grateful towards my PhD committee members, Professor Martin A. Crimp, Professor Thomas R. Bieler, from the Department of Chemical Engineering and Materials Science, and Professor Tom Pence, from the Department of Mechanical Engineering, for giving valuable comments and suggestions during my PhD study. I will also thank my collaborators, Chang Ye, Gary J. Cheng at Purdue University for diversifying my research experience. Last but not least, I will thank my colleagues Ke-bin Low, John W. Foltz, my undergraduate assistants Corey O'Connell, Matt Weir, Neil Murphy, Scott Sutton, Doug Schriener for all the help and laughter in the laboratory. Without them, a lot of work will not be accomplished.

## TABLE OF CONTENTS

LIST OF TABLES .....	ix
LIST OF FIGURES .....	x
NOMENCLATURES.....	xviii
CHAPTER 1	
BACKGROUND AND LITERATURE REVIEW .....	1
1.1 Introduction .....	1
1.2 NiTi Shape Memory Alloys.....	4
1.2.1 Historic Development .....	4
1.2.2 The Shape Memory Effect .....	4
1.2.3 Thermodynamics of Shape Memory Alloys .....	11
1.3 Two-way Shape Memory Effects .....	14
1.3.1 Introduction.....	14
1.3.2 Review of TWSME Training Methods.....	15
1.3.3 The Mechanisms of TWSME .....	25
1.3.4 Indentation in Shape Memory Alloys .....	34
1.3.5 The Indentation Induced TWSME .....	38
1.4 Contact Mechanics .....	40
1.4.1 Elastic Contact .....	41
1.4.2 Elastic-Plastic Contact .....	44
1.4.3 Indentation Related Contact Mechanics .....	47
1.5 Finite Element Modeling the Subsurface Deformation Zone .....	51
1.5.1 Introduction .....	51
1.5.2 The 3D Superelastic Model .....	52
1.6 Summary .....	55
CHAPTER 2	
EXPERIMENTAL METHODOLOGY .....	57
2.1 Introduction .....	57
2.2 Materials .....	58
2.2.1 NiTi Shape Memory Alloys .....	58
2.2.1.1 Source and Thermal Response .....	58
2.2.1.2 Stress-strain Response .....	59
2.2.1.3 Indentation Response .....	61
2.2.2 Stainless Steel, Aluminum, and Indenter Materials .....	62
2.2.3 Laser Shock Peening Materials .....	63
2.3 Indentation Methods .....	63

2.3.1	Indenter Materials and Properties .....	63
2.3.2	Indentation Loading .....	64
2.3.3	Post Indentation Thermal Cycling .....	64
2.3.4	Laser Shock Peening (LSP) .....	65
2.4	Indent and Displacement Characterization .....	66
2.5	Obtaining SFM by Indentation/Planarization .....	67
2.5.1	Thermo-mechanical Preparation .....	67
2.5.2	Grinding Techniques .....	68
2.5.2.1	Cold Planarization .....	68
2.5.2.2	Post-recovery A-planarization .....	70
2.6	Maximizing Indentation-induced TWSME .....	71
2.6.1	Effect of $a/r$ Ratio .....	71
2.6.2	Effect of Thermal Cycling .....	71
2.6.3	Effect of Indentation Spacing .....	72
2.6.4	Effect of Multiple Indentations .....	73
2.6.5	Effect of Indentation Temperature .....	74
2.6.6	Effect of Prior Cold Rolling .....	74
2.7	Determining the Size of the Active Zone .....	75
2.7.1	Front-Thinning Experiments .....	76
2.7.2	Back-Thinning Experiments .....	76
2.7.3	Direct Observation of the Indent Deformation Zone .....	77
2.8	Indent Replication and Energy Estimates .....	78
2.8.1	Introduction .....	78
2.8.2	One Shot Replica Indentation .....	78
2.8.3	Reversible Replica Indentation by SFM .....	80
2.9	Finite Element Modeling .....	83
2.9.1	The 3D Constitutive Model .....	83
2.9.2	Finite Element Program Implementation .....	84

## CHAPTER 3

RESULTS and DISCUSSION .....	86
3.1 Introduction .....	87
3.2 Developing and Maximizing the Indentation-Induced TWSME .....	87
3.2.1 Indent Recovery by the Indentation-Induced TWSME .....	87
3.2.2 Maximizing Indent Recovery .....	88
3.2.2.1 Effect of $a/r$ Ratio .....	88
3.2.2.2 Effect of Thermal Cycling .....	94
3.2.2.3 Effect of Indentation Spacing .....	98
3.2.2.4 Effect of Multiple Indentations .....	100
3.2.2.5 Effect of Indentation Temperature .....	102
3.2.2.6 Effect of Prior Cold Rolling .....	106
3.2.2.7 Maximum Two-way Response .....	108
3.3 Planarization for Surface Form Memory .....	111
3.3.1 Introduction to the Indentation-Planarization Method .....	111

3.3.2	Post-recovery M-planarization .....	111
3.3.3	Pre-recovery M-planarization .....	117
3.3.4	Post-recovery A-planarization .....	118
3.4	Characterization of the Active Deformation Zone .....	122
3.4.1	Front Thinning Experiments .....	122
3.4.2	Back Thinning Experiments .....	128
3.4.3	Two-way Strain in the Active Subsurface Zone .....	132
3.4.4	Direct Observation of the Indentation Deformation Zone .....	141
3.5	Indent Replication .....	145
3.5.1	Introduction .....	145
3.5.2	One Shot Spherical Replica Indentation .....	146
3.5.3	Reversible Spherical Replica Indentation .....	149
3.5.3.1	Spherical Exdent and Replica Indent .....	149
3.5.3.2	Effect of Preload Stress .....	152
3.5.3.3	Low Cycle Fatigue Test .....	155
3.5.3.4	Factors Affecting the Constrained Recovery .....	157
3.5.3.5	Work Output and Energy Density Calculation .....	160
3.6	SFM from Dynamic Indentation (LSP) .....	163
3.6.1	Indent Recovery and SFM .....	163
3.6.2	Mechanism of SFM in Dynamic Indents .....	172
3.7	Modeling Indent Recovery and SFM .....	180
3.7.1	Finite Element Modeling of the Deformation Zone .....	180
3.7.1.1	Spherical Indentation and the Deformation Zone .....	180
3.7.1.2	Cylindrical Indentation and the Deformation Zone .....	183
CHAPTER 4		
CONCLUSIONS AND FUTURE WORK .....		187
4.1	Conclusions .....	187
4.2	Future Development .....	189
APPENDIX .....		191
BIBLIOGRAPHY .....		193

## LIST OF TABLES

Table 2.1	Transformation Temperatures measured by DSC and SQUID .....	58
Table 2.2	Parameters of the Initial Spherical Indents in Martensitic NiTi .....	79
Table 3.1	Curve-fitting model for two-way indent depth change for spherical and cylindrical indents .....	94
Table 3.2	Thermal cycling parameters and indent depth changes for spherical indents with $a/r$ ratios of 0.4 and 0.65 .....	95
Table 3.3	The parameters and their effects on maximizing the two-way responses of the spherical indents .....	109
Table 3.4	The indent responses of spherical and cylindrical indents at different $a/r$ ratios .....	127
Table 3.5	Summarize the $a/r$ ratios and $D^*$ measured in the front and back thinning experiments .....	133
Table 3.6	Replica Indent and Residual Exdent Dimensions .....	148
Table 3.7	Path dependency effect on the replica indent depth at the preload of 250 MPa .....	160
Table 3.8	Calibration Indentation Data for 440 SS, 304 SS, and Al 6061-T6 at 433 K .....	160
Table 3.9	Calculation of Energy Density for Replica Indents made under 250 MPa .....	163
Table 3.10	Comparison of Quasistatic and LSP Indent with same contact radius.....	171
Table 3.11	Comparison of Quasistatic and LSP Indent Parameters with same two-way indent depth change .....	172
Table 3.12	Data and regression coefficients used in estimating the dynamic yield stress for slip deformation in the martensite for the present work...	177

## LIST OF FIGURES

Figure 1.1	Recovery of spherical indents made in martensitic NiTi upon heating..2	2
Figure 1.2	Flat-to-bump transition or Surface Form Memory (SFM) of the GM logo made by the indentation-planarization method in a NiTi SMA ..2	2
Figure 1.3	Schematic illustration of austenite and martensite phase with invariant plane as a habit plane .....	6
Figure 1.4	The lattice change from B2 parent (a) to B19' martensite (b). $i, j,$ and $k$ refer to parent lattice, and $i', j',$ and $k'$ refer to martensite phase. $a, b, c$ refer to lattice parameters, $\beta$ refers to the angle between $[-1\ 0\ 0]$ and $[0\ -1\ -1]$ . [Otsuka and Ren, 2005] .....	7
Figure 1.5	Sterographic projection of 24 habit plane variants for positive shear based on WLR theory for $\langle 011 \rangle_m$ Type II twinning [Otsuka et al. 2005] .....	10
Figure 1.6	TEM observation and the analysis (right-hand side) of a) typical triangular morphology of B19' martensite, b) selected area diffraction pattern [Madangopal et al. 1997] .....	10
Figure 1.7	(a) Microstructure of un-deformed martensite twins; (b) microstructure of martensite twins after 4% deformation strain in tension; (c) microstructure of deformation bands inside martensite twins after 4% deformation strain in compression [Liu et al. 1998] .....	11
Figure 1.8	Stress-strain curve of a NiTi specimen under uniaxial tension and compression [Liu et al. 1998] .....	11
Figure 1.9	Schematic drawing of superelasticity in temperature-stress space....	14
Figure 1.10	Schematic drawing of the thermomechanical training of NiTi two-way shape memory spring [Yu et al. 2006]. The specimen was annealed at 500 °C.....	17
Figure 1.11	TWSME strain $\varepsilon_{TW}$ as a function of the number of thermal cycles and training strain $\varepsilon_t$ [Lahoz et al. 2002] .....	17

Figure 1.12	Plot of the two-way displacement ratio (or two-way strain) as a function of the number of training cycles. $\Delta_T$ is the total elongation due to training [Perkins et al. 1984] .....	18
Figure 1.13	Demonstration of “all-round shape memory effect” in Ti–51Ni alloy from (a) to (e) when cooled down to 77 K [Nashida et al. 1984] .....	19
Figure 1.14	Mechanism of “all-round shape memory effect” [Kainuma et al. 1987] .....	20
Figure 1.15	Effect of the number of training cycles on the two-way shape memory strain of the $Ti_{36}Ni_{49}Hf_{15}$ alloy with different training strains [Meng et al. 2004] .....	22
Figure 1.16	Effect of compressive prestrain on the development of two-way shape memory effect in NiTi shape memory alloys [Kim et al. 2009] .....	22
Figure 1.17	The TWSME obtained after a single deformation of 6.2% strain in an equiatomic NiTi alloy [Liu et al. 1999] .....	24
Figure 1.18	Effect of prestraining in tension on the development of two-way shape memory effect in an equiatomic NiTi alloy [Liu et al. 1999] .....	24
Figure 1.19	Dark Streaks in the austenite phase after several training cycles. (a) to (d) 3 cycles, (e) to (f) 5 cycles [Perkins et al. 1984] .....	27
Figure 1.20	MD simulations show martensite nucleation and growth, (a)-(c) for a pair dislocation, (e)-(g) for two pair dislocations. (d) and (h) show the stress fields of one pair and two pair dislocations [Zhang et al. 2003] .....	28
Figure 1.21	Transmission electron micrograph showing a “Comb-shaped” arrangement of dislocations observed in the thermomechanical cycled Cu-Zn-Al alloy. (a) zone axis $G=[-1-11]$ . (b) Same zone as in (a) but under a $B=[001]\beta_1$ direction of observation. Here the projection of both dislocations in a pair are coincident: the plane containing a pair is $(1-10)\beta_1$ which corresponds to their glide plane [Rios-Jara et al. 1987] .....	29
Figure 1.22	a) and b) Shear stress-strain curves obtained at $T=285$ K during isothermal shearing test in the first training and second training [Manach et al. 1993] .....	31
Figure 1.23	Shear stress-strain curve obtained during a super-elastic cycle with strain of $\pm 5\%$ at $T=313$ K after first shearing cycling. The dash line in	

	the hysteresis indicates the estimated reversible stress contribution to the hysteresis. $\tau_{irr}$ is the irreversible stress contribution induced by training [Manach et al. 1993].....	33
Figure 1.24	Shear stress-strain curve obtained during a superelastic simple shear cycling with strain of $\pm 5\%$ at $T=313$ K. The dash line in the hysteresis indicates the estimated reversible stress contribution to the hysteresis [Manach et al. 1993] .....	33
Figure 1.25	Plots of the recovery ratio, true stress against the representative strain ( $0.2 a/r$ ). Complete recovery occurs when the representative strain is less than 5%, beyond which slip plasticity occurs [Ni et al. 2002] ...	36
Figure 1.26	a) Indent depth recovery upon heating for pseudoelastic, shape memory alloys and [111] Ni with max load up to 16000 $\mu$ N; b) Indent depth recovery upon heating for pseudoelastic and shape memory alloys with max load up to 2000 $\mu$ N [Frick et al. 2006].....	37
Figure 1.27	Two-way indent depth change of a deep spherical indent upon heating and cooling [Zhang et al. 2006] .....	38
Figure 1.28	Three dimensional profiles of reversible surface exdents: (a) a 3x3 array of spherical exdents on the surface of the austenite phase of NiTi at high temperature which disappears when the sample is cooled to the martensite phase. (b) A protruding line on the surface of the austenite phase that nearly disappears in the martensite phase. (c) A nanoscale reversible protrusion on the surface a NiTi film. [Zhang et al, 2006] .....	39
Figure 1.29	Representative strain vs. mean stress in spherical indentation, and its correlation with equivalent true stress-true strain behavior in uniaxial tension (Solid line). Metal A is Steel and metal B is Copper. [Tabor 1948, 1996] .....	46
Figure 1.30	Finite element modeling of indentation of an elastic-plastic half space by a rigid sphere: development of the plastic zone. Broken line: contour of $J_2$ . $P_Y$ is the normal load needed to first initiate plastic flow [Hardy et al. 1971] .....	46
Figure 1.31	Flow patterns exhibited in a material that piles up [Mata et al. 2002] .....	47
Figure 1.32	Comparison of the plastic zone size between conical and spherical indentations at different values of $a/r$ for (a) highly elasto-plastic solid	

	( $E = 200$ GPa, $\sigma_s = 1000$ MPa, and $n = 0.4$ ), (b) a solid with reduced elasto-plastic character ( $E = 200$ GPa, $\sigma_s = 400$ MPa, and $n = 0.2$ ), and (c) a fully plastic solid ( $E = 200$ GPa, $\sigma_s = 50$ MPa, and $n = 0.1$ ) [Mata et al. 2006] .....	48
Figure 2.1	a) DSC, b) SQUID measurements of the transformation temperatures of the equi-atomic NiTi shape memory alloys.....	59
Figure 2.2	Compressive stress strain behavior for the martensitic NiTi used in the study. $\sigma_1$ is the stress for slip deformation, $\sigma_2$ is the stress for martensite detwinning.....	60
Figure 2.3	Nanoindentation in NiTi by MTS XP Nanoindenter with an indentation depth of $1.5 \mu\text{m}$ .....	61
Figure 2.4	a) Load-Displacement curves of 304 Stainless Steel (Upper), b) 6061-T6 (Lower) used in the constrained recovery experiment.....	62
Figure 2.5	Schematic illustration of the laser shock peening process on NiTi shape memory alloys.....	65
Figure 2.6	Optical image of the laser shock peened NiTi discs. The left has indent made with beam size of $0.5$ mm and the right with beam size of $1$ mm .....	66
Figure 2.7	Comparison of post-recovery M-planarization after first recovery and pre-recovery M-planarization without first recovery.....	69
Figure 2.8	Schematic illustration of the setup of the constrained recovery experiment. 304 stainless steel (SS) is used as an example of the replica material.....	82
Figure 3.1	Schematic illustration of initial indent depth recovery of the spherical indent made with a $0.79$ mm diameter tungsten carbide ball under $700$ N in the martensitic state.....	88
Figure 3.2	Plot of the indent depth change (normalized to the indenter radius) as a function of the $a/r$ ratio for spherical indents .....	90
Figure 3.3	Plot of the two-way response, normalized to $h_0$ as a function of $a/r$ ratio based on the experimental results and calculations based on Eq. (3.2).....	91
Figure 3.4	Two-way indent depth changes for cylindrical indents, normalized to the indenter radius, plotted as a function of the $c/r$ ratio .....	93

Figure 3.5	Change of the indent depth upon thermal cycling for spherical indents with $a/r$ ratios of 0.4 and 0.65.....	96
Figure 3.6	Change of the indent depth during heating and cooling for spherical indents with $a/r$ ratios of 0.4 and 0.65 .....	96
Figure 3.7	SQUID measurements of the as-indented specimen before and after thermal cycling and the as-received NiTi specimen .....	98
Figure 3.8	Plot of the indent depth change against the normalized indentation spacing $d/a$ for 500 N spherical indents.....	99
Figure 3.9	Change of indent depth as a function of repeated indentation times for 500 N spherical indents.....	101
Figure 3.10	Plot of the initial indent depth as a function of repeated indentation times for 500 N spherical indents .....	102
Figure 3.11	Plot of initial indent depth as a function of indentation temperature for 500 N spherical indents.....	104
Figure 3.12	Plot of indent depth change as a function of indentation temperature for 500 N spherical indents .....	105
Figure 3.13	Plot of the indent depth change ratio (normalized to initial indent depth) as a function of indentation temperature for 500 N spherical indents .....	105
Figure 3.14	Plot of the initial indent depth as a function of the percentage of cold rolling for 500 N spherical indents .....	107
Figure 3.15	Plot of indent depth change as a function of the percentage of cold rolling for 500 N spherical indents .....	108
Figure 3.16	Comparison of the two-way response due to thermal cycling for spherical indents made by double indentation at 333 K and single indentation at 293 K with similar $a/r$ ratios .....	111
Figure 3.17	Indent training (a-c) and planarization (d) to obtain Surface Form Memory (SFM) ‘exdents’ in NiTi. Thermally cycling between (b) $\Leftrightarrow$ (c) and (d) $\Leftrightarrow$ (e) is indefinitely repeatable. Indentation results in three deformation zones under the indent: a: Plastic Slip Zone, b: Detwinned Martensite Zone, c: Elastic Deformation Zone (Semi infinite volume) .....	113

Figure 3.18	Cyclic exdent-to-flat surface transition after planarization of a spherical indent .....	115
Figure 3.19	Profiles of various exdent shapes measured after indentation-planarization in a series of hot-cold-hot: a) cylindrical bumpy-to-flat transition; b) punch bumpy-to-flat transition; c) mesh bumpy-to-flat transition; d) pyramidal bumpy-to-flat transition; e) spherical exdent is compared to pyramidal exdent. (The vertical scale is adjusted for better visualization) .....	115
Figure 3.20	Surface profiles of the initial 500N spherical indent, exdent upon heating and cooling after pre-recovery M-planarization .....	119
Figure 3.21	Six possible variations of Surface Form Memory in NiTi SMAs ...	120
Figure 3.22	Surface Profiles of 200 N spherical indent, indent upon cooling after post-recovery A-planarization, and subsequent heating .....	124
Figure 3.23	Subsequent thermal cycling of 200 N spherical indentation after post-recovery A-planarization to ensure the reversibility of surface feature transition .....	125
Figure 3.24	Schematic illustration of the front thinning experiment.....	125
Figure 3.25	Results of the front-thinning experiments. The stable cyclic exdent height is plotted as a function of surface removal depth for spherical indents with $a/r$ ratios between 0.4 and 0.95 .....	126
Figure 3.26	Results of successive planarization experiments. The stable cyclic exdent height is plotted as a function of surface removal depth for cylindrical indents with $a/r$ ratios between 0.4 and 0.95 .....	127
Figure 3.27	Schematic illustration of the back thinning experiment .....	129
Figure 3.28	Plot of indent depth change as a function of the remained material, normalized over the contact radius $a$ .....	130
Figure 3.29	Plot of the indent in martensite and austenite, normalized over the contact radius $a$ , as a function of the remained material, normalized over the contact radius $a$ .....	131
Figure 3.30	Plot of $D^*$ based on front and back thinning experiments with spherical indentation deformation zone modeled by ABAQUS.....	131

Figure 3.31	Exdent heights for both spherical and cylindrical indents with various $a/r$ ratios between 0.4 and 0.95 plotted as a function of the size of the subsurface active zone, $D^*$ . The slope of the linear curve fit gives the average strain in the volume defined by $D^*$ .....	134
Figure 3.32	Stable cyclic exdent height for spherical indents as a function of the depth of the subsurface active zone, $D^*$ , in the front and back thinning experiments .....	134
Figure 3.33	Data for spherical indents for all $a/r$ ratios studied normalized to the experimentally determined depth of the subsurface active zone, $D^*$ . The data may be adequately fitted to eq. (3.7) which has a single adjustable parameter .....	135
Figure 3.34	2D illustration of residual spherical cap after a depth of $d_{pl}$ of material being removed.....	136
Figure 3.35	Data for cylindrical indents for all $a/r$ ratios studied normalized to the experimentally determined depth of the subsurface active zone, $D^*$ .....	140
Figure 3.36	Schematic illustration of residual area in the cylindrical cap after a depth of $d_{pl}$ of material away. $A_{fan}$ is the area of the fan with angle $\theta$ , $A_{tri}$ is the area of a triangle inside the fan. $A_{res}$ is double the rest area of the fan. $A_{tot}$ is the area of the hemisphere. $d_{pl}$ is the depth of material being removed and $D^*$ is the size of the deformation zone.....	140
Figure 3.37	Schematic drawing of the cross-sectional view of the spherical indent after cutting .....	142
Figure 3.38	The cross-sectional view of a spherical indent at room temperature (293 K) after polishing, after heating to 433 K, and after cooling to 243 K and measured at 293 K optically.....	143
Figure 3.39	Schematic drawing of the cylindrical indent after cutting.....	144
Figure 3.40	The cross-sectional view of a cylindrical indent at room temperature (293 K) after polishing, after heating to 433 K, and after cooling to 243 K and measured at 293 K optically.....	145
Figure 3.41	Residual exdents in NiTi (left) and Replica indents in aluminum (right) at 293 K made directly following the replication experiments. Images (a,b), (c,d) and (e,f) correspond to initial indent $a/r$ ratios of 0.42, 0.68 and 1.00 respectively. In each image the field size is 1.9 mm x 2.5 mm. Vertical scales vary, as shown. Images on the left have been inverted to	

	correspond to the relative orientations of the features during their formation.....	147
Figure 3.42	Depths of replica indents plotted as a function of the post-replication height of the corresponding NiTi exdents when re-warmed to 423 K (the austenitic condition).....	148
Figure 3.43	The optical image of the NiTi exdent and replica indent in 304 stainless steel after replica indentation with a preload of 250 MPa.....	150
Figure 3.44	The surface profiles of NiTi exdent heated to 433 K (the upper left figure) and a replica indent in 304 stainless steel at 293 K (the lower left figure) after replication under preload of 250 MPa. The dimensions of the exdent and replica indent are plotted in the right figure.....	151
Figure 3.45	The relation between replica indent depth and preload stress for stainless steel and aluminum. No replica indent is assumed at 0 preload stress.....	152
Figure 3.46	The relation between the replica indent depth and material hardness at preload stress of 250 MPa.....	153
Figure 3.47	Plot of replica indent depth against the material hardness at preload stresses of 125, 200, 250, and 300 MPa.....	154
Figure 3.48	Plot of $H^*$ against the preload stress. Parabolic curve fitting suggests 480 MPa is the largest preload stress that can be used to make a replica indent.....	155
Figure 3.49	Plot of the preload stress against $H^*/$ preload. Linear curve fitting suggests 480 MPa is the largest preload stress that can be used to make a replica indent.....	155
Figure 3.50	Low cycle fatigue of NiTi exdent in the constrained recovery experiments.....	157
Figure 3.51	Path dependency of replica indentation: A) cooling without load; B) cooling under load.....	159
Figure 3.52	Schematic illustrations of (a) initial indent depth-recovery, and (b) exdent-to-flat surface transition during heating and cooling after planarization of the LSP indent.....	166

Figure 3.53	Cyclic exdent-to-flat surface transition after planarization of the dynamic indent.....	167
Figure 3.54	Comparison of the initial indent depth between the spherical indent made under 700 N with $r=400\ \mu\text{m}$ spherical ball and the dynamic indent under laser intensity of $2.5\ \text{GW}/\text{cm}^2$ and beam size of 0.5 mm .....	170
Figure 3.55	Comparisons of the initial indent depth, two-way recovery between the quasi-static spherical indent and the dynamic indent. The dynamic indent is magnified to have the same vertical length as the spherical indent.....	170
Figure 3.56	Comparisons of initial indent depth and two-way recovery between the spherical indent and the LSP indent. Vertical scales are identical for each impression but the base of the quasistatic indent is off the scale .....	171
Figure 3.57	Finite element mesh with 15,000 nodes and a refined area as the contact region and 4 mm spherical indenter .....	180
Figure 3.58	Finite element model of the spherical indentation process: a) 10% of the indentation steps; b) 60% of the indentation steps; c) 100% of the indentation steps (Indentation step finished) .....	182
Figure 3.59	Effective plastic strain developed after spherical indentation with an $a/r$ of a) 0.4, b) 0.65, and c) 0.95 simulated by ABAQUS finite element model.....	182
Figure 3.60	Effective plastic strain developed after cylindrical indentation with an $a/r$ of a) 0.41, b) 0.65, and c) 0.95 simulated by ABAQUS finite element model.....	184
Figure a	Schematic illustration of the indentation-planarization process.....	190

## LIST OF NOMENCLATURES

*DSC* : Differential Scanning Calorimetry

*TEC* : Thermal Electric Cooler

*SQUID* : Super-conducting Quantum Interferometry Device

*LSP* : Laser Shock Peening

*SFM* : Surface Form Memory

*TWSME* : Two-way Shape Memory Effect

*SMA*s : Shape Memory Alloys

*M<sub>s</sub>* : Martensite Start Temperature

*M<sub>f</sub>* : Martensite Finish Temperature

*A<sub>s</sub>* : Austenite Start Temperature

*A<sub>f</sub>* : Austenite Finish Temperature

*R<sub>a</sub>* : Squar-Root-Mean Roughness

*h<sub>o</sub>* : Initial Indent Depth

*H<sub>m</sub>* : Hardness of Martensite

*H\** : The Hardness Limit in Replica Indentation

*h<sub>max</sub>* : Maximum Exdent Height

*a* : Contact Radius of a Spherical Indent

*c* : Half Trench Width of a Cylindrical Indent

*r* : Indenter Radius

*d<sub>pl</sub>* : Depth of Planarization

$D^*$  : Depth of the Active Zone

$A_{repl}$  : Area of the Replica Indent

$P_{repl}$  : Load of the Replica Indent

$R_{QS}$  : Radius of Quasistatic Indenter

$C_{el}$  : Elastic Wave Propagation Speed

$C_{pl}$  : Plastic Wave Propagation Speed

$HEL$  : Hugoniot Elastic Limit

$P$  : LSP Pressure

$D_p$  : Plastified Depth

$\delta_c$  : Two-way Indent Depth Change

$h_e$  : Two-way Exdent Height

$\sigma$  : Stress

$\varepsilon$  : Strain

$\varepsilon_p$  : Peak Strain

$\varepsilon_r$  : Representative Strain

$\varepsilon_p$  : Pressure Pulse Duration

$\rho$  : Material Density

$\lambda$  : Lamé's Constant

$\mu$  : Shear Modulus

$\varepsilon_{r,(sph\ or\ cyl,crit)}$  : Critical representative strain (5%) for spherical or cylindrical indents

$\chi_{sph\ or\ cyl}$  : Coefficient of representative strain for spherical or cylindrical indents

# Chapter 1 BACKGROUND AND LITERATURE REVIEW

## 1.1 Introduction

Various macro-, micro-, and nano-indentation methods have been used in shape memory alloys (SMAs) as alternatives to conventional tensile tests for measuring shape memory and superelastic characteristics of SMAs. For example, as shown in Figure 1.1, shallow spherical\* indents made by a Continuous Stiffness Machine (CSM) instrumented indenter can completely recover after heating above  $A_f$  due to the shape memory mechanism, while deep spherical indents became shallower but remained after heating due to irreversible slip deformation. These indents deepened after cooling below  $M_f$ , generating a two-way depth change. When a planarization step was used in the martensitic state after the indent's initial heating and cooling, a thermally-reversible flat-to-bumpy transition can be observed, as shown in Figure 1.2. We have termed this surface transition "Surface Form Memory" (SFM). These transitions are fully reversible and cyclically stable.

It is demonstrated that SFM can be achieved by indenting with a variety of tools in a martensitic NiTi surface, heating and cooling, and then planarizing in the cool condition to restore a flat surface. An inverted image of the tool will repeatedly appear and vanish as the temperature is varied from  $M_f$  to  $A_f$  and back to  $M_f$ .

---

\*It should be noted that only shallow spherical or cylindrical indents can recover completely.

† Experiments have recorded tens of cycles with apparent convergence on a

Indenting arrays of balls or rods has led to the observation of some of the largest SFM amplitudes.

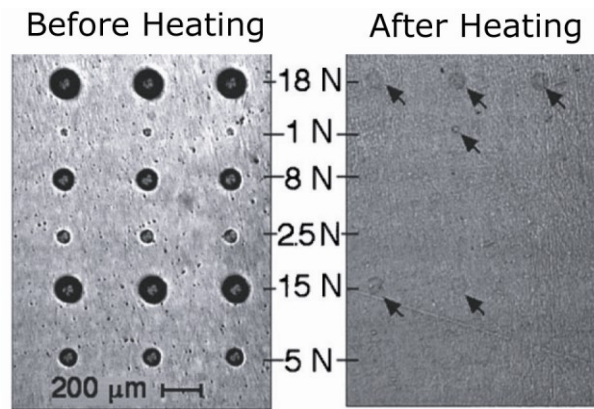


Figure 1.1 Recovery of spherical indents made in martensitic NiTi upon heating [Ni et al. 2002].

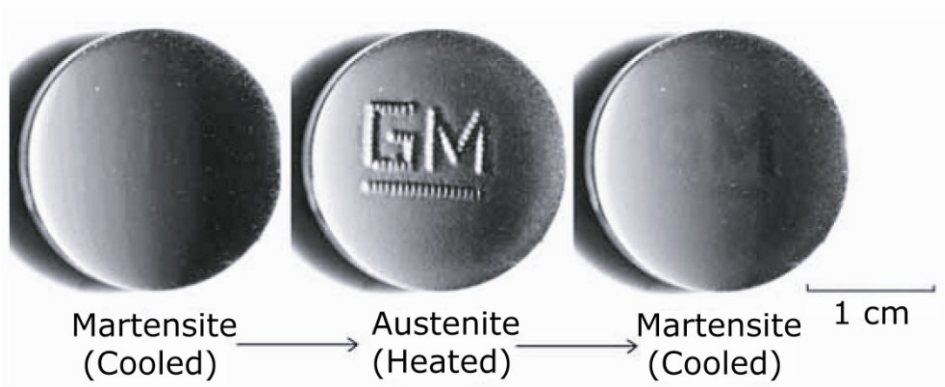


Figure 1.2 Flat-to-bump transition or Surface Form Memory (SFM) of the GM logo made by the indentation-planarization method in a NiTi SMA.

Shot peening such as sand blasting can also give rise to SFM. However, this stochastic process has no control over indent position and indent depth. Laser shock peening, on the other hand, allows precise position control and creation of complex arrays.

Indentation methods have been demonstrated as a robust technique to achieve SFM. The ability to transition from a flat to a bumpy surface may find applications in a number of areas. SFM in NiTi thin films at very small length scales allows its application to the fabrication of thermally switchable diffraction gratings or other optical devices. Other applications include information storage and smart aerodynamic and hydrodynamic surfaces. SFM transitions generate appreciable mechanical work during austenitization, which may find application to MEMS actuators, mold-release surfaces, thermal clutches, mechanical joining, and variable friction surfaces and interfaces.

This dissertation work concerns the development, understanding, and applications of SFM. Detailed discussion on experimental results, and possible mechanisms of SFM, are presented in this dissertation. In this chapter, the NiTi system will be reviewed with an emphasis on transformation behavior and the mechanisms of the shape memory effect (SME) and transformational superelasticity. The development of training methods and the mechanisms of the two-way SME (TWSME) will be discussed in detail. Recent advances in indentation-induced TWSME will also be reviewed, associated with the contact mechanics and the indentation deformation zones. The principles of a three-dimensional finite element model on the indentation-induced shape memory effect will be discussed at the end.

## **1.2 NiTi Shape Memory Alloys**

### **1.2.1 Historic Development**

The discovery of shape memory alloys can be dated back to the early 1950s, but the engineering significance of shape memory alloys was not well recognized until the shape memory effect was discovered in NiTi alloys [Buehler et al. 1962]. NiTi shape memory alloys in particular have been favored by industry due to their higher thermal stability, larger recoverable strain, greater shape memory effect (SME) and superelasticity (SE). In addition, NiTi alloys have very good corrosion resistance and biocompatibility, which are critical to applications in the biomedical field [Morgon et al. 2004]. Due to the desire to better develop SMAs' application in aerospace, biomedical, and consumer sectors, much attention has been given to develop better understanding of the system and mechanisms of SE and SME, which are discussed below.

### **1.2.2 The Shape Memory Effect**

Shape memory metals consist of many alloys, of which the iron based alloys, the copper based alloys, and the nickel based alloys are the technically most important. For simplification and the relation to the present work, the near-equiatomic NiTi shape memory alloy will be taken as an example, with a focus on the B2-B19' transformation route to illustrate the mechanism of SME.

In the NiTi alloy system, the high temperature austenite (A) parent phase with B2 CsCl type ordered bcc structure can transform displacively to the martensite (M) phase with monoclinic B19' type lattice at low temperature. During phase transformation, as shown in Figure 1.3, martensite matrix and martensite twin form in the martensite phase and displace along an invariant plane called habit plane. A single twinned martensite domain is also called a habit plane variant (h.p.v.). The martensite twins (LCV1 and LCV2), which are the smallest martensite variants, are called lattice correspondence variants (L.C.V) and have correspondence with the parent phase.

The lattice structure change from B2 to B19' during the martensitic transformation is shown in Figure 1.4. During cooling,  $[-1\ 0\ 0]_p$  in B2 are contracted and  $[0\ -1\ -1]_p$  are extended. A shear strain causes the angle  $\beta$  to change from  $90^\circ$  to  $96.8^\circ$  and the monoclinic lattice structure is created. Due to the differences in crystallographic structures in M and A phases, elastic strain is created during martensitic transformation and dissipated by twinning (the lattice invariant shear). This shear strain created during the martensitic transformation can only be removed by the self-accommodation motion where a combination of multiple martensite variants forms a triangular structure to cancel out shear strain macroscopically.

To see this clearly, we know  $\{110\}_m$  has 6 equivalent planes, according to the WLR theory [Lieberman et al. 1955], in which each plane has two lattice correspondence variants that are caused shearing at opposite directions, positive shear

in (+) and negative shear (-). Since there are two lattice invariant shears ( $[011]_m$  and  $[0\bar{1}1]_m$  Type II twinning), there are totally 24 habit plane variants in the NiTi system that cluster around the poles of  $\langle 011 \rangle$  in the austenite phase according to the stereographic projection in Figure 1.5 [Otsuka and Ren, 2005]. A particular habit plane variant in the stereographic projection is represented such as  $3'-4'$ (+), where  $3'$  represents a martensite matrix, and  $4'$  represents a martensite twin.  $4'$  is related to  $3'$  by  $[01-1]_m$  Type II twinning in positive shear. Generally, during martensitic transformation by cooling, 2 or 4 habit plane variants in each pole interact in a self-accommodation motion to cancel out the transformation strain. This is has also been analyzed in Cu-Zn-Ga, Cu-Al-Ni, etc by Saburi-Wayman [1979].

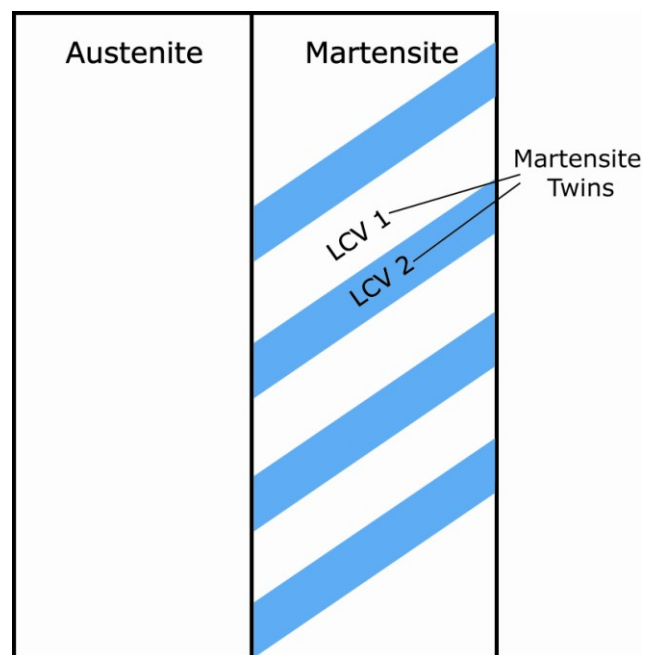


Figure 1.3 Schematic illustration of austenite and martensite phase with invariant plane as a habit plane. (For interpretation of the references to color in this and all other figures, the reader is referred to the electronic version of this dissertation.)

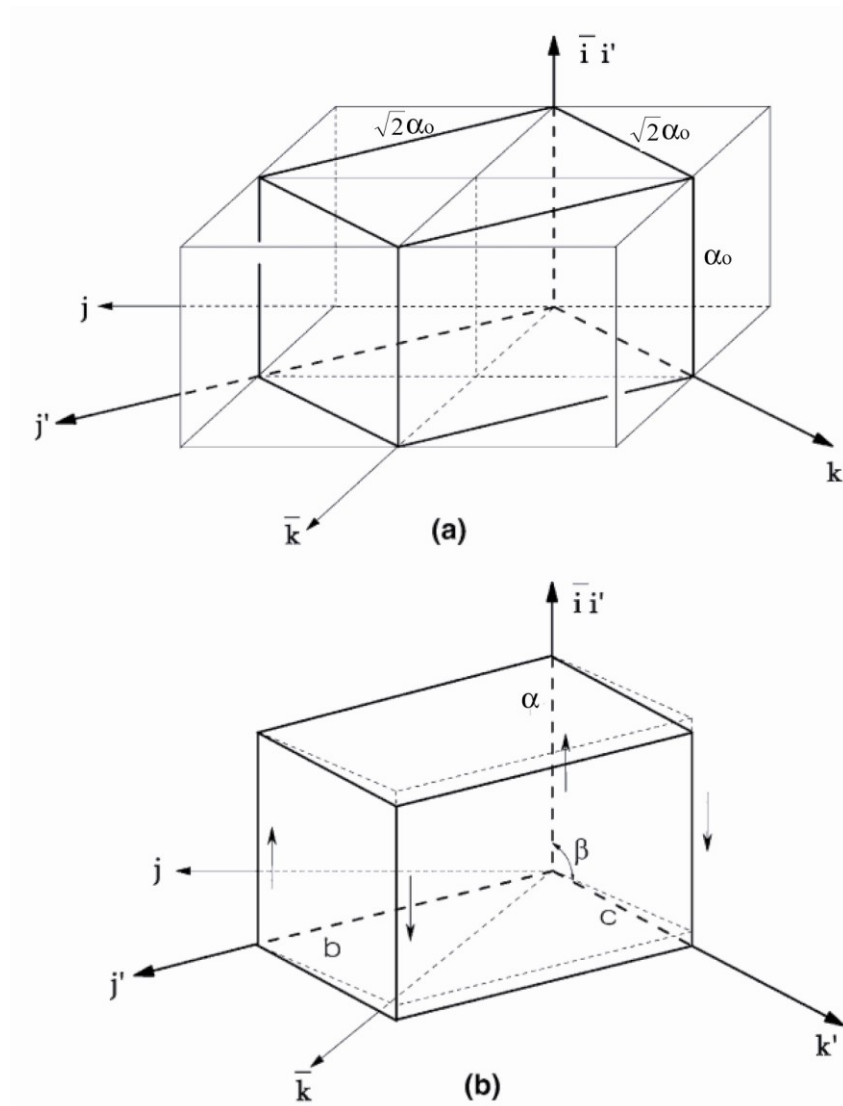


Figure 1.4 The lattice change from B2 parent (a) to B19' martensite (b).  $i$ ,  $j$ , and  $k$  refer to parent lattice, and  $i'$ ,  $j'$ , and  $k'$  refer to martensite phase.  $a$ ,  $b$ ,  $c$  refer to lattice parameters,  $\beta$  refers to the angle between  $[-1\ 0\ 0]$  and  $[0\ -1\ -1]$ . [Otsuka and Ren, 2005]

However, due to the monoclinic structure of B19' martensite in NiTi, the self-accommodation mechanism is rather complex. The triangular morphology was observed TEM and used to explain the self-accommodation motion successfully [Madangopal et al. 1997], as shown in Figure 1.6. As a result, the macroscopic

transformation strain was canceled out in the triangular morphology formed by three habit plane variants.

If the self-accommodated martensite variants are deformed in tension after cooling, the deformation proceeds through twin boundary motion that essentially converts one martensite variant to another. The most favorable martensite variant that gives the largest strain under the external stress grows at the expense of the others until, in the limiting case, the specimen becomes a single crystal of the most favorable martensite variant. It is important to note that further plastic deformation would require dislocation-mediated slip. Upon heating to a temperature above  $A_f$  (Austenite finish temperature), martensite variants undergo a reverse transformation to the original shape in the parent phase due to the lattice correspondence. This effect is called the Shape Memory Effect (SME).

Of significance to the present work, the deformation mechanism varies if the specimen is placed in compression, due to tension-compression asymmetry. Liu et al. [1998] studied the stress-strain curves and the microstructure of NiTi shape memory alloys in tension and compression, as shown in Figure 1.7. Figure 1.7a shows the microstructure of the un-deformed self-accommodated martensite. Figure 1.7b shows the microstructure of martensite twins after 4% strain in tension. Martensite variants have detwinned and started to align with the maximum shear stress direction. Figure 1.7c shows the microstructure of deformation bands inside martensite twins after 4%

strain in compression. The martensite has fully detwinned with large deformation bands being formed. It was found that the martensitic deformation in compression was not through the movement of adjacent martensite variants to align with the maximum stress direction as it was in tension, but through the generation and rearrangement of lattice defects, especially dislocations. This “tension-compression asymmetry” arises from the different Schmid factors between tension and compression directions due to the low symmetry in martensite variants [Patoor et al. 1995]. It was reported by Liu et al. [1998] that NiTi alloys work harden more quickly in compression than in tension, as shown in Figure 1.8, causing the stress to be larger in compression than in tension for the same amount of strain. Slip deformation is hence larger in compression than in tension for the same pre-strain. As a result, the recoverable strain is smaller in compression than in tension for the same deformation strain because the lattice defects generated in compression inhibit complete shape recovery.

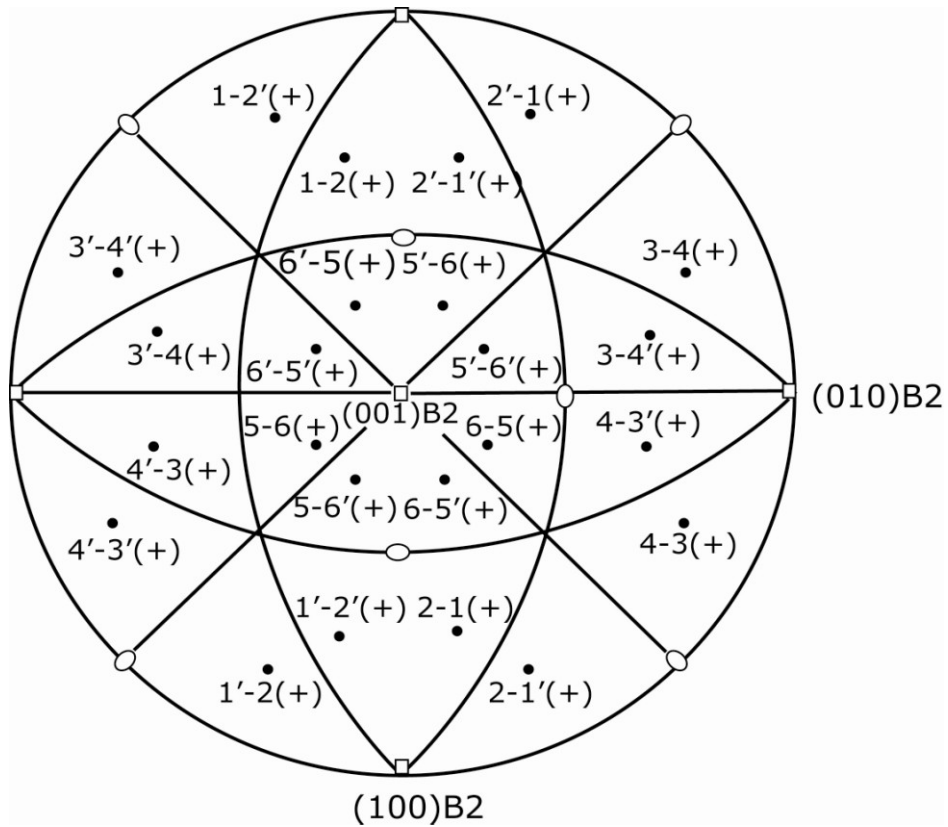


Figure 1.5 Stereographic projection of 24 habit plane variants for positive shear based on WLR theory for  $\langle 011 \rangle_m$  Type II twinning [Otsuka et al. 2005].

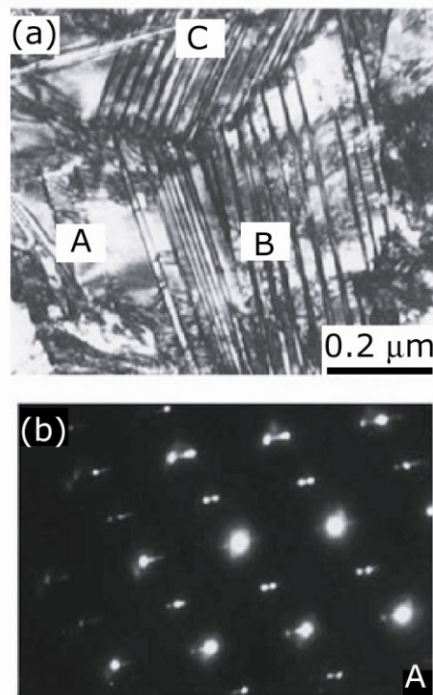


Figure 1.6. TEM observation and the analysis (right-hand side) of a) typical triangular morphology of B19' martensite, b) selected area diffraction pattern [Madangopal et al. 1997].

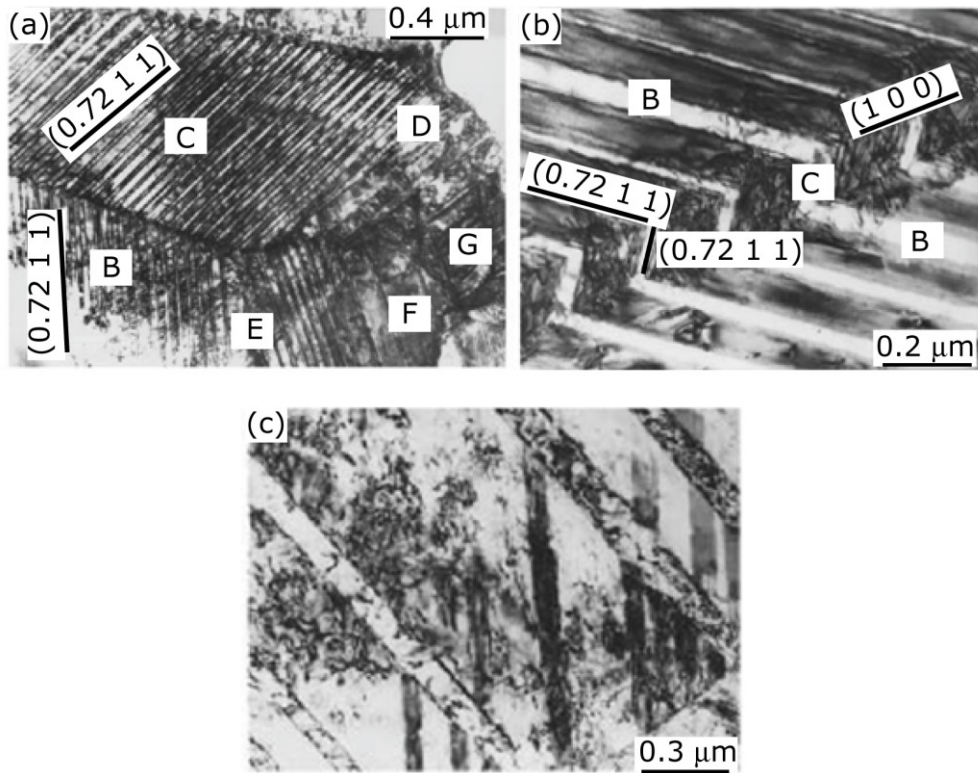


Figure 1.7 (a) Microstructure of un-deformed martensite twins; (b) microstructure of martensite twins after 4% deformation strain in tension; (c) microstructure of deformation bands inside martensite twins after 4% deformation strain in compression [Liu et al. 1998].

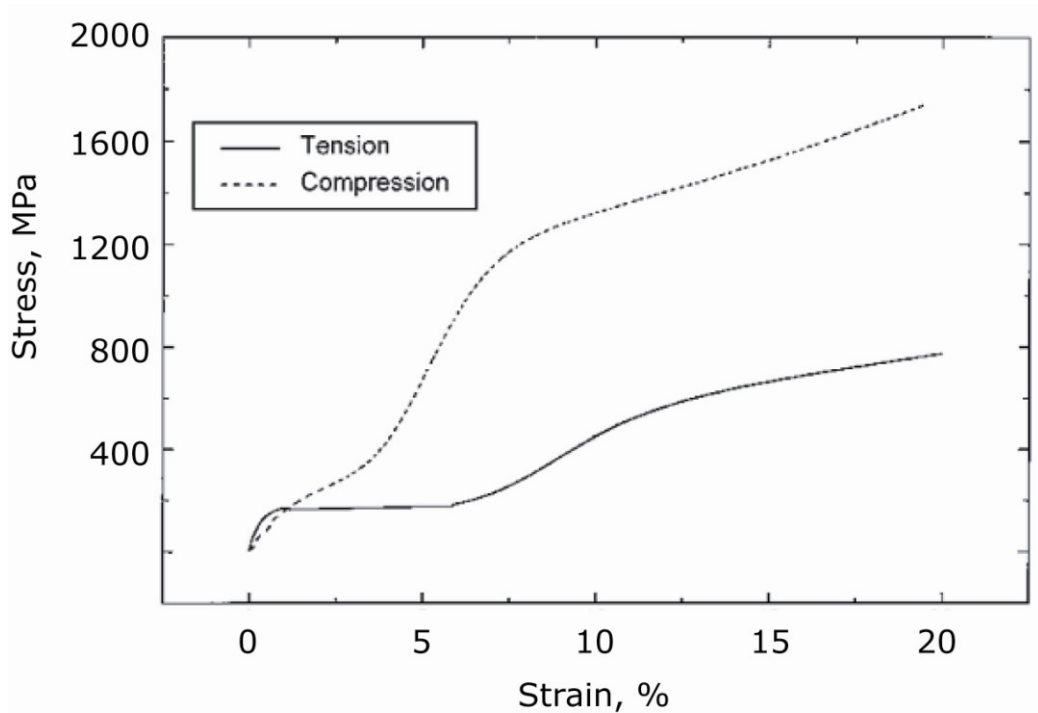


Figure 1.8 Stress-strain curve of a NiTi specimen under uniaxial tension and compression [Liu et al. 1998].

### 1.2.3 Thermodynamics of Shape Memory Alloys

Since martensitic transformations are diffusionless, shear-like transformations, stress can be a driving force for martensitic transformation. Therefore, martensite can be formed by stressing at temperature higher than  $M_s$ . The stress that is needed to stress induce martensite is governed by the modified Clausius-Clapeyron equation expressed in Eq. (1.1).

$$\frac{dT_{TRANS}}{d\sigma} = -\frac{\varepsilon}{\Delta S} = -\frac{\varepsilon T_O}{\Delta H} \quad \text{Eq. (1.1)}$$

Where  $\sigma$  is the externally-applied deviatoric stress,  $T_{TRANS}$  is the stress-induced transformation temperature,  $\Delta S$  is the martensitic transformation entropy per unit volume,  $\varepsilon$  is the transformation strain,  $\Delta H$  is the martensitic transformation enthalpy per unit volume,  $T_O$  is the stress-free  $B2-B19'$  equilibrium temperature.

If the ambient temperature is above  $A_f$ , Martensitic transformation is reversed when the applied stress is removed upon unloading. This reversion of stress induced martensite and recovery of deformation upon unloading is known as Superelasticity.

In section 3.5.3, we will estimate the change of transformation temperature due to loading in a constrained recovery experiment. Equation 1.1 is modified to be

$dT_{TRANS} = -\epsilon T_0 d\sigma / \Delta H$  to estimate the change of transformation temperature under stress.

Figure 1.9 schematically shows the fundamental limits on superelasticity, plotted in stress- temperature space. It is important to note that the critical stress to induce martensite is positively (linearly) related to temperature in the stress-temperature space. This can be explained based on Eq 1.1 where  $dT_{TRANS}/d\sigma$  is positive since martensitic transformation is an exothermic process. If NiTi is subjected to sufficient external stress at temperature  $T_x$  above  $M_s$ , a value between  $A_f$  and  $M_d$ , as shown in Figure 1.9, the austenite phase becomes thermodynamically unstable and transforms to the martensite phase. The minimum stress to start inducing martensite is found to be  $\sigma_x$ . Upon releasing the stress, the martensite spontaneously reverts to austenite phase due to the instability of martensite in the absence of stress, given that  $T_x > A_f$ . The ability to stress induce martensite, however, also depends on whether the stress level exceeds the temperature dependent critical stress for slip,  $\sigma_d$  in the austenite. If the applied stress magnitude during deformation is larger than the critical stress for slip, slip occurs before stress-inducing martensite, resulting in permanent deformation with partial or even no strain recovery, depending on the stress level used. Therefore,  $M_d$ , the temperature at which the critical stress loci cross, is the maximum temperature for stress inducing martensite with full recovery.

In summary, superelasticity occurs when the work done by stress-inducing martensite equals the free energy change of the NiTi alloy in forming martensite by

cooling, the behavior of which is governed by the modified Clausius-Clayperon equation.

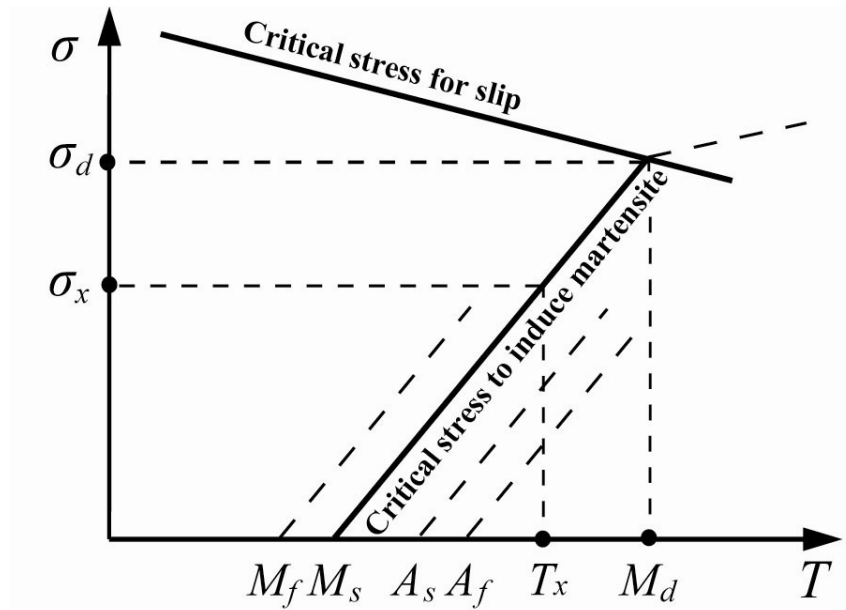


Figure 1.9 Schematic drawing of superelasticity in temperature-stress space.

### 1.3 Two-way Shape Memory Effects

#### 1.3.1 Introduction

Different from one-way SME, in which the deformed martensite returns to the original austenite shape after heating but no shape change upon subsequent cooling, two-way shape memory effect (TWSME) drives a shape change upon both heating and cooling. For the shape change to occur on cooling, certain martensite variants need to be selected to return to the shape in martensite. Due to the nature of the selective formation of martensite variants, TWSME is a weak effect compared to one-way SME, in which strong reversibility and lattice correspondence take place. The selective formation of martensite variants is not an intrinsic property of SMAs,

thus methods such as thermo-mechanical cycling, constrained aging, slip deformation, have often been involved in training for TWSME.

In this section, the most common training methods for TWSME will be reviewed and the usefulness of the methods will be evaluated. The mechanisms of TWSME developed in the literature in the past several decades will be discussed. Understanding the training methods and the mechanisms of TWSME is critical to understand the indentation induce TWSME and Surface Form Memory.

### **1.3.2 Review of TWSME Training Methods**

#### ***1.3.2.1 Thermo-Mechanical Cycling***

Bending, extension and tensile deformation are often coupled with thermo-mechanical cycles to develop TWSME in shape memory alloys. Specifically, if a NiTi specimen is deformed under bending, tension, or compression in the martensite phase, then the specimen would be heated to austenite and cooled to martensite without load to finish one thermo-mechanical cycle and start another one. If the specimen was deformed in the austenite phase, then the specimen would be cooled to martensite under load, followed by releasing the load and reheating the specimen to austenite to start another training cycle.

Yu et al. [2006] used thermo-mechanical training on NiTi springs to develop TWSME. The training cycle was first extending the NiTi spring in the martensitic state to various strains, unloading, and then heating and cooling the spring between  $A_f$

and  $M_f$  without stress to measure two-way strain. As a result, the NiTi spring shortened upon heating and elongated upon cooling (as shown in Figure 1.10). Lahoz et al. [2002] used two bending modes for training. In method 1, a NiTi wire was bent in the martensitic state to various strains and heated and cooled *without* load between  $A_f$  and  $M_f$  to finish one training cycle. In method 2, a NiTi wire was first bent in the martensitic state to various strains and then repeatedly thermally cycled between  $A_f$  and  $M_f$  *with* load to induce TWSME. It was reported that method 1 rather than method 2 is more effective to increase two-way strain, as shown in Figure 1.11. The two-way strain, which is defined as the ratio of reversible bending angle change over the bending angle after unloading, reaches a plateau after around five thermo-mechanical cycles and the maximum two-way displacement ratio ( $\frac{\Delta l}{l_o}$ ) was found to be 8%.

Perkins et al. [1984] thermo-mechanically cycled a CuZnAl shape memory alloy in tension and used TEM to study the dislocations in the trained specimens. The training method is a little different from above since the author deformed the specimen in the austenite and cooled to martensite under stress, then unloaded and heated to austenite to start another thermo-mechanical training cycle. It was reported that the optimum training for TWSME was at approximately fifteen training cycles, as shown in Figure 1.12.

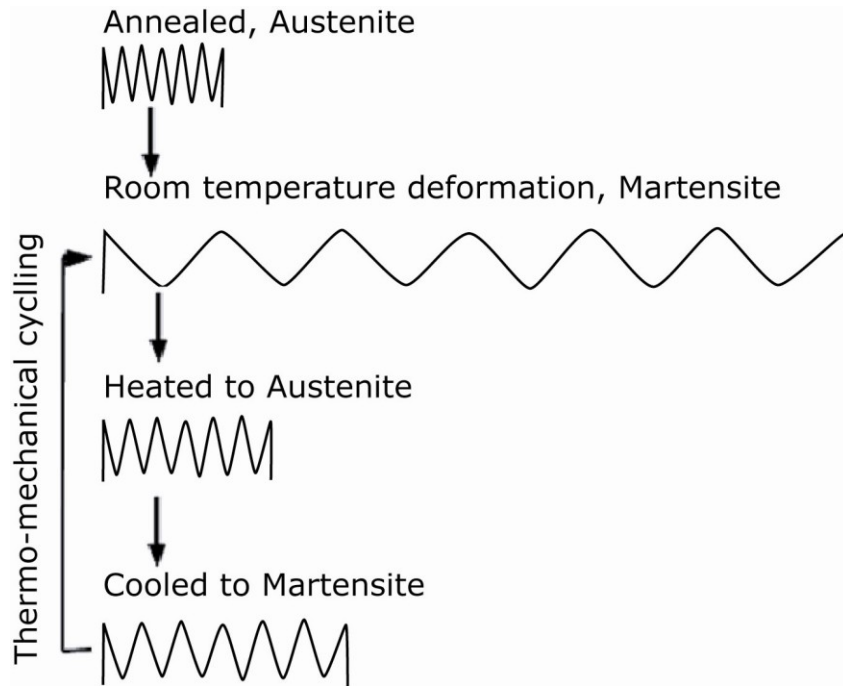


Figure 1.10 Schematic drawing of the thermomechanical training of NiTi two-way shape memory spring [Yu et al. 2006]. The specimen was annealed at 500 °C.

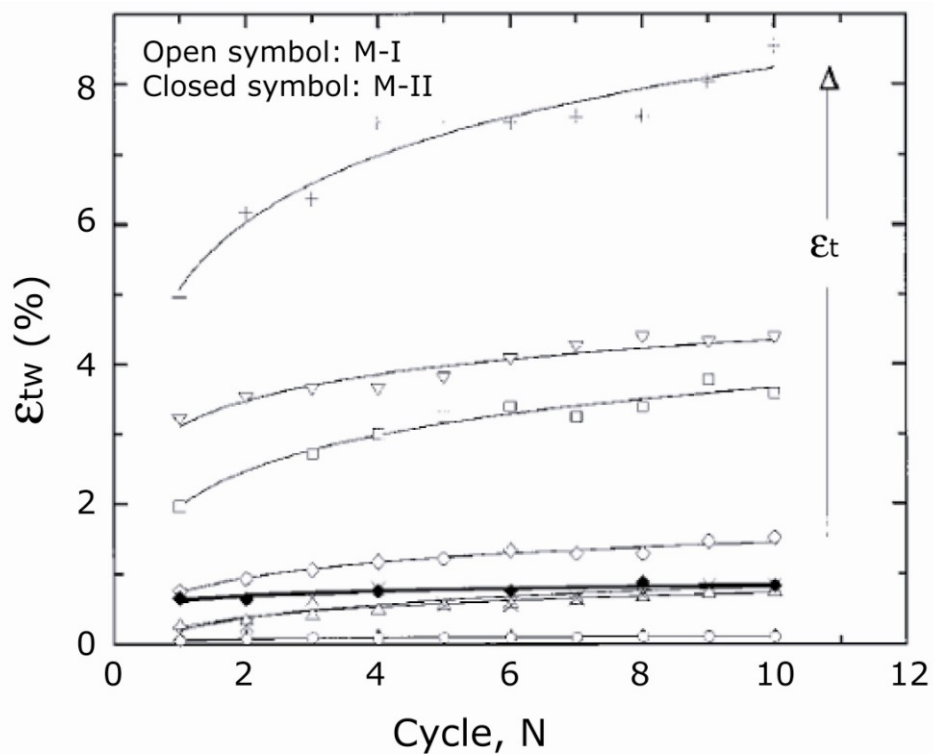


Figure 1.11 TWSME strain  $\epsilon_{tw}$  as a function of the number of thermal cycles and training strain  $\epsilon_t$  [Lahoz et al. 2002].

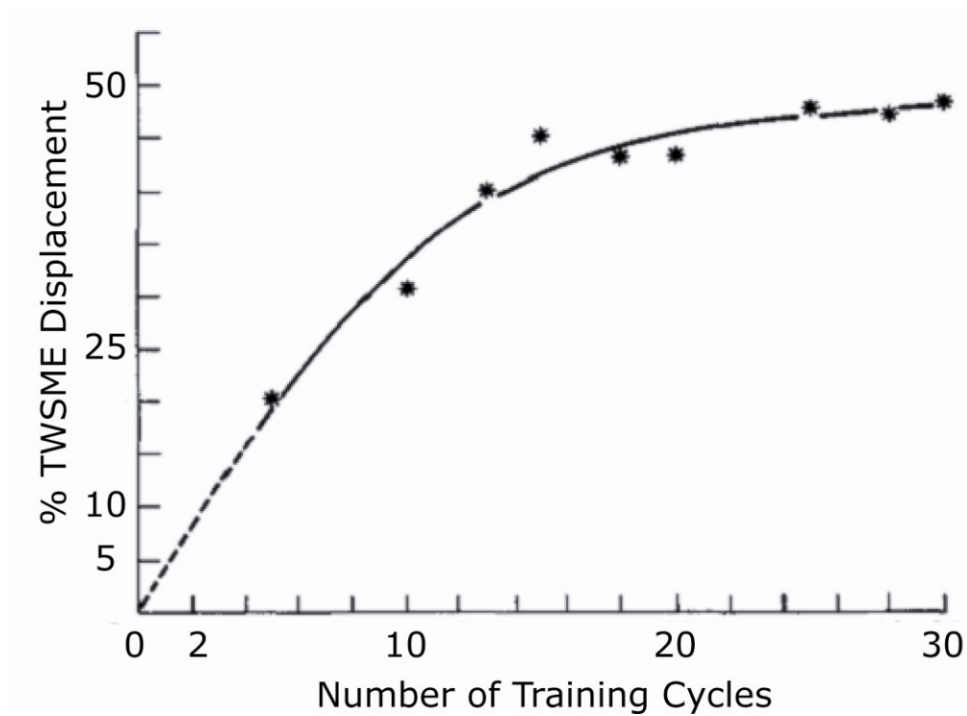


Figure 1.12 Plot of the two-way displacement ratio (or two-way strain) as a function of the number of training cycles.  $\Delta_T$  is the total elongation due to training [Perkins et al. 1984].

### 1.3.2.2 Constrained Aging

Constrained aging can create internal stress fields that lead to TWSME.

Fukuda [Fukuda et al. 2001] aged a single crystal Ti-51at% Ni under a compressive stress along [111]. The specimen was first solution-treated at 1123 K for 3.6 ks followed by quenching into ice water. After that, the specimen was aged at 773 K for 6 ks under a compressive stress of 300 MPa applied along the [111] direction.  $\text{Ni}_4\text{Ti}_3$  precipitates were formed coherently along {111} plane of the parent phase. The thermally induced R phase had a single variant and the expansion strain along [111] direction was about 0.8%.

Nishida and Honma [1984] reported “all-round shape memory effect”. The strips of the Ti-51.at% Ni alloy they used were solution-treated at 1073 K for 7.2 ks. Then they were subjected to constrained-aging at 773 K for 3.6 ks as a half-circular form as shown in Figure 1.13a. If the specimen is cooled down to 77 K, the shape changed from Figure 1.13(a)–(e). Upon heating the exact reverse change of the shape was observed from Figure 1.13(e)–(a). Figure 1.14 schematically shows the stress state of the sample. Compressive stress and tensile stress arise in the lower part and upper part respectively. The bending stress is relieved if the precipitates are formed normal to the compressive stress which is normal to  $\{111\}$  plane, as shown in Figure 1.14. A TEM study in [Kainuma et al. 1987] confirmed that constrained-aging induced precipitates are formed in such a way that a special microstructure and stress field were developed to promote TWSME.

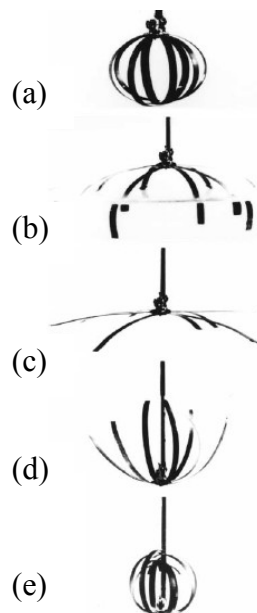


Figure 1.13 Demonstration of “all-round shape memory effect” in Ti–51Ni alloy from (a) to (e) when cooled down to 77 K [Nashida et al. 1984].

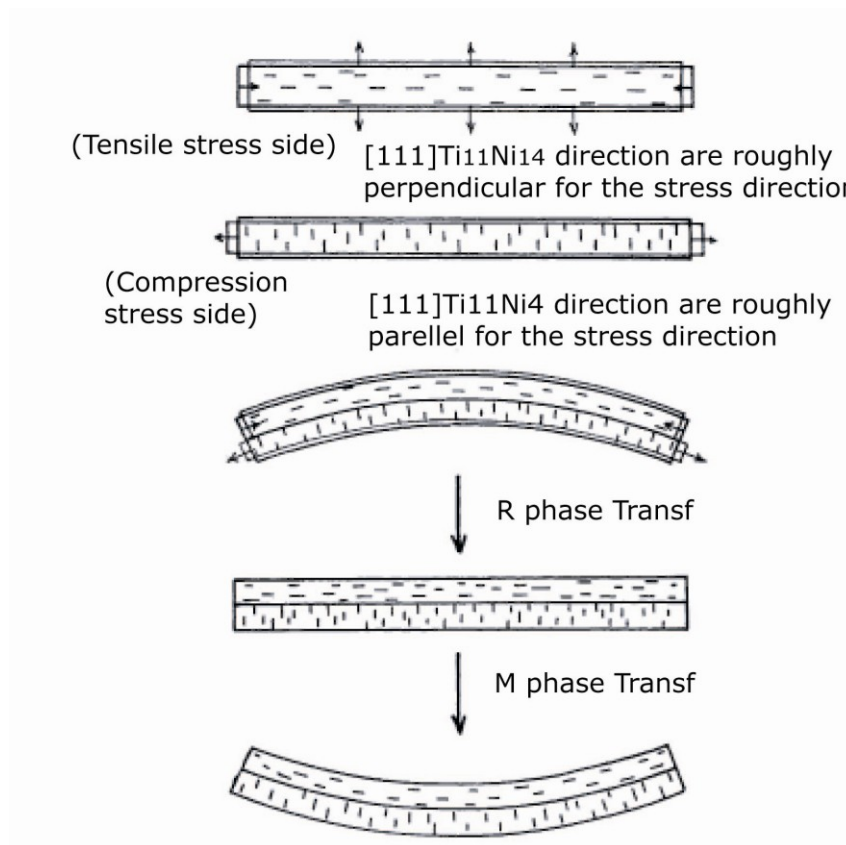


Figure 1.14 Mechanism of “all-round shape memory effect” [Kainuma et al. 1987].

Precipitates formed in constrained aging training can be observed using TEM [Zhang et al. 2003]. It has been shown the oriented strained fields around precipitates in NiTi can cause martensite variants to align in preferential directions. The stress fields around the precipitates can be recovered again after reversion to austenite phase. The mechanism of the precipitate-enabled TWSME is clear. However, the available two-way shape memory strain was not large (less than 1%), and the increase of Ni to form  $\text{Ti}_3\text{Ni}_4$  precipitates results in the lowering of  $M_s$  below ambient temperature, limiting its applications.

### ***1.3.2.3 Plastic Deformation and TWSME***

Plastic deformation training methods were used in early studies of TWSME. Researchers favored severe deformation in NiTi SMAs in order to achieve maximum two-way response [Liu et al. 1990]. Deformation in the martensitic state was used to introduce dislocations [Zhang et al. 1986; Otsuka et al. 1986; Kainuma et al. 1987; Meng et al. 2004; Omori et al. 2003]. The dislocation-related stress fields induced by martensitic deformation enable the formation of directional martensite variants upon cooling. For example, Meng et al. [2004] bent a TiNiHf high temperature shape memory alloy in the martensitic state to create slip deformation in the alloy. Figure 1.15, which plots the two-way shape memory strain as a function of the number of training cycles, shows that the two-way strain increases with the plastic deformation strain. The maximum two-way strain was reached around 0.9% after 6 training cycles at deformation strain of 7.1%.

Kim et al. [2009] studied the effect of compressive loading on the development of TWSME in NiTi shape memory alloys. The author did compressive load cycling to preset strains (1-6% in the experiment) in the martensitic state, and thermally cycled the specimen after unloading to measure the two-way strain. The two-way strain data, as shown in Figure 1.16, indicated a strong linear relation with compressive deformation strain. The maximum two-way strain reached around 2.3% on average for NiTi specimens at a compression of 6%. However, these results could not generate a whole picture of the relationship between two-way strain and

compressive strain. If the compressive strain was increased further, the two-way strain may further increase or possibly decrease due to heavy slip deformation.

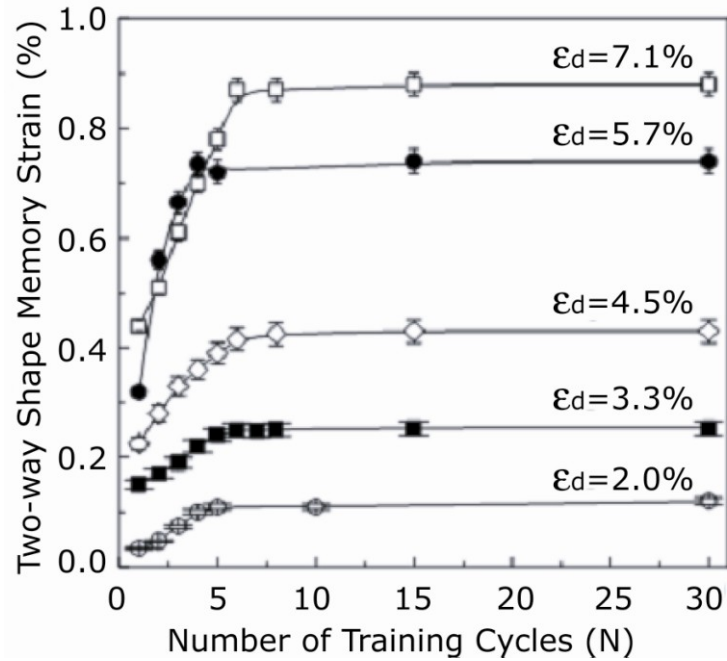


Figure 1.15 Effect of the number of training cycles on the two-way shape memory strain of the  $Ti_{36}Ni_{49}Hf_{15}$  alloy with different training strains [Meng et al. 2004].

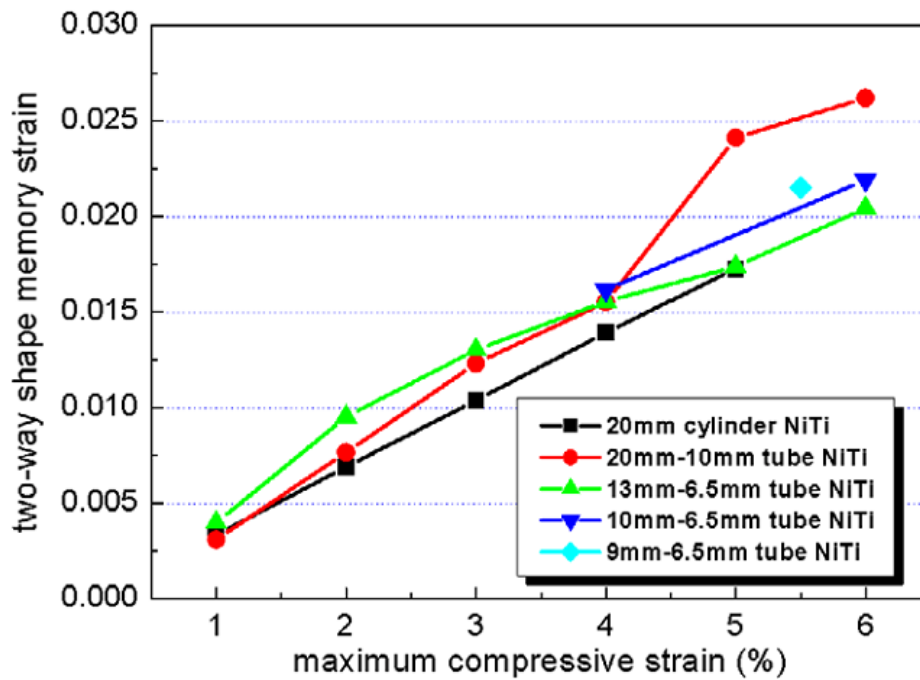


Figure 1.16 Effect of compressive prestrain on the development of two-way shape memory effect in NiTi shape memory alloys [Kim et al. 2009].

Slip-plasticity training has the advantage of requiring fewer training cycles (often just a single cycle) compared to traditional thermo-mechanical training methods. Figure 1.17 shows the TWSME obtained from a single uniaxial tensile deformation training [Liu et al. 1999]. Plastic deformation to a strain of 6.2% led to a 1.44% two-way strain upon subsequent thermal cycling. Tensile pre-strain of 8% leads to a two-way strain of 2.4%, as shown in Figure 1.18, which agrees with the 2.6% two-way strain developed by tensile deformation to 8% strain reported by Prader et al. [1997] for a cold-worked and annealed NiTi specimen. However, the two-way strain (1.44% at 6.2% tensile strain) is lower than what was developed under compression strain (2.3% at 6% compressive strain), as shown in Figure 1.16. This difference might be due to tension-compression asymmetry [Patoor et al. 1995]. It was reported that the critical deformation stress is higher in compression than in tension, which suggests that there are more dislocations developed in compression than in tension for the same deformation strain. It is possible that these dislocations help increase the two-way strain in compression. From Figure 1.18, it can also be seen that the maximum two-way strain was 4.1% for a tensile strain of 13.3%. This important evidence suggests the two-way strain in compression can be higher than 2.3% if the deformation strain increases (refer to Figure 1.16). Also shown in Figure 1.18, further increasing the deformation strain decreases the two-way strain because heavy slip deformation serves as a barrier for the specimen to recover.

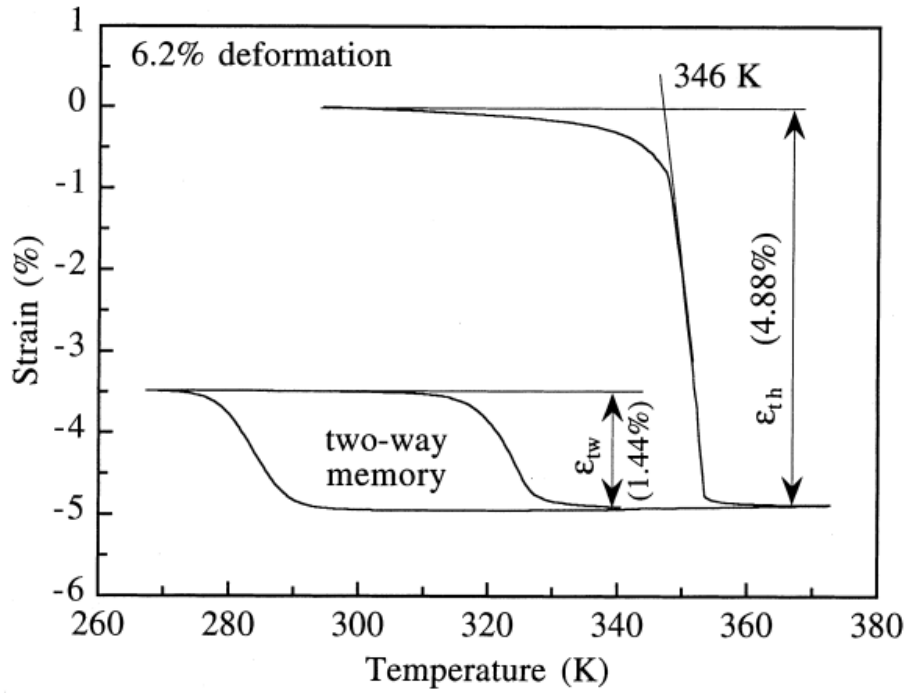


Figure 1.17 The TWSME obtained after a single deformation of 6.2% strain in an equiatomic NiTi alloy [Liu et al. 1999].

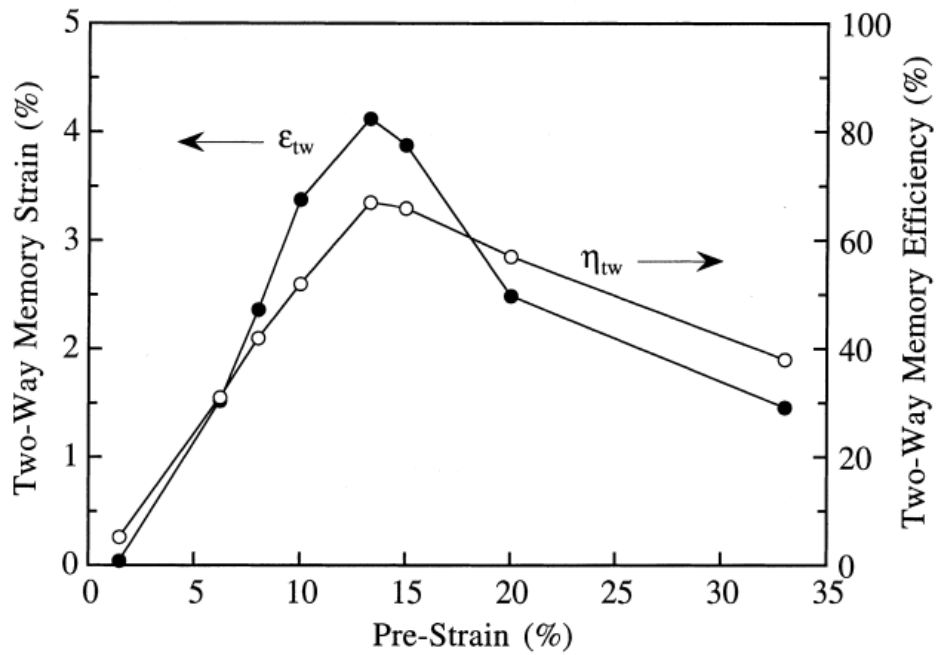


Figure 1.18 Effect of prestraining in tension on the development of two-way shape memory effect in an equiatomic NiTi alloy [Liu et al. 1999].

### **1.3.3 The Mechanisms of TWSME**

#### ***1.3.3.1 Introduction***

There are 3 mechanisms proposed for TWSME in the literature: the retained martensite theory [Saburi et al. 1974], the internal residual stress field theory [Zhang et al. 2003], and the microstructural anisotropy and thermodynamical anisotropy theory [Stalmans et al. 1992], the details of which will be reviewed below.

It was speculated by Saburi et al. [1974] that the retained martensite variants at temperature above  $A_f$  can preferentially grow and modify the arrangement of other variants upon cooling. It was also reported by Zhang et al. [2003] that the residual stress changed thermoelastic martensitic transformation from the formation of 24 self-accommodated martensite variants to certain directional martensite variants upon cooling. It was also found by Stalmans et al. [1992] that, in the Cu-Zn-Al alloys, a great number of dislocations in the parent phase could favor the growth of certain martensite variants out of the 24 possible habit plane variants. Below is the detailed discussion of these mechanisms of TWSME in the literature.

#### ***1.3.3.2 The Retained Martensite Theory***

Saburi found a reversible shape memory effect in Cu-Zn-Ga alloys due to slip deformation in the martensitic phase and proposed the retained martensite theory in which the retained martensite variants at a temperature above  $A_f$  can preferentially grow and modify the arrangement of other variants upon cooling [Saburi et al. 1974;

Perkins et al. 1984]. These retained martensite variants can be generated by overstraining the martensite in the martensitic state or stress-inducing martensite at a temperature above  $A_f$ . The overstrained martensite is thought to be stabilized by dislocation induced strain fields generated under repeated training cycles. These may then serve as nucleation sites for the formation and preferential growth of martensite variants upon cooling. However, experimental results also show the retained martensite can be removed by overheating during martensite-to-austenite transformation without affecting TWSME. Thus the retained martensite theory is thus an unlikely mechanism of TWSME.

### ***1.3.3.3 The Residual Stress Field Theory***

Shroeder and Wayman [1977] did thermo-mechanical cycling on Cu-Zn single crystals where the specimens were first deformed in the martensitic state and then recovered to austenite without load in each training cycling. After training, a single orientation of martensite variant was formed during cooling, thus showing TWSME. Delaey and Thienel [1975] documented the changes occurring in the microstructure of a polycrystalline CuZnAl sample as it was subject to up to ten training cycles. The conclusion was that nucleation of a particular martensite variant is responsible for the spontaneous shape change on cooling. Delaey further noted that plastic deformation developed during training results in a residual stress field that may influence martensite microstructures during cooling. Perkins et al. [1984] also noted that the plastically deformed local regions may explain TWSME. As shown in Figure

1.19, the thermo- mechanically trained specimen has dark streaks which are thought to be full of tangled dislocations. Martensite plates once residing in these regions will form into these regions again upon martensitic transformation. These preferentially formed martensite variants reoriented the subsequently formed martensite variants, thus generating TWSME.

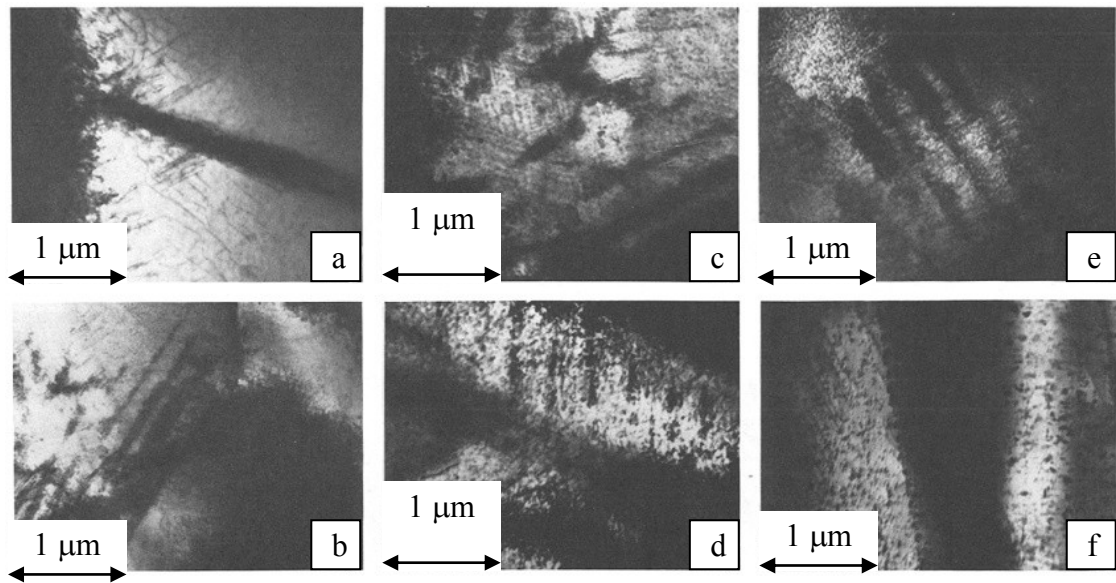


Figure 1.19 Dark Streaks in the austenite phase after several training cycles. (a) to (d) 3 cycles, (e) to (f) 5 cycles [Perkins et al. 1984].

Moreover, molecular dynamics simulation [Zhang et al. 2003] suggested that thermally induced martensite nucleation sites are either above or below the paired dislocations, where there are tension or compression stress fields of the dislocations, as shown Figure 1.20. During growth, nuclei of martensite line up in the middle of the paired dislocations and grow to a single variant via the movement of dislocation by shear. Therefore, dislocation arrays in the material developed by thermomechanical cycling selectively grow certain martensite variants to accommodate the

dislocation-induced stress field. The existence of these directional martensite variants serves as the basis of dislocation assisted TWSME.

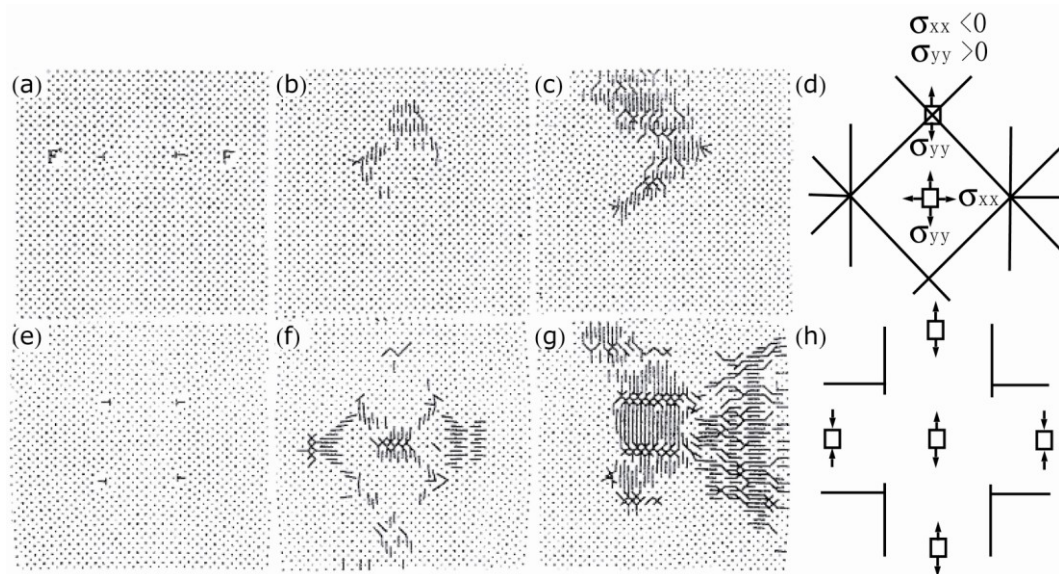


Figure 1.20 MD simulations show martensite nucleation and growth, (a)-(c) for a pair dislocation, (e)-(g) for two pair dislocations. (d) and (h) show the stress fields of one pair and two pair dislocations [Zhang et al. 2003].

In addition, Rios-Jara and Guenin [1987] studied in detail the correspondence between dislocation arrays and repeatedly induced variants in thermo-mechanically cycled single crystal Cu-Zn-Al alloy. They reported that all of these dislocations in the single crystal of the  $\beta_1$  parent phase formed by thermo-mechanical cycling of copper based alloys have the same  $\langle 110 \rangle_{\beta_1}$  type Burgers vector, as shown in Figure 1.21. The maximum shear in a strain field of this type of dislocation coincided with the macroscopic shear observed in the martensitic transformation. These dislocations shared the same  $\langle 110 \rangle_{\beta_1}$  Burgers vector and accumulated in bands parallel to the trace given by the habit plane of the induced variant. By studying the isolated dislocations, it was found that the glide planes of these dislocations correspond to the

basal planes of the induced martensite variants, thus achieving minimal free energy in these variants. However, there are 4 out of 24 crystallographically equivalent martensite variants that satisfy this condition. Therefore, this theory could not describe the one-to-one correspondence between martensite variant and austenite, as required by TWSME.

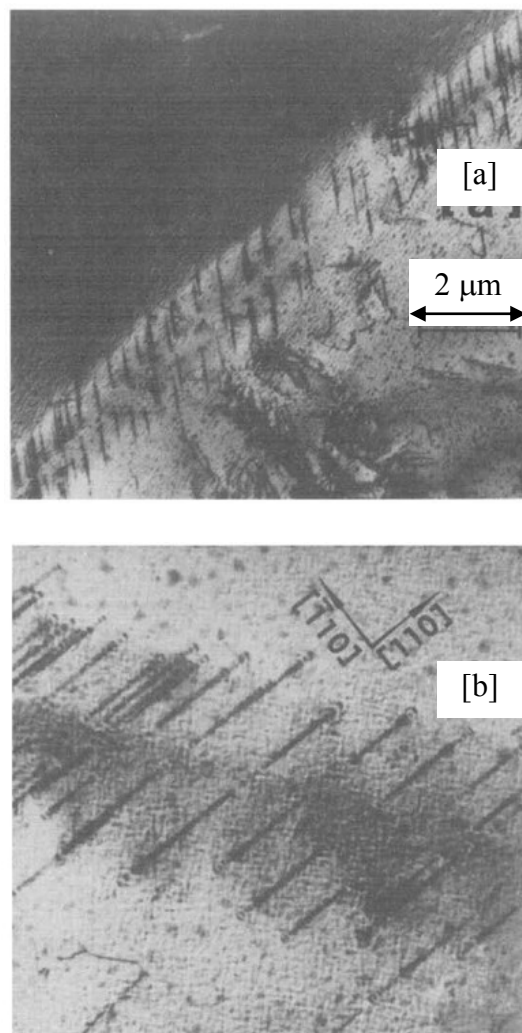


Figure 1.21 Transmission electron micrograph showing a “Comb-shaped” arrangement of dislocations observed in the thermomechanical cycled Cu-Zn-Al alloy. (a) zone axis  $G=[-1-11]$ . (b) Same zone as in (a) but under a  $B=[001]\beta_1$  direction of observation. Here the projection of both dislocations in a pair are coincident: the plane containing a pair is  $(1-10)\beta_1$  which corresponds to their glide plane [Rios-Jara et al. 1987].

Furthermore, Manach et al. [1993] thermo-mechanically trained a room temperature austenitic Ti-50.2 at% Ni shape memory alloy on a hydraulic tension-compression device to develop TWSME. The first training procedure consisted of 20 cycles of heating to 363 K ( $A_f$  was 305 K) and cooling to 285 K ( $M_s$  was 276 K) without load, followed by an isothermal loading up to a shear strain of 5% and unloading to 0% (the stress went to zero before the strain went to zero). The deformation strain was recovered by heating in the second training cycle. It should be noted with cyclic training deformation strain accumulated and could not be fully recovered. A superelastic cycle via shearing was then performed between -5% and 5% in the austenitic state at  $T=313$  K to observe the stress-strain characteristics of the trained material. After this, the specimen underwent a second training procedure that was in the exactly same way as the first procedure, but with a reversed shearing direction.

Figure 1.22 shows the shear stress-strain curves during the first and second training cycles. The difference in the shear stress during the first and second training cycles indicates the existence of internal stress fields. This is more clearly shown in Figure 1.23 and 1.24 which show stress-strain curves being asymmetric in the opposite directions. Since the existence of an internal stress field will assist martensitic transformation in the stressed direction and act as an obstacle in the opposite direction, the shear stress needed to induce martensitic transformation has to be lower for the training direction (the same as the stress direction) than for the

opposite one. The asymmetry in the hysteresis also suggests that internal stresses create friction between the martensite variants during phase transformation. Some variants have to overcome this friction energy, thus making them thermodynamically unfavorable to form during cooling, which leads to a thermo-dynamical anisotropy theory that will be discussed in the next section. The thermodynamically favorable martensite variants will preferentially form during cooling, competing with the formation of the self-accommodated martensite variants.

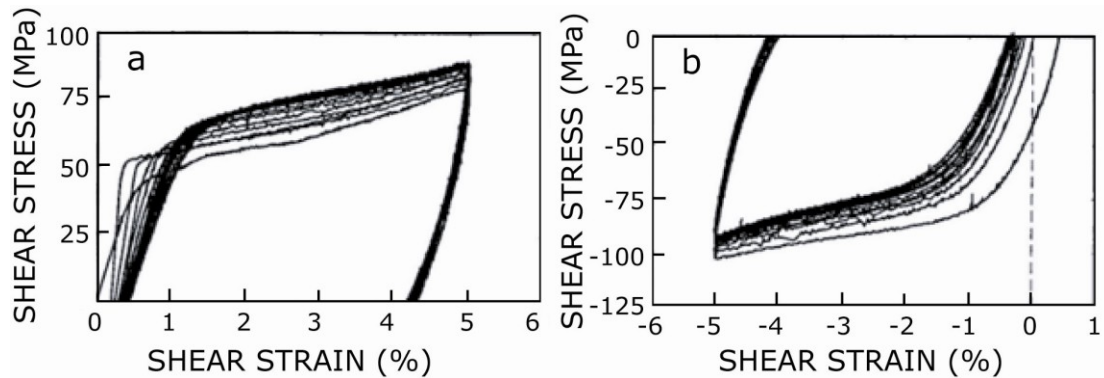


Figure 1.22 a) and b) Shear stress-strain curves obtained at  $T=285$  K during isothermal shearing test in the first training and second training [Manach et al. 1993].

#### 1.3.3.4 Thermodynamic Anisotropy Theory

Stalmans et al. [1992(a) and (b)] studied TWSME induced by thermo-mechanical training of Cu-based SMAs and speculated that dislocations developed during training induced a microstructural anisotropy. The microstructural anisotropy leads to martensite variants having different free energies, thus causing a thermodynamic anisotropy.

It was found that TWSME reached a maximum after about 30 training cycles and decreased thereafter due to an increasingly imperfect one way shape memory recovery caused by dislocation accumulation. They also calculated the free energies of the martensite variants developed after two-way training and compared them to the case of the untrained thermoelastic martensite variants (The training stress dependent free energy,  $\Delta G_{\delta}$  which is derived from Clausius-Claperyon equation equals the product of training stress ( $\delta$ ) and transformation strain ( $\Delta \varepsilon_{TR}(m)$ ) of martensite variant ( $m$ ) resolved along the direction of external stress:  $\Delta G_{\delta} = \delta \cdot \Delta \varepsilon_{TR}(m)$ ). The martensite variants formed after two-way training were found to have lower free energies than the untrained thermo-elastic martensite variants, thus being thermodynamically favored and preferentially formed during cooling. It is the dislocation arrays in the martensite variants that lower the free energy and provide suitable sites for martensite variants to form. Therefore, plastic deformation to generate dislocation arrays is assumed to be a prerequisite to develop TWSME.

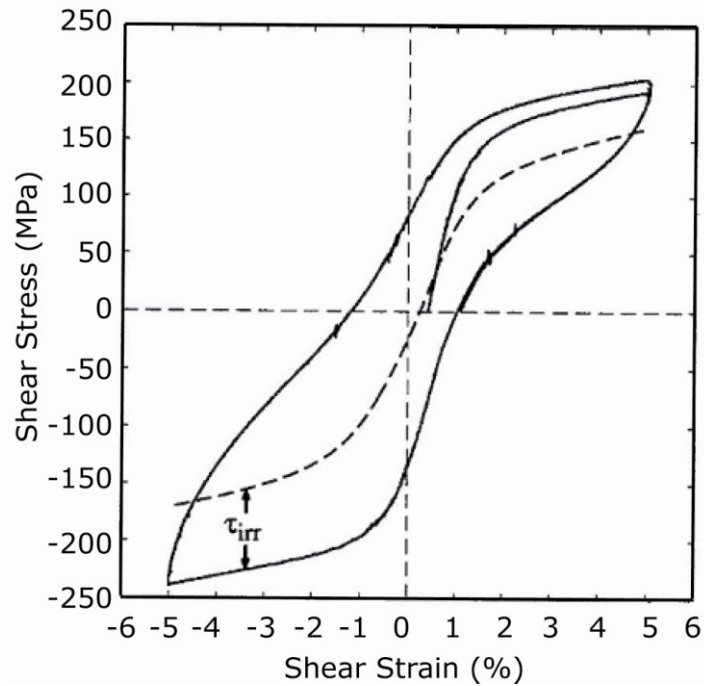


Figure 1.23 Shear stress-strain curve obtained during a super-elastic cycle with strain of  $\pm 5\%$  at  $T=313$  K after first shearing cycling. The dash line in the hysteresis indicates the estimated reversible stress contribution to the hysteresis.  $\tau_{irr}$  is the irreversible stress contribution induced by training [Manach et al. 1993].

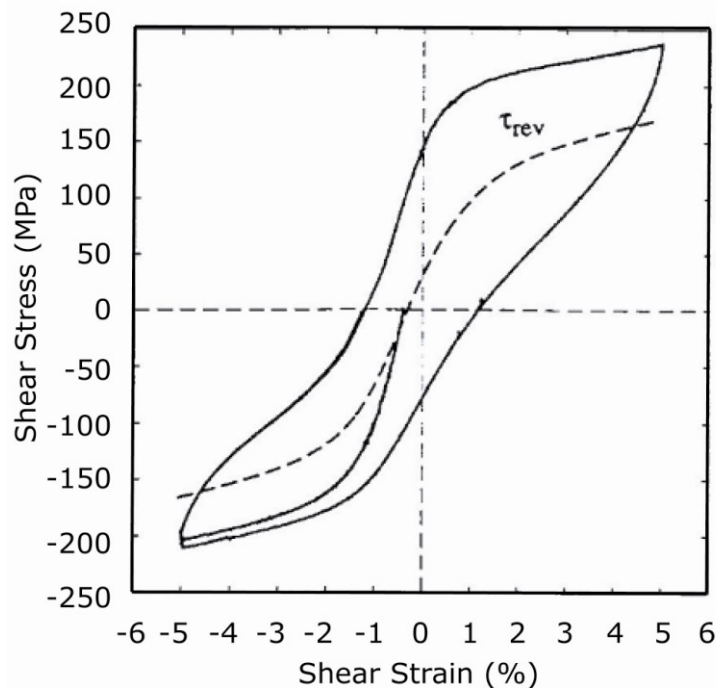


Figure 1.24. Shear stress-strain curve obtained during a superelastic simple shear cycling with strain of  $\pm 5\%$  at  $T=313$  K. The dash line in the hysteresis indicates the estimated reversible stress contribution to the hysteresis [Manach et al. 1993].

To conclude, it is clear that retained martensite is not the origin of TWSME since the retained martensite can be removed by overheating without greatly affecting TWSME. Dislocations developed by plastic deformation are important for the TWSME observed. However, over deformation negatively affects TWSME because experimental results suggest that a large number of dislocations developed by over deformation can resist M-A-M phase transformations. Therefore, the training induced microstructural anisotropy and thus thermodynamic anisotropy maybe the most likely mechanism of TWSME, because martensite variants are found to be different thermodynamically after training. Even though it is difficult to directly observe how dislocation arrays preferentially select martensite variants, dislocation arrays are calculated to have lowest energy in the martensite variants where they were originally formed. Therefore, the existence of these dislocation arrays helps form these thermodynamically favorable martensite variants. However, there is limited study on the origin of TWSME in literature. Many researchers tend to agree with the thermodynamic anisotropy theory proposed by Stalmans et al. [1992].

#### **1.3.4 Indentation in Shape Memory Alloys**

As stated in the introduction to this chapter, indentation methods have historically provided an alternative to conventional tensile tests to characterize mechanical properties. Compared to other mechanical testing techniques, the indentation method has several advantages, such as the simplicity of sample preparation, characterization ability under wet environments, and the quantitative

characterization at the nanometer scales. Furthermore, as is well known, indentation can induce just the sort of dislocation substructures that drive TWSME.

Indentation has also been used to probe shape memory and superelastic effects at multiple length scales and under complex loading conditions. Ni et al. [2003] used both micro-indentation and nano-indentation on bulk NiTi shape memory alloys and observed the indentation-induced shape memory and super-elastic characteristics. As was shown in Figure 1.1, shallow spherical indents made by an instrumented indenter can completely recover after heating above  $A_f$  due to the shape memory mechanism. Deeper spherical indents became shallower on heating but were not completely removed.

Figure 1.25 shows that a complete shape memory recovery occurs up to the point at which the representative strain is larger than 5%. The representative strain,  $\varepsilon_r$ , equals  $0.2a/r$  for spherical indents, where  $a$  is the indent contact radius and  $r$  is the indenter radius.  $\varepsilon_r$  correlates with the true strain in the uniaxial tensile test. (A detailed discussion on representative strain will be given in section 1.4.2.) Above a representative strain of 5%, slip plasticity occurs in martensite and dislocations remain after heating above  $A_f$ , generating a residual indent in austenite.

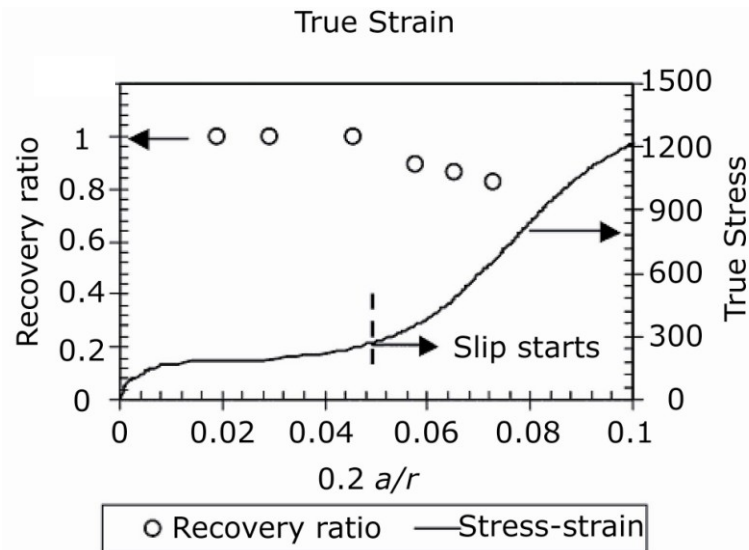


Figure 1.25 Plots of the recovery ratio, true stress against the representative strain ( $0.2a/r$ ). Complete recovery occurs when the representative strain is less than 5%, beyond which slip plasticity occurs [Ni et al. 2002].

Frick et al. [2006] used a Berkovich nanoindenter to characterize the stress-induced martensitic transformation and shape memory response at the nano scale. Figure 1.26 shows the indent depth recovery upon heating for pseudoelastic and shape memory NiTi alloys, and [111] Ni. Full depth recovery was achieved in the shape memory alloy at 100  $\mu\text{N}$ . This is probably because the blunting of the Berkovich indenter tip leads to spherical-like indentation under low load such as 100  $\mu\text{N}$ . However, when the load is increased, the depth recovery decreased due to severe deformation under the sharp indenter.

Apart from indenting bulk material, Shaw et al. [2003] indented shape memory thin films and characterized shape memory and super-elastic responses in thin films. Several other groups have also investigated shape memory and superelastic

effects using micro- and nano-indentation techniques [Liu et al. 1999; Cheng et al. 2001; Gall et al. 2001; Ma et al. 2003, 2004; Qian et al. 2004; Liu et al. 2005; Shaw et al. 2005; Frick et al. 2005; Huang et al. 2005; Komvopoulos et al. 2005; Zhang et al. 2006; Wood et al. 2006; Su et al. 2007; Crone et al. 2007; Yan et al. 2007; Arciniegas et al. 2008]. Indenter type, indentation depth, and indentation temperature play an important role in the shape memory and superelastic responses after indentation. These parameters were used to maximize the indentation-induced TWSME in the present study.

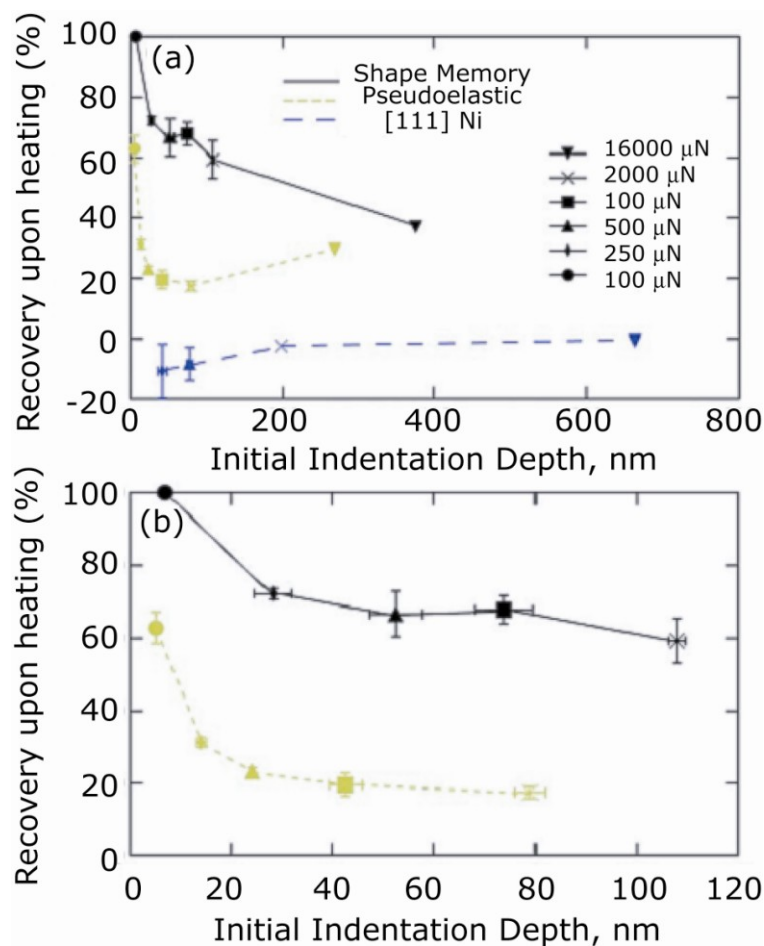


Figure 1.26 a) Indent depth recovery upon heating for pseudoelastic, shape memory alloys and [111] Ni with max load up to 16000  $\mu\text{N}$ ; b) Indent depth recovery upon heating for pseudoelastic and shape memory alloys with max load up to 2000  $\mu\text{N}$  [Frick et al. 2006].

### 1.3.5 The Indentation Induced TWSME

Plastic deformation can generate dislocations in martensite that strongly affect subsequent shape-memory mechanisms [Fernandez et al. 2003; Stalmans et al. 1992; Liu et al. 1998; Wang et al. 2005; Lahoz et al. 2002], causing shape changes upon both heating and cooling.

Zhang et al. [2006] also reported that deep spherical indentation can induce slip deformation that causes the indent to become shallow upon heating and deepen upon cooling, as shown in Figure 1.27. When indents were removed by a planarization step, thermally-reversible flat-to-bumpy surface transitions were observed for both wrought NiTi shape memory alloys, and in NiTi thin films. We call this transition *Surface Form Memory* (SFM).

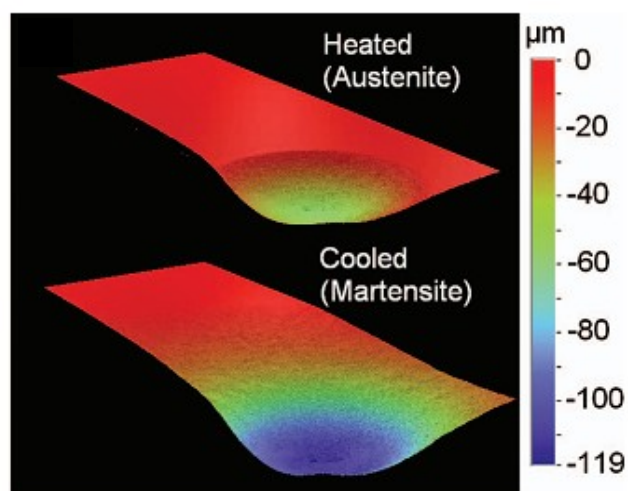


Figure 1.27 WYKO optical profile measurement of the two-way indent depth change of a deep spherical indent upon heating and cooling [Zhang et al. 2006].

Figure 1.28(a) shows SFM of a 3x3 array of spherical exdents made by planarization of an array of spherical indents in a bulk martensite NiTi sample, after heating to austenite, and cooling to martensite. This exdent-to-flat surface transition is cyclical reversible indefinitely<sup>†</sup>. Figure 1.24(b) and (c) show the exdent-to-flat surface transition of a scratch made by a conical indenter in a bulk martensitic NiTi sample and a micro-indent made by a conical indenter in a thin film martensitic NiTi sample [Zhang et al. 2006].

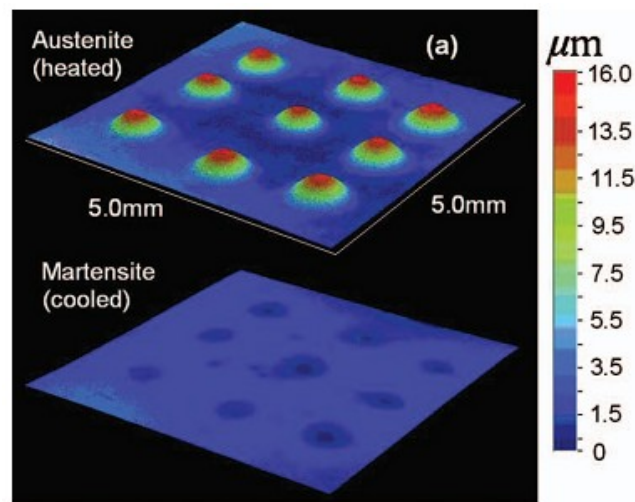


Figure 1.28 Three dimensional profiles of reversible surface exdents: (a) a 3x3 array of spherical exdents on the surface of the austenite phase of NiTi at high temperature which disappears when the sample is cooled to the martensite phase. (b) A protruding line on the surface of the austenite phase that nearly disappears in the martensite phase. (c) A nanoscale reversible protrusion on the surface a NiTi film. [Zhang et al. 2006]

---

<sup>†</sup> Experiments have recorded tens of cycles with apparent convergence on a steady state.

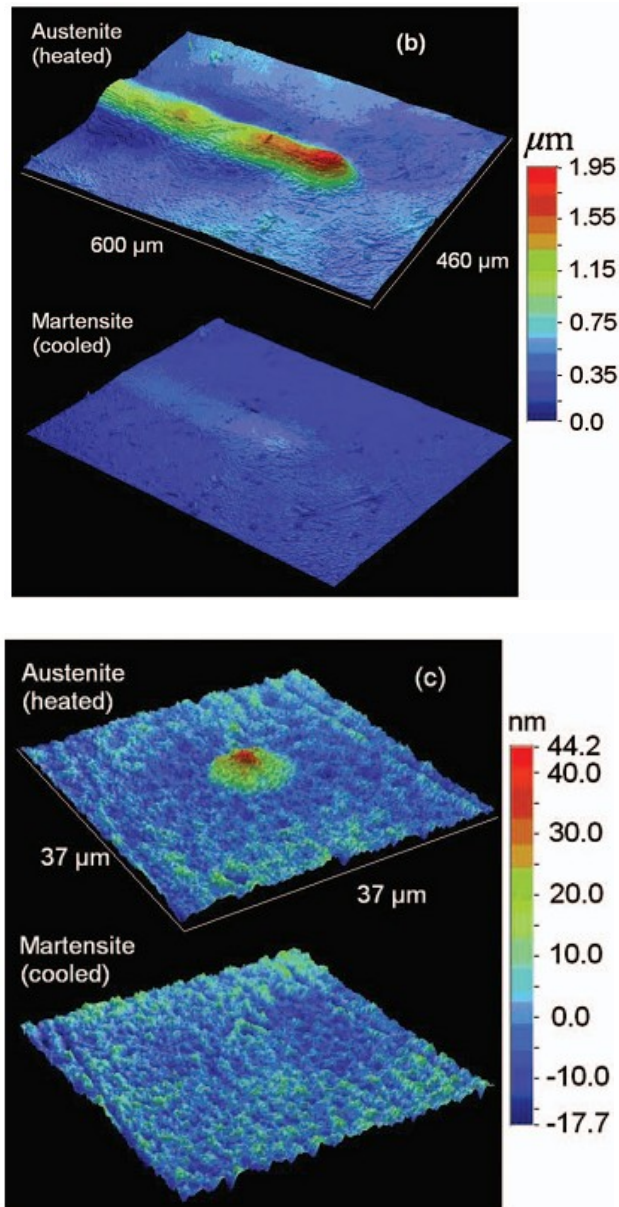


Figure 1.28 cont'd.

#### 1.4 Contact Mechanics

The concept of contact mechanics was first introduced by Hertz in 1888 [Hertz, 1896; Johnson, 1985]. However, the development of the theory stalled until the early 20<sup>th</sup> century, until it was revived, driven by engineering developments on the railways, marine reduction gears, and in the rolling-contact bearing industries. The theory

generally applies to normal contact between two rigid smooth solids. Contact problems are important in the context of wear, scratch testing, and indentation.

#### 1.4.1 Elastic Contact

Elastic contact problems for spherical and sharp indenters into a half space are important because they underlie the measurement of hardness, which is indicated as the mean contact pressure  $P_m$ .  $P_m$  is defined as the normal load  $F$  on the indenter divided by the contact area:  $P_m = F/\pi a^2$ . We can also refer to the mean contact pressure as the “indentation stress” and  $0.2a/r$  as the “indentation strain”. This then connects the indentation stress-strain response with the commonly obtained conventional uniaxial tension and compression stress-strain response.

Tabor proposed using the representative strain or the “indentation strain”, as a function of the  $a/r$  ratio, to characterize spherical indentation into elasto-plastic solids [Tabor, 1948, 1996]. The representative strain is  $\mathcal{E}_r = 0.2 a/r$ . It is deduced by plotting the indentation and uniaxial deformation data of copper and steel (see Figure 1.29) where the representative strain is equal to the true strain, and the hardness  $H$  is about 2.8 times of the true stress,  $Y$ . The empirical correlation between spherical indentation and uniaxial tensile data shows that the representative strain can be used to measure the true stress-strain relationship.

For elastic contact, several assumptions are generally made.

1. The radii of curvature of the contact bodies are large compared with the in-plane radius of the circle of contact. So we can treat each surface as an elastic half-space to derive stresses and displacements information.
2. The dimensions of each body are large compared with the radius of the circle of contact. This allows indentation stresses and strains to be considered independently of those arising from the geometry, method of attachment, and boundaries of each solid.
3. The contact is frictionless. Only a normal pressure is transmitted between the indenter and the specimen.

Spherical indentation contact problems are of special interest due to their relationship to the present work. The most well-known scenario is the contact between a rigid sphere and a flat surface, where Hertz found that the elastic contact radius,  $a$ , can be calculated as:  $a = \left(\frac{3FR}{4E^*}\right)^{1/3}$ , where  $F$  is the indenter load,  $R$  is the radius of indenter, and  $E^*$  is the reduced modulus, which is a combined function of the modulus of the indenter and the substrate, as seen in Eq. (1.2):

$$\frac{1}{E^*} = \frac{1-\nu^2}{E} + \frac{1-\nu'^2}{E'} \quad \text{Eq. (1.2)}$$

where  $E'$  and  $\nu'$ , and  $E$  and  $\nu$ , are the elastic modulus and Poisson's ratio of the indenter and the specimen respectively.

On the contact surface the contact pressure is not uniformly distributed. The maximum contact pressure  $P_o$  is  $3/2$  of  $P_m$  at the depth of contact radius  $a$ , as expressed in Eq. (1.3) as

$$P_o = \frac{3F}{2\pi a^2} = \left( \frac{6FE^*}{\pi^3 R^2} \right)^{1/3} \quad \text{Eq. (1.3)}$$

$P_o$  reaches maximum when  $a=r$ .

The vertical displacement of the surface within the contact radius, measured with respect to the original specimen free surface, is given by Eq. (1.4):

$$u_z(r) = -\frac{1-\nu^2}{E} \frac{\pi P_o}{4a} (2a^2 - r^2), \quad r \leq a \quad \text{Eq. (1.4)}$$

Cylindrical contact cannot be calculated solely by the Hertzian theory since it is an elastic compression of a two-dimensional body, which needs adjustments of the shape and size of the body and the way in which it is supported. Line contacts such as gear teeth and roller bearings are difficult to calculate due to its support system while the compression of circular cylinder in between two compressors can be analyzed successfully.

For a cylindrical indenter, the compressive load per unit axial length,  $F$ , gives rise to a Hertzian distribution of pressure  $P$  at the lower contact point

$$P = \frac{2F}{\pi a} \left(1 - \frac{x^2}{a^2}\right)^{1/3}, \quad \text{where } a^2 = \frac{4FR}{\pi E^*}. \quad \text{The vertical displacement is}$$

$$\delta = 2P\left(\frac{1-\nu^2}{\pi E}\right)\left[2 \ln\left(\frac{4R}{a}\right) - 1\right] \quad \text{Eq. (1.5)}$$

#### 1.4.2 Elastic-Plastic Contact

In metals, slip-plasticity develops when the elastic contact stress exceeds the material's yield stress in compression, which means that  $P_m/Y$  is larger than 1. One can visualize that as the indenter is pressed deep into the substrate, a plastic zone appears below the indenter tip, surrounded by an elastic region. This is called the “contained mode”, where  $P_m/Y$  is between 1 and 3. The plastic zone grows deep into the substrate with indentation and also eventually breaks out to the free surface. From then on, the displaced material is free to escape by plastic flow to the sides of the indenter. This is the “uncontained mode” of indentation. This “uncontained mode” begins when the mean contact pressure  $P_m$  reaches about triple the yield stress  $Y$  [Johnson, 1986].

Both finite element analysis and semi-analytical models are commonly used in analyzing elastic-plastic contact problems. A semi analytical spherical cavity model was proposed by Johnson to explain the elastic-plastic indentation process [Johnson, 1986]. In this spherical cavity model, the contact surface of the indenter is encased in a hemispherical “core” with a hydrostatic component,  $p$ . Outside of the core it is assumed that the material will respond the same way as in an elastic half space containing a spherical cavity under hydrostatic pressure,  $p$ . The elastic-plastic

boundary is somewhere outside the spherical cavity. The hydrostatic pressure,  $p$ , below the indenter can be expressed in Eq. (1.6) as

$$\frac{p}{Y} = \frac{2}{3} \left\{ 1 + \ln \left[ \frac{E^* t a \beta + 4(1-2\nu)}{6(1-\nu)} \right] \right\} \quad \text{Eq. (1.6)}$$

where  $Y$  is the yield stress of the indented material in compression.  $\beta$  is the angle of the indenter at the edge of the contact (for example:  $\beta$  is  $19.3^\circ$  for Berkovich indenter and  $\beta = \arcsin(a/r)$  for spherical indenter).

Figure 1.30 shows the finite element modeling of the expansion of plastic zone during spherical indentation [Hardy et al. 1972]. Plastic flow leads to a flattening of the pressure distribution as can be seen for the  $p/k$  value against  $r/a_Y$ . The development of the plastic zone roughly follows the contours of  $J_2$ , which is the second invariant of the deviatoric part of the Cauchy stress, and is contained beneath the contact area. In the fully plastic state for the spherical cavity model,  $P/P_Y$  equals 400, which refers to the elastic-plastic boundary. Sinclair et al. [1985] carried out a detailed finite element analysis of the spherical indentation on elastic-plastic solids. They confirmed Tabor's experimental correlations for work-hardening materials using the representative strain, and found generally good agreement between theory and other physical evidence. In addition, they also found there was high strain gradient near the contact edge that was not predicted before.

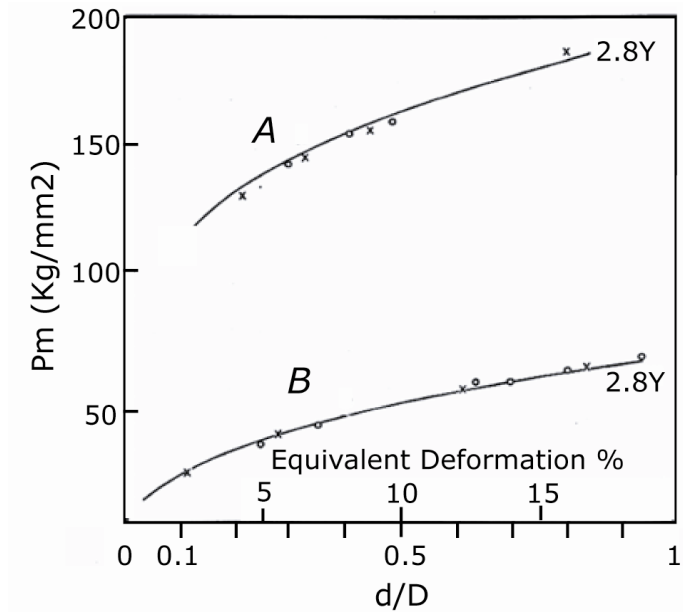


Figure 1.29 Representative strain vs. mean stress in spherical indentation, and its correlation with equivalent true stress-true strain behavior in uniaxial tension (Solid line). Metal A is Steel and metal B is Copper. [Tabor 1948, 1996]

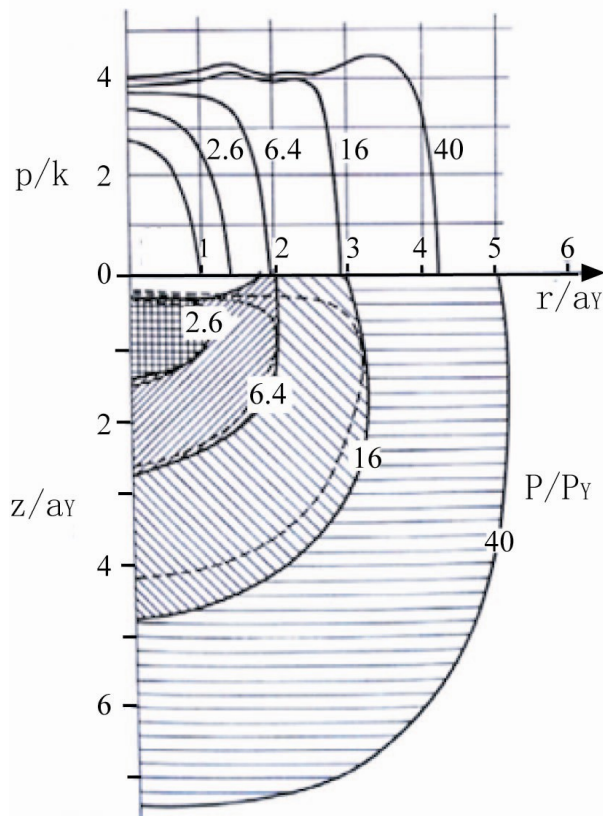


Figure 1.30 Finite element modeling of indentation of an elastic-plastic half space by a rigid sphere: development of the plastic zone. Broken line: contour of  $J_2$ .  $P_Y$  is the normal load needed to first initiate plastic flow. [Hardy et al. 1971]

### 1.4.3 Indentation Related Contact Mechanics

The indentation process is a highly nonlinear problem where large strains and deformations as well as material nonlinearities and contact are involved. Indentation related contact problems need the understanding of elastic-plastic deformation regime and material flow.

Figure 1.31 shows the plastic flow motion under Vickers indentation [Mata et al. 2002]. The solid at the indenter's tip flows primarily toward the  $z$  direction while the solid at the indenter's face flows toward the  $r$  direction because the downward motion needs to be compensated by upward flow adjacent to it, based on slip line field theory.

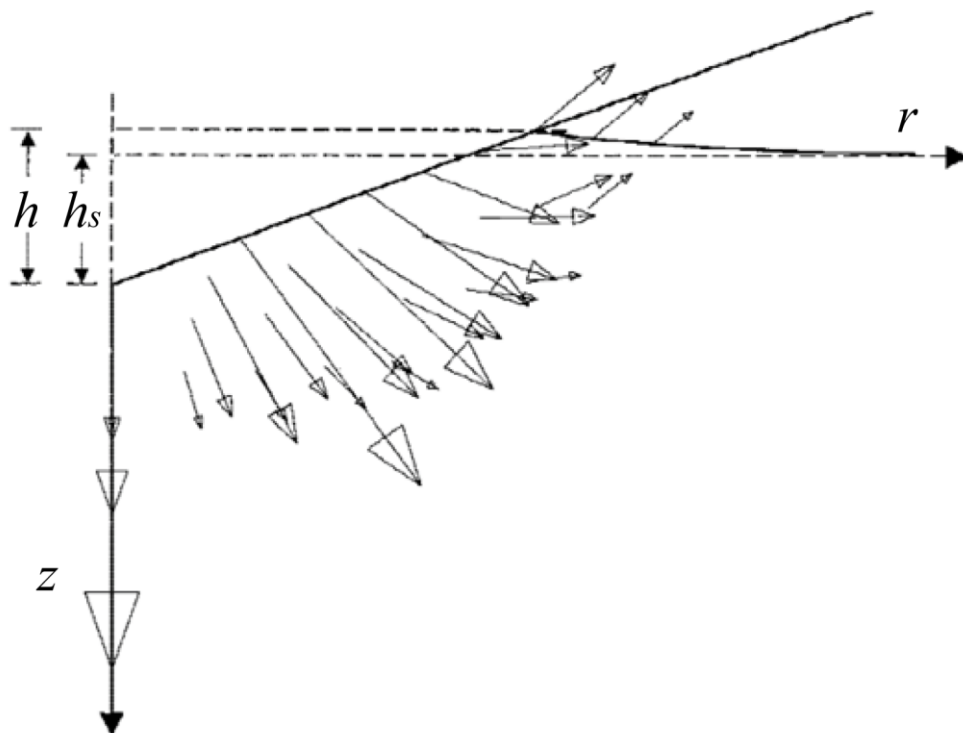


Figure 1.31 Flow patterns exhibited in a material that piles up [Mata et al. 2002].

During the process of indentation, the contact regime evolves from (i) an elastic deformation, to (ii) an elastic-plastic transition, and to (iii) a fully plastic regime. Sink-in and pile-up transitions can be observed for different materials.

Figure 1.32 compares the plastic zone size between spherical indent and conical indent at different  $a/r$  ratios and illustrated the transition from sink-in to pile-up for materials with different strain hardening exponent  $n$  [Mata et al. 2006].

The following observations are pertinent:

(i) For a material with large values of  $n$  and high yield strength ( $E = 200$  GPa,  $\sigma_s = 1000$ MPa, and  $n = 0.4$ , as shown Figure 1.32 (a)), it is noted that sinking-in of material occurs around the contact boundary for both the conical and spherical indents. Plastic deformation is contained by elastic deformation zone. It is also shown that the size of the plastic zone for the conical indent with indenter half angle of  $70.3^\circ$  matches up with that of the spherical indent when the  $a/r$  reaches 0.635, indicated by the normalized plastic zone size,  $z_{ys}/h_s$ .

(ii) As  $n$  and yield strength decrease ( $E = 200$  GPa,  $\sigma_s = 400$ MPa, and  $n = 0.2$ ), the plastic zone breaks out to the free surface leading to an uncontained deformation mode, as shown in Figure 1.32b. The plastic zone size of conical indent still matches up with spherical indent at  $a/r$  of 0.635.

(iii) For even lower values of  $n$  and yield strength ( $E = 200$  GPa,  $\sigma_s = 50$ MPa, and  $n = 0.1$ ), the material in the contact boundary flows primarily toward the free surface thus leading to the development of pileup, as shown in Figure 1.32c. Still, the plastic zone size of conical indent matches up with spherical indent at  $a/r$  of 0.635.

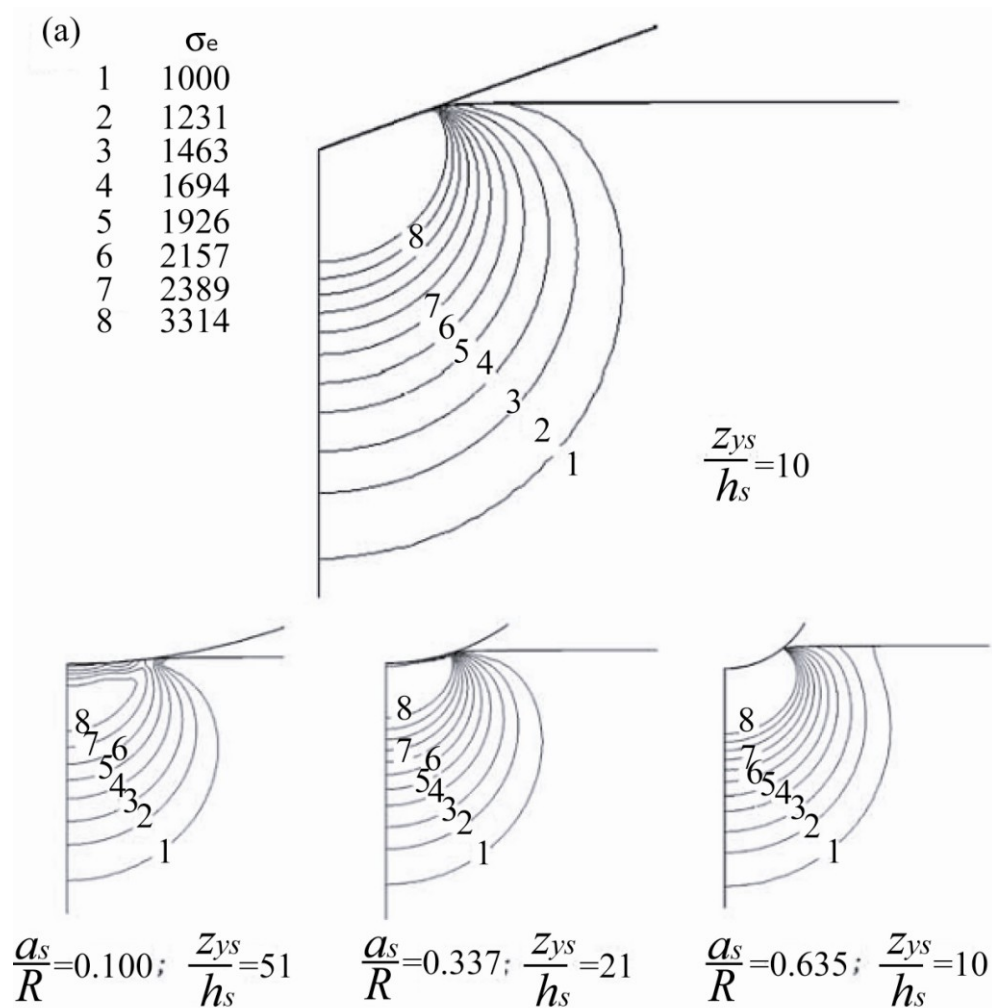


Figure 1.32 Comparison of the plastic zone size between conical and spherical indentations at different values of  $a/R$  for (a) highly elasto-plastic solid ( $E=200$  GPa,  $\sigma_s = 1000$  MPa, and  $n = 0.4$ ), (b) a solid with reduced elasto-plastic character ( $E=200$  GPa,  $\sigma_s = 400$  MPa, and  $n = 0.2$ ), and (c) a fully plastic solid ( $E = 200$  GPa,  $\sigma_s = 50$  MPa, and  $n = 0.1$ ). [Mata et al. 2006]

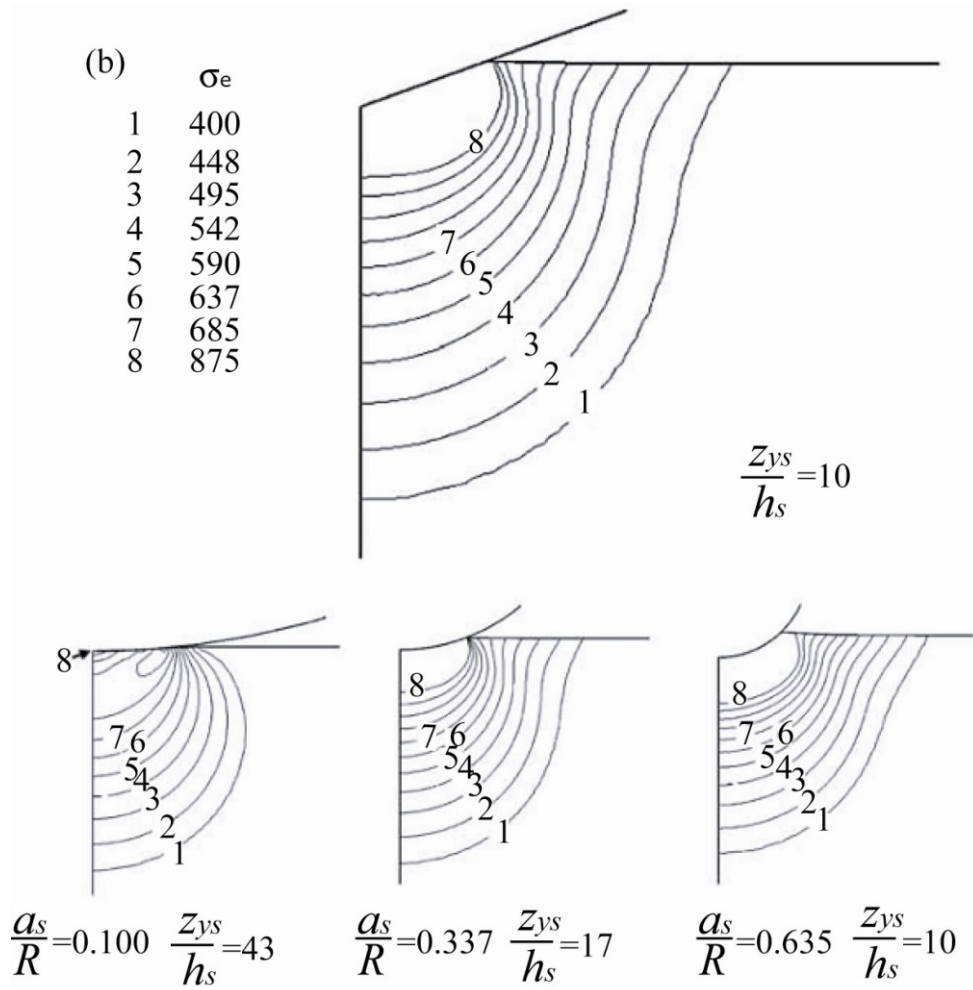


Figure 1.32 cont'd.

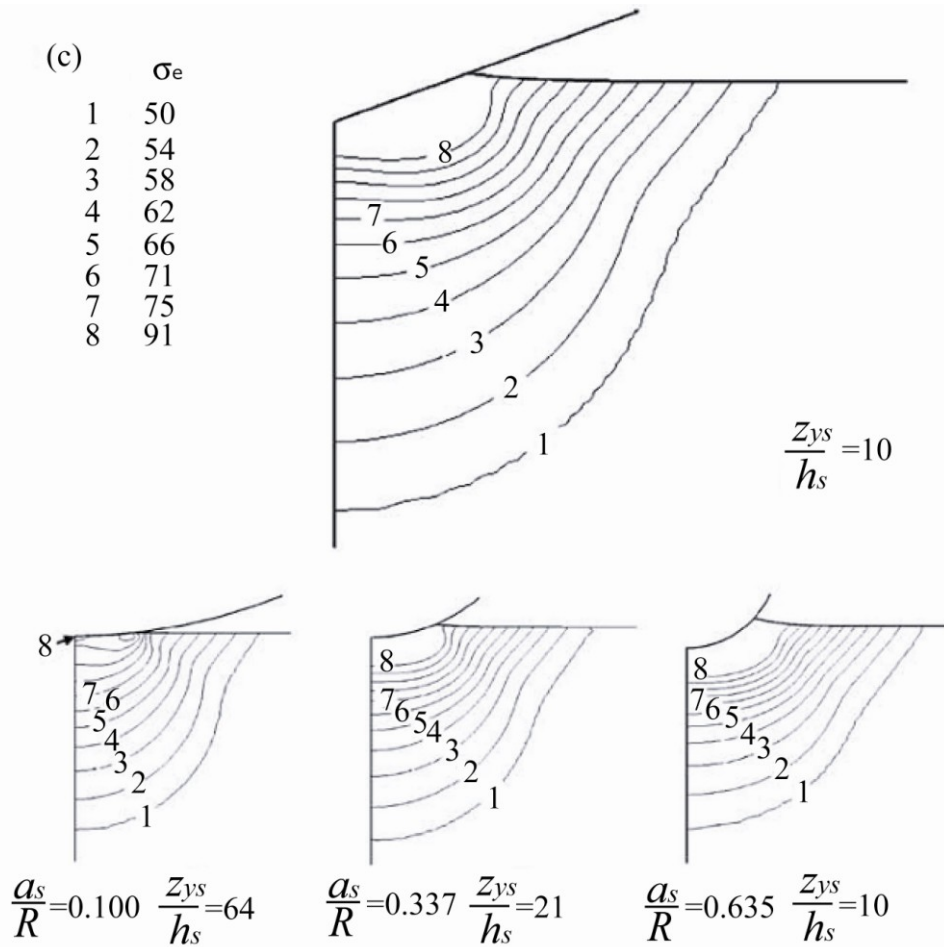


Figure 1.32 cont'd.

## 1.5 Finite Element Modeling of the Subsurface Deformation Zone

### 1.5.1 Introduction

In the present work it is hypothesized that the deformation zone under the indent drives the indentation induced two-way response that underlies surface form memory. Understanding the characteristics of the deformation zone is critical to understanding the two-way response. Therefore, finite element modeling has been used, in addition to experimental studies, to determine the size of the deformation zone and the distribution of stress and strain under the indent.

Shape memory alloys are often modeled by either a phenomenological or a micromechanical approach. The phenomenological models use measurable parameters that can make the model computationally efficient and thus suitable for engineering applications [Tanaka et al. 1982; Ivshin and Pence 1994; Brinson and Huang 1996]. The micromechanical models follow closely with the crystallography and use micromechanics to calculate the interaction energy during phase transformation. Stresses and strains are represented in terms of volume averages and martensite variants are not differentiated. Furthermore, the micromechanical models are more computationally demanding since they keep track of many changing variables. But based closely on physical metallurgy, the models can yield more detailed information [Patoor et al. 1993; Huang et al. 1998; Goo et al. 1997].

### **1.5.2 The 3D Superelastic Model**

Theoretical understanding of the indentation-induced phase transformations in NiTi SMAs is challenging because of the coupling of martensitic phase transformation and plastic slip deformation under complex contact loading conditions. A number of three-dimensional constitutive models have been proposed based on existing one-dimensional models. For phenomenological models, the expansion from one to three dimensions is based on generalized plasticity theory, assuming that the martensite-austenite phase transformation also holds for the assumptions of classical plasticity theory. These assumptions are: 1) yield stress is insensitive to hydrostatic stress; 2) inelastic deformation due to the shape memory effect, like plastic

deformation, is volume conserving; 3) the plastic strain increment in each direction is proportional to the stress deviator component in that direction.

In this work, a three dimensional constitutive model is developed based on Zhang's 3D superelastic model [Zhang et al. 2007] that develops from the one-dimensional Ivshin-Pence constitutive model [Ivshin and Pence 1994], to describe evolution of the subsurface deformation zone under contact loading conditions. The Ivshin-Pence model carefully constructs transformation kinetics to capture various aspects of the shape memory effect. Zhang's 3D superelastic model simulates the superelasticity of NiTi SMAs in multiple loading directions.

The 3D superelastic model is presented in terms of total strain rate  $\dot{\epsilon}_{ij}$ . This total strain rate is decomposed into elastic part  $\dot{\epsilon}_{ij}^E$  and a transformation strain (inelastic) part  $\dot{\epsilon}_{ij}^T$ , as seen in Eq. (1.7)

$$\dot{\epsilon}_{ij} = \dot{\epsilon}_{ij}^E + \dot{\epsilon}_{ij}^T \quad \text{Eq. (1.7)}$$

The elastic strain rate is  $\dot{\epsilon}_{ij}^E = E_{ijkl}^{-1} \dot{\sigma}_{kl}$ . The stiffness tensor  $E_{ijkl}^{-1}$  is represented in terms of Young's modulus  $E$  and Poisson's ratio  $\nu$ .

Lubliner and Auricchio [1996] proposed a 3D framework for the shape memory effect based on the generalized plasticity theory. The transformation strain rate is determined by Eq. (1.8):

$$\dot{\varepsilon}_{ij}^T = \dot{\lambda} \left( \frac{\sqrt{3}}{2\sqrt{J_2}} S_{ij} \right) \quad \text{Eq. (1.8)}$$

Where  $S_{ij}$  is the deviatoric stress,  $J_2$  is the second invariant of stress, and  $\lambda$  is the effective plastic strain, the rate of which is expressed in Eq. (1.9):

$$\dot{\lambda} = -\delta\dot{\alpha} \quad \text{Eq. (1.9)}$$

Here  $\alpha$  is the austenite volume fraction, whereas  $\delta$  is a material constant that gives the maximum transformation strain that can be induced by the shape memory effect. This maximum transformation strain  $\delta$  is typically about 5%. The austenite volume fraction  $\alpha = \alpha(x, t)$  is a material dependant function of current von Mises stress and the overall loading history. The  $\alpha$  value is calculated using the Ivshin and Pence constitutive model. Combining the elastic part and transformation part, the complete strain rate was expressed as:

$$\dot{\varepsilon}_{ij} = E_{ijkl}^{-1} \dot{\sigma}_{kl} - \delta\dot{\alpha} \left( \frac{\sqrt{3}}{2\sqrt{J_2}} S_{ij} \right) \quad \text{Eq. (1.10)}$$

After elastic loading, the constitutive model switches algorithmically to the slip-plasticity model. The plastic strain continues to increase according to Von Mises plasticity so long as the change of the second invariant  $\dot{J}_2 \geq 0$ . Unloading is elastic and linear, which ends when the stresses go to zero.

## 1.6 Summary

In this chapter, the literature on the discovery of shape memory alloys, mechanisms of shape memory and the superelastic effect, contact mechanics, and finite element modeling has been briefly reviewed. The thermoelastic nature of martensitic phase transformations, twin boundary motion, and lattice correspondence are three pillars of SME. Tension-compression asymmetry results from the different Schmid factors between tension and compression directions due to low symmetry in martensite variants.

Greater attention is given to the mechanisms of two-way shape memory effect, indentation induced TWSME, and its finite element modeling, due to their importance to the current work. Most of the literature is focused on training methods instead of reaching deep into the mechanism of the two-way shape memory effect. The few reports on TWSME that focused on mechanisms were reviewed. It was reported that dislocations have been calculated to have lowest energy in the martensite variants where they were originally formed. This helps to form thermo-dynamically anisotropic martensite variants, which preferentially form during martensitic transformation, thus remembering martensite cool shape.

Indentation in martensitic NiTi SMAs leads to a complete recovery for shallow spherical indent when the representative strain is less than 5%. Deep spherical indents show a two-way indent depth change upon heating and cooling. This two-way

response can be converted to a cyclic extend-to-flat surface transition, giving rise to *Surface Form Memory* (SFM) when the indent is removed by planarization.

## **CHAPTER 2:        EXPERIMENTAL METHODOLOGY**

### **2.1     Introduction**

Experiments on indent recovery and indentation/planarization SFM were conducted in order to learn how to develop functional surfaces with various features at multiple length scales, how to maximize the indentation-induced two-way response, what drives the two-way shape memory effect, and how much work can be performed via SFM.

Details of the experimental procedures are discussed in this chapter. Specifically, methodologies for specimen planarization, such as hot vs cold planarization, partial vs post-recovery M-planarization, and direct vs pre-recovery M-planarization will be discussed in the detail. Procedures for the indent/exdent measurements will be illustrated, followed by the methodologies for maximizing TWSME and for measuring the indentation deformation zone. Details of constrained recovery experiments that measure work output and energy density of SFM will be discussed. A novel Laser Shock Peening process will also be introduced.

## 2.2 Materials

### 2.2.1 NiTi Shape Memory Alloys

#### 2.2.1.1 Source and Thermal Response

A 3 mm thick 50.26 at % Ni wrought NiTi alloy sheet was acquired from Special Metals Corporation. The transformation temperatures,  $M_f$ ,  $M_s$ ,  $A_s$ , and  $A_f$ , were determined by both Differential Scanning Calorimetry (DSC) and SQUID magnetometry, as listed in table 2.1. The profiles of DSC and SQUID measurement were shown in Figure 2.1. The enthalpy for transformation is 15.6 J/g.

Table 2.1 Transformation temperatures measured by DSC and SQUID

Transformation Temperatures	DSC, K	SQUID, K	Average, K
$M_f$	295	313	$304 \pm 9$
$M_s$	331	329	$330 \pm 1$
$A_s$	343	335	$349 \pm 6$
$A_f$	390	386	$388 \pm 2$

Specimens were first electro-discharge cut into 12.7 mm diameter discs, ground, and polished, finishing with 0.05  $\mu\text{m}$  colloidal silica. Before indentation specimens were chilled to 243 K to ensure a fully martensitic condition at room temperature.

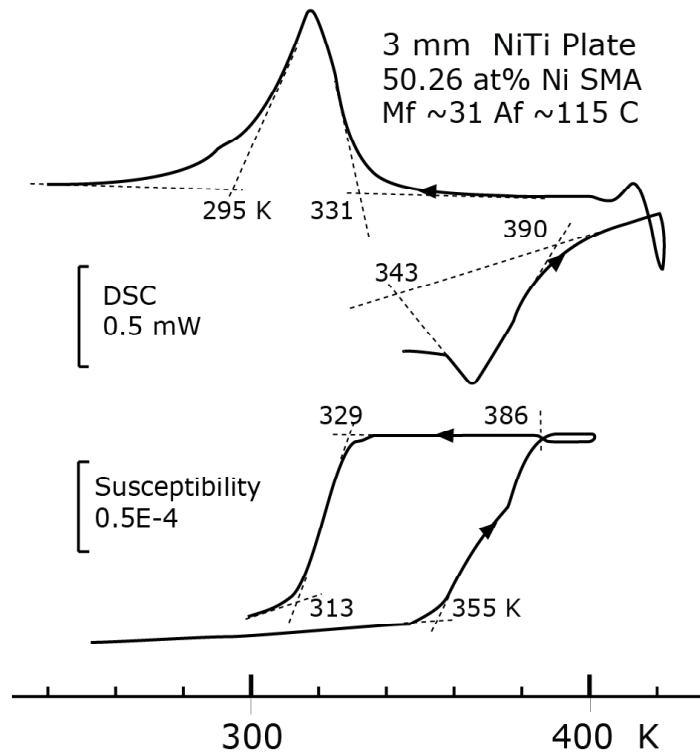


Figure 2.1 DSC and SQUID measurements of the transformation temperatures of the equi-atomic NiTi shape memory alloys.

### 2.2.1.2 Stress-Strain Behavior

Figure 2.2 shows the stress-strain curve of a NiTi specimen under compression at a strain rate of 0.01/s. It is shown that the material exhibit two yield stresses. The upper yield stress indicated as  $\sigma_1$  is the yield stress for slip at a level of 315 MPa, while the lower yield stress indicated as  $\sigma_2$  is the martensite detwinning stress at a level of 93 MPa. The Young's Modulus was measured to be 5.6 GPa. During compression, the material first detwins when the stress reaches 93 MPa at around 1.5% compressive strain. During martensite detwinning, martensite variants reorient to accommodate the deformation strain, which exhibit a plateau where stress stays the same when the strain increases. Liu et al. [1998] conducted detailed study on

martensitic deformation using Ti-50.0 at% Ni plate and thought the plateau region represents Luders deformation. Toward the end of the plateau, slip mechanism starts to play a role. When the stress rises to 315 MPa, martensite detwinning mechanism ends and slip deformation is the only mechanism that controls the stress-strain curve.

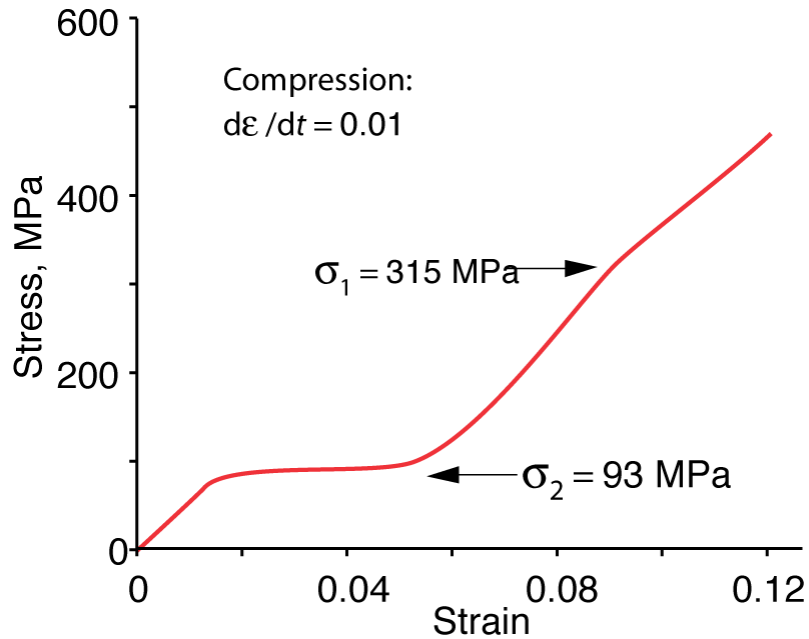


Figure 2.2 Compressive stress strain behavior for the martensitic NiTi used in the study.  $\sigma_1$  is the stress for slip deformation,  $\sigma_2$  is the stress for martensite detwinning.

### 2.2.1.3 Indentation Response

Nanoindentation tests were conducted on the as-received NiTi SMA. Figure 2.3 shows the load-displacement curve during the indentation process. The NiTi specimen was mechanically ground with 2000 Grit SiC paper and polished down to 0.05  $\mu\text{m}$ , using colloidal silica for 6 hours on the vibratory polisher. A Berkovich diamond indenter was used to make an indent with a controlled depth of 1.5  $\mu\text{m}$ . The actual indent depth,  $h$ , after unloading was 1.55  $\mu\text{m}$ . The peak load was 200 mN.

Therefore, the hardness of the NiTi specimen used can be calculated to be 3.4 GPa based on  $H=P/A$ , where  $A=24.5h^2$  for a Berkovich indenter. The Young's Modulus was calculated to be around 5.8 GPa using the stiffness measurement in the unloading curve.

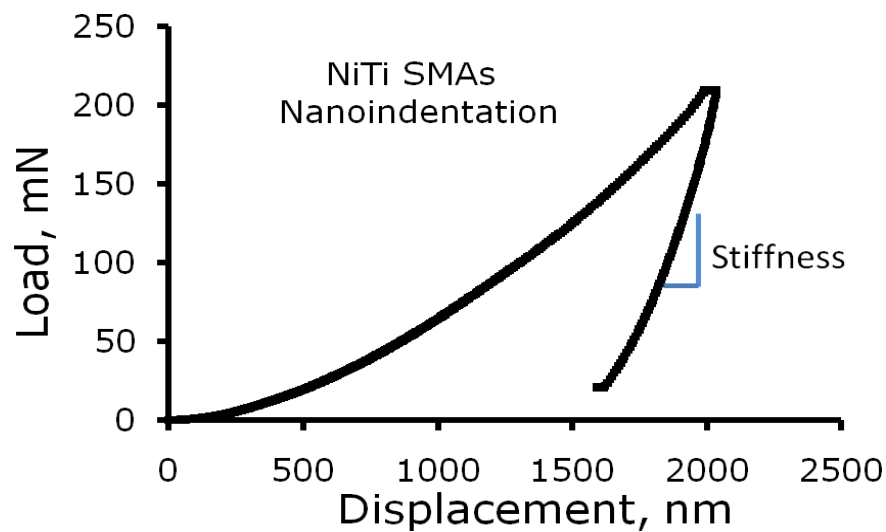


Figure 2.3 Nanoindentation in NiTi by MTS XP Nanoindenter with an indentation depth of 1.55  $\mu\text{m}$ .

### 2.2.2 Stainless Steel, Aluminum, and Indenter Materials

Stainless steel grade 304 was used in constrained recovery experiments to determine the work energy density associated with SFM. The Young's modulus and Poisson's ratio of this material are 200 GPa and 0.3. The micro-hardness response measured by CSM instrumented indenter is shown in Figure 2.4a. The hardness is measured to be around 0.9 GPa.

6061-T6 aluminum has around 96% aluminum and 0.4% copper. The Young's modulus and Poisson's ratio of this material are 70 GPa and 0.33. The hardness is measured to be around 0.7 GPa, as shown in Figure 2.4b.

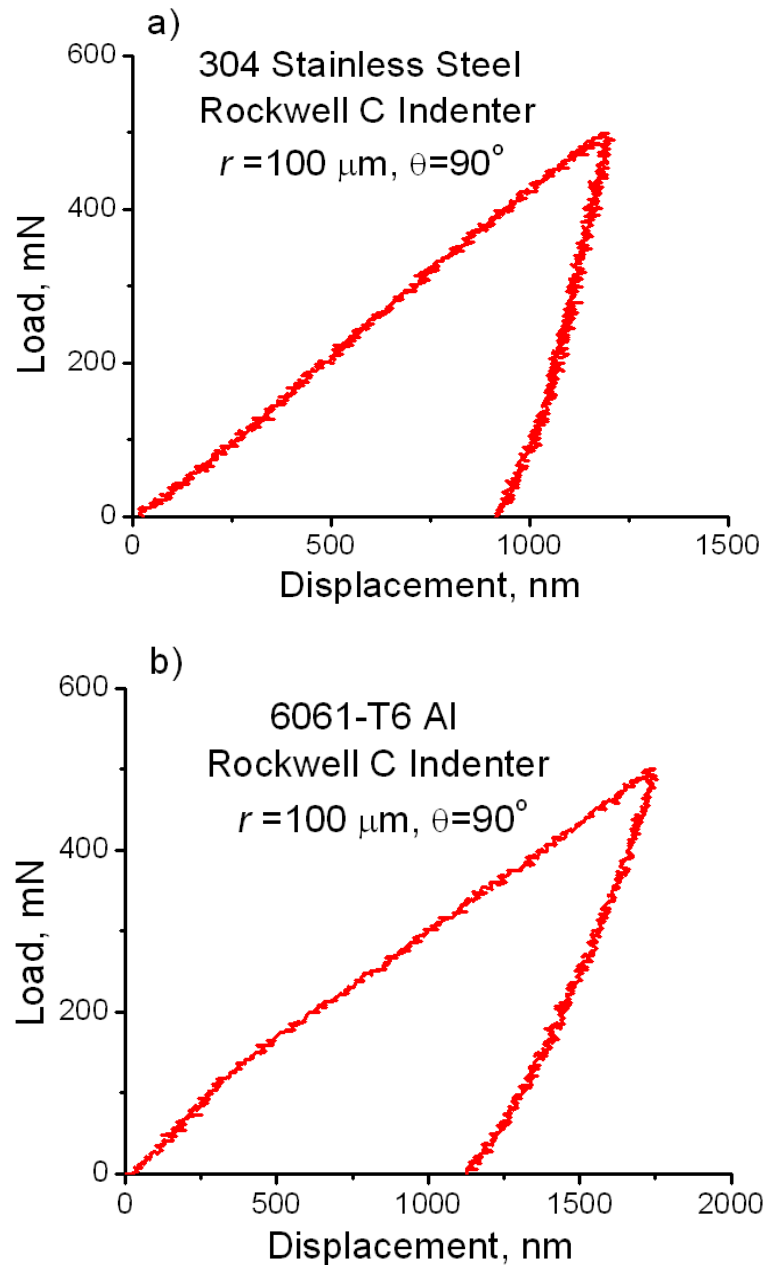


Figure 2.4 a) Load-Displacement curves of 304 Stainless Steel (Upper), b) 6061-T6 (Lower) used in the constrained recovery experiment.

### **2.2.3 Laser Shock Peening Materials**

The materials used in the laser shock indentation experiments were 1/8" thick 1/2" in diameter NiTi discs as previously described, a 65  $\mu\text{m}$  thick aluminum foil tape purchased from 3M Corporation, BK-7 type optical glass, and a Continuum Surelite III laser for laser pulse generation. Details of the experiment are discussed further below.

## **2.3 Indentation Methods**

### **2.3.1 Indenter Materials and Properties**

The indenters that were used in the experiments are 1/32" and 1/16" diameter tungsten carbide spherical balls with 6% cobalt (Young's modulus of 650 GPa and Poisson's ratio of 0.26) purchased from McMaster-Carr Corporation; 1/100" and 1/16" diameter high purity tungsten rods (Young's modulus of 400 GPa and Poisson's ratio of 0.28) from ESPI Metals Corporation; a Berkovich diamond nanoindenter with Young's modulus of 1140 GPa and Poisson's ratio of 0.07; a Vickers diamond cone indenter with a facial angle of 136 degrees; a 1.59 mm diameter tungsten rod used as a punch indenter; and a 1 cm x 1 cm stainless steel screen mesh with thickness of 0.254 mm and mesh size of 0.5 mm.

### **2.3.2 Indentation Loading**

All indentation specimens were cooled by liquid Freon to 243K before indentation to ensure a fully martensitic state, and allowed to return to room temperature before indentation. A screw driven Instron load frame was used to drive

the indenter into the specimen in the martensitic state. During indentation, the strain rate was 0.01/s. The indentation tests were usually done at room temperature unless otherwise specified, such as in the replica indentation test and the indentation temperature variation test.

### **2.3.3 Post Indentation Thermal Cycling**

Thermal cycling after indentation was used to stabilize the two-way indent depth change prior to planarization. The indents were heated to  $433 \pm 2$  K (above  $A_f$ ) using a thermo-electric cooler (TEC) and cooled to  $243 \pm 2$  K (below  $M_f$ ) using liquid Freon. The profiles of the indents during each heating and cooling cycle were recorded optically.

### **2.3.4 Laser Shock Peening**

Laser Shock Peening (LSP) was done through collaboration with Professor Gary Cheng's group at Purdue University. LSP was used to improve indentation efficiency and to observe how NiTi SMAs react to dynamic loading conditions at ultra high strain rates. The NiTi specimens were polished down to 0.05  $\mu\text{m}$  colloidal silica in the martensitic state. Before Laser Shock Peening, a 65  $\mu\text{m}$  thick aluminum foil tape purchased from 3M Corporation was attached to the surface of NiTi disc. A confining media of BK7 type optical glass was used to contain the plasma generated by laser beam impingement on the aluminum foil. The contained pressure generated by the plasma penetrated into the base material (NiTi) and made a dent with a large amount of

residual compressive stress. Figure 2.5 shows a schematic drawing of the LSP process in NiTi shape memory alloys. The laser beam was generated by a Continuum Surelite III laser with a wavelength of 1064 nm and pulse duration of 5 nanoseconds. The beam sizes used were 0.5 and 1 mm. The laser intensities were varied from 1 GW/cm<sup>2</sup> to 3.5 GW/cm<sup>2</sup> to vary the indent depth. Figure 2.6 shows the optical image of the as-shock peened specimens. The NiTi specimen on the left has indents made under a beam size of 0.5 mm with indent spacing to be 2 mm. The NiTi specimen on the right has indents made under a beam size of 1 mm with indent spacing to be 2 mm.

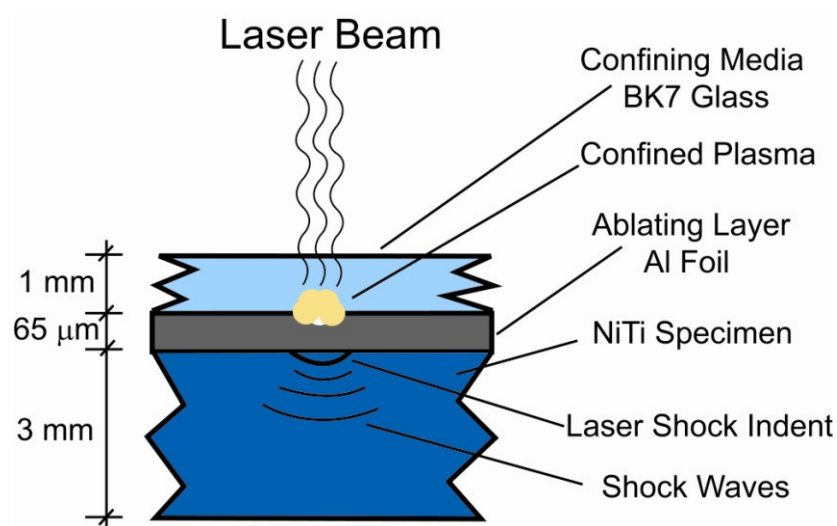


Figure 2.5 Schematic illustration of the laser shock peening process on NiTi shape memory alloys (not to scale).

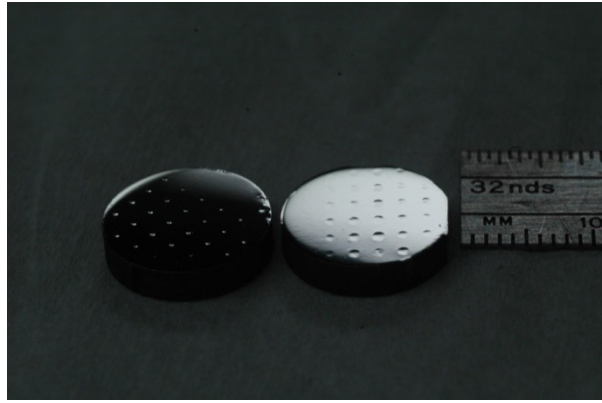


Figure 2.6 Optical image of the laser shock peened NiTi discs. The left sample has indents made with beam size of 0.5 mm and the right with beam size of 1 mm.

#### **2.4 Indent and Displacement Characterization**

The WYKO optical profilometer is a white light interferometer that can measure surface roughness and 3D image topography non-destructively, as well as execute statistical computations on surface data. It has high lateral and vertical resolution and can measure surface height up to 500 microns. It is used here to measure the initial indent depth in the martensite, indent depth changes upon heating and cooling, and indent height and morphology on heating and cooling. Measurement on heating was achieved by using a thermoelectric cooler (TEC) to 433K and on cooling by liquid Freon down to 243K and then warming up to room temperature (about 298K) in air. 2D line profiles and 3D topographical profiles are generated by the WYKO software for further analysis, which are shown in the results and discussion chapter.

## **2.5 Obtaining SFM by Indentation/Planarization**

### **2.5.1 Thermo-mechanical Preparation**

Various types of indentation were made in the martensitic NiTi to achieve the indentation-induced TWSME. A heating and cooling cycle was conducted to obtain the initial recovery of the indents. The indent profiles were recorded optically. Detailed procedures are described in Section 2.4.1. After this, the indents were planarized to obtain SFMs, the procedure of which is discussed in the following section. By indenting with various forms, and by varying the planarization temperatures, various classes of SFM were obtained (i.e: flat-to-exdentated on heating vs flat-to-indentated on cooling.)

### **2.5.2 Grinding Technique**

#### **2.5.2.1 Cold Planarization**

##### ***2.5.2.1.1 Post-recovery M-planarization***

To explore the scope of surface transition responses, various geometries of indenters were used for indentation, as listed in the indenter characteristics section. After indentation, profiles of the indents were measured optically using temperature profilometry procedures described above. After the first recovery (heating above  $A_f$  and cooling below  $M_f$ ), the indents were planarized to restore to a flat surface. In the planarization step, material was removed by mechanical grinding and polishing with

0.05  $\mu\text{m}$  colloidal silica to ensure a fine surface finish<sup>‡</sup>. The amount of material removal below the base of the cool indent was carefully controlled via thickness measurements with a resolution of 1-2  $\mu\text{m}$ . Since the indent was completely removed by the planarization step, we call this “Post-recovery M-planarization”. After planarization, the specimen surface profiles were recorded using the temperature profilometry procedures discussed previously. Thermally-reversible surface transitions, and SFM, were then observed after planarization.

#### **2.5.2.1.2 Pre-recovery M-planarization**

In the post-recovery M-planarization and partial planarization experiments, the indents were planarized once they were thermally cycled to observe the initial two-way indent depth change or “first recovery”. Pre-recovery M-planarization, on the other hand, means planarization before indent recovery.

As shown in Figure 2.7, post-recovery generated an exdent with an amplitude of  $\delta_1$  on heating, while pre-recovery generated an exdent with an amplitude of  $\delta_2$  on heating.  $\delta_2$  is substantially larger than  $\delta_1$ . This is because that the detwinned martensite zone developed after initial indentation helps to push the material up due to

---

<sup>‡</sup> True planarization cannot be accomplished using electrolytic methods because the latter would simultaneously etch the base of the indent and degrade subsequent SFM amplitude.

shape memory mechanisms. As the detwinned martensite zone had been recovered during first recovery, the extent formed on the post-recovery planarized specimen was thus smaller. The larger extent formed on the pre-recovery specimen has potential application in one-way actuation, which was investigated in the constrained recovery experiment where the extent formed during austenitization can be used to make replica indent into a base metal when they are coupled and compressed in the Instron machine.

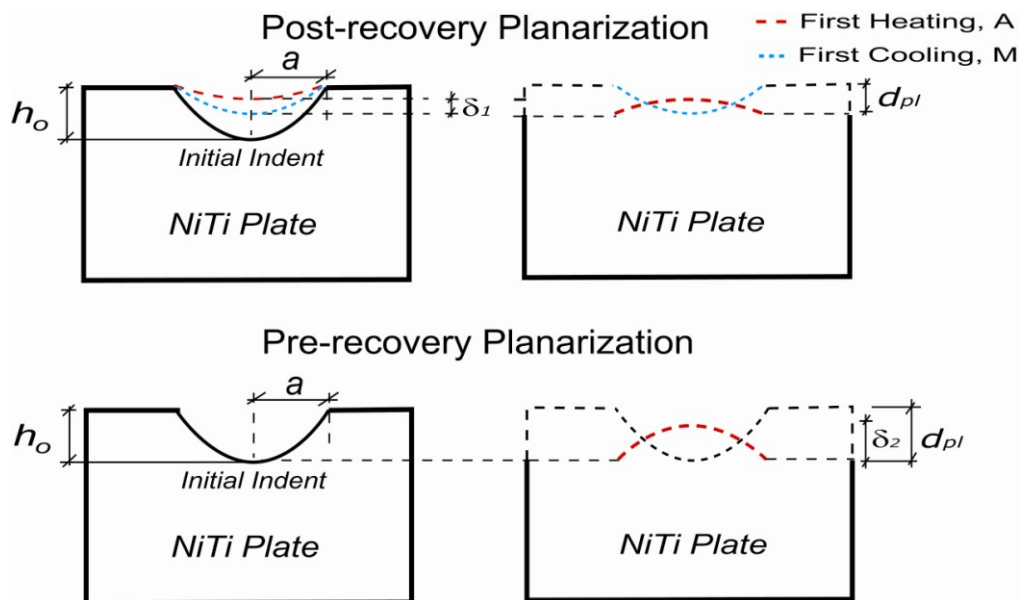


Figure 2.7 Comparison of post-recovery M-planarization after first recovery and pre-recovery M-planarization without first recovery.

### 2.5.2.2 Post-recovery A-planarization

As illustrated above, deep spherical indents made in the martensitic state exhibit two-way response either in the form of two-way indent depth change in the as-indented specimens, or as an extent-to-flat surface transition in as-planarized

specimens, both driven by thermal excursion between  $M_f$  and  $A_f$ . The planarization process just described was done in the martensitic state. It is also interesting to carry out the planarization in the austenitic state. As will be shown, a flat-to-indent transition (as opposed to an indent-to-flat transition) on cooling may possibly be achieved in the subsequent thermal cycling. That is, the indent may form upon cooling and fully recover to a flat surface upon heating. This effect can also be cycled for an indefinite time. Detailed experiment procedures are described below.

Spherical indents were made under loads of 200, 500, and 700 N with a 0.794 mm diameter spherical tungsten carbide ball. The surface profiles of the initial indents were measured optically. The spherical indents were then heated to 473 K by a hot plate to ensure a fully austenitic state. The specimens were then ground down to 2000 Grit sandpaper on the hot plate at 373 K in order to keep the specimens in the austenitic state. The grinding procedure was carefully controlled so that the indent was just ground away at 2000 Grit sandpaper without removing material beneath the indent at the austenitic state. After planarization, the indents were fully martensitized by cooling in liquid Freon to 243 K. The surface profiles of the indents after cooling at room temperature and after subsequent heating to 433 K were recorded optically. Thermal cycling was done 10 times at the temperature range between 243 K and 433 K to ensure a full reversibility in the change of surface features.

## **2.6 Maximizing Indentation-induced TWSME**

### **2.6.1 Effect of $a/r$ Ratio**

For this series of experiments, spherical indents were made in martensitic NiTi discs (12.7 mm in diameter) using a 0.794 mm diameter tungsten carbide ball with loads of 200, 700, 1500, and 3000 N. Cylindrical indentations were made with a 0.254 mm diameter 6 mm long tungsten rod under loads of 500, 1500, 3500, and 5000 N, with the cylinder axis parallel to the indented surface. As described before, the  $a/r$  ratio for spherical indent refers to the ratio of indent contact radius over indenter radius. For cylindrical indents, the indenter radius is taken as the cylinder radius, and the indent “radius” was taken as the indent half width,  $c$ .

Three dimensional profiles of the as-indented surfaces, and profiles for first recovery of spherical and cylindrical indents were acquired optically using the temperature profilometry procedures, as described in section 2.4.1.

### **2.6.2 Effect of Thermal Cycling**

For the above spherical indents made under loads of 200 and 700 N, 25 heating and cooling cycles were applied to assess both the cyclic reversibility of the shape change and the effect of cycling on the two-way response. Profiles of the indents after each heating and cooling cycle were recorded. The indent depth change suggests a thermal cycling effect which is further analyzed by measurement of changes in transformation temperatures by a Superconducting Quantum Interference

Device (SQUID). Magnetic susceptibility is the ratio of an induced magnetization to the applied magnetic field. The susceptibility of conduction electrons in a metal, i.e. The Pauli susceptibility, depends on the density of states at the Fermi level. Different crystallographic lattice structures, such as martensite and austenite, possess different hole-carrier densities and thus display different susceptibilities. In the present study, the SQUID was used to measure the transformation temperature change of the as-indented specimen before and after thermal cycling. The specimen used in the SQUID test was prepared by cutting a 3 gram 3 mm thick NiTi piece and making a closed packed array of spherical indents on both sides of the specimen in order to maximize both the dislocation density and the extent of the indentation deformation zone. A control specimen with no indents was also used to serve as a baseline for measuring transformation temperature changes.

### **2.6.3 Effect of Indentation Spacing**

As a rule of thumb, indents need to be made away from each other and from the edge of the sample in order to effectively measure the material's mechanical properties such as hardness and stiffness (for instrumented indentation). Indents made close to each other will be influenced by overlapping the indentation subsurface deformation zones. As far as SFM is concerned, however, maximizing this interaction may be a way to maximize SFM. Therefore, experiments with various indent spacings were designed to evaluate how subsurface deformation zone overlap affects

indentation two-way response, and SFM, as the indent spacing is reduced from infinity to zero (double indentation).

In this experiment, spherical indents were made with different spacing under 500 N using a 0.794 mm tungsten carbide ball and assessed the effect of indentation spacing on the indentation-induced two-way response. The surface profiles of the initial indents and the indents after heating to  $433 \pm 2$  K and cooling to  $243 \pm 2$  K were measured optically. Two heating and cooling cycles for each indent were carried out. Indentation at zero spacing is discussed below.

#### **2.6.4 Effect of Multiple Indentations**

A variation of maximizing the deformation zone by varying indent spacing is to make indents at the same location for a number of times. This repeated indentation method has been investigated by Zarudi et al [2003] to study the plastic deformation behavior of monocrystalline silicon under cyclic microindentations with a spherical indenter. In the present study, repeated deformation was used to increase plastic deformation, thus the size of subsurface deformation zone, and finally the two-way response. Specifically, spherical indents were made under 500N load using 0.794 mm tungsten carbide ball in the same location 2, 5 and 10 times. The surface profiles of the initial indents and the indents after heating to  $433 \pm 2$  K and cooling to  $243 \pm 2$  K were measured optically. Two heating and cooling cycles for each indent were

observed. The effect of multiple indentations on the two-way response was then extrapolated.

### **2.6.5 Effect of Indentation Temperature**

Due to the transformational behaviors of NiTi SMAs, temperature was used as a parameter to vary the mechanical and shape memory properties. Specifically, spherical indents were made under 500 N using a 0.794 mm tungsten carbide ball at temperatures of 333 K (16 K below  $A_s$ ), 293 K (11 K below  $M_f$ ), 273 K, and 213 K (well below  $M_f$ ). Temperatures were measured by the thermocouples spot welded on both sides of the specimens. 333 K was reached by slowly heating the specimens under convection using two heat guns. 273 K was reached by ice water and 213 K was reached by using liquid nitrogen and an acetone slurry bath to cool the NiTi specimen as it sat on an aluminum block inside the slurry bath. Three dimensional profiles of the initial indents made under these temperatures, and the indents after heating to  $433 \pm 2$  K and cooling to  $243 \pm 2$  K were measured optically.

### **2.6.6 Effect of Cold Rolling**

Cold rolling is a metalworking process that increases the yield strength and hardness of a metal by introducing defects into the metal's crystal structure. These defects inhibit further slip. Interest in the study of the effect of cold rolling prior to indentation was based on the fact that slip deformation is necessary for the indentation-induced two-way effect. It is important to find out if cold rolling induced

deformation can sum with indentation-induced deformation to achieve a larger two-way effect.

Spherical indents were made under 500 N load using an 0.794 mm tungsten carbide ball in martensitic NiTi that had been pre-cold-rolled to 0%, 5%, 10%, and 30%. The surface profiles of the initial indents, and the indents after heating to  $433 \pm 2$  K and cooling to  $243 \pm 2$  K, were measured optically. Three heating and cooling cycles for each indent were observed. The effect of cold rolling on the two-way response will be further discussed in the Results and Discussion chapter.

## **2.7 Determining the Size of the Active Zone**

The operating hypothesis for two-way indent depth change or SFM is that indentation-induced two-way response is driven by the subsurface deformation zone. The amplitude of two-way response, whether measured as an indent depth change, or as an extend-to-flat transition, is presumed to be directly related to the size of the subsurface deformation zone,  $D^*$ . Therefore, it is important to measure this size of this zone,  $D^*$ , which may provide direct information for understanding the indentation-induced TWSME. This has been accomplished with a series of controlled serial planarization experiments described below.

### **2.7.1 Front-Thinning Experiments**

The front thinning experiments incrementally removed surface material below the base of the as-recovered indent until the measurable extent amplitude for each increment decays to near zero during a subsequent thermal cycle. The depth of removal by each planarization increment was determined by measuring the thickness change at a chosen reference point with a high-precision micrometer having a resolution of 1-2  $\mu\text{m}$ . The surface profiles of the extent were independently measured optically. The measured extent amplitudes were recorded as a function of the depth of material removal. Both cylindrical and spherical indents with 3 different  $a/r$  ratios were used in the front-thinning experiments to determine the depth of the active deformation zone.

### **2.7.2 Back-Thinning Experiments**

Instead of removing material from the front surface, back thinning experiments remove material from the back side, step by step, to an extent that the two-way indent depth change or extent amplitude (if the indent was planarized before back thinning) just begins to decrease during a subsequent thermal cycle following the most recent thinning step. This depth presumably corresponds to the deepest active region in the deformation zone. The remaining depth of material up to the base of the indent provides a second measurement of the depth of the active deformation zone.

A spherical indent was made under 500 N with a 0.794 mm tungsten carbide ball in martensitic NiTi. The specimen was then heated and cooled to observe the initial two-way response using the temperature profilometry procedure. Then the specimen was thinned from the backside and the depth of removal was again determined by measuring the thickness change at a chosen reference point with a high-precision micrometer. The specimen was heated and cooled using the temperature profilometry procedure after each back thinning experiment to observe any change in two-way response.

### **2.7.3 Direct Observation of the Indent Deformation Zone**

A spherical indent was made under a load of 7500 N using a 1.59 mm stainless steel ball in a martensitic NiTi specimen. A cylindrical indent was made under a load of 6000 N using a 6 mm long 1.59 mm in diameter tungsten rod with the NiTi in the martensitic state. After indentation, the block containing the spherical indent was cut into two halves along the indent centerline using a diamond saw. The cross section face was then hot mounted and cooled to 243 K by liquid Freon before being polished down to 0.05  $\mu\text{m}$  colloidal silica in the martensitic state at room temperature (293 K). Due to hot mounting, the indent recovered which was not intentionally designed. However, this does not greatly affect the study of the active subsurface deformation zone.

The profiles of the initial indent, the residual half indent, and the cross-sectioned surface after heating to  $433 \pm 2$  K and cooling to  $243 \pm 2$  K were measured by optical profilometry.

## **2.8 Indent Replication and Energy Estimates**

### **2.8.1 Introduction**

NiTi SMAs are well known for their high work energy density and wide application to actuation. SFM is different as compared to conventional actuators made out of NiTi SMAs because it is a surface morphology change. However, SFM has good potential in application into NEMS/MEMS devices, aero/hydrodynamic surfaces, and robotic systems. Therefore, it is important to measure the energy density associated with the formation of surface exdents in order to evaluate its application potential. Constrained recovery experiments were designed to evaluate SFM in single shot and reversible application conditions. When combined with measurements of the deformation zone depth, the effective transformational energy density can be estimated.

### **2.8.2 One Shot Replica Indentation**

Spherical indents were made with a 0.794 mm diameter tungsten carbide ball using loads of 200, 700, and 3000 N. Each sample was indented at the same location twice since this had been found in the previous work to give a stronger training effect. Surface profiles of the as-indented surfaces were acquired with the optical

profilometer. The loads used gave  $a/r$  ratios of 0.42, 0.68 and 1.0 respectively, as summarized in Table 2.2. After indentation, but before any heating above  $A_f$  and while still in the martensitic condition, the surfaces were ground and polished just enough to remove visible traces of the indent. This method, called pre-recovery M-planarization, was used in order to maximize the extent amplitude during indentation in the constrained recovery experiment.

Table 2.2 Parameters of the Initial Spherical Indents in Martensitic NiTi

Load N	Depth $\mu\text{m}$	Contact radius $a$ $\mu\text{m}$	$a/r$ ratio
200	37	167	0.42
700	107	271	0.68
3000	380	397	1.00

Constrained recovery experiments were designed to obtain a rough estimate of the work output capability of the exdents when they develop under strong reaction forces. After planarization, the optically-flat NiTi samples were placed in contact with coupons of 3 mm thick 6061-T6 aluminum and positioned between compression platens in a screw-driven load frame. The NiTi-aluminum sandwich was preloaded to a compressive stress of 100 MPa. The assembly was then slowly heated by convection to 423 K to austenitize the NiTi, thus allowing the NiTi exdent to indent the aluminum coupon. (Thermal expansion in the assembly caused the stress to rise to about three times the initial preload.) After reaching 423 K, the specimen was unloaded immediately and cooled to room temperature (298 K) via air cooling.

Dimensional profiles of the indented aluminum surfaces were subsequently acquired using the WYKO profilometer. Additionally, profiles were obtained for the residual exdents in the NiTi samples, both directly following the indent replication experiment (at room temperature), and also in the austenitic condition, with samples heated to 423 K, *in situ* in the profilometer stage, using a thermoelectric module.

To provide a basis for estimation of the work output of the NiTi exdent, conventional spherical indents were made in the same 6061-T6 aluminum plate using a 6.3 mm diameter tungsten ball under various loads. The diameter of this ball was chosen to match the radius of curvature of the replica indents. Indents that were found to have  $a/r$  ratios comparable to those of the replica indents were chosen to provide force-displacement data to give a rough measure of the work of conventional (Hertzian) indentation in 6061-T6 aluminum.

### **2.8.3 Reversible Replica Indentation by SFM**

Reversible replica indentation by SFM is interesting in 2 aspects: 1) it demonstrates the repeatability of SFM; 2) it shows the fatigue property of SFM. The experimental procedures are described in the following.

Spherical indents were made with a 1.59mm diameter stainless steel ball using a load of 3000 N. Surface profiles of the as-indented surfaces were acquired with the optical profilometer. The initial indent depth was 240 microns and the  $a/r$

ratio was calculated to be 0.71. 15 heating and cooling cycles were applied to assess cyclic reversibility of the shape change. Temperatures were measured by thermocouples spot-welded at points on either side of the specimen. After thermal cycling, while still in the martensitic condition, the surfaces were ground and polished just enough to remove visible traces of the indent.

A schematic illustration of the constrained recovery experiment is shown in Figure 2.8. After planarization, the optically-flat NiTi samples were placed in contact with coupons of standard 6061-T6 aluminum, 304 stainless steel, and 440 stainless steel positioned between compression platens in a servo-hydraulic machine. A servo-hydraulic apparatus was set up to maintain a constant load throughout the test, since heating induced expansion will lead to an increase in applied load if placed in Instron machine. The NiTi-replica material sandwich was preloaded to compressive stresses of 50, 125, 200, 250, and 300 MPa using a servo hydraulic load frame to maintain a constant load under conditions of changing temperature. The assembly was then heated by four Cartridge Heaters placed next to the sandwich to 433 K to fully austenitize the NiTi, thus allowing the NiTi extent to indent the replica materials. Two thermocouples were attached to the sandwich during heating and cooling to have an accurate measurement of temperature. After heating to 433 K, the sandwich was immediately unloaded to zero Newton, then cooled down to 293 K in air. Profiles of the indented replica material surfaces were subsequently acquired optically.

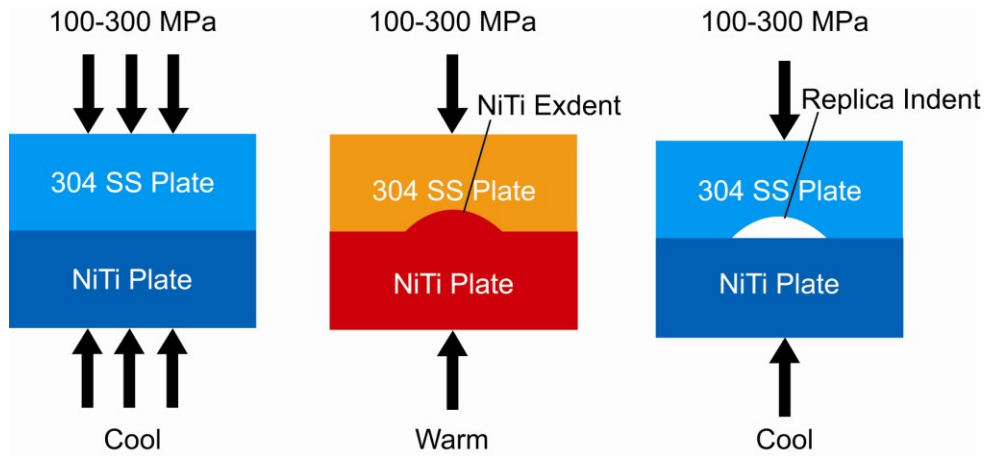


Figure 2.8 Schematic illustration of the setup of the constrained recovery experiment. 304 stainless steel (SS) is used as an example of the replica material.

The effect of cooling under load was also evaluated by unloading the sandwich after it was cooled down to 293 K. Experimental results show that cooling under load leads to a larger response. The detailed results will be reported in Section 3.5.3.4. Dimensional profiles of the indented replica material surfaces were also acquired optically.

To provide a basis for the estimation of the work output of the NiTi exdent, spherical calibration indentation was conducted to measure the hardness of the material being preloaded to 250 MPa and heated to 433 K using 1.59 mm diameter tungsten ball under load of 30, 50, and 100 N. (250 MPa was chosen because this load generated the maximum replica indent depth for these three materials.) The hardness, measured by the load divided by the projected area, was used to calculate the equivalent load needed to make the replica indent and for the estimation of the work output of the NiTi exdent.

To estimate the volumetric energy density, these measurements were combined with experimental estimations of  $D^*$ , taken as the depth of a normally hemispherical active deformation zone. This measurement effectively ignores any contribution from elastic strain energy release in regions below  $D^*$ .

## **2.9 Finite Element Modeling**

### **2.9.1 The 3D Constitutive Model**

A three dimensional constitutive model is developed based on Zhang's 3D superelastic model [Zhang et al. 2007] that develops from the one-dimensional Ivshin-Pence constitutive model [Ivshin and Pence 1994], to describe evolution of the subsurface deformation zone under contact loading conditions. The Ivshin-Pence model carefully constructs transformation kinetics to capture various aspects of the shape memory effect. Zhang's 3D superelastic model simulates the superelasticity of NiTi SMAs in multiple loading directions. The 3D constitutive model, however, simplifies the superelastic model and simulates the indentation process into elasto-plastic materials. The constitutive model is temperature independent since the indentation process is modeled at 25°C and below  $M_f$ . Slip-plasticity is included in this model to capture the mechanical response of NiTi SMA at large deformation strains. NiTi material parameters were extracted from the tensile test, as shown in the experimental section (Figure 2.2). Implementation of the model used a commercial finite element program (ABAQUS) and a user material subroutine (UMAT).

The difference between the constitutive model and the superelastic model is that the constitutive model does not account for the austenite volume fraction since the material stays in the martensitic condition. Therefore, the effective plastic strain cannot be expressed as a function of the austenite volume fraction. Instead, it is solely a function of the current von Mises stress, as shown below:

$$\dot{\lambda} = \frac{1}{h} \frac{\sqrt{3}}{2\sqrt{J_2}} S_{ij} \dot{\sigma}_{ij} \quad \text{Eq. (2.1)}$$

Where  $h$  is the plastic hardening slope with units of stress.

Thus the total strain can be calculated to show Eq. (2.2):

$$\dot{\varepsilon}_{ij} = E_{ijkl}^{-1} \dot{\sigma}_{kl} + \dot{\lambda} \left( \frac{\sqrt{3}}{2\sqrt{J_2}} S_{ij} \right) \quad \text{Eq. (2.2)}$$

## 2.9.2 Finite Element Program Implementation

The finite element implementation is accomplished using the User Material Interface provided by ABAQUS. The strain increment is passed to the user material subroutine and the corresponding stress increment is calculated from the constitutive relations using a return mapping algorithm. The state variables, including effective plastic strain, are updated. The strain increment can be expressed as Eq. (2.3):

$$d\varepsilon_{ij} = E_{ijkl}^{-1} d\sigma_{kl} + \frac{1}{h} \frac{3}{4J_2} S_{ij} \cdot S_{pq} d\sigma_{pq} \quad \text{Eq.(2.3)}$$

Multiplying both sides of the equation by the elastic modulus gives the trial stress increment, shown in Eq. (2.4).

$$d\sigma_{ij}^t = E_{ijkl} d\varepsilon_{kl} = d\sigma_{ij} + \frac{1}{h} E_{ijkl} \frac{3}{4J_2} S_{kl} \cdot S_{pq} d\sigma_{pq} \quad \text{Eq.(2.4)}$$

The elastic trial stress increment can also be expressed as Eq. (2.5):

$$d\sigma_{ij}^t = (\delta_{ip} \delta_{jq} + \frac{1}{h} E_{ijkl} \frac{3}{4J_2} S_{kl} S_{pq}) d\sigma_{pq} = C_{ijpq} d\sigma_{pq} \quad \text{Eq.(2.5)}$$

After  $C_{ijpq}$  is calculated, the real stress increment  $d\sigma_{pq}$  can be obtained by the correction of the elastic trial stress increment  $d\sigma_{ij}^t$ .

The mesh for the indentation model comprises 15,000 axisymmetric 4-node bilinear elements. The indenter was modeled as a rigid body sphere for spherical indentation and the friction coefficient between the indenter and the substrate is assumed to be zero. For cylindrical indentation, the 3D model was reduced to 2D due to the plain strain nature of cylindrical indentation. The indenter was simplified to a quarter of a circle and the friction coefficient between the indenter and the substrate is assumed to be zero.

## CHAPTER 3: RESULTS AND DISCUSSION

### 3.1 Introduction

Various indentation methods have been used in shape memory alloys (SMAs) to study shape memory and superelastic characteristics. Ni and Zhang in Grummon's group reported that shallow spherical indents made by a CSM instrumented indenter can completely recover after heating above  $A_f$  due to the shape memory mechanism, while deep spherical indents became shallower but remained after heating due to irreversible slip deformation. Following partial thermal recovery, cooling caused these deep indents to deepen, reflecting a two-way depth change. When a planarization step was applied to the indented martensite after the indent's initial recovery, a thermally-reversible flat-to-bumpy transition was observed. We now call this surface transition "Surface Form Memory" (SFM). These transitions are fully reversible and cyclically stable.

In this chapter, experimental results will be presented on developing SFM using different indenter geometries and different planarization steps (full vs partial, hot vs cold, and direct vs indirect). Ways to maximize surface form memory will be discussed considering the effects of  $a/r$  ratio, thermal cycling, indentation spacing, multiple indentations, indentation temperature, and pre-cold-rolling. Experimental results on probing the size of the active zone to understand surface form memory will

be compared to finite element modeling. The potential application of surface form memory for actuation will be examined in terms of its work output and energy density via one-shot and reversible constrained recovery experiments. Finally, an advanced laser-based technique for making the initial indents will be demonstrated, allowing an interesting comparison of indentation response between quasi-static (ball) and dynamic (strain rate  $>10^6$ ) conditions.

## **3.2 Developing and Maximizing the Indentation-Induced TWSME**

### **3.2.1 Indent Recovery by the Indentation-Induced TWSME**

Figure 3.1 schematically shows results for a typical indent made, in this case, with a 794 micron diameter sphere at a load of 700 N. The indent had an initial depth of 96.8  $\mu\text{m}$ , giving an  $a/r$  ratio of 0.65, and thus a representative strain of 0.13. Upon heating to above  $A_f$ , the indent depth decreased from 96.8  $\mu\text{m}$  to 56.9  $\mu\text{m}$  by shape memory mechanisms. This initial shape-change represents a depth recovery that is 41.2% of the initial indent depth. When cooling the specimen back below  $M_f$  the indent depth increased to 65.9  $\mu\text{m}$  by two-way shape-memory mechanisms. We call this indent depth change upon heating and cooling right after indentation “indent first recovery”. This two-way indent depth change induced by a single indentation method represents a non-trivial shape memory phenomenon, as compared to various thermo-mechanical training methods usually used in achieving TWSME. The magnitude of the indent depth change will be compared with traditional TWSME and its mechanism will be extrapolated based on experimental results.

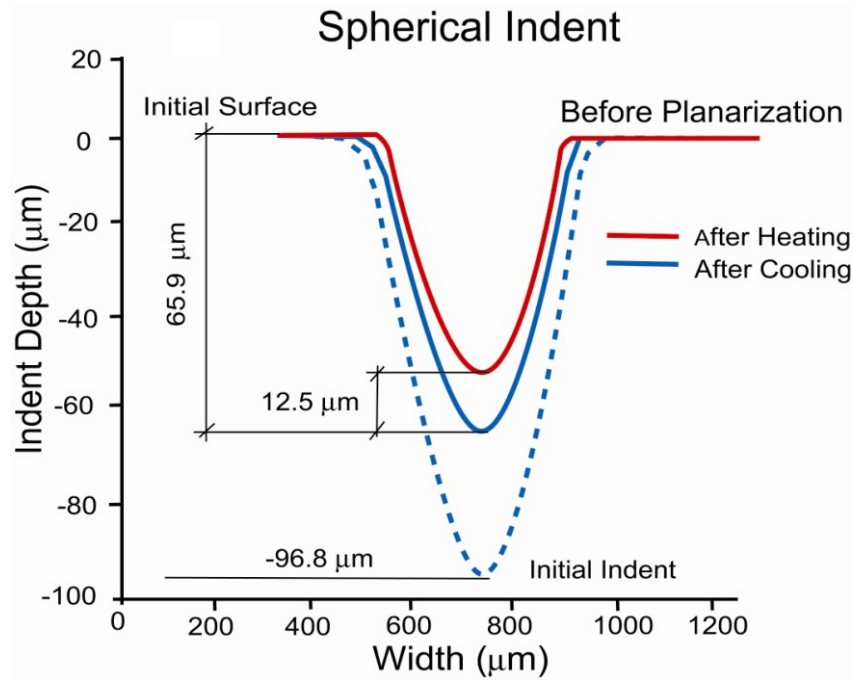


Figure 3.1 Schematic illustration of initial indent depth recovery of the spherical indent made with a 0.79 mm diameter tungsten carbide ball under 700N in the martensitic state.

### 3.2.2 Maximizing Indent Recovery

#### 3.2.2.1 Effect of $a/r$ Ratio

##### 3.2.2.1.1 Spherical Indents

Spherical indents are not geometrically the same at different indentation depths. They are generally characterized by  $a/r$ , the ratio of the in-plane indent contact radius  $a$  and the indenter radius  $r$ . This ratio determines the representative strain ( $\epsilon_p = 0.2 a/r$ ), which characterizes the deformation strain in spherical indentation.

Spherical indents were made under various loads that resulted in  $a/r$  ratios ranging from 0.4 to 0.95. (Note that for  $a/r = 1.0$  the sphere would be pushed down to

its equator.) Figure 3.2 plots the normalized indent depth change  $\delta$  over indenter radius,  $r$ , as a function of the  $a/r$  ratio for the indentation experiments in this series. The normalized cyclic indent depth change is seen to increase linearly with the  $a/r$  ratio, reaching a maximum for  $a/r = 1.0$  at which point the depth change is 4.3% of the indenter radius. Furthermore, the depth change extrapolates to zero for an  $a/r$  ratio of 0.26, reflecting a representative strain of roughly 5%, consistent with our previous observation that spherical indents producing less than 5% representative strain have one-way (not two-way) shape memory effect [Ni et al. 2003]. The curve fitting equation suggests an empirical way to predict the two-way amplitude based on an  $a/r$  ratio, as shown in the figure.

$$100 \delta / r = 5.97 \pm 0.15 a / r - 1.55 \quad \text{Eq. (3.1)}$$

The higher the  $a/r$  ratio, the larger the two-way response is.

Eq. (3.1) can be modified to express the relation between two-way indent depth and the initial indent depth,  $h_o$ , as shown in Eq. (3.2)

$$100 \delta / h_o = 5.97 \pm 0.15 \sqrt{2 r / h_o - 1} - 1.55 r / h_o \quad \text{Eq. (3.2)}$$

Figure 3.3 shows the relationship between two-way response and  $a/r$  ratio based on the experimental results and calculations based on Eq. (3.2). As shown in the figure, the maximum two-way response is about 11.5% when normalized to the initial indent depth. Based on equation 3.2, we can calculate that when  $a/r$  of 0.5 or

$r/h_o=7.95$ , the two-way response reaches a maximum of 10.8%. Based on the close match between calculation and experimental results, it is reasonable to use Eq. (3.2) to predict the amplitude of the two-way response based on the initial indent depth and the indenter radius. This allows us to better control how deep the indent should be to reach a certain two-way response on a given indenter. To predict based on Eq. (3.2) what load to use when we change the size of the indenter, it is necessary to modify Eq. (3.2) to include the indentation load,  $F$ , into the equation, as shown in Eq. (3.3):

$$100\delta = 5.97 \pm 0.15 \sqrt{F/\pi * H_m} - 1.55r \quad \text{Eq.(3.3)}$$

where the hardness of martensite is  $H_m = F/\pi * a^2$ .

Based on Eq. (3.3), we can predict the amplitude of the two-way response based on an indenter with any size and an indentation load at whichever magnitude.

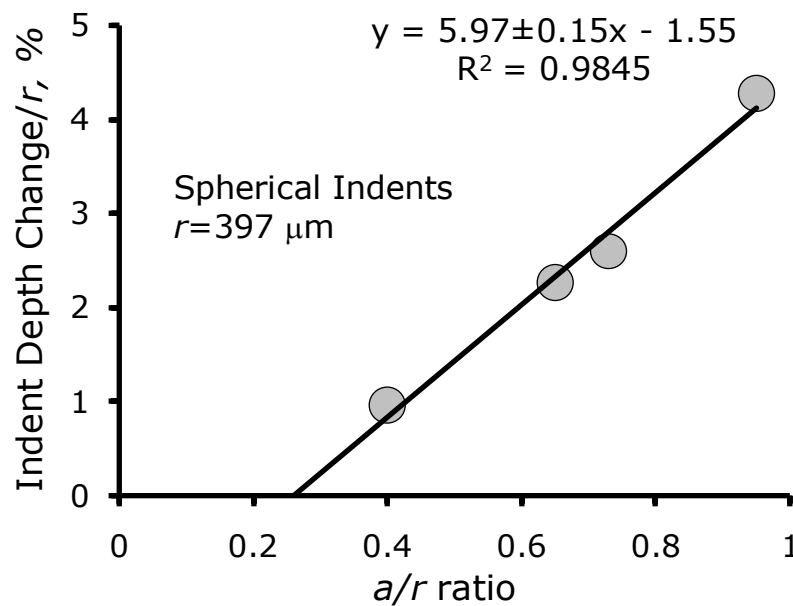


Figure 3.2 Plot of the indent depth change (normalized to the indenter radius) as a function of the  $a/r$  ratio for spherical indents.

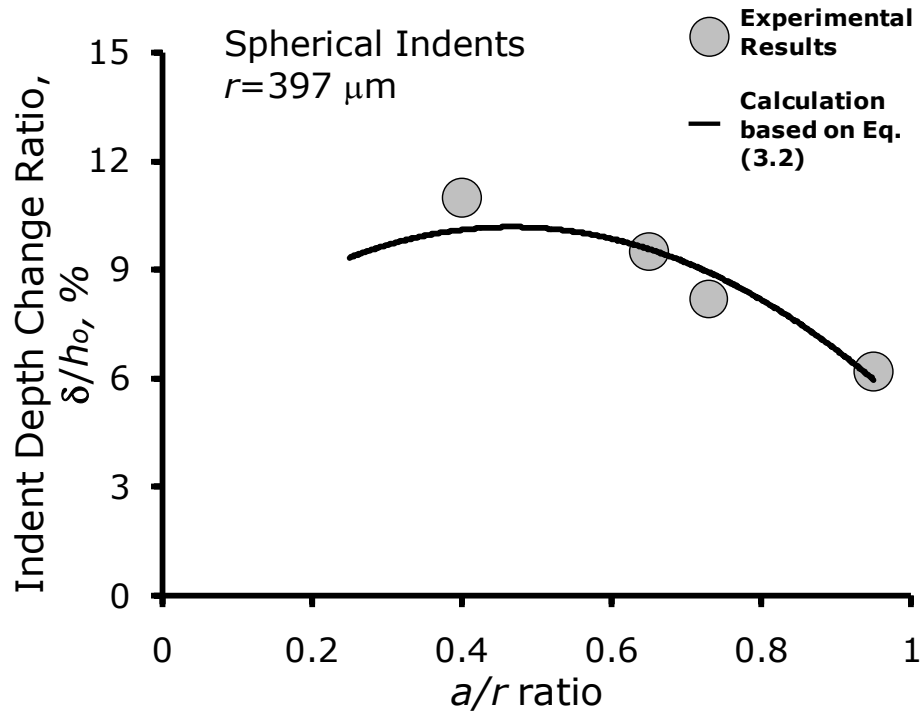


Figure 3.3 Plot of the two-way response, normalized to  $h_o$  as a function of  $a/r$  ratio based on the experimental results and calculations based on Eq. (3.2).

### 3.2.2.1.2 Cylindrical Indents

Similar to spherical indents, cylindrical indents are not geometrically the same for different indentation depths. The  $c/r$  ratio, instead of  $a/r$  ratio, taken as the cylindrical indent trench half-width,  $c$ , divided by cylinder radius,  $r$ , can be used to represent the cylindrical indentation strain. Different from spherical indents, where the representative strain is  $0.2 a/r$ , the literature does not give a value for the representative strain of a cylindrical compression. However, we can make a simple model to estimate that constant, as shown below.

Assuming the threshold of representative strain to induced TWSME in NiTi SMAs is 5%, for both spherical and cylindrical cases<sup>§</sup>, the empirical equation of representative strain for the spherical case is  $\varepsilon_{r,(sph,crit)} = \chi_{sph} a/r$ , where  $\chi_{sph}$  is 0.2. As shown in Figure 3.4, the two-way response drops to zero at a  $c/r$  of 0.2, thereby giving  $\chi_{cyl} = \varepsilon_{r,(cyl,crit)}/0.2 = 0.25$ . This coefficient  $\chi_{cyl}$  of 0.25 can thus be used to calculate the representative strain for the cylindrical compression.

Cylindrical indents were made with a tungsten rod lying parallel to the surface and placed under various loads to give  $c/r$  ratios between 0.4 to 0.95. The length of the cylindrical rod was about 6 mm, sufficiently greater than the indenter radius, to eliminate end-effects. Figure 3.4 plots the initial indent recovery (normalized to the indenter radius,  $r$ , of 127  $\mu\text{m}$ ) as a function of the  $c/r$  ratio. Unlike the spherical case, the cylindrical indent recovery amplitude increases non-linearly with the  $c/r$  ratio, again reaching a maximum for a  $c/r = 1.0$ , with an amplitude of 10.3% of the indenter radius (more than twice the corresponding amplitude found for the spherical case).

---

<sup>§</sup> We assume the threshold strain for indentation is also 5% even though NiTi has a high tension and compression asymmetry.

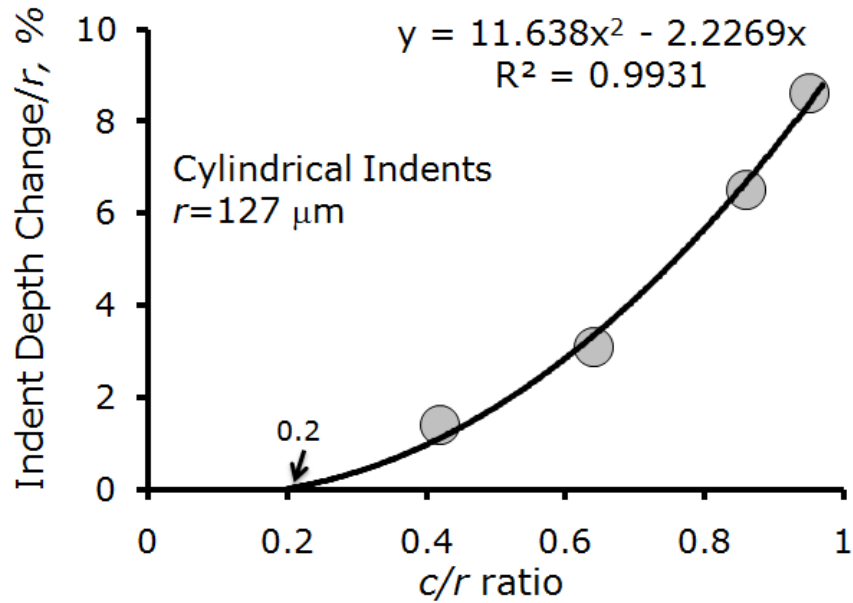


Figure 3.4 Two-way indent depth changes for cylindrical indents, normalized to the indenter radius, plotted as a function of the  $c/r$  ratio.

Curve fitting the dataset is used to get a sense of the trend of the relation between indent depth change ratio and the  $c/r$  ratio, as shown in Eq. (3.4).

$$100\delta/r = 11.6(c/r)^2 - 2.2 c/r \quad \text{Eq. (3.4)}$$

The initial indent depth can be included in the equation to show the relation between indent depth change and the initial indent depth, as shown in Eq. (3.5).

$$100 \delta/h_o = 11.6(2-h_o/2r) - 2.2 \text{sqrt}(2r/h_o - 1) \quad \text{Eq. (3.5)}$$

This equation can be further modified to show the relation between indent depth change and the indentation load, as shown in Eq. (3.6).

$$100 \delta = 11.6 F/2rL * H_m - 2.2 \text{sqrt}(F/2L * H_m) \quad \text{Eq. (3.6)}$$

Where  $F$  is the indentation load,  $L$  is the indenter length,  $H_m$  is the hardness of martensite, and  $c^2 = F/2L * H_m$ .

Table 3.1 Curve-fitting model for two-way indent depth change  $\delta$  for spherical and cylindrical indents

Indentation Parameter Affecting $\delta_c$ (two-way depth change)	Spherical Indentation	Cylindrical Indentation
Indenter Radius $r$	$100 \delta/r = 5.97 \pm 0.15 a/r - 1.55$	$100 \delta/r = 11.6(c/r)^2 - 2.2 c/r$
Indent Depth $h_o$	$100 \delta/h_o = 5.97 \pm 0.15 \sqrt{2 r/h_o - 1} - 1.55 r/h_o$	$100 \delta/h_o = 11.6(2-h_o/2r) - 2.2 \sqrt{2r/h_o - 1}$

### 3.2.2.2 Effect of Thermal Cycling

Thermal cycling is usually used as a method to stabilize the two-way response and assess cyclic stability of the two-way response. Table 3.2 summarizes the thermal cycling parameters and indent depth changes at  $a/r$  ratios of 0.4 and 0.65 for spherical indents. As the table shows, thermal cycling *increases* indent depth change by about 40% at  $a/r$  of 0.4 and 0.65. Specifically, thermal cycling increases indent depth change rapidly during the first few cycles, then the effect levels off, as shown in Figure 3.5. This ‘negative-fatigue’ behavior is yet to be understood, but one

possibility is that a cyclic softening effect involving dislocations in the subsurface zone leads to a decrease of  $A_f$  after thermal cycling.

More details of this cyclic evolution can be seen in Figure 3.6, which shows the variation of the indent depth in the fully austenitic and the fully martensitic state on thermal cycling, for spherical indents, at  $a/r$  of 0.4 and 0.65. It is apparent in Figure 3.6 that the indent depth (plotted in negative value) in austenite increases with thermal cycling, whereas the higher the  $a/r$  ratio, the larger the increase is. Note that it is the austenite depth that changes, while upon cooling, the indent depth remains unchanged along with thermal cycling. It may be that more and more retained martensite transforms to austenite with thermal cycling, leading to an increase of indent depth (negative value in Figure 3.6) in the austenitic state. Martensite may be retained by the residual stress exerted by the defects in the deformation zone after indentation. If the softening of the defects upon thermal cycling relaxes the residual stress, it may allow more and more retained martensite to transform.

Table 3.2 Thermal cycling parameters and indent depth changes for spherical indents with  $a/r$  ratios of 0.4 and 0.65

$a/r$	1 <sup>st</sup> indent recovery (μm)	25 <sup>th</sup> indent recovery (μm)	Change%	Heating Temp	Cooling Temp
0.4	3.8	5.4	42.1%	433 K	243 K
0.65	9	12.5	38.9%	433 K	243 K

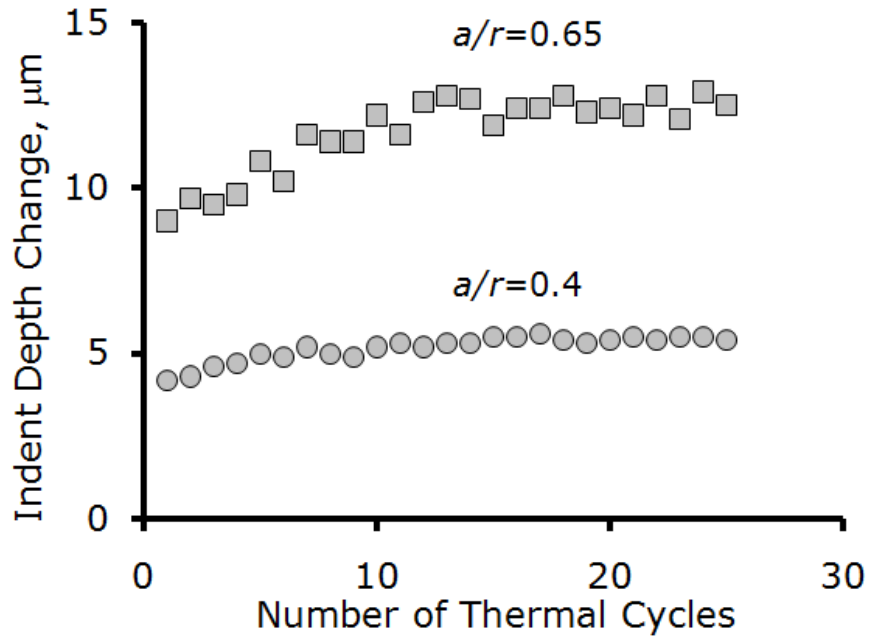


Figure 3.5 Change of the indent depth upon thermal cycling for spherical indents with  $a/r$  ratios of 0.4 and 0.65.

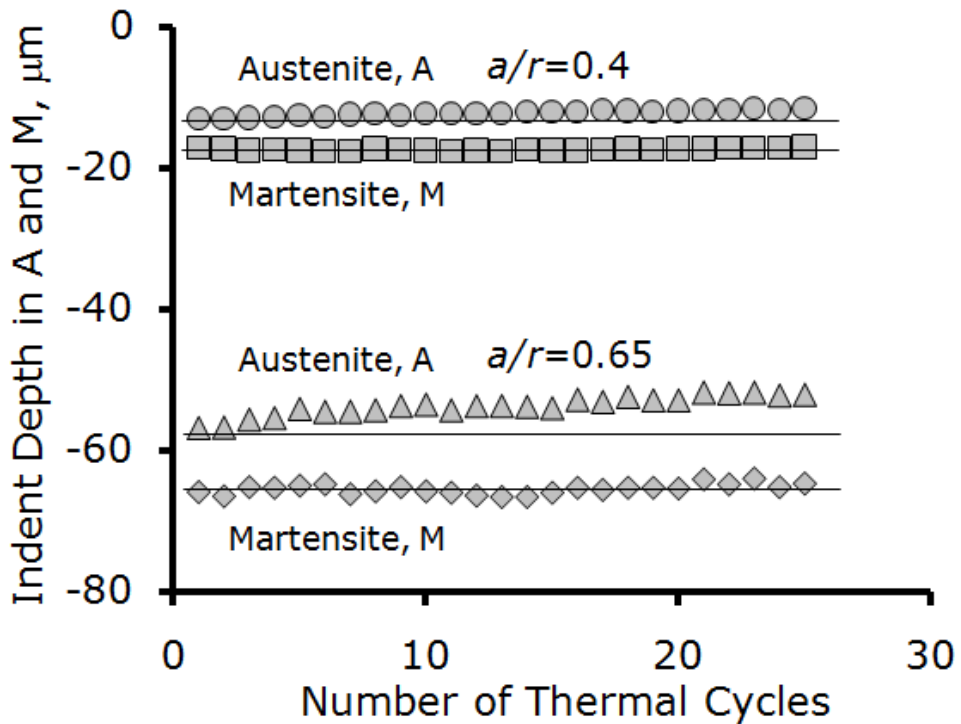


Figure 3.6 Change of the indent depth during heating and cooling for spherical indents with  $a/r$  ratios of 0.4 and 0.65.

Another possible outcome of dislocation relaxation is the decrease of transformation temperature  $A_f$  as is shown in Figure 3.7, which plots the change of magnetic susceptibility due to phase transformation against temperature change. The experiment was conducted in a Superconducting Quantum Interface Device (SQUID), which can investigate deformation related properties and localize plastic deformation during crack growth [Bonavolonta et al. 2007]. The samples used in the present study were a three gram un-indented NiTi specimen and a four gram indented NiTi specimen. Spherical indentations was made under a load of 500 N with a 0.79 mm spherical ball. We know the measured magnetization or susceptibility is related to the density of dislocations inside the specimen [Loloe et al. 1995]. The as-received specimen shows the least amount of susceptibility, as shown in Figure 3.7, while the indented specimen has larger susceptibility due to the indentation induced dislocations. After thermal cycling of the indent, SQUID measurements show the transformation temperatures do in fact shift towards lower temperatures.  $A_f$  decreases from 400 K to 364 K and  $A_s$  decreases from 358 K to 330 K.  $M_s$  and  $M_f$  remain unchanged after thermal cycling. This is a direct evidence for the measured thermal cycling effect and the change of indent depth in the austenitic state with repeated heating. While  $A_f$  keeps decreasing, more and more retained martensite transforms into austenite at the fixed thermal cycling temperature range used in the current experiment. Note too that this suggests that ‘negative fatigue’ result would vanish if a suitably high upper temperature were used during thermal cycling.

### 3.2.2.3 Effect of Indentation Spacing

Assessing the effect of indent spacing is essentially asking about the effect of overlapping the deformation zones beneath the indents. Figure 3.8 shows the effect of the indentation spacing on the indent depth change for a spherical indent made under 500 N. The indentation spacing does not have a significant effect on the two-way response until the indentation spacing is decreased to  $2.9 a$ . This is a significant data point because the indent made under 500 N with a  $r=400 \mu\text{m}$  spherical ball in the martensitic state has an  $a/r$  ratio around 0.6. Based on the front thinning experiments which will be discussed later, the  $D^*$  can be estimated to be around  $1.4 a$  for a spherical indent with  $a/r$  of 0.6. The overlapping effect is not supposed to play a role until the spacing gets below  $2.8 a$ , as shown in 3.8.

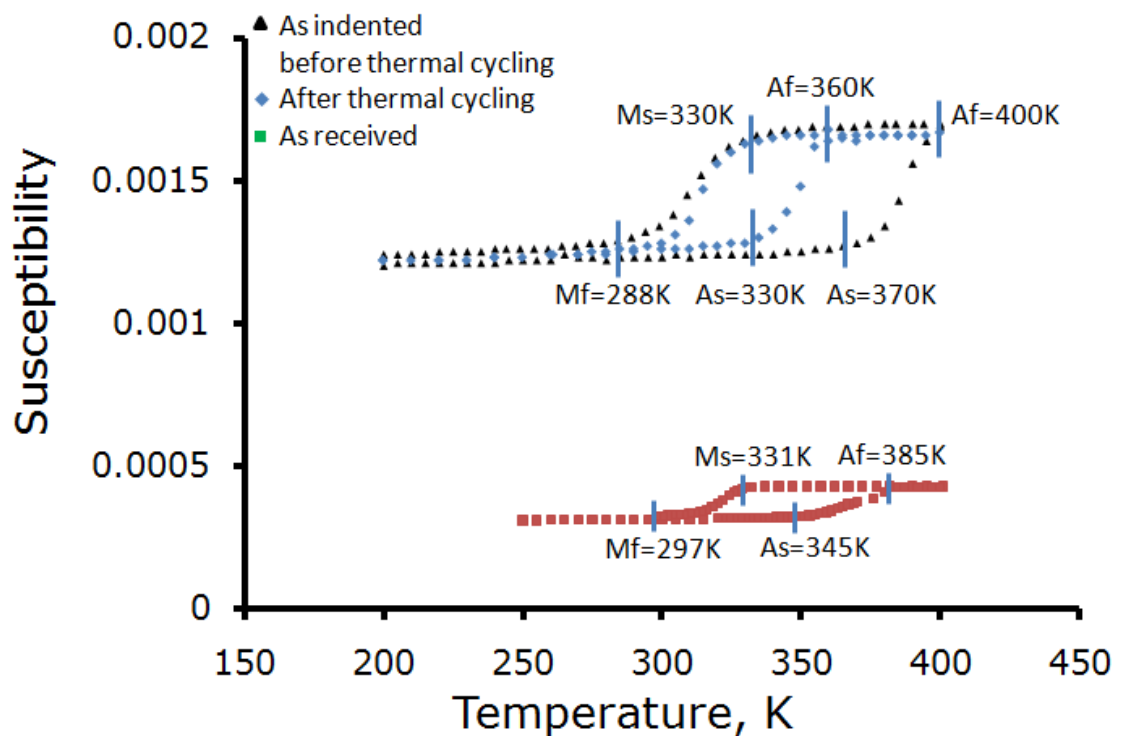


Figure 3.7 SQUID measurements of the as-indented specimen before and after thermal cycling and the as-received NiTi specimen.

At a spacing of  $2.9 a$ , where 10% of the indentation induced active zones between two indents overlap, the indent depth change increases by a small amount (about 5%) and the overlapping effect begins. When the two deformation zones completely overlap (“double indentation”), a maximum increase in two-way response of around 30% (from  $6.8$  to  $9 \mu\text{m}$ ) is observed. The two-way response further increases to  $10.7 \mu\text{m}$  (from  $9 \mu\text{m}$ ), showing another 20% increase. This shows double indentation and thermal cycling can be coupled to maximize the two-way response. Double indentation is thought to increase the size of the deformation zone that drives the two-way response. Continuing the effect of double indentation, further tests on multiple indentations are presented below.

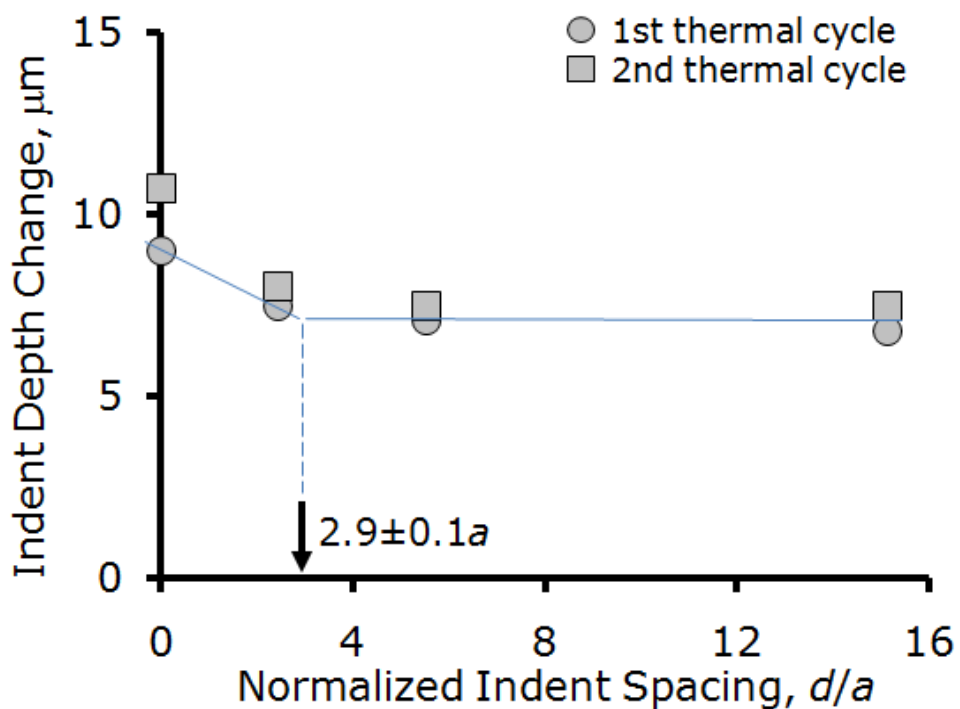


Figure 3.8 Plot of the indent depth change against the normalized indentation spacing  $d/a$  for 500 N spherical indents.

#### 3.2.2.4 *Effect of Multiple Indentations*

Double indentation increases the two-way response as shown above in Figure 3.8. Multiple indentations to 5 and 10 repetitions of spherical indentation were used to see if the two-way response can be further increased, with results shown in Figure 3.9. As can be seen, multiple indentations have a larger two-way response than the double indentation. This might be due to the fact that multiple indentations increases the indent depth, as shown in Figure 3.10, where the initial indent depth is plotted as a function of the number of repeated indentation. From the single indentation to 10 times of indentation, the initial indent depth increases from 70.7  $\mu\text{m}$  to 89.6  $\mu\text{m}$ . The  $a/r$  ratio increases from 0.57 to 0.63. Based on Eq. (3.1), as shown in Figure 3.2, we can calculate that the two-way response should change from 7.3  $\mu\text{m}$  to 8.9  $\mu\text{m}$  if the  $a/r$  ratios changes from 0.57 to 0.63 based on the effect of  $a/r$  ratio. Since the results show that the two-way response changes from 7 to 9.5  $\mu\text{m}$ , we can infer that it is the increase of indent depth, thus  $a/r$  ratio, that accounts for the increase in two-way response observed in the multiple indentation experiments.

Furthermore, as shown in Figure 3.10, the second thermal cycle increases the two-way response by about 20% on average (from 9 to 11  $\mu\text{m}$ ), which is almost three times the increase of the single indentation (7%, from 7 to 7.5  $\mu\text{m}$ ). Based on study of the thermal cycling effect described in section 3.3.2, we know that the second thermal cycle of a spherical indent made by single indentation has an  $a/r$  of 0.65, with an increase in indent depth change by 10% (from 9 to 10  $\mu\text{m}$ ). Therefore, multiple

indentations have a larger thermal cycling effect than single indentation. It also suggests that multiple indentations not only increase  $a/r$  ratio, but also helps to decrease  $A_f$  faster to achieve full transformation between martensite and austenite after indentation. However, this hypothesis is not verified and can be supported by the thermal cycling study.

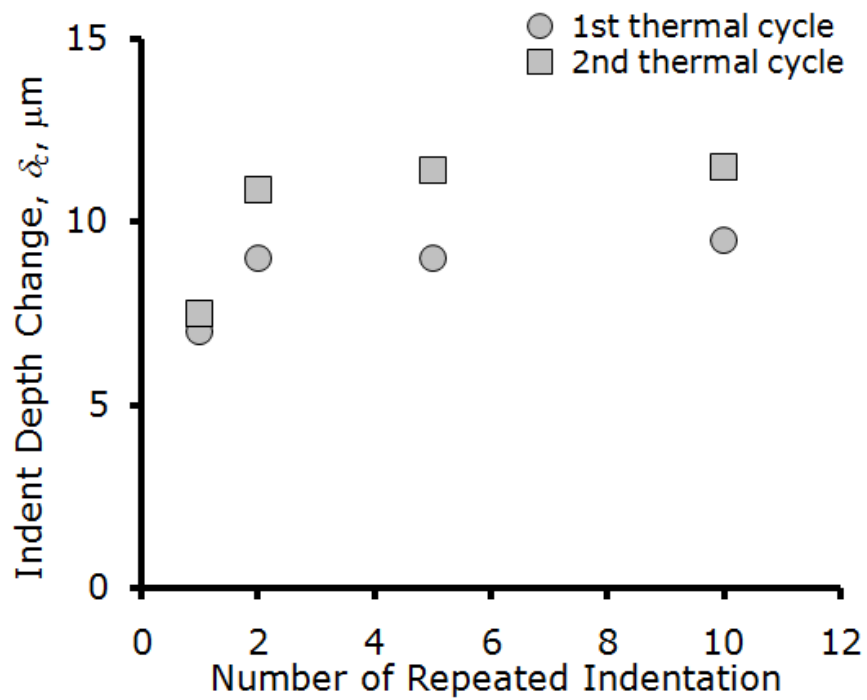


Figure 3.9 Change of indent depth as a function of repeated indentation times for 500 N spherical indents.

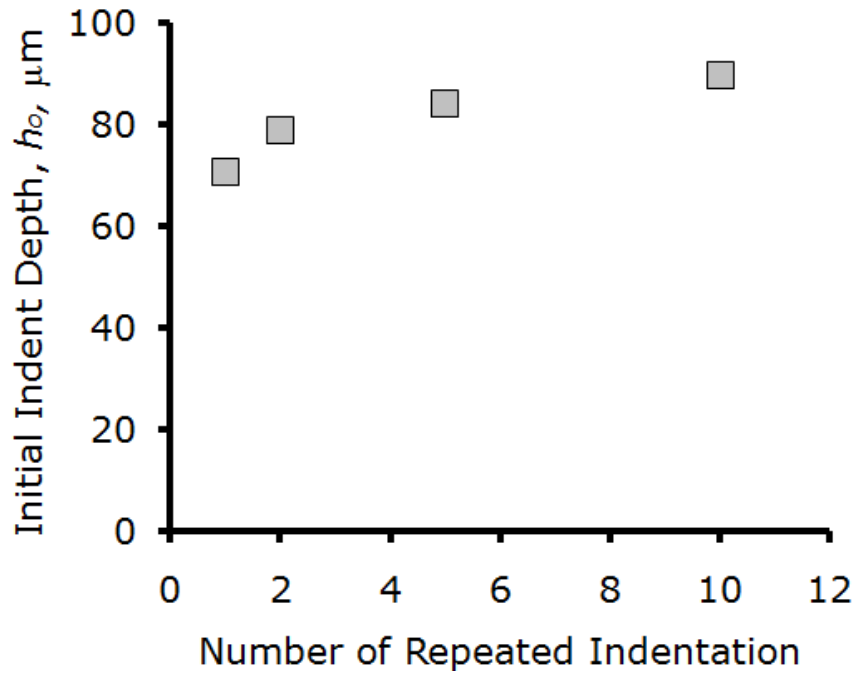


Figure 3.10 Plot of the initial indent depth as a function of repeated indentation times for 500 N spherical indents.

### 3.2.2.5 Effect of Indentation Temperature

Mechanical properties such as hardness, yield stress, and young's modulus are all different in martensite and austenite. Therefore, temperature can be effectively used to change the indentation response in NiTi SMAs.  $M_s$ ,  $M_f$ ,  $A_s$ ,  $A_f$  are 4 major characteristic transformation temperatures characterizing the phase transformation.

Spherical indents were made in both martensite and austenite for studying the two-way response. Specifically, spherical indents were made at temperatures of 213, 293, 328, 333 and 383 K under a load of 500 N with a 794  $\mu\text{m}$  diameter spherical ball. Since the specimens were first cooled in liquid Freon to 243K and  $M_f$  is 295 K,  $A_s$  is

343 K, the specimens were ensured to be in the martensitic state at a temperature below 343 K while in the austenitic state at 383 K.

Figure 3.11 plots the initial indent depth as a function of the indentation temperature. It is shown that the lower the temperature is, the shallower the indent depth is for a given load for indentation of the martensite below  $A_s$ . This is due to the fact that the material hardness increases with decreasing temperature in the martensitic state. The flow stress for deformation increases accordingly, leading to a decrease of the indent depth. It is shown that the maximum initial indent depth in the martensitic state is 104  $\mu\text{m}$  ( $a/r$  is 0.67), which can be achieved at a temperature just below  $A_s$ . The smallest initial indent depth in this experiment occurs at 213 K and is 69  $\mu\text{m}$  deep ( $a/r$  is 0.56), which is 50% less than the indent made at 333 K. Heating above  $A_s$  transforms the specimen into the austenite phase. The indent depth in austenite decreases because austenite is generally harder than martensite.

Figure 3.12 is a plot of the indent depth change as a function of indentation temperature. We can see that the lower the indentation temperature is, the smaller the indent depth change is. This is probably because the harder the material is at low temperature, the less slip deformation the indentation load can induce, thus generating less two-way response.

The maximum indent depth change occurs in a specimen that has the largest initial indent depth. It is more than twice as large as for the indent with the lowest initial indent depth. It is interesting to see that two-way response also occurs for the indent made in the austenite phase. It is possible that slip deformation occurred during deformation in austenite and remained in the specimen after unloading. This suggests that the indentation induced two-way response is directly related to slip deformation.

Figure 3.13 plots the indent depth change ratio (normalized over the initial indent depth) as a function of the indentation temperature. The maximum indent depth change ratio is 13.4%, which is about 50% larger than the ratio of the indent made at the lowest temperature.

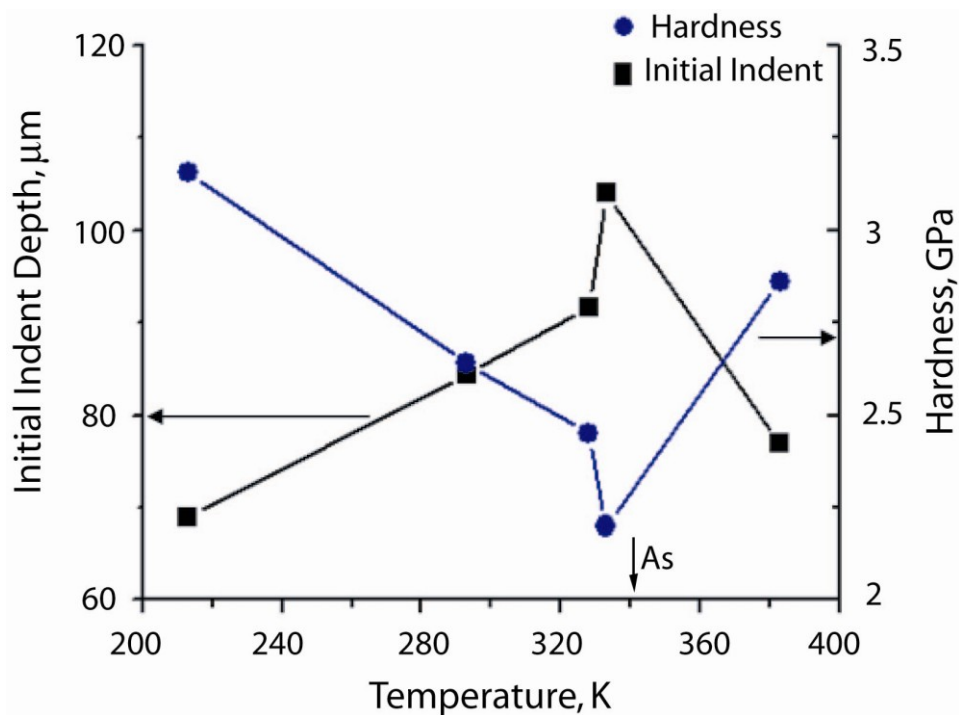


Figure 3.11 Plot of initial indent depth as a function of indentation temperature for 500 N spherical indents.

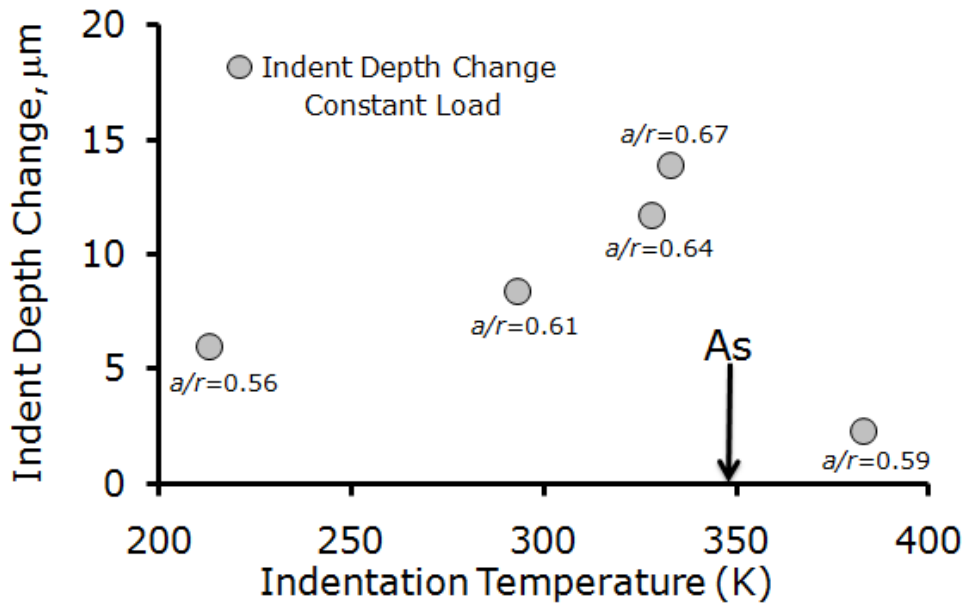


Figure 3.12 Plot of indent depth change as a function of indentation temperature for 500 N spherical indents.

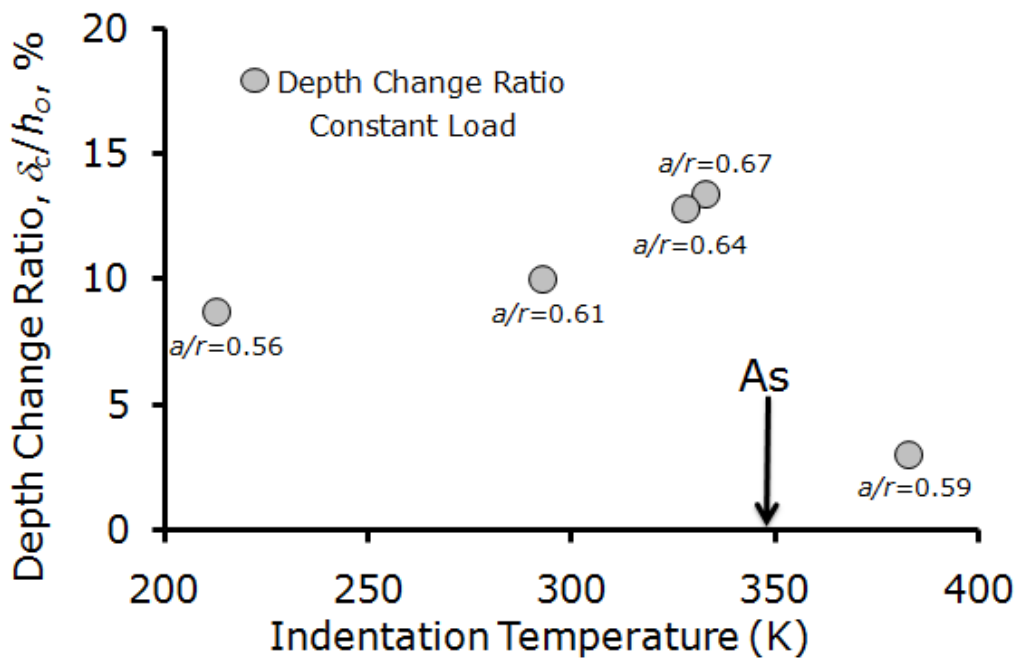


Figure 3.13 Plot of the indent depth change ratio (normalized to initial indent depth) as a function of indentation temperature for 500 N spherical indents.

### 3.2.2.6 *Effect of Prior Cold Rolling*

It is hypothesized that the slip deformation zone under the indent helps induce the two-way shape memory effect underlying SFM phenomena. Therefore, the cold rolling experiment was designed to plastically deform the specimen *before* indentation to see if this would maximize the slip deformation zone and to increase the two-way response.

Spherical indents were made under 500 N in the pre-cold rolled specimens with 5%, 10%, and 30% compressive pre-strains produced by cold rolling in the M-state. The 500 N spherical indent made in the un-deformed specimen was used as a control experiment. Three thermal cycles were applied to the specimens to obtain the two-way indent depth change. Figure 3.14 plots the change of the initial indent depth against the percentage of cold rolling. It can be seen that cold rolling work hardens NiTi specimen and leads to a decrease of indent depth up to 50% for the 30% cold rolled specimen, as compared to the un-deformed specimen. Figure 3.15 plots the two-way indent depth change as a function of the cold rolling percentage. Prior cold rolling greatly decreases the two-way indent depth change at the first thermal cycle by up to 90% for the 30% cold rolling specimen, as compared to the control specimen. 2<sup>nd</sup> and 3<sup>rd</sup> thermal cycles increase the indent depth change for the indents in the control specimen and the 5% cold-rolled specimen. The 10% and 30% cold rolled specimens may be too heavily deformed to show any change in two-way response upon thermal cycling.

Admittedly, the conclusion on the effect of cold rolling could be better supported if spherical indents with same  $a/r$  ratios were made in the cold rolled specimens. However, making indents with same  $a/r$  ratios in specimens cold rolled to various percentages requires a lot of trial and error and is not practical in engineering applications, thus is not the concern of this study.

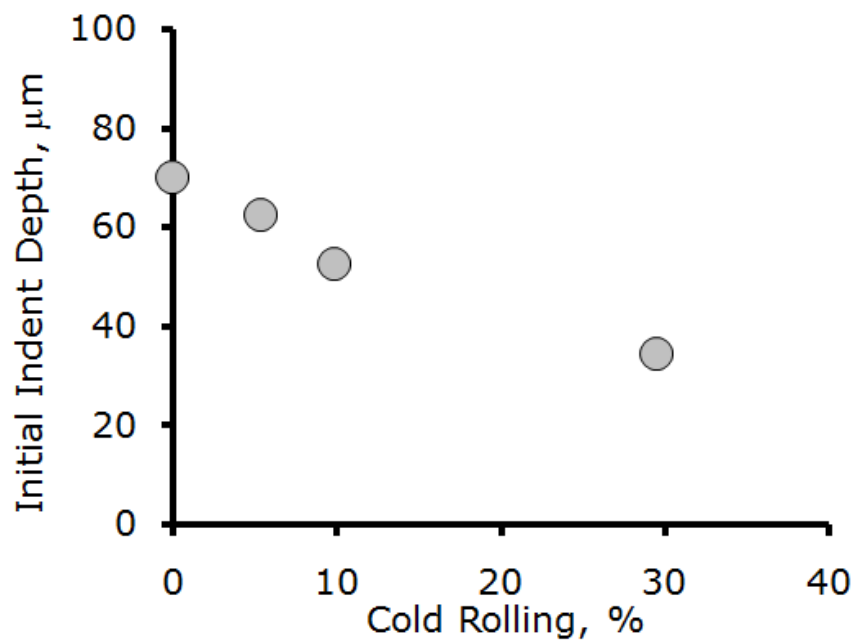


Figure 3.14 Plot of the initial indent depth as a function of the percentage of cold rolling for 500 N spherical indents.

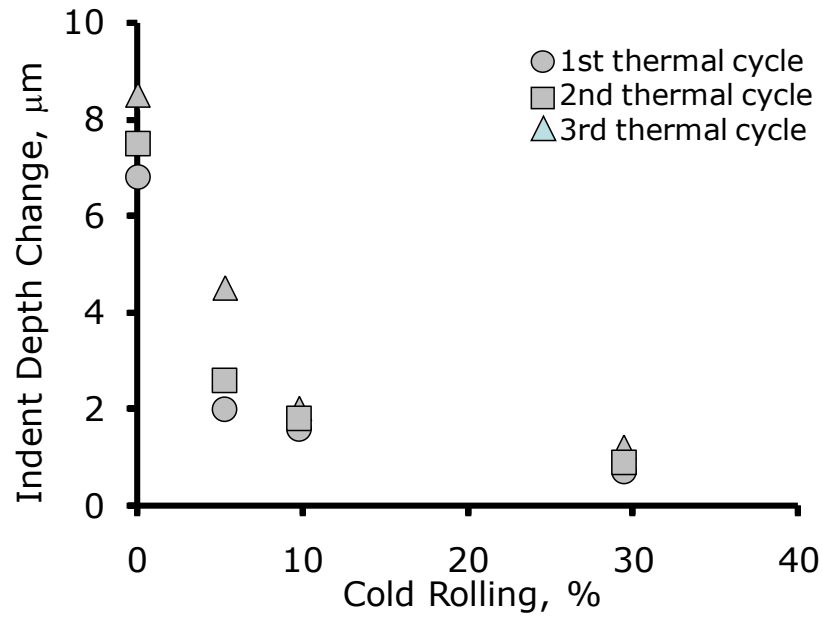


Figure 3.15 Plot of indent depth change as a function of the percentage of cold rolling for 500 N spherical indents.

### 3.2.2.7 Maximum Two-way Response

Table 3.3 summarizes the effects of all the parameters used to improve indentation induced two-way response. It is shown that an indentation temperature of 333 K, double indentation, and thermal cycling can be effectively used to increase the two-way response. Therefore, experiments were designed to combine all these effects. A spherical indent was double indented under load of 500 N at temperature of 333 K with a  $r=400\ \mu\text{m}$  spherical ball. After indentation, the indent was thermal cycled 15 times and measurement of indent depth change was made at the 1<sup>st</sup>, 5<sup>th</sup>, 10<sup>th</sup>, and 15<sup>th</sup> thermal cycle.

Table 3.3 The parameters and their effects on maximizing the two-way responses of the spherical indents.

Parameters	<i>Initial response</i>	Max two-way response, %	<i>Change %</i>
<i>a/r</i>	11.8 % at <i>a/r</i> of 0.4	11.8 % at <i>a/r</i> of 0.4	Baseline
Thermal Cycling*	11.8 % at <i>a/r</i> of 0.4	16.7 % after thermal cycling	<b>42%</b>
Indentation Spacing	9.9% at <i>a/r</i> of 0.6	10.9 % with 0 indent spacing	10%
Multiple Indentation	9.9% at <i>a/r</i> of 0.6	10.9 % with double indentation	10%
Indentation Temp	9.9% at <i>a/r</i> of 0.56	13.4% with 60°C indentation	<b>34%</b>
Cold Rolling	9.9% at <i>a/r</i> of 0.56	9.9 % at <i>a/r</i> of 0.56	0

\*Indent two-way response is 9.9-10.2% of the initial indent depth at *a/r* of 0.56.

The initial indent was measured to be 90.3  $\mu\text{m}$ , with *a/r* being calculated to be 0.64. The indent depth change on the first heating and cooling cycle was measured to be 12  $\mu\text{m}$ . This is 13.3% of the initial indent depth, larger than the maximum effect (11.8%) observed in the *a/r* ratio experiments. Figure 3.16 plots the thermal cycling effect on the double indented indent made at 333 K, compared to the single indented indent made under 700 N at 293 K at an *a/r* of 0.65. These two experimental results are comparable due to similar *a/r* ratio. As shown in the figure, double indentation at higher temperature indicates a larger initial recovery and a drastic increase at the initial 5 thermal cycles. The maximum increase from 12 to 17  $\mu\text{m}$  for double indentation by thermal cycling again demonstrates a 40% increase, the same as that of a single indentation (from 9 to 12.5  $\mu\text{m}$ , a 39% increase). Interestingly, the two-way

response of the double indented spherical indent decreases thereafter and stabilizes at 13  $\mu\text{m}$ , matching the maximum response (12.5  $\mu\text{m}$ ) of the single indent with similar  $a/r$  ratio. This result again adds support to the hypothesis that thermal cycling decreases  $A_f$  and completes the phase transformation between martensite and austenite. The result also suggests that double indentation at temperature close to  $A_s$  does not necessarily make the active zone larger, but facilitates phase transformation, thus having a larger initial recovery and reaches a saturation point faster.

To summarize, various methods such as  $a/r$  ratio, thermal cycling, indentation spacing, multiple indentation, indentation temperature, and cold rolling have been used to evaluate their effects on the two-way response of the spherical indents. Only cold rolling has demonstrated a negative effect on maximizing two-way response, as shown above. Table 3.3 summarizes the parameters used and their effects on maximizing the two-way responses. It is shown that a combination of  $a/r$  ratio, indentation temperature, and thermal cycling can be used to most efficiently increase the two-way response. It is estimated that the increase can be up to 90% for an indent with  $a/r$  of 0.56 and the maximum two-way response can be 19.1% --- [10.2%\*(1+34%)\*(1+40%)]. The experimental results support the hypothesis by showing that the maximum response 17  $\mu\text{m}$  is 19% of the initial indent depth (90.3  $\mu\text{m}$ ) or as a 90% increase from the two-way response of a single indent (9  $\mu\text{m}$ ).

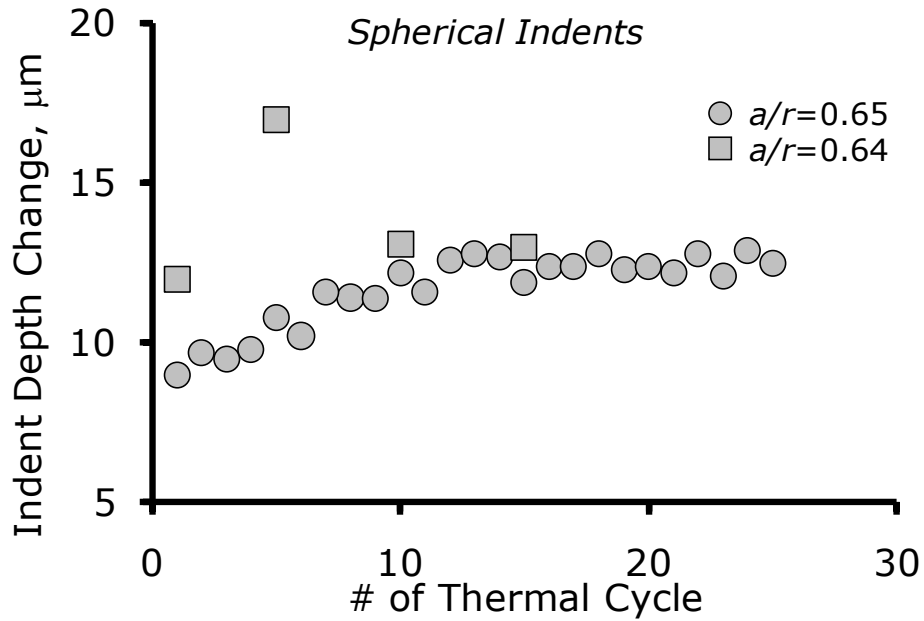


Figure 3.16 Comparison of the two-way response due to thermal cycling for spherical indents made by double indentation at 333 K and single indentation at 293 K with similar  $a/r$  ratios.

### 3.3 Planarization for Surface Form Memory

#### 3.3.1 Introduction to the Indentation-Planarization Method

The indentation-planarization method used to develop two-way surface form memory is schematically shown in Figure 3.17. A spherical indent is made in the martensitic NiTi using a spherical ball with a radius of  $r$  at a load  $P$  to a depth  $h$ . The indentation develops three subsurface deformation zones:  $a$  represents the slip zone;  $b$  represents martensite detwinned zone;  $c$  represents elastic deformation zone, as indicated in Figure 3.17b. Thermal cycling between  $A_f$  and  $M_f$  leads to a two-way indent depth change with amplitude  $\delta_i$ , as shown in Figure 3.17c. Thermal cycling after planarization (in Figure 3.17d) results in a reversible extend-to-flat transition

with amplitude  $\delta_2$ . Both indent depth change and exdent-to-flat transitions have been demonstrated to occur for up to 25 thermal cycles.

### 3.3.2 Post-recovery M-planarization

Surface profiles of the exdent-to-flat transition for a specimen made by spherical indentation-planarization are shown in Figure 3.18, as measured optically. The spherical indent was made under 700 N with a 0.794 mm tungsten carbide ball. The  $a/r$  ratio is 0.65. The exdent height is around 9  $\mu\text{m}$ . The size of the exdent is around 500  $\mu\text{m}$ . This makes the contact angle of around  $2^\circ$ . Here, the contact angle is used to compare exdent responses at different  $a/r$  ratios and to characterize various exdent shapes made from different indenters. For spherical exdents, the maximum contact angle is calculated to be  $2.4^\circ$ , where the exdent amplitude is around 16  $\mu\text{m}$ , the size of the exdent is around 800  $\mu\text{m}$ , and the  $a/r$  ratio of the indent is 0.95.

Figure 3.19 shows (a) a reversible cylindrical exdent-to-flat transition, (b) a punch exdent-to-flat transition, (c) a mesh exdent-to-flat transition, (d) a pyramidal exdent-to-flat transition and (e) a comparison between a pyramidal exdent and a spherical exdent. In figure 3.19 (e), the vertical scale is adjusted for better visualization.

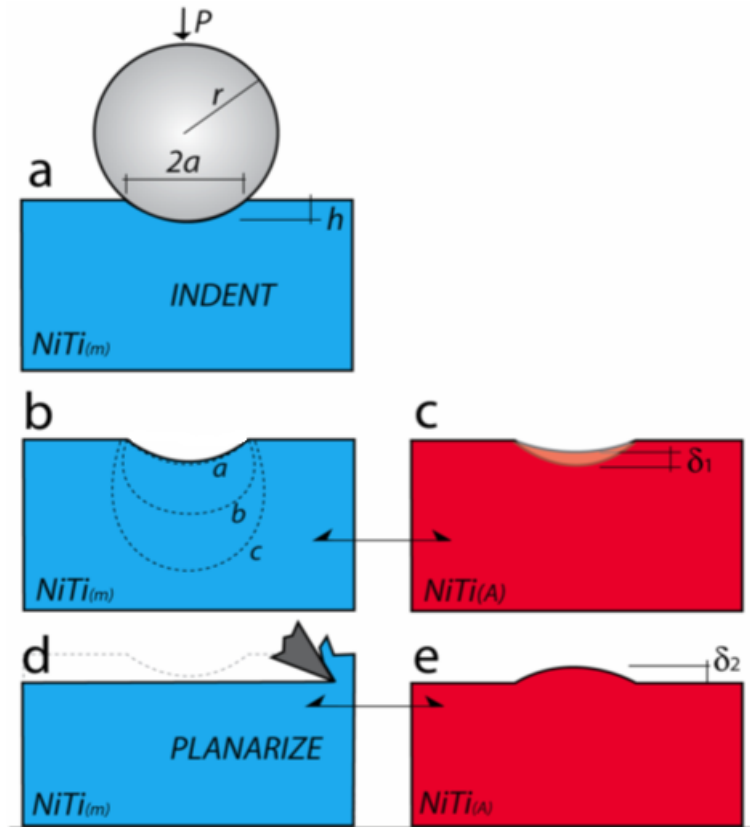


Figure 3.17 Indent training (a-c) and planarization (d) to obtain Surface Form Memory (SFM) ‘exdents’ in NiTi. Thermally cycling between (b)  $\leftrightarrow$  (c) and (d)  $\leftrightarrow$  (e) is indefinitely repeatable. Indentation results in three deformation zones under the indent: *a*: Plastic Slip Zone, *b*: Detwinned Martensite Zone, *c*: Elastic Deformation Zone (Semi infinite volume).

A cylindrical indent was made by indenting a 0.254 mm diameter tungsten rod with cylinder axis parallel to the indented surface under 1500 N. The cylindrical indent can be thought as an extension of spherical indents with a 2 dimensional deformation zone. The maximum contact angle is calculated to be around  $5.7^\circ$  when the exdent amplitude is  $12\ \mu\text{m}$ , the size of exdent is  $240\ \mu\text{m}$ , and the  $a/r$  ratio is 0.95.

Flat punch indents were made by indenting a 0.254 mm in diameter and 2 mm long tungsten rod with rod axis perpendicular to the sample surface. The indent replicates the punch indent shape, as shown in Figure 3.19 (b). Owing to the flat punch geometry, a maximum contact angle ( $90^\circ$ ) can be achieved. The flat punch indents can be placed close to each other to achieve maximum indent density. These closely packed punch indents can be used to generate larger actuation response.

Mesh indents were made by indenting a stainless steel screen mesh with a mesh size of 0.5 mm. The junction points in the mesh indent can be thought as stress concentration points which induce larger indentation deformation zone underneath it and generate higher indent response, as shown in Figure 3.19 (c).

A Vickers indenter having a half angle of  $68^\circ$  was used to develop pyramidal indents. As shown in Figure 3.19 (d), a pyramidal indent-to-flat transition occurs repeatedly upon heating and cooling after planarizing a Vickers indent. The indent shares the same contact angle as is the half angle of the Vicker's indenter ( $70.3^\circ$ ).

Figure 3.19 (e) compares the shape of a spherical indent with a pyramidal indent. Spherical indent has a smooth transition in curvature. Pyramidal indent replicates the shape of the Vickers indenter with a sharp peak in the center. The plastic strain at the peak is assumed to reach singularity due to stress concentration. The vertical scale is exaggerated for better visualization.

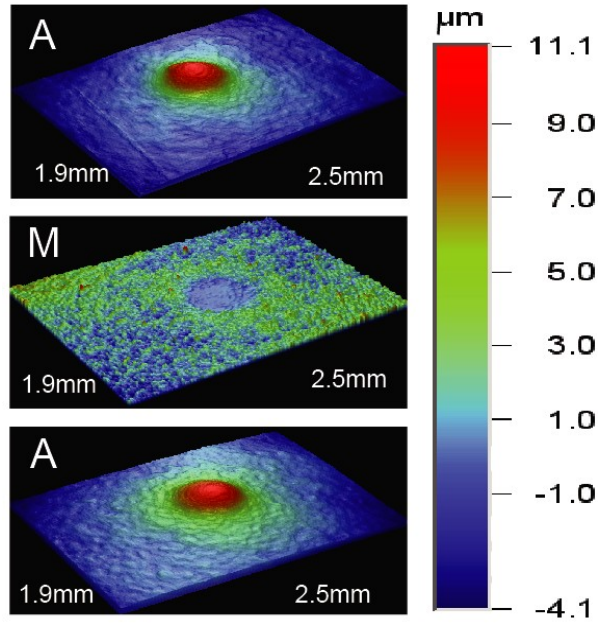


Figure 3.18 Cyclic exdent-to-flat surface transitions after planarization of a spherical indent.

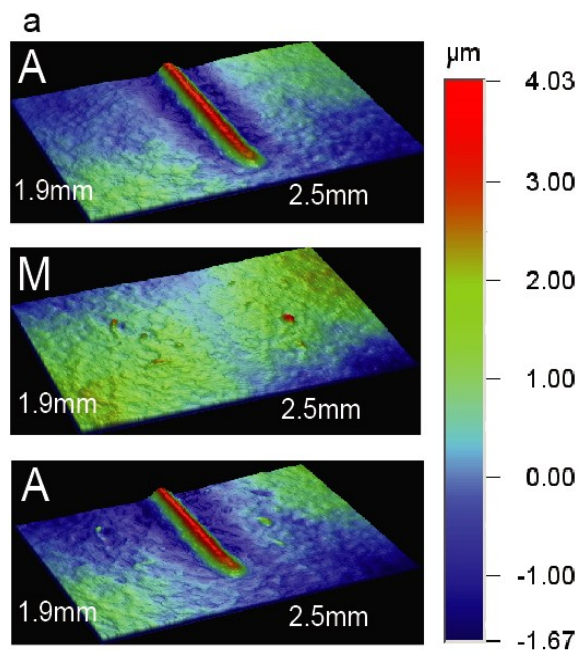


Figure 3.19 Profiles of various exdent shapes measured after indentation-planarization in a series of hot-cold-hot: a) cylindrical bumpy-to-flat transition; b) punch bumpy-to-flat transition; c) mesh bumpy-to-flat transition; d) pyramidal bumpy-to-flat transition; e) spherical exdent is compared to pyramidal exdent. (The vertical scale is adjusted for better visualization).

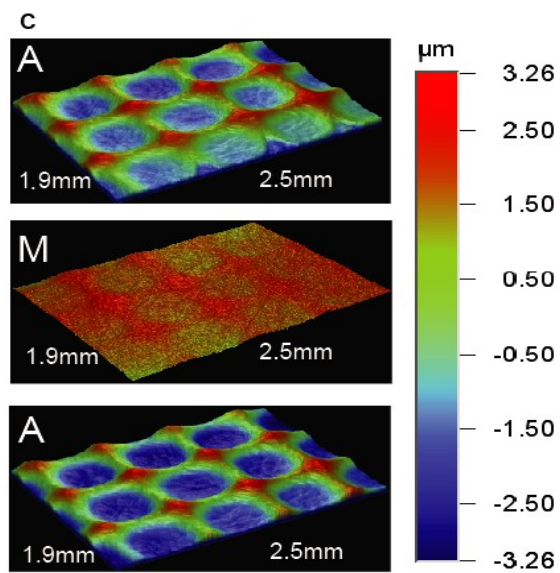
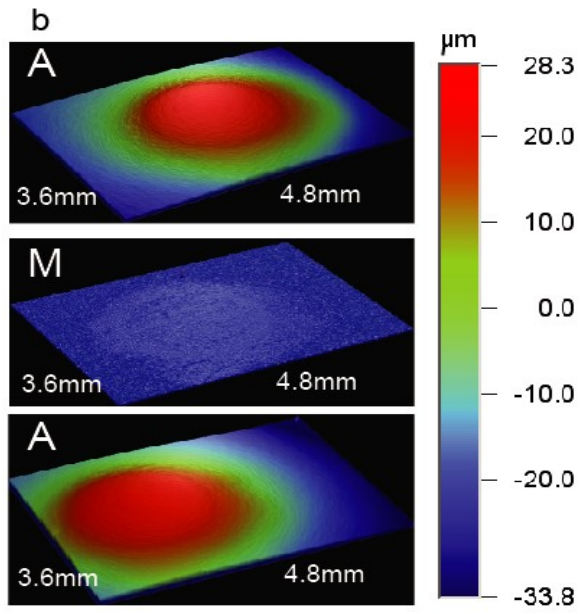


Figure 3.19 cont'd.

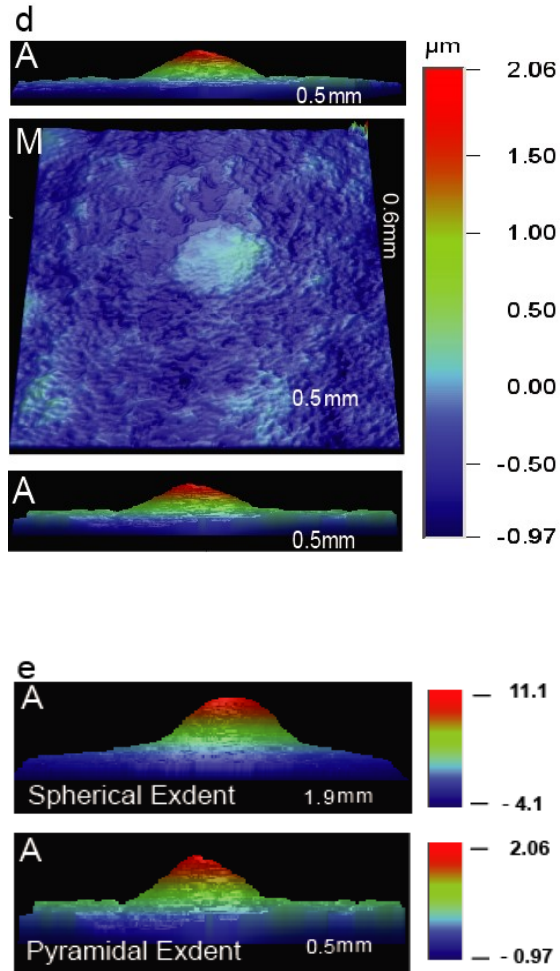


Figure 3.19 cont'd.

### 3.3.3 Pre-recovery M-planarization

To further the understanding of first recovery, a planarization step was conducted on indents before recovery in the martensitic state. A spherical indent was made under a load of 500N with a  $r=0.794$  mm spherical ball in the martensitic state. The initial indent depth was optically measured to be 78.6  $\mu\text{m}$ . The  $a/r$  ratio was calculated to be 0.6. After indentation, the indent was planarized in the martensitic state to restore a flat surface *without* first recovery. We call this procedure “Pre-recovery M-planarization”. The specimen was then heated to  $433 \pm 2$  K (above

$A_f$ ) and cooled to  $283 \pm 2$  K (below  $M_f$ ) using a thermo-electric cooler (TEC). The surface profiles of the specimen upon heating and cooling were obtained optically, as shown in Figure 3.20. Heating after pre-recovery M-planarization generated an exdent with amplitude of  $38 \mu\text{m}$ , which is around 50% of the initial indent depth. Cooling, however, could not lead to a transition to complete flatness, but to an exdent with amplitude of around  $28.8 \mu\text{m}$ . This confirms that the detwinned martensite zone recovered after heating cannot fully recover upon cooling. Interestingly, the decrease in amplitude of around  $9 \mu\text{m}$  upon cooling was found to be the same as the first recovery of a spherical indent with a similar  $a/r$  ratio. This suggests that planarization does not change the slip deformation zone. The material with a larger volume underneath the indent plays an important role in the indentation-induced TWSME. Apparently the material in the radial zone around the indent contributes little to the effect.

The large exdent formation after pre-recovery M-planarization generates appreciable energy and can be applied to high energy actuation devices. To this end, replica indentation experiments were carried out to study the work output and energy density of NiTi SFM, the detail of which will be illustrated in section 3.5.2.

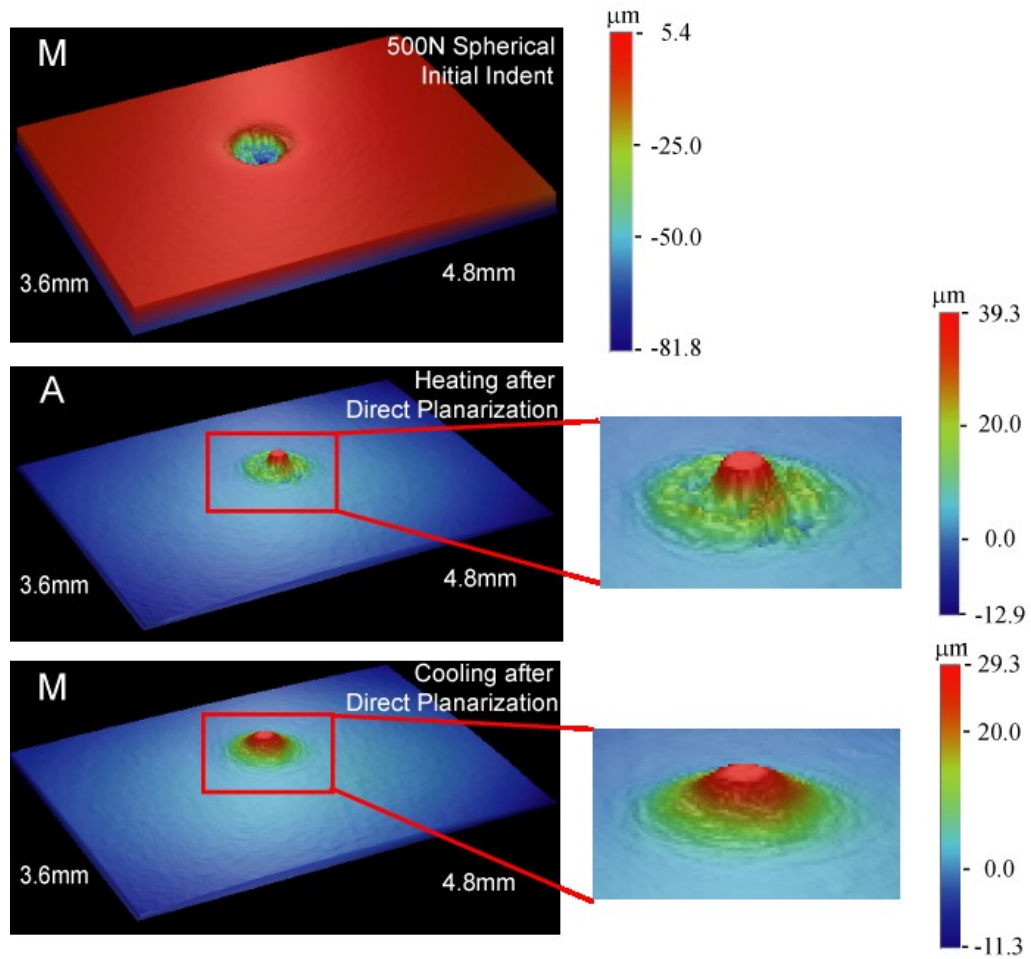


Figure 3.20 Surface profiles of the initial 500 N spherical indent, extent upon heating and cooling after pre-recovery m-planarization.

### 3.3.4 Post-recovery A-planarization

In the current research, NiTi specimens at a given temperature have one of three possible surface *forms*: exdented, flat, and indented. There are consequently totally  $3^2=9$  possible classes of surface form memory. Exdent-exdent, flat-flat, and indent-indent transitions are trivial cases, since there is no change in form. Therefore, 6 variations are left to be developed, as shown in Figure 3.21, with variation 1 being the class demonstrated up to this point. In order to develop the remaining five variations, indentation and exdentation methods in the martensitic state were

developed and planarizations at hot, median, and cold temperatures were used. Median temperature refers to a temperature at which martensite and austenite coexist (optimal condition is 50% martensite and 50% austenite). Indent-to-exdent or exdent-to-indent transition (variation 5 and 6) can possibly be developed using median temperature planarization method.

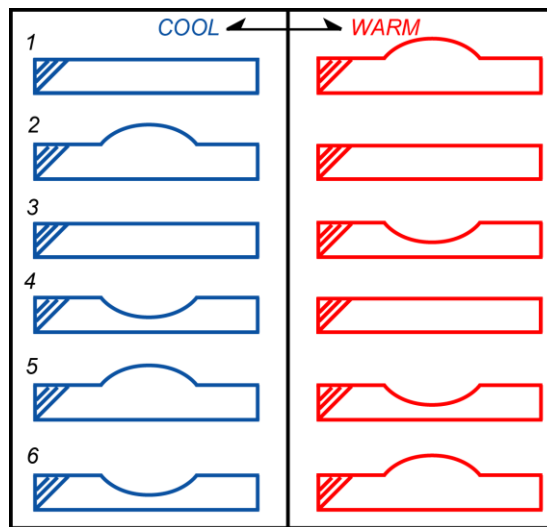


Figure 3.21 Six possible variations of Surface Form Memory in NiTi SMAs.

Thus far it has been demonstrated that indentation and planarization in the martensitic condition turns the indent depth change into reversible exdent-to-flat surface transition (variation 1). It is possible to achieve a flat-to-indent transition (variation 4) by planarizing the indent in the austenitic state. This planarization method is called “Post-recovery A-planarization”. To this end, a spherical indent was made under 200 N with a  $r=0.794$  mm spherical ball in the martensitic state. Figure 3.22 shows the surface profiles of the 200 N spherical indent, specimen under cooling

after post-recovery A-planarization, and under subsequent heating. The initial indent depth was measured to be 38.2  $\mu\text{m}$  and the  $a/r$  ratio was calculated to be 0.42. After post-recovery A-planarization, the specimen was cooled to 243 K and a spherical indent was observed with a measured depth of 5.6  $\mu\text{m}$  at 293 K. This indent depth after first recovery is 14.7% of the initial indent depth. This effect is larger than what we have observed for the initial indent depth change ratio (the maximum is 11.4% [Fei et al. 2009]). The surface roughness  $R_a$  for the specimen is optically measured to be 500 nm. The specimen was then heated to 433K and the surface profile measured optically shows a flat surface with roughness  $R_a$  to be 100 nm and Peak-to-Valley difference  $R_t$  on the order of 1 micron. Apparently, heating has smoothed the surface due to shape memory recovery.

Subsequent cooling drove the formation of the indent again, while heating afterward led to a flat surface with a small extent having amplitude of around 0.6  $\mu\text{m}$ . This extent occurred consistently on the following thermal cycles, as shown in Figure 3.23. At the 10<sup>th</sup> thermal cycle, the indent depth in cooling was measured to be 6.4  $\mu\text{m}$ , while the extent height in heating was measured to be 1.1  $\mu\text{m}$ . This difference of 7.5  $\mu\text{m}$  is about 34% increase from the initial indent recovery (5.6  $\mu\text{m}$ ). This result matches with what we observed for the spherical indent that has been thermal cycled 25 times and shown a 40% increase in amplitude. The small extent amplitude on heating is unexpected but can be removed by a subsequent fine polish of the surface

in austenite. The details of the thermal cycling effect have been discussed in Section 3.2.2.2.

To conclude, the surface exdents are thought to be related to the indenter geometries and deformation zones under the indents. The maximum contact angle of the surface exdents is  $90^\circ$  for flat punch exdent. Spherical exdents have the lowest contact angle due to the smooth transition of the curvature of the spherical exdent. The mechanism of forming surface exdent is further studied in Section 3.4. Methods such as indentation, exdentation, and hot, median, cold planarizations can generate six variations of surface form memory, which can be possibly applied into many areas.

### **3.4 Characterization of the Active Deformation Zone**

#### **3.4.1 Front Thinning Experiments**

##### ***3.4.1.1 Spherical Indents***

It was previously shown that the material above the base of the indent does not affect the two-way response based on the comparison between post-recovery M-planarization after first recovery and pre-recovery M-planarization without first recovery. Therefore, it becomes important to study the deformation zone underneath the indent in order to understand the indentation-induced TWSME and SFM. To this end, step by step front-thinning experiments were conducted in order to locate a critical depth of material removal ( $d_{pl}$ ) that would cause the exdent effect to vanish, as

shown in Figure 3.24. This critical depth is represented by  $D^*$  in the following discussion and refers to an active zone that drives two-way shape recovery.

Figure 3.25 shows the relationship between exdent height ( $h_e$ ) and the amount of material removed by polishing ( $d_{pl}$ ) for the case of spherical indents with  $a/r$  of 0.4, 0.65, and 0.95, respectively. Not surprisingly, as successive layers of material are removed the exdent amplitude decreases. The decrease is nonlinear but can be fitted to a parabolic curve. Extrapolation of these curves to zero exdent amplitude is a gauge of the depth of the subsurface deformation zone responsible for the exdent effect (referred to the initially planarized flat surface). This depth  $D^*$  has values of 179, 378, and 718  $\mu\text{m}$  for the spherical indents with  $a/r$  ratios of 0.4, 0.65 and 0.95, respectively. Normalized to the initial indent contact radius,  $a$ , these depths are  $1.13a$ ,  $1.47a$ , and  $1.90a$ , respectively.

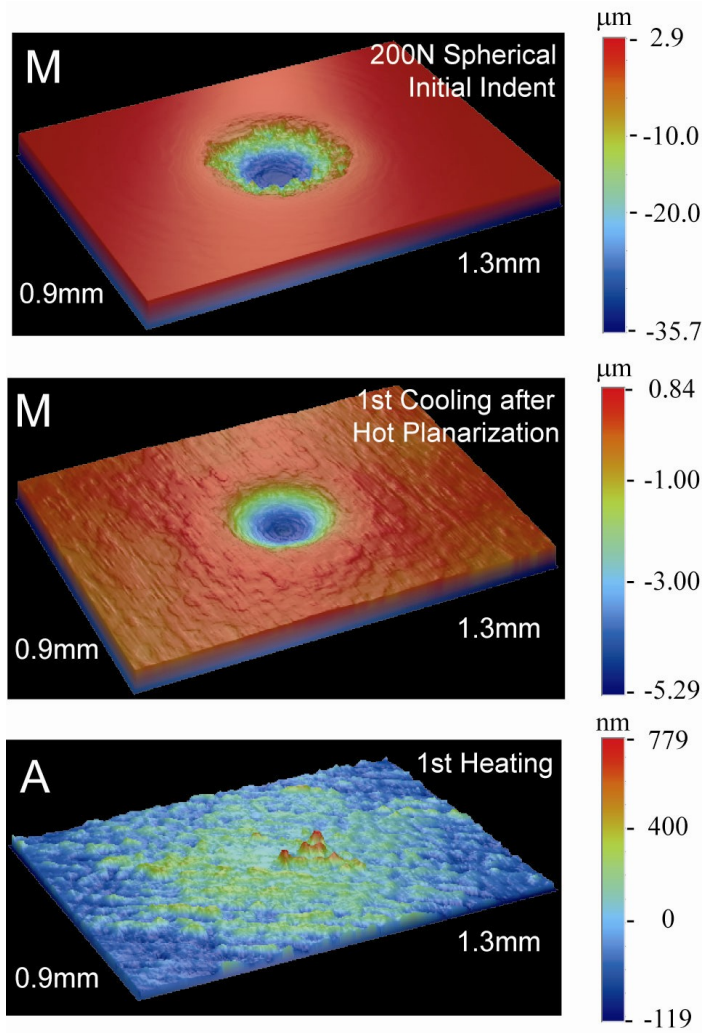


Figure 3.22 Surface Profiles of 200N spherical indent, indent upon cooling after post-recovery A-planarization, and subsequent heating.

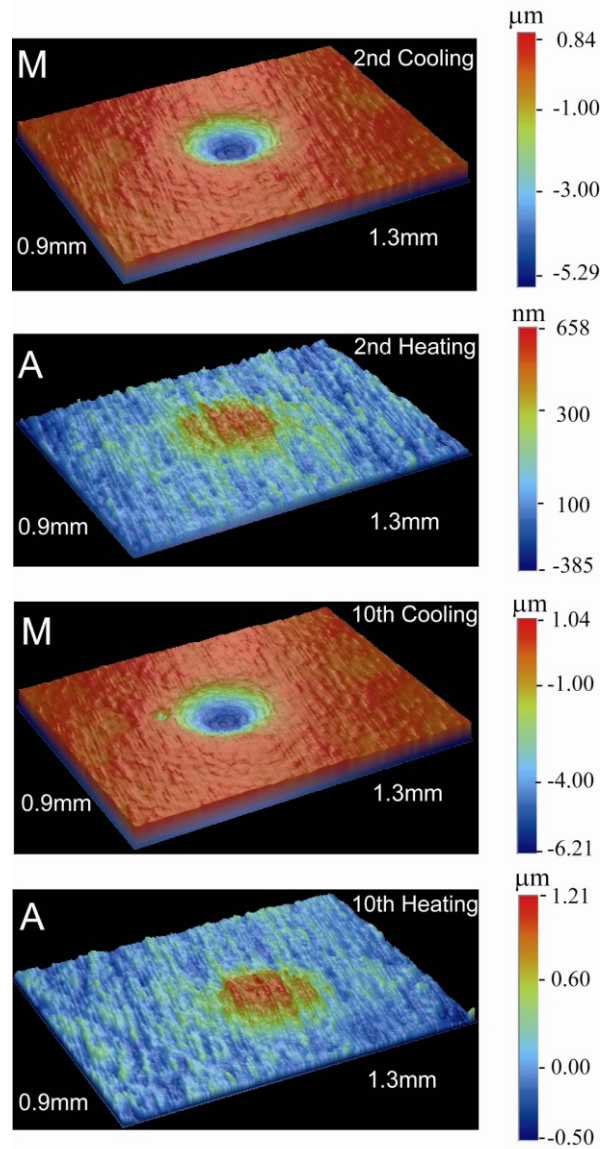


Figure 3.23 Subsequent thermal cycling of 200 N spherical indentation after post-recovery A-planarization to ensure the reversibility of surface feature transition.

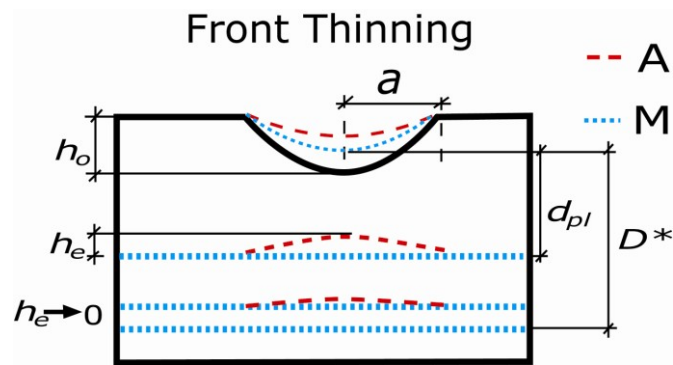


Figure 3.24 Schematic illustration of the front thinning experiment.

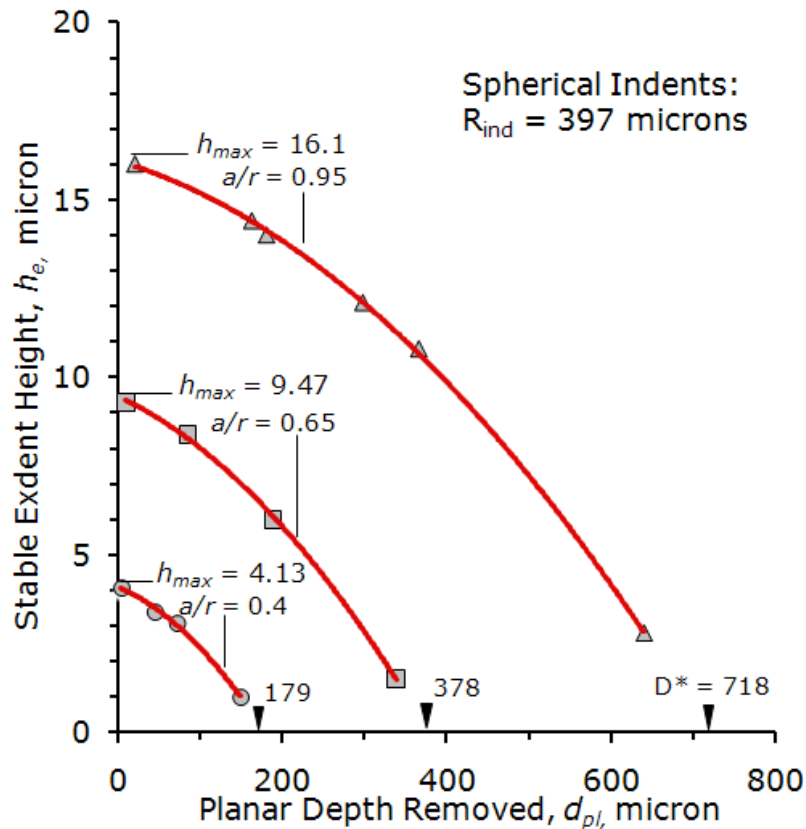


Figure 3.25 Results of the front-thinning experiments. The stable cyclic exdent height is plotted as a function of surface removal depth for spherical indents with  $a/r$  ratios between 0.4 and 0.95.

### 3.4.1.2 Cylindrical Indents

The cylindrical indentation deformation zone was also studied using front-thinning experiments. Figure 3.26 shows exdent height vs. material removal for cylindrical indents with  $a/r$  ratios of 0.42, 0.64, and 0.95. This data can be linearly curve-fitted and could again be extrapolated to determine the removal depth,  $D^*$ , expected to cause zero exdent amplitude.  $D^*$  values for the cylindrical indents were 95.2, 186 and 502  $\mu\text{m}$ , or  $1.78a$ ,  $2.28a$ , and  $4.15a$ , for  $a/r$  ratios of 0.42, 0.64, and 0.95 respectively, all substantially larger than found for spherical indents having

comparable  $a/r$  ratios. Table 3.4 summarizes the indent responses ( $h_{max}$ ,  $D^*$ ) for both spherical and cylindrical indents at various  $a/r$  ratios.

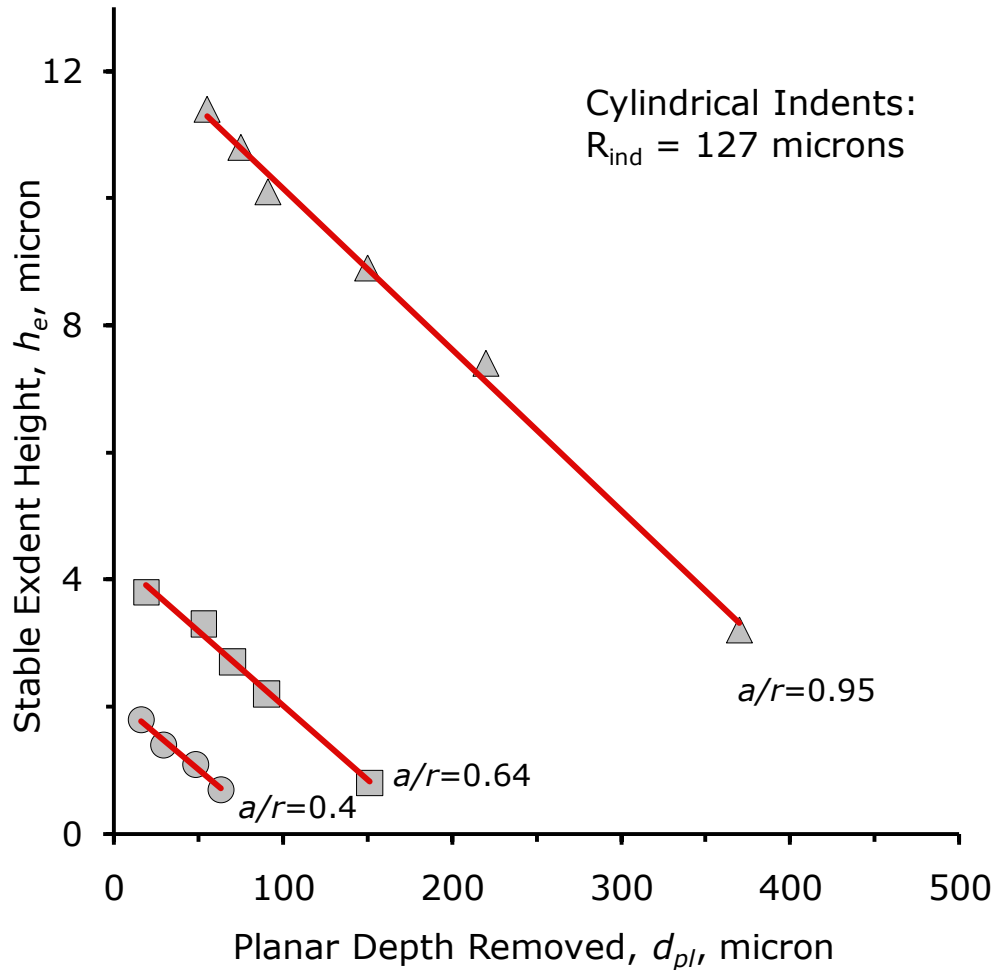


Figure 3.26 Results of successive planarization experiments. The stable cyclic exdent height is plotted as a function of surface removal depth for cylindrical indents with  $a/r$  ratios between 0.4 and 0.95.

Table 3.4 Responses of spherical and cylindrical indents at different  $a/r$  ratios

Indent Type	$a/r$	$h_{max}(\mu m)$	$D^*(\mu m)$	$D^*/a$
Spherical	0.4	4.1	179	1.13
	0.65	9.5	378	1.47
	0.95	16.1	718	1.9
Cylindrical	0.4	2.1	94	1.78
	0.64	4.3	185	2.28
	0.95	12.5	500	4.15

### 3.4.2 Back Thinning Experiments

Front thinning experiment registers the size of deformation zone,  $D^*$ , successfully. However, it cannot provide support whether it is the plastic deformation zone itself that induces two-way response in NiTi SMAs. It may well be that the elastic deformation zone under the indent serves as a “bias spring” that pushes the indent up upon heating and pulls the indent down upon cooling. To address this problem, back thinning experiments were designed to: 1) verify the size of the active zone,  $D^*$ ; 2) show whether the elastic deformation zone is responsible for indentation induced two-way response. (Note that the zone laterally outside the  $D^*$  hemisphere may contribute.)

A spherical indent with initial indent depth of 91.3  $\mu\text{m}$ , thus  $a/r$  of 0.64, was used in back-thinning experiments in which material from the backside of the specimen was removed by successive grinding up to a depth close to the base of the indent, as shown in Figure 3.27.

With back thinning, the difference between the indent depth in heating and cooling did not decrease, but instead increased by about 12% due to the thermal cycling effect, as shown in Figure 3.28, which plots the indent depth change upon heating and cooling as a function of the material remained, divided by over contact

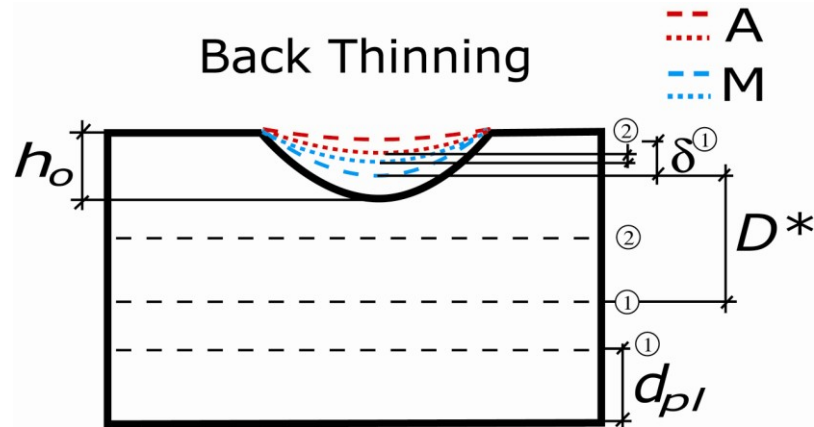


Figure 3.27 Schematic illustration of the back thinning experiment.  $\delta$  decreases after a critical depth of material was removed from the backside of the specimen.

radius  $a$ . It was until the deformation zone was just beginning to be polished away where the indent depth change rapidly decreased. In Figure 3.28, zero refers to the bottom of the indent after first recovery, thus matching closely with the results of the incremental front thinning experiment. The result shows the size of the deformation zone measured by back-thinning experiment was  $1.7a$  for a spherical indent with an  $a/r$  of 0.64. Figure 3.29 plots the indent depth in martensite and austenite as a function of material remained, normalized to the contact radius. It is shown that the indent depth in martensite decreases quickly after the active zone starts being polished away.

Figure 3.30 shows the results of front and back thinning experiments, and the spherical indentation deformation zone modeled by ABAQUS [Fei et al, 2010]. The spherical indentation deformation zone was modeled by indenting an elasto-plastic material under general elasticity and *Von Mises* plasticity mechanisms. The material properties used in the model were measured by tensile testing of the martensitic NiTi

dog-bone shaped specimen. In Figure 3.30, the experimentally measured  $D^*$  from back thinning matches with the front thinning experiment relatively well and corresponds to a deformation zone that has deformation strain of around 7% which is beyond the strain that can be accommodated by martensite deformation twinning mechanism. Therefore, it is concluded that slip deformation occurs in the active zone and dislocations are responsible for the indentation-induced TWSME. Elastic deformation zone is ruled out in the back thinning experiment as being responsible for two-way response.

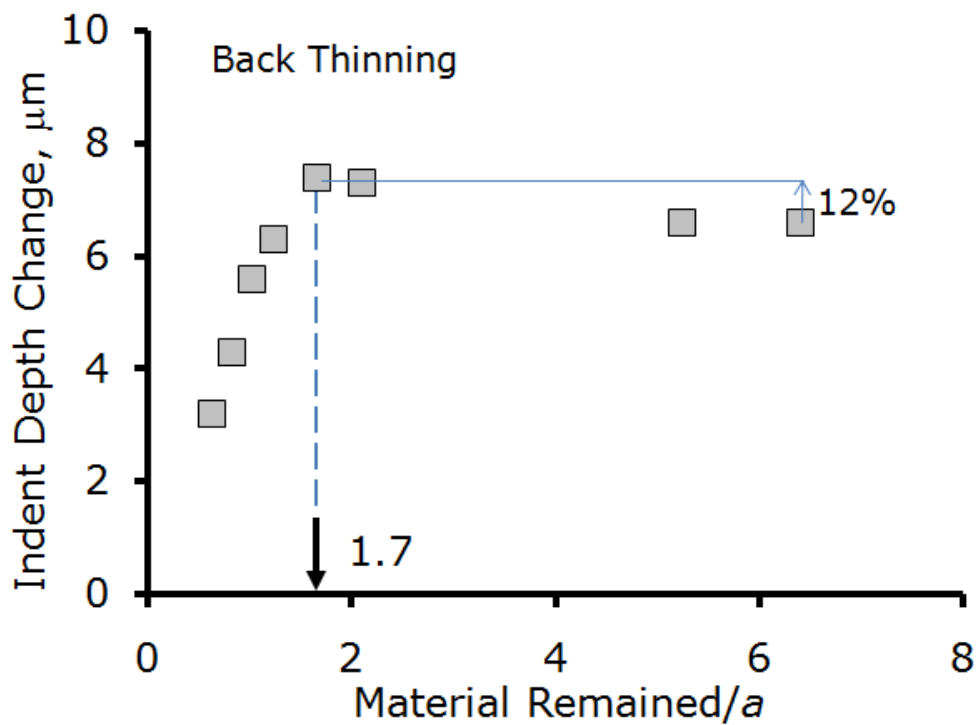


Figure 3.28 Plot of indent depth change as a function of the remained material, normalized over the contact radius  $a$ .

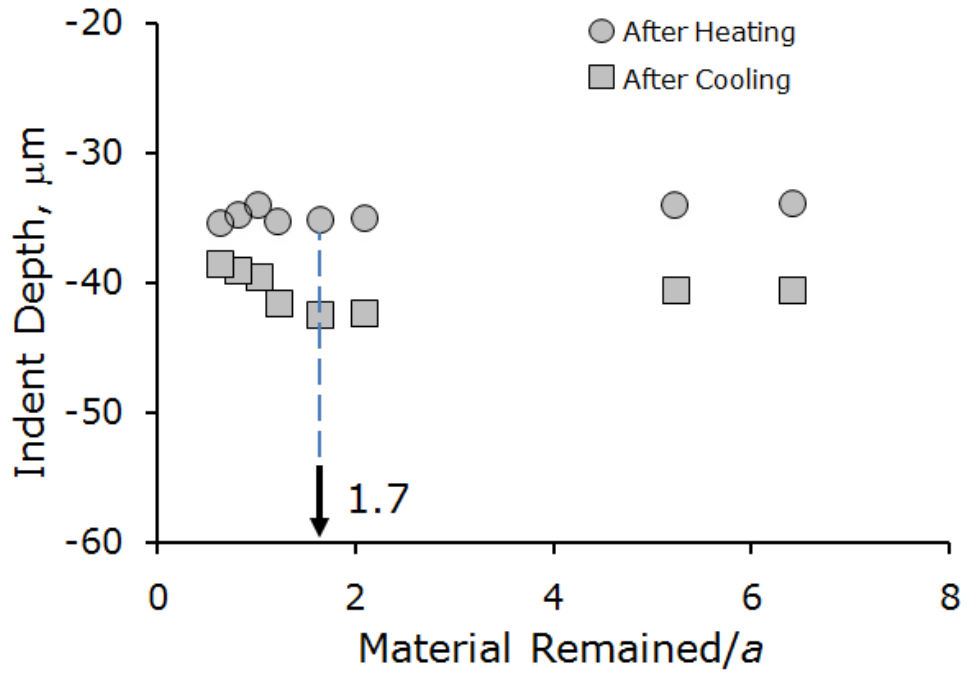


Figure 3.29 Plot of the indent in martensite and austenite, normalized over the contact radius  $a$ , as a function of the remained material, normalized over the contact radius  $a$ .

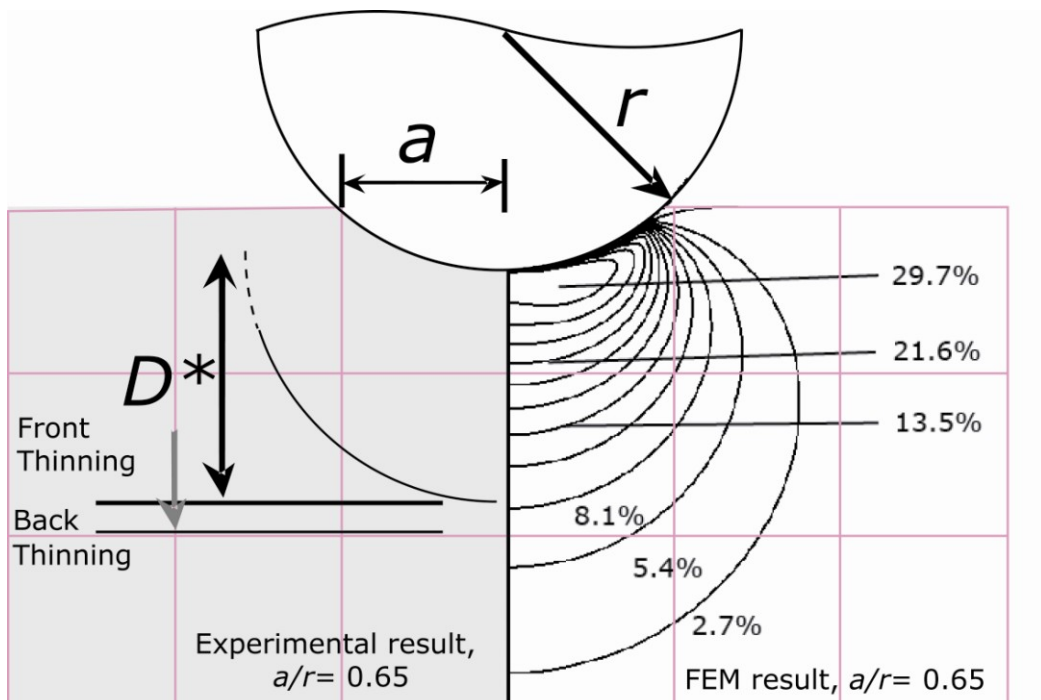


Figure 3.30 Plot of  $D^*$  based on front and back thinning experiments with spherical indentation deformation zone modeled by ABAQUS.

### 3.4.3 Two-way Strain in the Active Subsurface Zone

Deep spherical indentation in the martensitic NiTi (Figure 3.17a) creates a slip zone, a detwinned martensite zone, and an elastic deformation zone, as shown in Fig. 3.17b. Both the amplitude of reversible indent depth changes ( $\delta_1$  in Figure 3.17), and the height  $\delta_2$  of the surface protrusions (or exdents) were found to be related to the depth of a subsurface zone in which indentation has induced strains beyond those that can be mediated by deformation twinning reactions in the martensite [Fei et al. 2009], as discussed in detail below.

Successive material removal experiments for larger  $a/r$  ratios (larger than 0.25) have identified a critical depth below the planarized indent,  $D^*$ , that defines the depth of material driving the observed two-way cyclic exdent phenomenon. Comparing the maximum exdent amplitude with the value of  $D^*$  determined by successive grinding reveals a simple relationship between these two quantities. Figure 3.31, which plots  $h_e$  as a function of  $D^*$  for both spherical and cylindrical indenters, shows that the data collapses onto a single line. A linear fit (forced through 0,0) gives a line with a slope of 0.024. It may thus be concluded that for both indenter types, and over a range of  $a/r$  ratios, *that the cyclic exdent amplitude is consistently 2.4% of the depth of the 'active zone' below the base of the indent.* This value apparently represents the average shape-memory recovery strain occurring within the active zone.

It has also been found that successive planarization results for spherical indents at various  $a/r$  ratios, which showed a non-linear dependence on material removal depth, can be collapsed onto a single curve using a fitting relation with a single adjustable parameter.

Table 3.5 shows the  $a/r$  ratios and  $D^*$  of various spherical indents measured in the front and back thinning experiments, which are used in the plot of stable cyclic extent height as a function of the depth of the subsurface active zone,  $D^*$ , as shown in Figure 3.32. The slopes of the linear curve fit in the front and back thinning experiments give an average strain in the volume defined by  $D^*$  of  $\sim 2.4\%$  and  $1.9\%$  respectively.

Table 3.5 Summarize the  $a/r$  ratios and  $D^*$  measured in the front and back thinning experiments

Pln Methods	Front Thinning			Back Thinning		
$a/r$	0.4	0.65	0.95	0.37	0.64	0.87
$D^*$	$1.13a$	$1.47a$	$1.9a$	$1.35a$	$1.7a$	$2a$

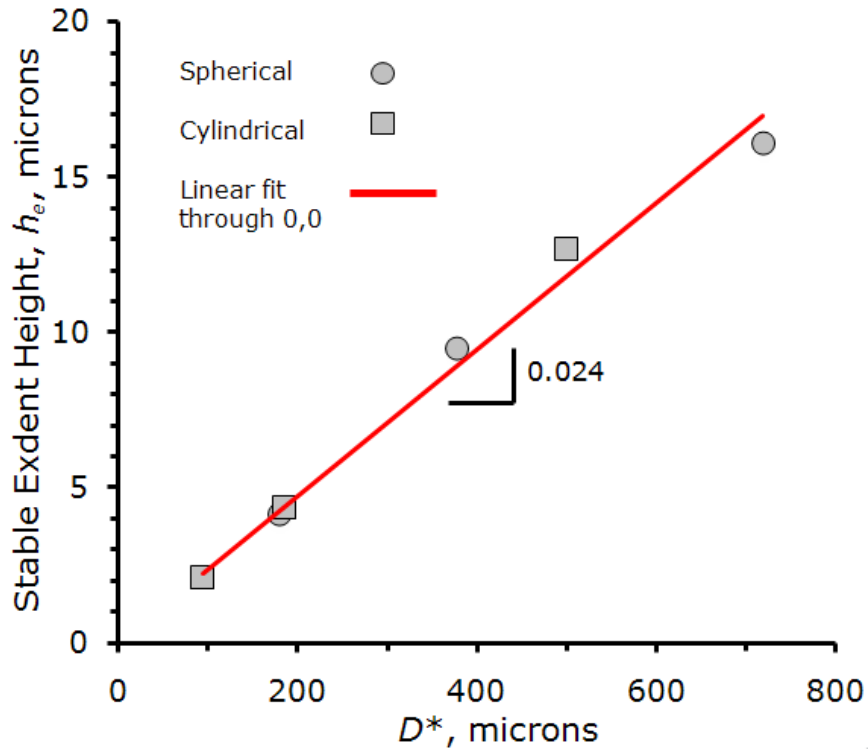


Figure 3.31 Exdent heights for both spherical and cylindrical indents with various  $a/r$  ratios between 0.4 and 0.95 plotted as a function of the size of the subsurface active zone,  $D^*$ . The slope of the linear curve fit gives the average strain in the volume defined by  $D^*$ .

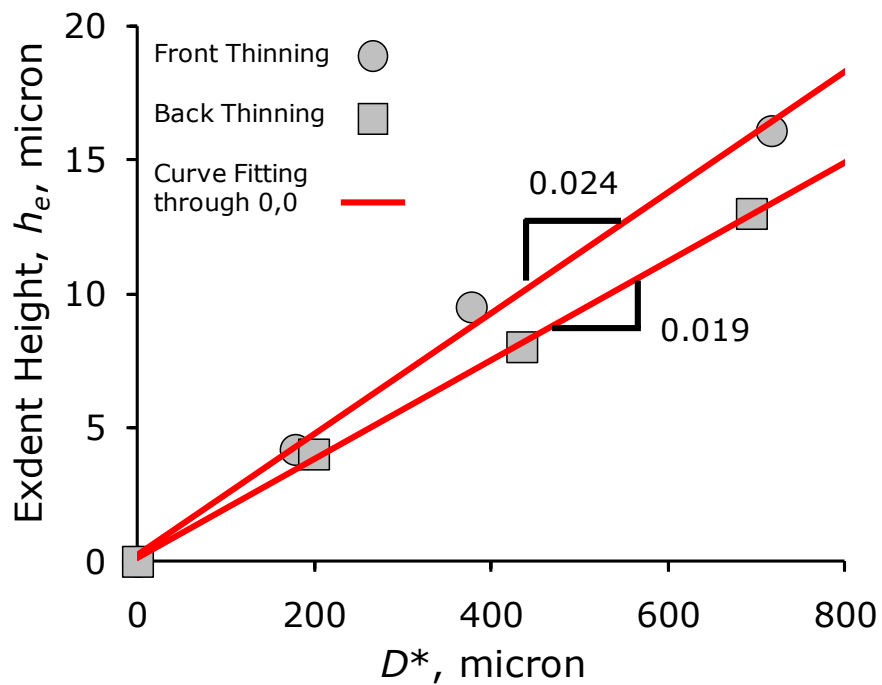


Figure 3.32 Stable cyclic exdent height for spherical indents as a function of the depth of the subsurface active zone,  $D^*$ , in the front and back thinning experiments.

Figure 3.33 show cyclic extent amplitude data for three  $a/r$  ratios fitted by the relationship:

$$\frac{h_e}{D^*} = C \left\{ 3 \left[ 1 - \left( \frac{d_{pl}}{D^*} \right)^2 \right] + \left( 1 - \frac{d_{pl}}{D^*} \right)^2 \right\} \quad \text{Eq. (3.7)}$$

Here,  $d_{pl}$  is the material depth removed by grinding (referenced to the flat, planarized surface),  $h_e$  is the cyclic extent amplitude for  $d_{pl} = 0$ , and  $C$  is a constant found to be 0.006. This relationship is similar to that found by Zhang (Zhang et al. 2008) except that the contact radius,  $a$ , used in the latter, has been replaced by the active zone depth,  $D^*$ , which allows collapse of curves for various  $a/r$  ratios on to a single plot.

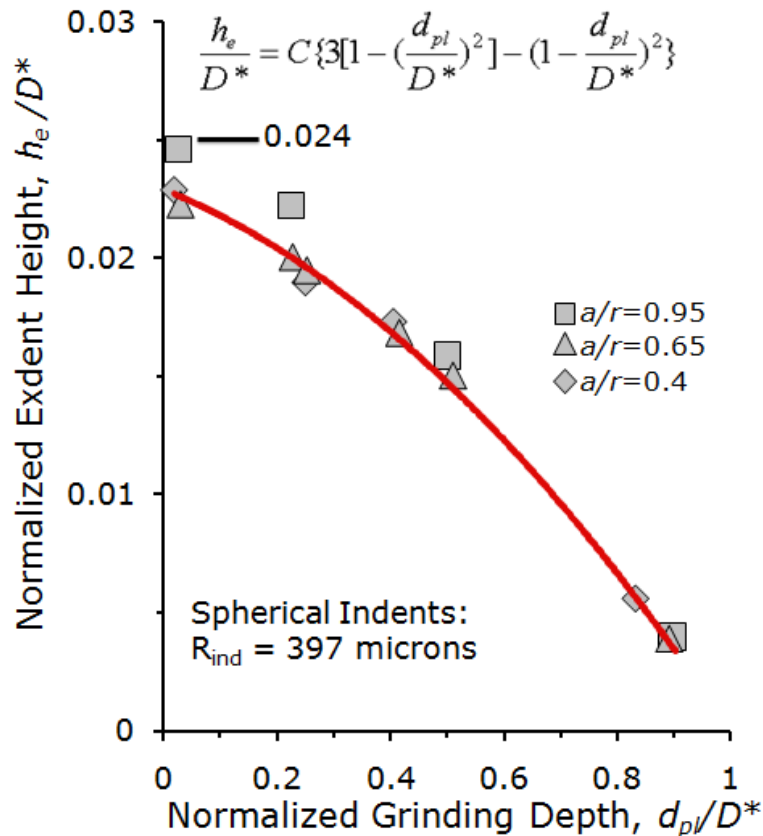


Figure 3.33 Data for spherical indents for all  $a/r$  ratios studied normalized to the experimentally determined depth of the subsurface active zone,  $D^*$ . The data may be adequately fitted to eq. (3.7) which has a single adjustable parameter.

### 3.4.3.1 The Spherical Cap Model

Based on the spherical cavity model [Johnson, 1986] in contact mechanics, as discussed in section 1.4, we speculate that the deformation zone is hemispherical under the indent. To understand the relationship between the indent height and residual deformation zone after planarization, we consider a mathematical model analyzing the residual volume of hemisphere underneath the indent after planarization in the following discussion.

The volume of residual spherical hemisphere can be calculated based on Figure 3.34 which shows a 2D cross-section of spherical hemisphere after a depth of material being removed,  $d_{pl}$ . This residual volume of the spherical hemisphere,  $V_{res}$ , is given by:

$$V_{res} = \frac{1}{6} \pi (D^* - d_{pl}) [3(D^{*2} - d_{pl}^2) + (D^* - d_{pl})^2] \quad \text{Eq. (3.8)}$$

Where  $D^*$  is the size of the spherical deformation zone.

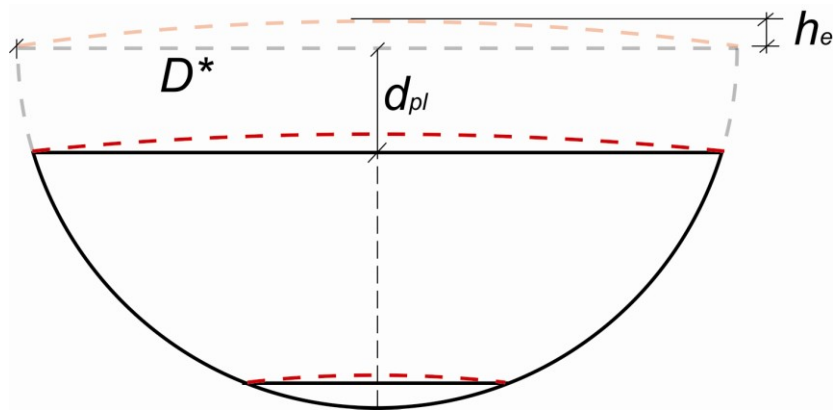


Figure 3.34 2D illustration of residual spherical cap after a depth of  $d_{pl}$  of material being removed.

$V_{tot}$  is the hemisphere with radius of  $D^*$  and equals to  $\frac{2}{3}\pi D^{*3}$ . Thus residual volume ratio can be calculated as shown in Eq. (3.9),

$$\frac{V_{res}}{V_{tot}} = \frac{\left(1 - \frac{d_{pl}}{D^*}\right) \left[ 3 \left(1 - \left(\frac{d_{pl}}{D^*}\right)^2\right) + \left(1 - \frac{d_{pl}}{D^*}\right)^2 \right]}{4} \quad \text{Eq. (3.9)}$$

Zhang [et al. 2008] found that the exdent height is proportional to the residual volume of the spherical hemisphere divided by the residual depth and the contact radius for an  $a/r$  ratio of 0.57. The normalized exdent height versus normalized depth removal can be closely fitted by Eq. (3.10) shown as below.

$$\frac{h_e}{a} = C \left\{ 3 \left[ 1 - \left( \frac{d_{pl}}{a} \right)^2 \right] + \left( 1 - \frac{d_{pl}}{a} \right)^2 \right\} \quad \text{Eq. (3.10)}$$

where  $C$  is a constant (independent of indentation depth and indenter radius),  $a$  which is the contact radius is exactly the radius of spherical hemisphere under the indent in the reference.

Here, we use  $D^*$  as a generalized term for the radius of the spherical hemisphere. Equation 3.7 fits the dataset for spherical front thinning experiment well and closely matches with Eq. 3.10.

The relationship between the normalized exdent and the normalized residual volume can be derived as following based on equation 3.7 and 3.9,

$$\frac{h_e}{D^*} = 4C \left(1 - \frac{d_{pl}}{D^*}\right)^{-1} \left(\frac{V_{res}}{V_{tot}}\right) \quad \text{Eq. (3.11)}$$

Equation 3.11 also suggests that the as-planarized exdent height is 2.4% of the size of deformation zone,  $D^*$ , for spherical indents regardless of the  $a/r$  ratios. The exdent amplitude can be related to the residual spherical volume after planarization with a coefficient  $(D^* - d_{pl})$  or residual depth.

### 3.4.3.2 The Cylindrical Cap Model

As seen in Figure 3.35, results for the cylindrical indents can fit into a single curve by normalizing the data to the respective values of  $D^*$  for various  $a/r$  ratios. The linear fitting curve fits the data points very well, showing the same result as for the spherical indents. That is, the exdent height is 2.4% of  $D^*$  regardless of the  $a/r$  ratios.

Assuming that the deformation zone under the cylindrical indent can be modeled as a cylindrical cap, we can construct a 2D mathematical model to describe the relation between the exdent and the residual volume per unit length (or cross section area), using the schematic drawing shown in Figure 3.36.

The residual cylindrical cross section area is calculated in Eq. (3.12),

$$A_{res} = D^{*2} \cos^{-1}\left(\frac{d_{pl}}{D^*}\right) - d_{pl} \sqrt{D^{*2} - d_{pl}^2} \quad \text{Eq. (3.12)}$$

where  $A_{fan}$  is the area of the fan with angle theta,  $A_{tri}$  is the area of a triangle inside the fan.  $A_{res}$  is double the rest area of the fan.  $A_{tot}$  is the area of the half circle with radius of  $D^*$ .

The ratio between residual cross section and total cross section area is then given by Eq. (3.13):

$$\frac{A_{res}}{A_{tot}} = \frac{2 \left( \cos^{-1} \left( \frac{d_{pl}}{D^*} \right) - \frac{d_{pl}}{D^*} \sqrt{1 - \left( \frac{d_{pl}}{D^*} \right)^2} \right)}{\pi} \quad \text{Eq. (3.13)}$$

Similar to the spherical indentation case, we assume that the exdent height is related to the residual cylindrical cap volume ratio. We then obtain Eq. (3.14):

$$\frac{h_e}{D^*} = C_{cylinder} \left( \cos^{-1} \left( \frac{d_{pl}}{D^*} \right) - \frac{d_{pl}}{D^*} \sqrt{1 - \left( \frac{d_{pl}}{D^*} \right)^2} \right) \quad \text{Eq. (3.14)}$$

Figure 3.35 shows that Eq. (3.14) fits very well the experimental data with two fitting parameters,  $C_{cylinder} = 1.5 \times 10^{-2}$  and  $D^* = 1.85a, 2.35a$  and  $4.35a$ .

Based on equation 3.13 and 3.14, the relation between exdent height and residual cross section area ratio is shown in equation 3.15.

$$\frac{h_e}{D^*} = \frac{\pi}{2} C \left( \frac{A_{res}}{A_{tot}} \right) \quad \text{Eq. (3.15)}$$

Equation 3.15 also suggests that the as-planarized exdent heights for cylindrical indents are 2.4% of  $D^*$  regardless of the  $a/r$  ratios. The exdent amplitude is linearly correlated with residual area after planarization with a coefficient of 2.4%.

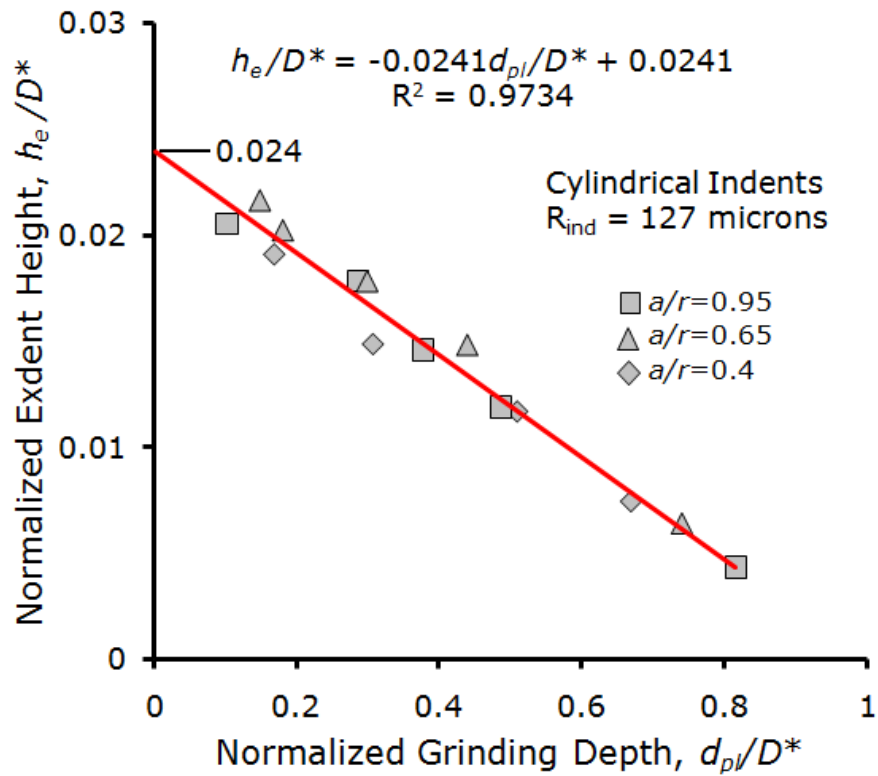


Figure 3.35 Data for cylindrical indents for all  $a/r$  ratios studied normalized to the experimentally determined depth of the subsurface active zone,  $D^*$ .

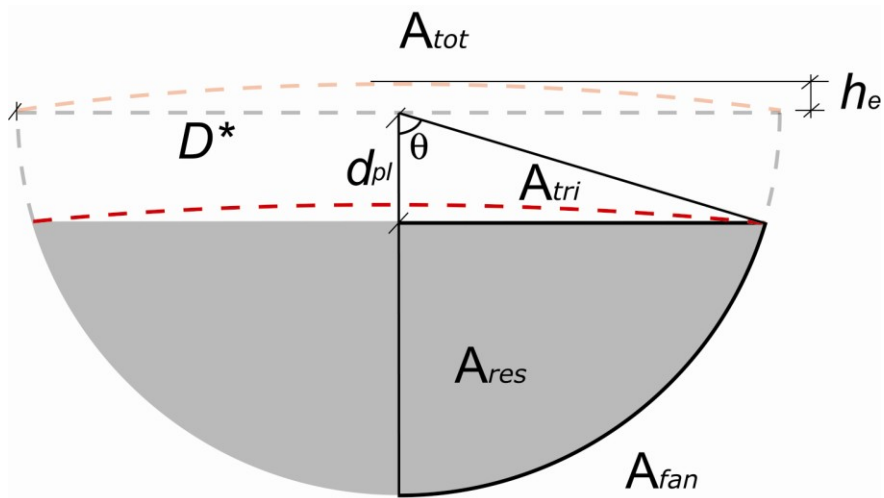


Figure 3.36 Schematic illustration of residual area in the cylindrical cap after a depth of  $d_{pl}$  of material away.  $A_{fan}$  is the area of the fan with angle  $\theta$ ,  $A_{tri}$  is the area of a triangle inside the fan.  $A_{res}$  is double the rest area of the fan.  $A_{tot}$  is the area of the hemisphere.  $d_{pl}$  is the depth of material being removed and  $D^*$  is the size of the deformation zone.

### 3.4.4 Direct Observation of the Indentation Deformation Zone

#### 3.4.4.1 Spherical Indent and Deformation Zone

We demonstrated that the behavior of the deformation zone under the spherical indent is consistent with a hemispherical shape. Here, we directly observe the shape of the spherical indentation deformation zone in NiTi shape memory alloys due to its response to thermal stimulus. A spherical indent was made under 7.5 KN with a  $r=800\ \mu\text{m}$  spherical ball. The initial indent was too deep to be measured optically (the limit is  $400\ \mu\text{m}$ ). After cutting along the center line of indent, the cross-section area was hot mounted and polished and measured to have an indent depth of  $315\ \mu\text{m}$ . (The indent recovered due to hot mounting.) Figure 3.37 schematically illustrates the cross-sectional view of the spherical indent. Figure 3.38 shows the surface profiles of the cross-sectional view of a spherical indent at room temperature, after heating to 433 K, and after cooling to 243 K, measured optically. The indentation deformation zone is clearly shown in Figure 3.38 after the specimen was heated to 433 K. The shape of the indent in the cross-section of the spherical indent after heating represents the shape of the subsurface deformation zone, which is hemispherical under the base of the indent. This agrees with our speculation about the shape of the deformation zone and supports our method to use  $D^*$  as an important parameter to represent the subsurface deformation zone size.

The residual indent depth was measured to be  $315\ \mu\text{m}$  for a  $r=800\ \mu\text{m}$  indenter. The indent depth changes from  $315\ \mu\text{m}$  to  $290\ \mu\text{m}$  on heating, representing a

25  $\mu\text{m}$  two-way amplitude. It has been reported that the two-way response is 2.4% of  $D^*$ . Therefore, the  $D^*$  can be calculated to be around 1036  $\mu\text{m}$ , as labeled in the middle graph of Figure 3.38. As can be seen in the figure, the extent showing the deformation zone matches with  $D^*$  closely.

#### 3.4.4.2 Cylindrical Indent and Deformation Zone

A cylindrical indent was made with 1.59 mm diameter 6 mm tungsten rod under 6 KN. The initial cylindrical indent was measured to have a depth of 94  $\mu\text{m}$  and the  $a/r$  ratio of 0.47. The first recovery of this indent was measured to be 16  $\mu\text{m}$ . After this, the indent was cut along the centerline by diamond saw in the martensitic state.

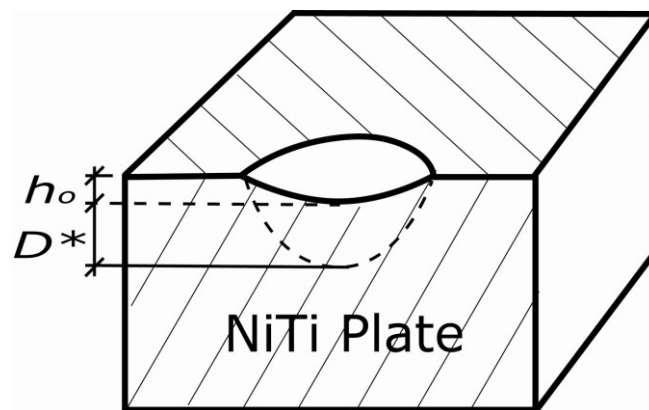


Figure 3.37 Schematic drawing of the cross-sectional view of the spherical indent after cutting.

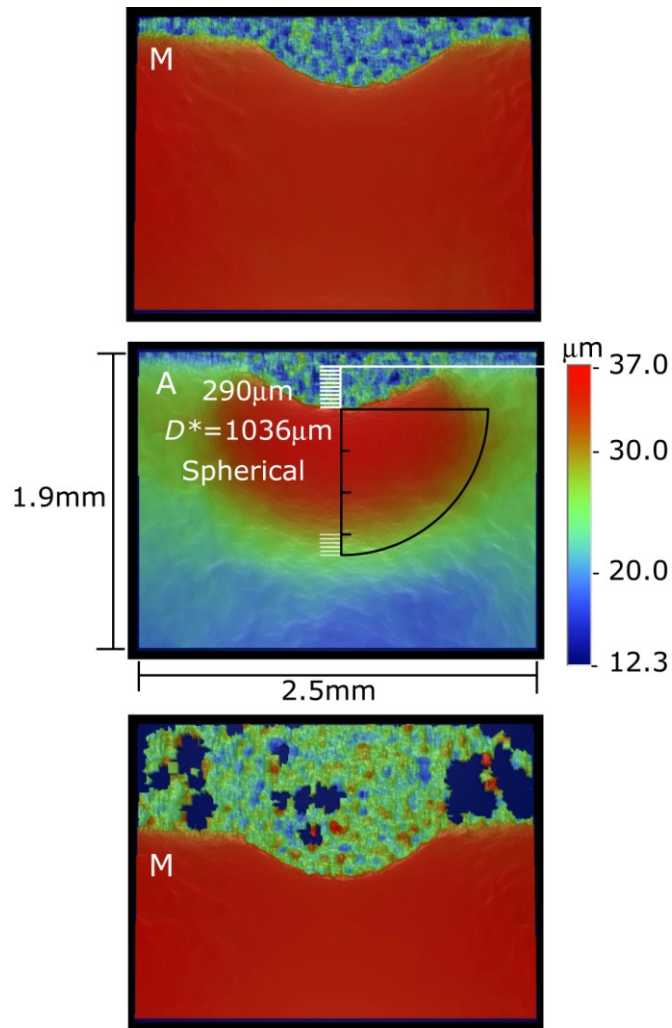


Figure 3.38 A cross-sectional optical image of a spherical indent at room temperature (293 K) after polishing, after heating to 433 K, and after cooling to 243 K and measured optically at 293 K.

Figure 3.39 schematically illustrates the cross-sectional view of the after-cut cylindrical indent. Figure 3.40 shows the surface profiles of the cross-sectional view of the after-cut cylindrical indent at room temperature, after heating to 433 K, and after cooling to 243 K, measured optically. The residual indent depth could not be easily determined optically because of the resolution of the color gradient and the fact that the indent depth is quite small compared to the size of scanning window. However, the indentation deformation zone can still be clearly observed optically.

The shape of the indent in the cross-section view of the cylindrical indent is linear in the horizontal direction which represents the geometrical property of a cylinder. Since the indent was cut along the centerline, the half indent can still represent the deformation zone of a cylindrical indent. Based on the result that the two-way indent depth change is 2.4% of  $D^*$ ,  $D^*$  is calculated to be around 660  $\mu\text{m}$ , as in Figure 3.40, which correlates with the size of the cylindrical deformation zone.

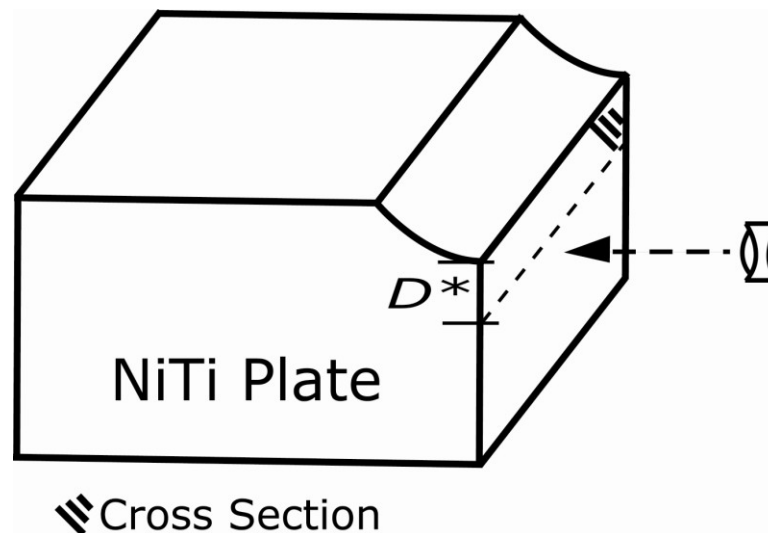


Figure 3.39 Schematic drawing of the cylindrical indent after cutting.

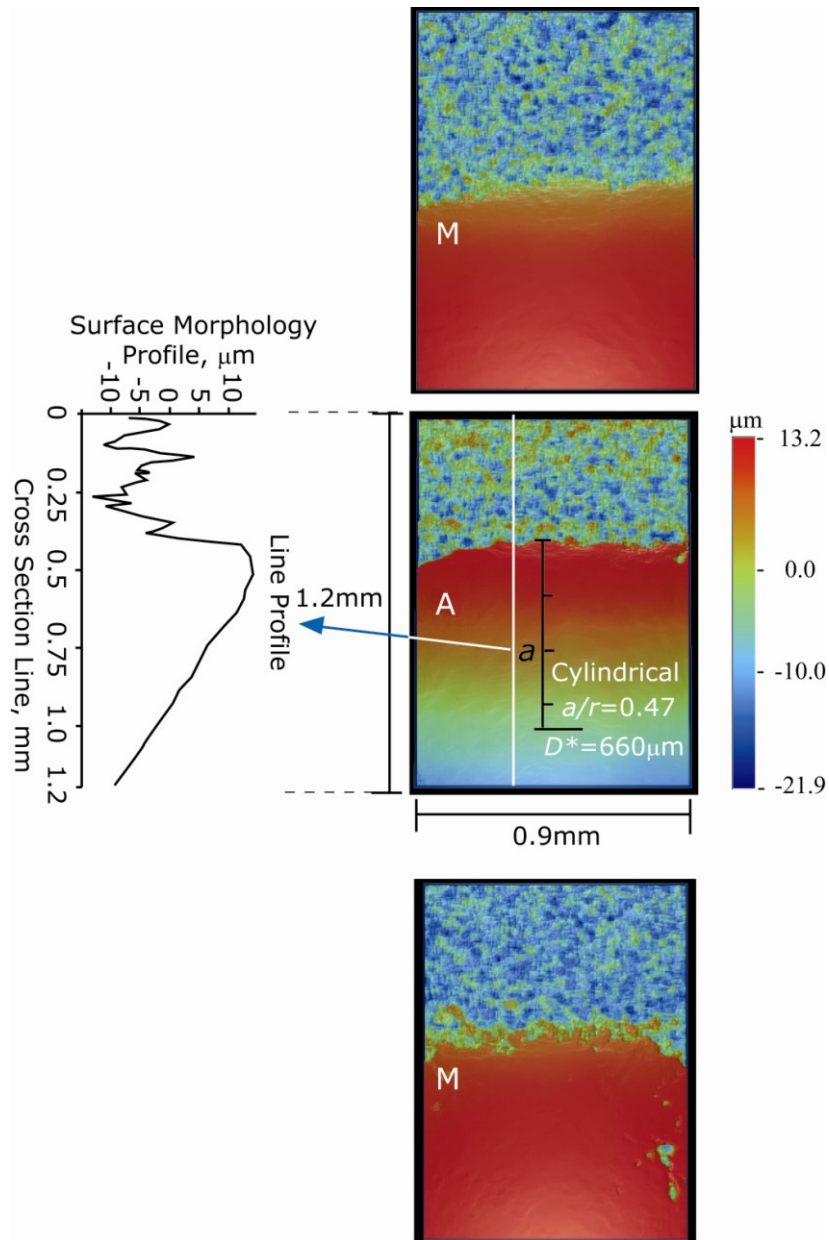


Figure 3.40 A cross-sectional optical image of a cylindrical indent at room temperature (293 K) after polishing, after heating to 433 K, and after cooling to 243 K and measured optically at 293 K.

### 3.5 Indent Replication

#### 3.5.1 Introduction

NiTi shape memory actuators can produce stresses excessing 400 MPa

--1000 times larger than the human muscle [Hunter et al. 1992]. Their energy density,

on the order of  $10 \text{ MJ/m}^3$ , is 10 times larger than that of piezoelectrics [Park et al. 1997]. These high stress and energy density characteristics allow SMA actuators to be used in various applications such as medical devices [Maeda et al. 1996], robots [Lee et al. 2004], and smart structures [Michaud et al. 2002]. It is important to determine the apparent work energy density associated with SFM events.

### **3.5.2 One Shot Spherical Replica Indentation**

Due to the interest in the application of surface indent into actuators, replica indentation experiments were made in aluminum using spherical indents during a constrained austenitization process. Combined with previously described measurements of  $D^*$ , this allows estimation of work-energy density in SFM. Spherical indents were made using double indentation under loads of 200, 700, and 3000 N with a 0.794 mm diameter tungsten carbide ball in the martensitic state and directly planarized in order to maximize the indent amplitude. Planarized NiTi specimen was placed against 6061-T6 aluminum and inserted in between two Instron platens. After heating to 150 °C, an indent formed and indented aluminum under a preload of 100 MPa. Surface profiles of the replica indents are shown in Figure 3.41, together with profiles of the corresponding NiTi indents taken at room temperature after the replica indents were made. Measurements derived from these profiles are summarized in Table 3.4, which additionally includes the measurements of the indents after the replication experiments as re-heated to 423 K in the profilometer.

The latter measurement may be construed as the free-recovery amplitudes of the exdents.

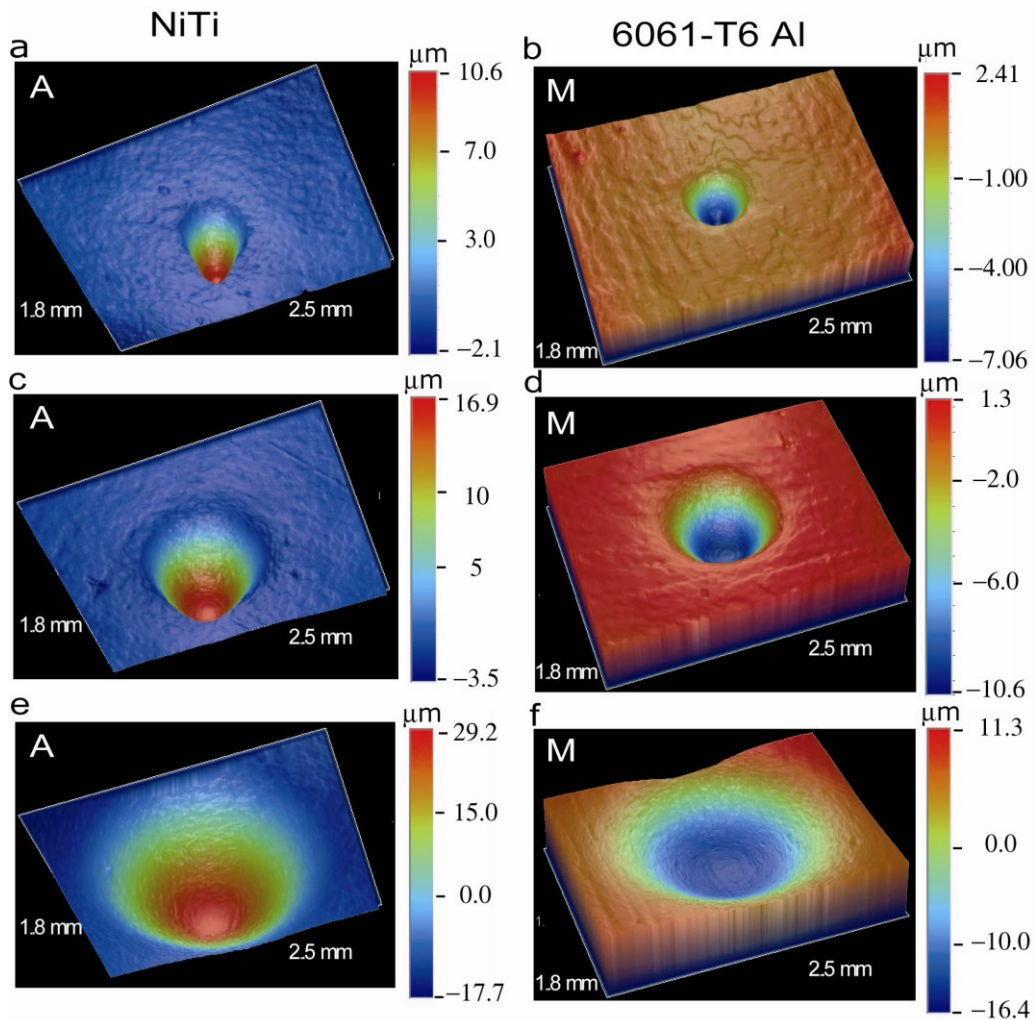


Figure 3.41 Residual exdents in NiTi (left) and Replica indents in aluminum (right) at 293 K made directly following the replication experiments. Images (a,b), (c,d) and (e,f) correspond to initial indent  $a/r$  ratios of 0.42, 0.68 and 1.00 respectively. In each image the field size is 1.9 mm x 2.5 mm. Vertical scales vary, as shown. Images on the left have been inverted to correspond to the relative orientations of the features during their formation.

It is of interest to compare the replica indent depth to the height of the corresponding NiTi exdent in the austenitic condition at 423 K (see right most column

in Table 3.6). This is shown in Figure 3.42 which plots these measurements. For the present case of indent replication in 6061-T6 aluminum, the replica indent depth is approximately half of the austenitic exdent height.

Table 3.6 Replica Indent and Residual Exdent Dimensions

Initial indent $a/r$ ratio	Replica indent depth, $d_{repl}$ $\mu\text{m}$	Replica radius of curvature, $\mu\text{m}$	Replica indent $a/r$ ratio	NiTi Exdent height, $\mu\text{m}$ (293 K)	NiTi Exdent height, $\mu\text{m}$ (423 K)
0.42	7.1	3808	0.061	10.7	16.4
0.68	11.4	8812	0.051	20	27.6
1.00	25.8	15443	0.058	42	51.2

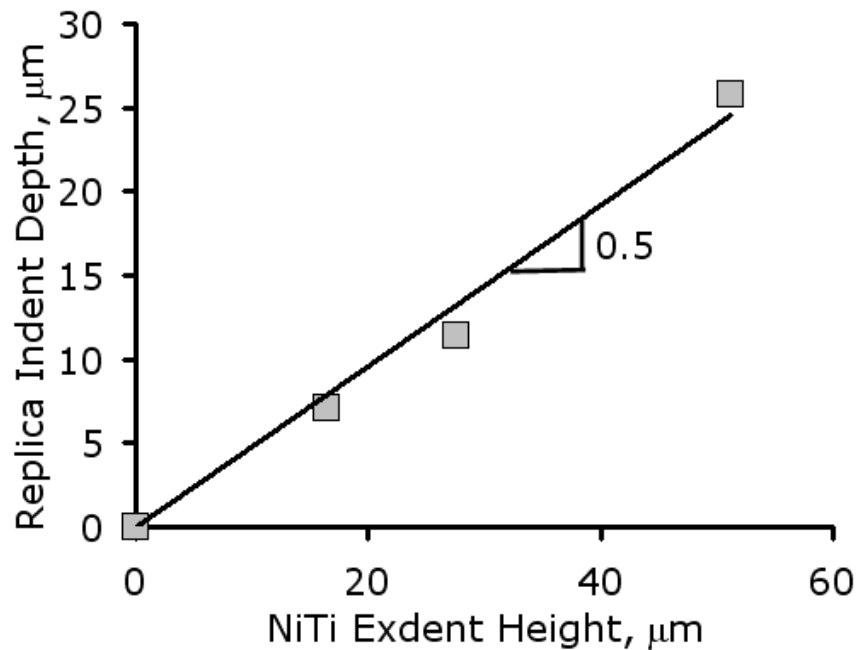


Figure 3.42 Depths of replica indents plotted as a function of the post-replication height of the corresponding NiTi exdents when re-warmed to 423 K (the austenitic condition).

### **3.5.3 Reversible Spherical Replica Indentation**

#### ***3.5.3.1 Spherical Exdent and Replica Indent***

A spherical indent was made under 3000 N with a 1.59 mm in diameter stainless steel ball in the martensitic state. After indentation, the indent was thermal cycled 15 times to maximize and stabilize the two-way response and then planarized to be used in a constrained recovery experiment. We know exdents will form upon heating and are cyclically reversible. Besides, the exdent height is thought to be the same as the stabilized two-way indent depth change, which was 30  $\mu\text{m}$ .

Replica indentations were made in 6061-T6 Aluminum, 304, and 440 stainless steels using these reversible exdents. After exdentation, the samples were cooled either under load or without load, (the difference of which will be discussed in the following section). Figure 3.43 shows the optical image of the NiTi exdent (left) and replica indent in 304 SS (right) after replica indentation with a preload of 250 MPa. This exdent was acquired by heating the NiTi specimen after replica indentation. The exdent has a diameter around 2 mm and height about 24.5  $\mu\text{m}$  as shown in Figure 3.44. The indent in 304 SS qualitatively demonstrates how large is the force that the exdent exerted on the 304 SS to make such a replica indent.

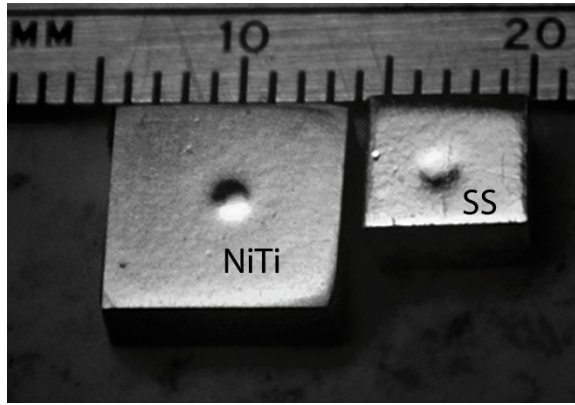


Figure 3.43 The optical image of the NiTi exdent and replica indent in 304 stainless steel after replica indentation with a preload of 250 MPa.

Figure 3.44 shows the WYKO surface profile of the NiTi exdent taken at 433 K after the replica indentation, together with the replica indent in 304 SS made at a preload of 250 MPa. The line profiles of the exdent and the indent match up well. The indent depth ( $17\ \mu\text{m}$ ) is around 56.7% of the original exdent height ( $30\ \mu\text{m}$ ). The exdent height after replica indentation decreased by 18.3% to  $24.5\ \mu\text{m}$ . This is because that cooling under load plastically deformed the martensite at a stress of 250 MPa. These plastically deformed martensite variants are not only un-transformative upon heating to austenite, but also restrain the matensite underneath the plastic deformation zone from transforming, thus substantially decreasing the exdent height.

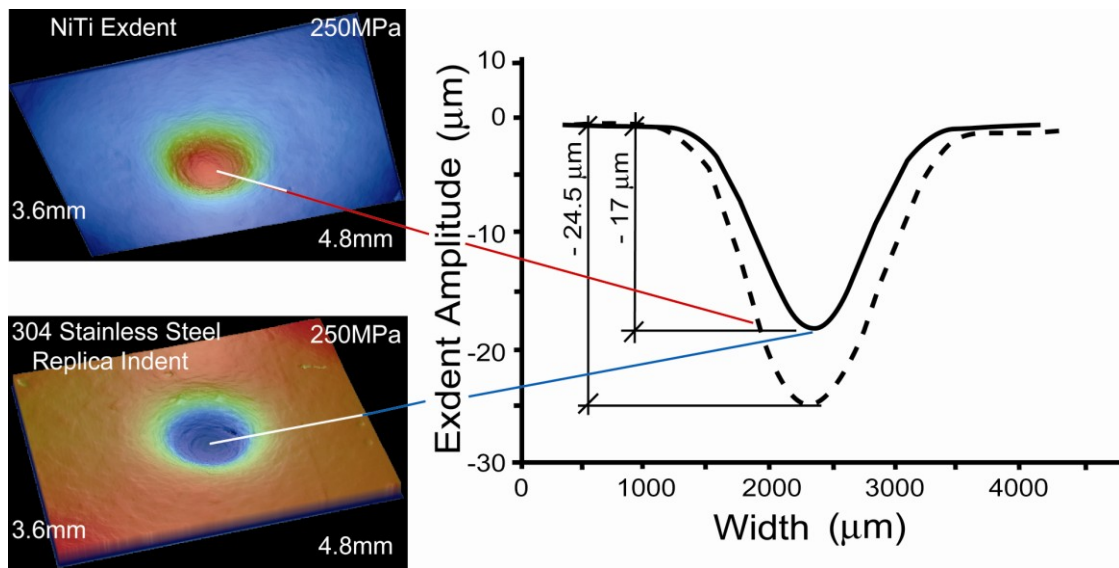


Figure 3.44 The surface profiles of NiTi exdent heated to 433 K (the upper left figure) and a replica indent in 304 stainless steel at 293 K (the lower left figure) after replication under preload of 250 MPa. The dimensions of the exdent and replica indent are plotted in the right figure.

The relationship between the replica indent depth and the preload for these three replica materials was investigated and shown in Figure 3.45. The replica indent depth increases with the increase of preload stress up to 250 MPa which is close to the yield stress of the austenite phase (250-300 MPa). Further increasing the preload stress leads to a drop of the replica indent depth because plastic deformation of NiTi decreases the NiTi exdent height. 6061 T6 Al has the deepest indents under replica indentation due to its lowest hardness value among three replica materials. Fei et al. [2009] shows that after planarization, the exdent height is about the same as the two-way indent depth change. Thus we use the indent depth change at the 15<sup>th</sup> cycle as the stabilized exdent amplitude. When the replica indent depth is normalized to the stabilized exdent height, aluminum has the largest indent/ exdent ratio of 0.7. This

result is 40% higher than what we achieved (0.5) using exdents made without prior thermal cycling in [Fei et al. 2009].

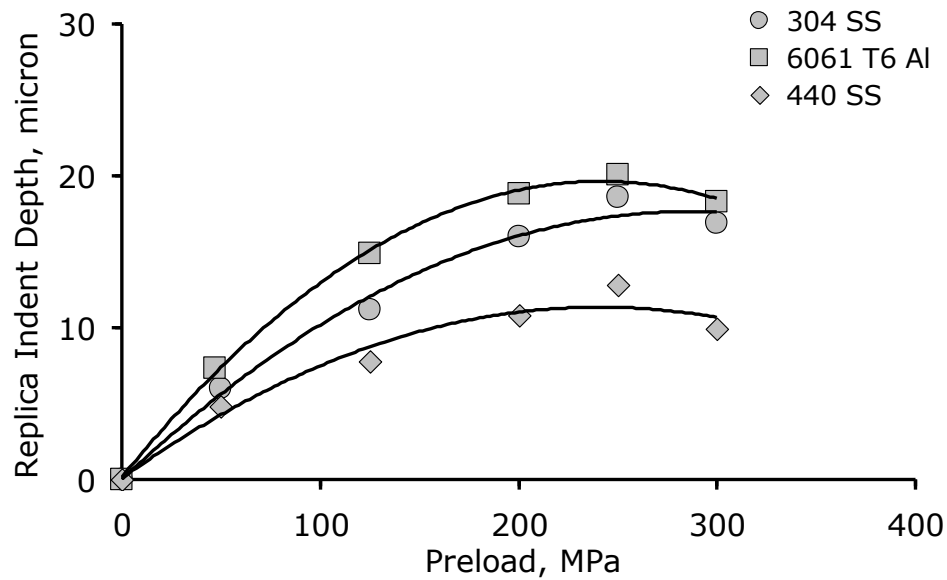


Figure 3.45 The relation between replica indent depth and preload stress for stainless steel and aluminum. No replica indent is assumed at 0 preload stress.

### 3.5.3.2 Effect of Preload Stress

The constrained recovery experiments demonstrate that NiTi exdents can be used to make replica indents in a variety of materials at various preload stresses.

Material hardness determines how deep the indent can be for a fixed preload stress.

Figure 3.46 plots the replica indent depth against the material hardness for a preload stress of 250 MPa. The fitting curve as shown in the figure is a linear line, which achieved an  $R^2$  value of 0.9968. The data point at the hardness of zero means that the exdent can make a replica indent with a depth as large as the exdent amplitude. It is shown in the curve that NiTi exdent cannot make a replica indent at a hardness of

above 2.6 GPa. We call this the hardness limit ( $H^*$ ). This value is close to the hardness of austenitic NiTi, showing that the limit of NiTi exdent is controlled by its bulk material property.

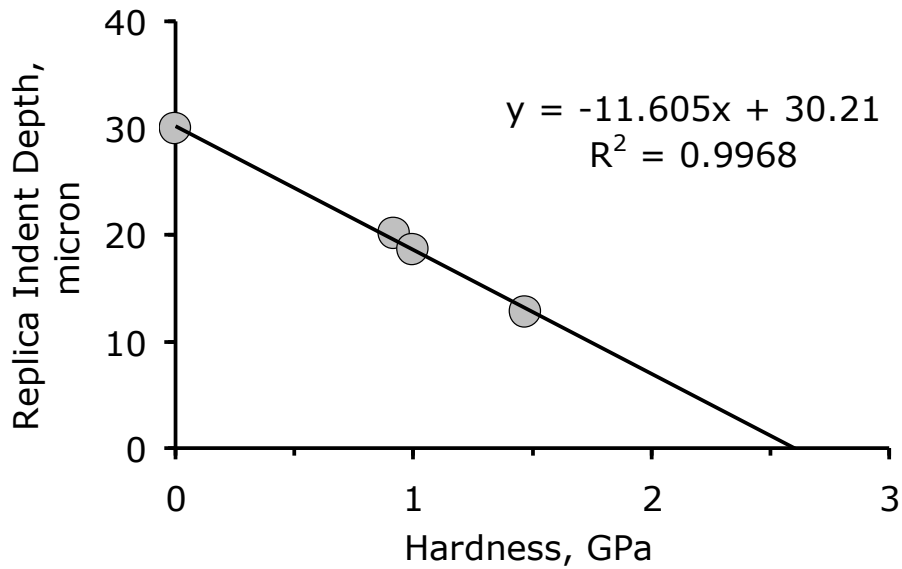


Figure 3.46 The relation between the replica indent depth and material hardness at preload stress of 250 MPa.

Figure 3.47 plots the replica indent depth with material hardness at preload stresses of 125, 200, 250, and 300 MPa. Curve-fitting lines suggest that  $H^*$  for these preload stresses are 1.87 GPa, 2.29 GPa, 2.6 GPa, and 2.26 GPa.

Figure 3.48 plots  $H^*$  as a function of the preload stress. Parabolic curve fitting of the data points leads to a peak around 250 MPa, which is the optimum preload to generate replica indent. As also shown by the curve fitting is a preload stress limit of around 480 MPa. This means at 480 MPa, no replica indent can be made because there is no exdent formed when heated under the preload stress of 480 MPa. Figure

3.49 plots  $H^*/\text{preload}$  as a function of preload. Linear curve fitting also suggests a preload stress limit of around 480 MPa.

The preload level of 480 MPa can increase the transformation temperature by 80K, making  $A_s$  429 K and  $A_f$  468 K according to the Clausius-Clapeyron equation

$$\frac{d\sigma}{dT} = \frac{\Delta H}{T\varepsilon_0} = 6 \text{ MPa} / \text{K} . \text{ So heating to } 433 \text{ K } (A_s+4 \text{ K}) \text{ cannot transform the martensite}$$

to austenite, thus causing no extent formation.

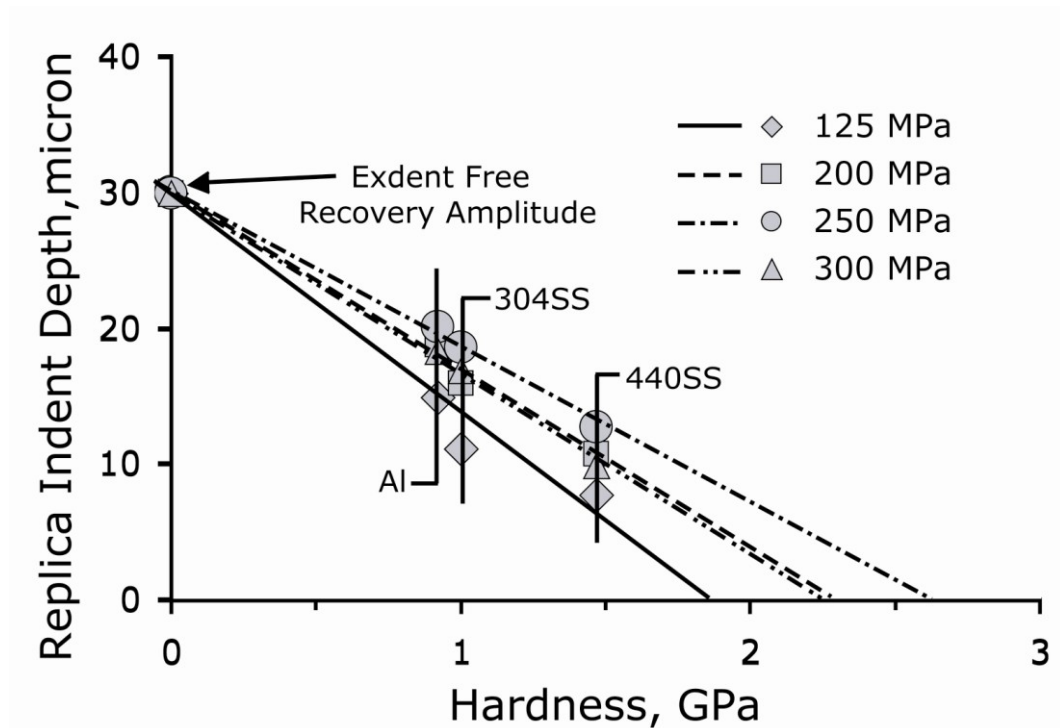


Figure 3.47 Plot of replica indent depth against the material hardness at preload stresses of 125, 200, 250, and 300 MPa.

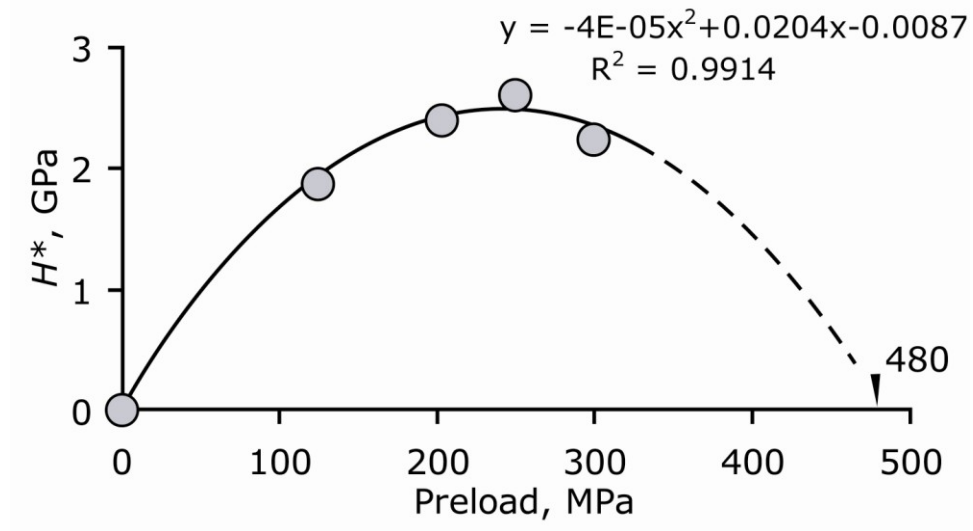


Figure 3.48 Plot of  $H^*$  against the preload stress. Parabolic curve fitting suggests 480 MPa is the largest preload stress that can be used to make a replica indent.

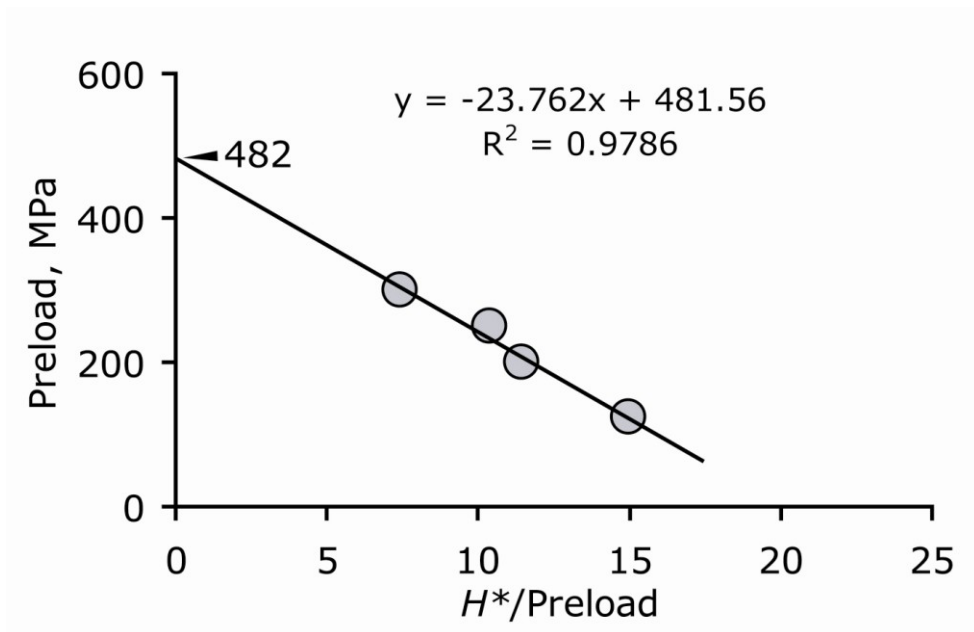


Figure 3.49 Plot of the preload stress against  $H^*/\text{preload}$ . Linear curve fitting suggests 482 MPa is the largest preload stress that can be used to make a replica indent.

### 3.5.3.3 Low Cycle Fatigue Test

In order to understand the fatigue response of the NiTi exdent, we studied the low cycle fatigue effect of NiTi exdent under preloads of 100 and 250 MPa for 440

stainless steel. 440 stainless steel was chosen simply because it is the hardest material used in these experiments and consequently it should generate the largest fatigue response.

Figure 3.50 plots the replica indent depth with the number of replica indentation cycles at preload stresses of 100 and 250 MPa. The higher preload stress generates a larger fatigue response out of the NiTi exdent due to the accumulation of plastic deformation at 250 MPa. Interestingly, the fatigue response stabilizes and converges after 6 cycles of replica indentation, showing the limit of the replica indent depth that each preload can generate after multiple indentations. This can be explained by the effect of NiTi work hardening playing against plastic deformation. Due to the work hardening effect, the NiTi cannot be further plastically deformed after a number of replica indentations. Thus, the exdent height becomes stable in the pre-stress and temperature regime. The higher the pre-stress, the larger number of replica indentation cycles it takes to work harden and to stabilize the exdent height. Since the replica indent depth is positively related to the exdent height, the higher the pre-stress, the slower the indent depth drops down and stabilizes, which is shown in Figure 3.50, demonstrating that the replica indent depth stabilizes slower at 250 MPa preload than at 100 MPa preload.

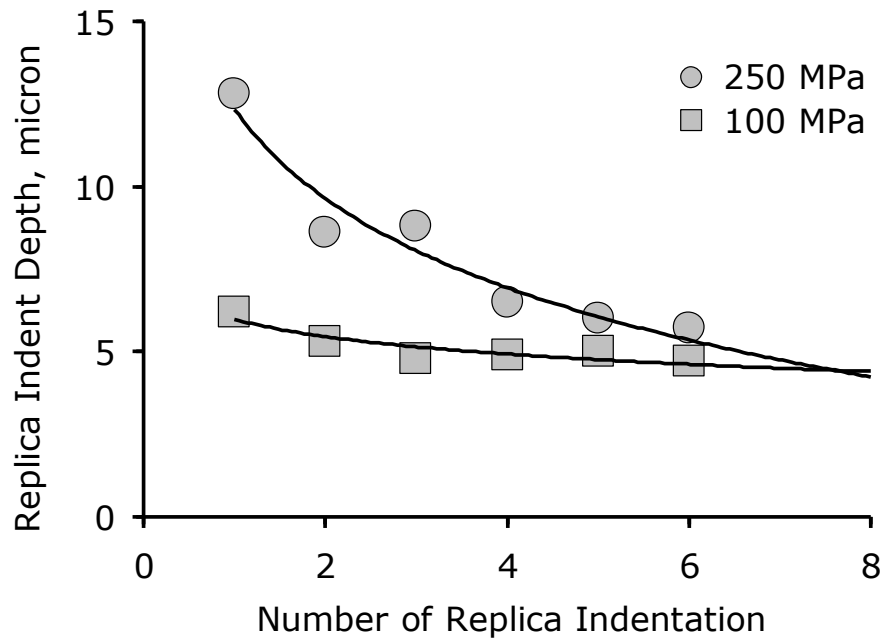


Figure 3.50 Low cycle fatigue of NiTi exdent in the constrained recovery experiments.

### 3.5.3.4 Factors Affecting the Constrained Recovery

#### 3.5.3.4.1 Effect of Temperature

Stressing can affect the phase transformation temperatures of NiTi SMAs, such that  $A_f$  increases after loading. Therefore, it is important to know how much the transformation temperature changes in order to determine the thermal cycling temperature range to be used in the experimental setting to achieve a full transformation between martensite and austenite.

The Clausius-Clapeyron equation is often used to estimate the change in transformation temperature due to stressing. The enthalpy of the SMAs measured by DSC is  $15.6 \text{ J/g}$ . This leads to a maximum increase in transformation temperature

about 50 K at a preload of 300 MPa since the Clausius-Claperyon equation indicates

$$\frac{d\sigma}{dT} = \frac{\Delta H}{T\varepsilon_0} = 6\text{MPa}/\text{K}, \text{ where } \frac{d\sigma}{dT} \text{ is first derivative of stress over temperature,}$$

$\Delta H$  is enthalpy which is 15.6 J/g,  $T$  is temperature which is the average of  $M_s$  and  $A_s$ , and  $\varepsilon_0$  is strain limit before plastic deformation which is 0.05.

The specimens were heated up to 433 K in the constrained recovery experiment. Such heating temperature almost accommodates the increase of  $A_f$  (438 K) by 50 K. Therefore, in the present experiments there is confidence that martensite was close to fully transformed to austenite during heating, and the maximum response was achieved.

#### ***3.5.3.4.2 Path Dependency of Replica Indentation***

We observed the path dependency effect of replica indentation based on the different indent depth measured on cooling without load (path *A*) and cooling under load (path *B*). Figure 3.51 schematically draws these two paths and explains the difference. The replica indent depth is smaller in path *A* than in path *B* because, upon cooling, the load exerts a large deformation into martensite, pushing the residual extent further into the replica material (see 304 SS in the graph). This further indentation in the replica material causes the replica indent depth to increase. The harder the replica material, the larger the deformation into martensite, and the larger is the replica indent depth or the path dependency effect.

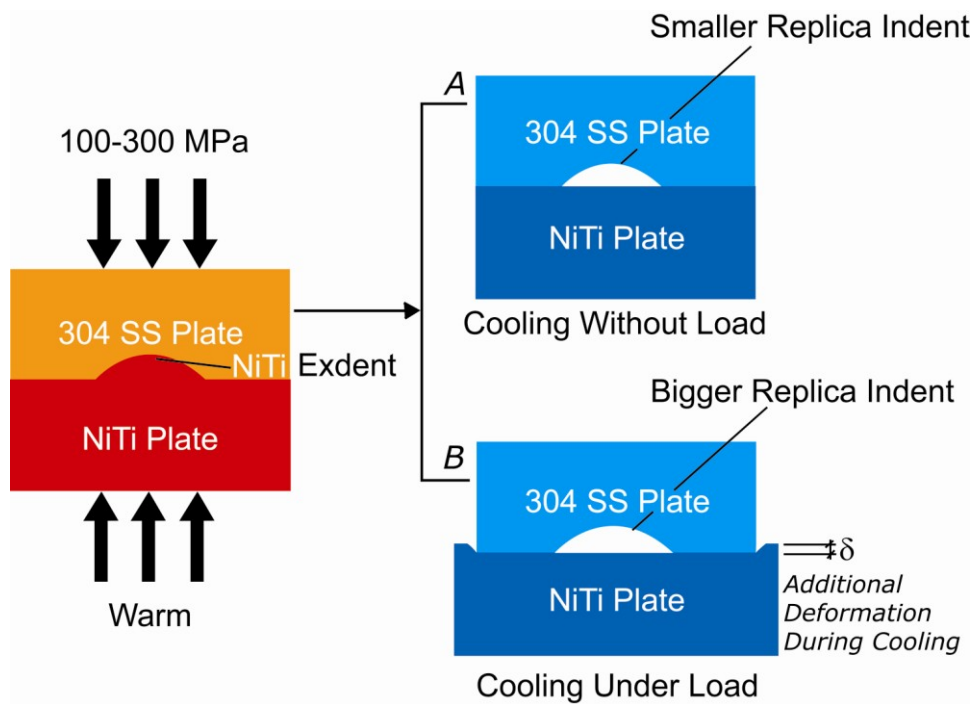


Figure 3.51 Path dependency of replica indentation: *A*) cooling without load; *B*) cooling under load.

Table 3.7 summarizes the effect of path dependency on the replica indent depth at the preload of 250 MPa. For aluminum samples, the replica indent depth under path *A* is about 30% lower than that under path *B*. For 440 SS, the replica indent depth under path *A* is about 37.5% lower than that under path *B*. Since 440 SS is harder than aluminum, we may conclude that the path dependency effect is related to the hardness of the replica material. The harder the material, the larger the effect is.

Table 3.7 Path dependency effect on the replica indent depth at the preload of 250 MPa

Path	Preload, MPa	Replica Indent Depth, $\mu\text{m}$ (Al)	Replica Indent Depth, $\mu\text{m}$ (440 SS)
<i>A</i> : cooling without load	250	14.3	8
<i>B</i> : cooling under load	250	20.1	12.8

### 3.5.3.5 Work Output and Energy Density Calculation

#### 3.5.3.5.1 Spherical Calibration Indentation at 433K

In order to estimate the energy density associated with exdent formation during the constrained recovery experiment, we made conventional spherical indents in the replica materials at 433 K using a ball with a radius of 1.59 mm and loads of 35, 50, and 100 N. Results for these calibration indentations are given in Table 3.8. The average hardness of each material obtained by spherical calibration indentation is used in the calculation of equivalent load that NiTi exdents generate to make the replica indents.

Table 3.8 Calibration Indentation Data for 440 SS, 304 SS, and Al 6061-T6 at 433K

#### 440C SS

Indent depth, $\mu\text{m}$	Load, N	Indenter radius, m	$a/r$ ratio	Contact radius, m	Contact area, $\text{m}^2$	Hardness, $H_{440}$ , Pa
5.0	35	8E-04	0.112	0.89E-04	2.51E-08	1.39E+09
7.7	55	8E-04	0.138	1.11E-04	3.85E-08	1.42E+09
12.5	100	8E-04	0.176	1.41E-04	6.25E-08	1.6E+09

Table 3.8 cont'd

**304 SS**

Indent depth, $\mu\text{m}$	Load, N	Indenter radius, m	$a/r$ ratio	Contact radius, m	Contact area, $\text{m}^2$	Hardness, $H_{304\text{ SS}}$ , Pa
7.9	38	8E-04	0.140	1.12E-04	3.94E-08	0.96E+09
11.3	56	8E-04	0.167	1.34E-04	5.64E-08	0.99E+09
19.0	105	8E-04	0.217	1.73E-04	9.40E-08	1.06E+09

**6061 T6 Al**

Indent depth, $\mu\text{m}$	Load, N	Indenter radius, m	$a/r$ ratio	Contact radius, m	Contact area, $\text{m}^2$	Hardness, $H_{\text{Al}}$ , Pa
7.5	35	8E-04	0.137	1.09E-04	3.73E-08	0.94E+09
11.8	55	8E-04	0.171	1.37E-04	5.89E-08	0.93E+09
23.3	103	8E-04	0.240	1.92E-04	11.6E-08	0.89E+09

**3.5.3.5.2 Energy Density Calculation**

The projected contact area during replica indentation is calculated as

$A_{repl} = \pi a_{repl}^2$  allowing us to estimate the peak replication force (assumed to be an increment above the pre-load force) as  $P_{repl} = A_{repl} H_{\text{Al}}$ . The indentation energy then becomes  $U_i = 1/2 P_{repl} d_{repl}$ . This is a rough estimation of the energy of indentation. It is correct only when there is no work hardening effect in the material during indentation. The Load-Displacement curves (see Figure 2.4) measured by the CSM instrumented indentation machine in General Motors Technical Center show no work hardening effect for the aluminum and stainless steel specimens that we used in the experiments.

To obtain the effective energy density it is necessary to make an estimate of the volume of material in which shape-memory recovery occurs, i.e., the active

subsurface volume contributing to the formation of the exdent. Previous experimentally determined active volume that drives exdent formation in [Fei et al. 2009] gives a  $D^*=1.56a$  when  $a/r$  ratio is 0.71. Back planarization may possibly give a  $D^*=1.74a$  based on Table 3.1. Therefore, the  $D^*$  on average is  $1.65a$  when  $a/r$  ratio is 0.71.

With a simplifying assumption that  $D^*$  represents the radius of a hemisphere centered on the indent, we estimate the volume of the active zone as

$V^* = (1/2)[4/3 \pi D^{*3}]$ . Dividing the energy of indentation,  $U_i$ , by this quantity then provides an estimate of the energy density associated with exdent formation in NiTi during an SFM event. Results of this calculation are summarized in Table 3.9. The calculation is based on the replica indent depth under path  $B$ . Energy densities estimated in this way have an average about  $12.1 \text{ MJ/m}^3$  for 3 materials at 250 MPa preload.

Since path  $a$  leads to an average 35% reduction of the replica indent depth, the average energy density can be recalculated to be  $7.84 \text{ MJ/m}^3$  under path  $A$ . This may be compared to the energy density exerted by a NiTi actuator that undergoes a shape memory strain of 4% under constraint conditions that cause a reaction stress to rise linearly from zero to 400 MPa during the actuation stroke. This energy is

$$U = 1/2 \sigma \varepsilon, \text{ or about } 8 \text{ MJ/m}^3.$$

Table 3.9 Calculation of Energy Density for Replica Indent made under 250 MPa

Mater	Ind dept, m	Repli contac radius $a_{repl}$ , m	Repli $a/r$ ratio	Replica contact area, $A_{repl}$ , $m^2$	Equiv replica load, $P_{repl}$ , N	Indent energy, $U$ , Joules	Estim $D^*$ , m	Est. Ene den. $MJ/m^3$
440 SS	12.8 E-06	868.7 E-06	0.029	2.37 E-06	3.49 E+03	2.23 E-02	0.94 E-03	<b>12.8</b>
304 SS	18.6 E-06	837.7 E-06	0.044	2.20 E-06	2.20 E+03	2.05 E-02	0.94 E-03	<b>11.8</b>
6061 Al	20.1 E-06	832.7 E-06	0.048	2.18 E-06	2.00 E+03	2.01 E-02	0.94 E-03	<b>11.6</b>

### 3.6 SFM from Dynamic Indentation (Laser Shock Peening)

#### 3.6.1 Indent Recovery and SFM

Laser shock peening produces very high shock pressures, ultra high strain rates ( $>10^6/s$ ) [Peyre et al. 1998], and allows precise control for localized treatment. It can introduce a strong work-hardened layer and compressive residual stresses that have been often used to improve fatigue performance, corrosion resistance, wear resistance and service life in various materials [Hu et al. 2006].

There are few reports on the effect of ultra-high strain rates on the deformation of NiTi-based SMAs, especially for the case of martensite behavior. Millett et al, [2002] reported that the strain rate sensitivity of austenitic NiTi increases the yield strength of NiTi from 500 to 794 MPa when deformation is caused by a shock wave instead of quasistatically. In the present case, martensite deformation is of interest,

which can proceed either by deformation twinning reactions, or by dislocation creation and slip mechanism. Both are of crucial significance in the case of two-way memory effects, and rather little is known about either of these mechanisms at ultra-high strain rates.

Therefore, dynamic indentation was conducted via the Laser Shock Peening (LSP) process in the martensitic NiTi specimen. Details of experimental procedures were given in Chapter 2. Two-way indent depth change and extent-to-flat transition were evaluated and compared to the quasi-static spherical indent response, as discussed below.

Figure 3.52a shows the schematic drawing of the indent made under laser intensity of  $2.5 \text{ GW/cm}^2$  and beam size of 0.5 mm, after heating, and after cooling. The initial indent depth is  $5.7 \text{ }\mu\text{m}$ . Upon heating to above  $A_f$ , the indent became shallow and reaches  $0.6 \text{ }\mu\text{m}$  by the shape memory mechanism. This depth change represents a recovery of 89.5% of the initial indent depth. Upon cooling to below  $M_f$ , the indent deepens to  $2 \text{ }\mu\text{m}$ . The two-way recovery upon heating and cooling is  $1.4 \text{ }\mu\text{m}$  and accounts for 24.6% of the initial indent depth, a ratio more than twice the maximum recovery ratio of the spherical indent (11.8%) made by quasi-static indentation [Fei et al. 2009].

The trace of the indent was removed by mechanical grinding, as in previous examples of planarization. After planarization, specimens were heated and cooled again over the same temperature range. Thermally-reversible surface transitions were then observed after planarization.

Figure 3.52b shows the schematic drawing of the thermally-reversible exdent-to-flat transition. An exdent with amplitude of  $1.2 \mu\text{m}$  was observed and was comparable to the two-way indent depth change.

Figure 3.53 shows a typical 3D profile for the thermally reversible exdent-to-flat transition illustrating the high degree of reversibility for this transition. The surface becomes bumpy when the specimen is warmed and returns to flatness when it is cooled. Due to the small scale of the exdent, the surface roughness change and thermal expansion and contraction during heating and cooling affect the surface flatness in a large degree. That is why the surface is not totally flat when the specimen is cooled to the martensitic state.

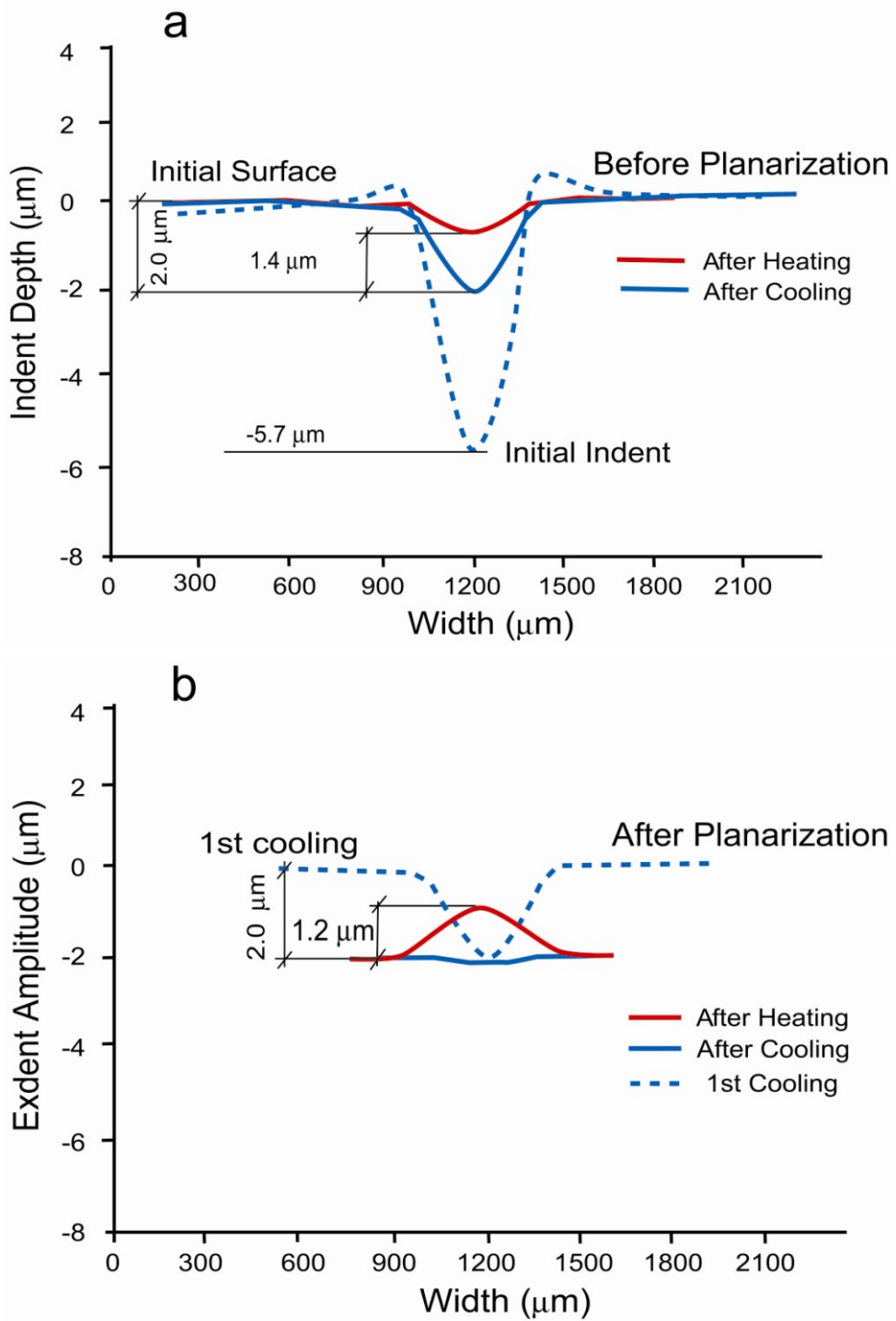


Figure 3.52 Schematic illustrations of (a) initial indent depth-recovery, and (b) extent-to-flat surface transition during heating and cooling after planarization of the LSP indent.

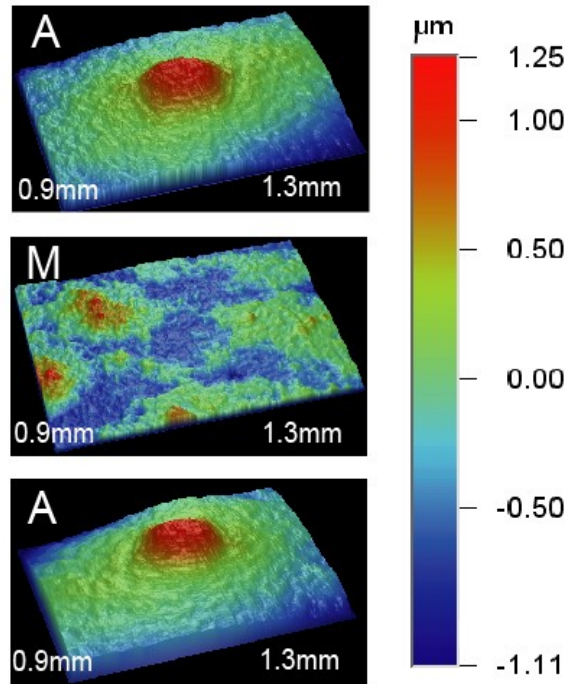


Figure 3.53 Cyclic indent-to-flat surface transition after planarization of the dynamic indent.

Having shown surface form memory developed by LSP with ultra high strain rate, it is interesting to compare high strain rate dynamic surface form memory with quasi-static indentation induced surface form memory with regard to both indent/indent responses and deformation zones. Figure 3.54 shows the comparison of initial indent depth between the spherical indent made under 700 N with a  $r=400\ \mu\text{m}$  spherical ball and the dynamic indent under laser intensity of  $2.5\ \text{GW}/\text{cm}^2$  and beam size of 0.5 mm. The spherical indent has an initial indent depth of  $96.8\ \mu\text{m}$ , thus  $a/r$  of 0.65 and  $a=260\ \mu\text{m}$ . The indent diameter is thus around 0.5mm, which is close to that of the dynamic indent. For the two indents with same indent diameter, the dynamic indent is significantly shallower than the quasi-static indent. Assuming the dynamic indent is spherical in shape, the equivalent indenter radius  $r$  to make such indent can be

calculated to be 5485  $\mu\text{m}$  by  $r = (a^2 + h^2)/2h$ , where  $a$  is the contact radius which is 250  $\mu\text{m}$  in this case,  $h$  is the indent depth which is 5.7  $\mu\text{m}$ . The  $a/r$  ratio for the dynamic indent is then calculated to be 0.05.

Ni et al. [2003] shows spherical indents with  $a/r$  less than 0.25 can fully recover after heating due to the absence of dislocations when the deformation strain is less than 5 %. As the result, no indent remains when the initial indent having an  $a/r$  of 0.05 is heated above  $A_f$ . Furthermore, for  $a/r < 0.5$ , no TWSME is observed. However, the dynamic indent shows a two-way indent depth change of 1.4  $\mu\text{m}$ , as shown in Figure 3.55, which shows the comparison of two-way recovery between the quasi-static spherical indent and the dynamic indent. It is clearly shown that the normalized two-way recovery ratio of the dynamic indent is larger than that of the spherical indent, i.e, when the dynamic indent is magnified to have the same vertical length as the spherical indent, shown in the right side of the figure. The dynamic indent has a two-way recovery ratio of 24.6% while the spherical indent under mechanical loading has a two-way recovery ratio of 9.3% in this case. This larger recovery ratio of the dynamic indent may be due to the strain rate sensitivity effect of NiTi. Table 3.10 summarizes the differences between the quasi-static spherical indent and the dynamic indent. It can be concluded that the indent response of the dynamic indent is 2.1 times larger than that of the quasi-static indent, when the indent diameter is the same.

Another way to compare these two types of indents is shown in the following. In the previous work [Fei et al, 2009], we found that the reversible indent depth change,  $\delta$ , for quasi-static indents depends on both the indenter radius  $r_{qs}$ , and the indent contact radius  $a$ , following such relation  $\delta = 0.06a - 0.0155r_{qs}$ . Therefore, the radius of a quasistatic indenter expected to give a 1.4 micron depth change when the in-plane indent radius is 250 microns is  $r_{qs} = (.06a - \delta)/.0155 = 877$  microns. This corresponds to an  $a/r_{qs}$  ratio of 0.285 for the quasistatic case. Figure 3.56 shows the differences between the quasi-static spherical indent and the dynamic indent when the two-way indent depth is kept the same. Indent and recovery parameters for both indent types are summarized in Table 3.11 below. It can be concluded that reversible indent or exdent displacement can be generated from a much smaller indent dynamically than quasi-statically, by a factor of approximately 6.5. This is significant because it reduces the SMA substrate thickness to express a similar SFM effect in application and also decreases the amount of material removal to achieve SFM.

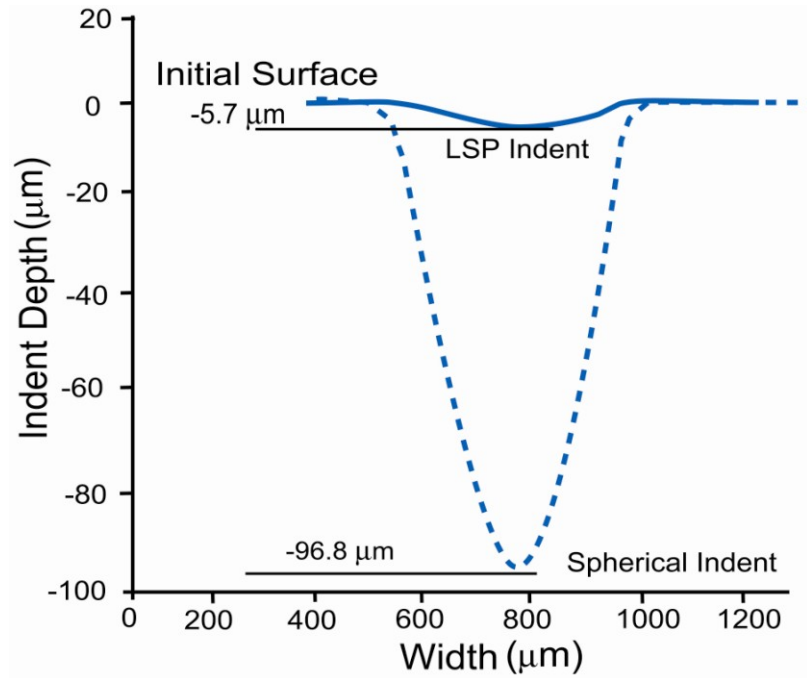


Figure 3.54 Comparison of the initial indent depth between the spherical indent made under 700 N with  $r=400\ \mu\text{m}$  spherical ball and the dynamic indent under laser intensity of  $2.5\ \text{GW}/\text{cm}^2$  and beam size of 0.5 mm.

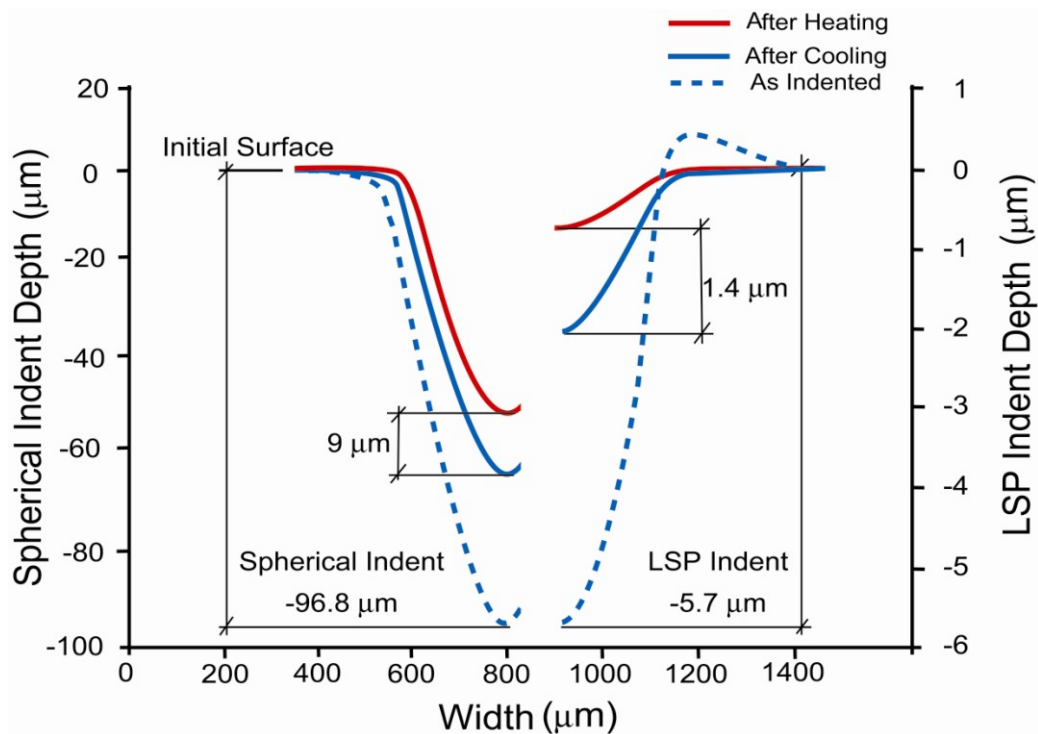


Figure 3.55 Comparisons of the initial indent depth, two-way recovery between the quasi-static spherical indent and the dynamic indent. The dynamic indent is magnified to have the same vertical length as the spherical indent.

Table 3.10 Comparison of Quasistatic and LSP Indent with same contact radius

	Quasistatic <sup>1</sup>		LSP <sup>2</sup>		LSP%/QS%
<i>a/r</i> Ratio	0.65		0.05		
	μm	%Change	μm	%Change	
Indenter Radius	397		5500		
Contact Radius	260		250		
Initial Indent Depth	96.8		5.7		
Initial Recovery	40.8	42.1	5.1	89.5	2.1 x
Reversible Depth Change	9	9.3	1.4	24.6	2.6 x

<sup>1</sup>Quasistatic parameters are interpolations based on previous experiments.

<sup>2</sup>LSP *a/r* ratio estimated assuming a spherical indent profile.

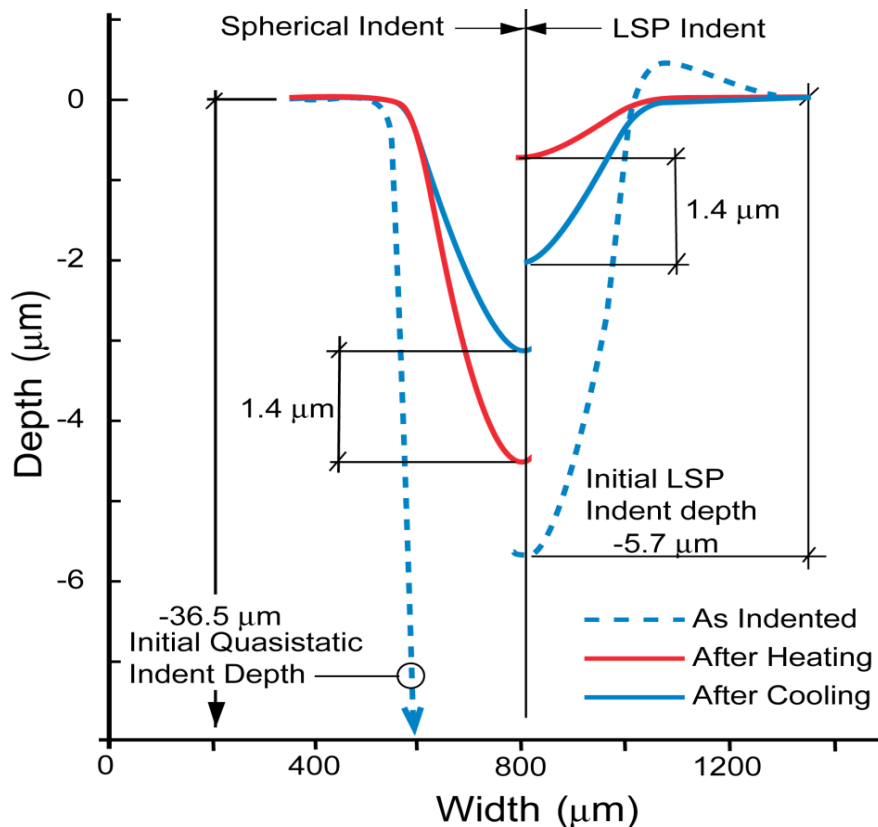


Figure 3.56 Comparisons of initial indent depth and two-way recovery between the spherical indent and the LSP indent. Vertical scales are identical for each impression but the base of the quasistatic indent is off the scale.

Table 3.11 Comparison of Quasistatic and LSP Indent Parameters with same two-way indent depth change

	Quasistatic <sup>1</sup>		LSP <sup>2</sup>		LSP%/QS%
<i>a/r</i> Ratio	0.285		0.05		
	μm	%Change	μm	%Change	
Indenter Radius	877		5500		
Initial Indent Depth	36.5		5.7		(6.5 x) <sup>-1</sup>
Initial Recovery	31.9	87.5	5.1	89.5	
Reversible Depth Change	1.4	3.8	1.4	24.6	6.5 x
Reversible Exdent Height	1.4	3.8	1.2	17.5	4.6 x

<sup>1</sup>Quasistatic parameters are interpolations based on previous experiments.

<sup>2</sup>LSP *a/r* ratio estimated assuming a spherical indent profile.

### 3.6.2 Mechanism of SFM in Dynamic Indents

Laser shock peening produces a high energy shock wave by laser pulse which penetrates into material substrate. The shock wave propagates faster than the speed of sound and at a strain rate larger than 10<sup>6</sup>/s. The shock wave propagation speed consists of two parts: The elastic wave propagation speed  $C_{EL}$ , and the plastic wave propagation speed  $C_{PL}$ , both of which are defined in the following equations [Ding et al. 2006]:

$$C_{EL} = \sqrt{\frac{\lambda + 2\mu}{\rho}} \quad \text{Eq. (3.17)}$$

$$C_{PL} = \sqrt{\frac{\lambda + 2\mu/3}{\rho}} \quad \text{Eq. (3.18)}$$

Here,  $\lambda$  is Lamé's constant which is 17.31 GPa in this case,  $\mu$  is shear modulus which is 11.54 GPa,  $\rho$  is density of the material (NiTi) which is 6.45 g/cm<sup>3</sup>. So  $C_{pl}$  is calculated to around 2,000 m/s, which is beyond the speed of twin boundary motion of martensite detwinning mechanism (the speed of which equals to 1/3 square root of young's modulus over density, which is around 700 m/s [Otsuka et al. 2005]). Therefore, plastic deformation occurs when the shock wave propagates into NiTi, generating a subsurface dislocation deformation zone. The dislocation deformation zone accounts for the observed TWSME even when the  $a/r$  ratio is 0.05.

Millett et al. [2002] reported that the strain rate sensitivity of austenitic NiTi increases the yield strength of NiTi from 500 MPa to 794 MPa by shock wave. As the shock wave propagates into the metallic target, plastic deformation occurs to a depth at which the peak pressure no longer exceeds the metal's Hugoniot elastic limit (*HEL*). A metal's *HEL* is related to the dynamic yield strength according to Johnson and Rhode [1971]:

$$HEL = \frac{1-\nu}{1-2\nu} \sigma_y^{dyn} \quad \text{Eq. (3.19)}$$

where  $\nu$  is Poisson's ratio and  $\sigma_y^{dyn}$  is the dynamic yield strength at high strain rates.

The literature contains one experimental estimate of the *HEL* for austenitic NiTi (3.5 GPa [Millett et al, 2002]), but there is considerable uncertainty regarding this rather high value, which in any case was determined in experiments on austenitic

(rather than martensitic) NiTi. The measured quasi-static compressive stress strain behavior of the NiTi material used in the present study is shown in Figure 2.2 for the data collected at a strain rate of  $1 \times 10^{-2}$ /s. Two yield features can be discerned. The first is unambiguously associated with the onset of plastic strain by martensite variant detwinning and occurs at 93 MPa, whereas the second, which can be associated with the onset of dislocation activity after detwinning mechanisms have been exhausted, is found at 315 MPa. For two-way shape memory to occur, both detwinning and slip must occur, and must do so in that temporal order. This is because memory of cool shape in the martensite requires that dislocations be created in the martensite *after* it has been largely detwinned. Only in this way can such dislocations stabilize the variant distribution of the deformed martensite. We therefore proceed on the assumption that the shock interacts with the martensitic structure on the basis of one *HEL* value for martensite detwinning, and another (higher) *HEL* applicable to slip deformation.

An estimate for the value of the dynamic (high strain rate) yield stress for the martensitic material in the present study can be obtained based on results presented in [Adharapurapu et al, 2006] and [Liu et al, 1999], both of which measured yield stresses for the martensite phase at different strain rates, in both the quasi-static and dynamic regimes. We first develop a logarithmic curve fit to low and high strain rate data for martensite deformation in these two studies, and use this regression to extrapolate the results to a strain rate of  $10^6$ /s (assumed to apply to deformation under

LSP conditions), and additionally to interpolate them for a strain rate of  $10^{-2}/s$  -- the rate used to obtain the data shown in Figure 2.2. Table 3.12 summarizes the data values used for this estimate, where regression parameters  $m$  and  $b$  are used to extrapolate  $\sigma_{\text{dyn}}$  at  $d\varepsilon/dt = 10^6/s$  and  $10^{-2}/s$ , for each of the two studies, according to

$$\sigma(d\varepsilon/dt) = [m \ln(d\varepsilon/dt) + b] \quad \text{Eq.(3.20)}$$

From this we extract the ratio,  $R = \sigma_{10^6}/\sigma_{10^{-2}}$ , for each study, take the average of the two values, and finally estimate  $\sigma_{10^6}$  for the present material as equal to  $R$  times the measured quasistatic slip-yield strength of 315 MPa. This procedure predicts that the dynamic yield stress for slip is 427 MPa. Assuming a Poisson ratio of 0.3, this value yields an *HEL* of 747 MPa for slip deformation.

It is of interest then to estimate the peak pressures, to determine the plastified depth likely produced by the LSP approach, and to compare these estimates to our previous experimental observations of the plastic zone produced by quasistatic spherical indents. The peak pressure of the shock produced using laser ablation is given by

$$P = 0.01[Z I_o \delta(2\delta+3)]^{1/2} \quad \text{Eq. (3.21)}$$

where  $I_o$  is the incident laser power density ( $\text{GWcm}^{-2}$ ),  $P$  is the pressure (GPa),  $Z$  is the reduced acoustic impedance between the target and the confining medium.  $\delta$  is the efficiency of the plasma-material interaction. ( $\delta = 0.1-0.2$ ) [Fabbro et al. 1998]. In the

glass confinement mode, the acoustic impedance of glass is  $1.3 \times 10^6 \text{ g/cm}^2\text{s}$ , while the acoustic impedance of NiTi is about  $1.34 \times 10^6 \text{ g/cm}^2\text{s}$ . As the laser intensity used for LSP was  $2.5 \text{ GW/cm}^2$ , the estimated peak pressure ranges from 3.2 GPa, assuming  $\delta = 0.1$ . The shock pressure of 3.2 GPa is therefore about four times the *HEL* and will clearly cause extensive plastic deformation. Applying the same procedure to the yield stress for detwinning gives an *HEL* estimate for the dynamic case of 133 MPa.

The plastified depth depends on the *HEL*, the pressure,  $P$ , and the pressure duration,  $\tau_p$ , and may be estimated according to [Peyre et al, 1996] as

$$D_p = C_{EL} C_{PL} \tau_p [(P-HEL)/2 HEL]/(C_{EL} - C_{PL}) \quad \text{Eq. (3.22)}$$

The latter two parameters are the elastic and plastic wave propagation speeds:  $C_{EL} = [(\lambda+2\mu)/\rho]^{1/2}$  and  $C_{PL} = [(\lambda+2\mu/3)/\rho]^{1/2}$  respectively [Johnson et al, 1971], where  $\lambda$  is Lamé's constant (16.2 GPa in this case),  $\mu$  is the shear modulus of the martensite, taken to be 10.77 GPa, and  $\rho$  is density of NiTi which is  $6.45 \text{ g/cm}^3$ .  $C_{EL}$  and  $C_{PL}$  are therefore about 2420 and 1900 m/s, respectively. The pressure pulse duration,  $\tau_p$ , is longer than the laser pulse duration by a factor of 1.8 [Fabbro et al, 1990] and is taken to be 9 ns in the present case. These parameters give an estimate for the depth,  $D_{S,P}$ , to be 131 microns, at which slip deformation begins. The strain in this zone saturates at  $P = 2.5 \text{ HEL}$  at a magnitude

$$\varepsilon_P = -2 \text{ HEL} (P/\text{HEL} - 1)/(3\lambda+2\mu) \quad \text{Eq. (3.23)}$$

giving  $\epsilon_S = 3.2\%$  in compression (for  $P = 2.5 \text{ HEL}$ ) for the present experiment. The saturation depth,  $D_{S,2.5}$ , by eq. 4 is 60.2 microns. Similar calculations for the detwinning  $\text{HEL}$  of 133 Mpa give a saturation strain,  $\epsilon_T$ , of 1% at the same saturation depth ( $D_{T,2.5} = 60.2$  microns). However, for the case of the detwinning yield, the depth at the  $\text{HEL}$ ,  $D_{T,P} = 512$  microns, is much greater than that for slip deformation.

Table 3.12 Data and regression coefficients used in estimating the dynamic yield stress for slip deformation in the martensite for the present work

Ref.	Strain Rate $d\epsilon/dt$	Compressive Yield Stress MPa	Yield Stress Ratio $R$ , $d\sigma/dt$ @ 10E6/10E2	Regress Parameter $m$	Regress Parameter $b$
[16]	1 x 10E-3	1290	1.416	30.719	1502.2
	1.2 x 10E2	1720			
	1 x 10E-2, interp.	1360			
	1 x 10E6, extrap.	1927			
[17]	3 x 10E-4	1250	1.293	21.094	1421.1
	3 x 10E3	1590			
	1 x 10E-2, interp.	1324			
	1 x 10E6, extrap.	1713			
Present work, slip	1 x 10E-2, meas.	315	1.355		
	1 x 10E6, est.	<b>427</b>			
Present Work, Detwi nning	1 x 10E-2 meas.	93	1.355		
	1 x 10E6, est.	<b>133</b>			

It is useful to assess the above estimates in terms of the observed initial LSP indent depth of 5.7 microns and the initial recovered depth of 0.6 microns. The

former should be consistent with the sum of strain contributions from detwinning and slip. Here it is assumed that the strain decays from the saturation value at the saturation depth ( $D_{S,2.5}$  and  $D_{T,2.5}$ ) to zero at the *HEL*. The total indent depth should therefore be

$$D_{TOT} = 1/2 \varepsilon_S (D_{S,P} + D_{S,2.5}) + 1/2 \varepsilon_T (D_{T,P} + D_{T,2.5}) \quad \text{Eq. (3.24)}$$

which is 6 microns if the above estimates are used, in reasonable agreement with the observed depth of 5.7 microns. The residual indent depth after heating should reflect only the slip component of the deformation, giving  $D_{Resid.} = 1/2 \varepsilon_S (D_{S,P} + D_{S,2.5})$  which is 3.1 microns – substantially greater than the 0.6 micron residual depth observed. This suggests that the above analysis has overestimated the plastic strain due to slip, or that the effect of surface relief waves has reversed some of the slip deformation. It has been reported [Peyre et al, 1996] that when the peak load is above 2.5 *HEL*, surface release waves focus and amplify from the edge of the impact. The peak load 3.2 GPa is considerably higher than 2.5 *HEL* for slip (1.87 GPa), which may additionally explain the observed 0.5 micron pile up effect observed in Figure 3.55.

Finally, for quasistatic spherical indents, extensive experimental measurements of the depth of the active zone, beneath the indent, show that this depth,  $D^*$ , to be approximately 40 times the height of the stable cyclic extent amplitude. Conversely, the stable extent amplitude is consistently found to be about 2.4% of the active zone

depth. If LSP indents respond in the same way, and estimate of the active zone depth in the present experiment would  $1.2/.024 = 58$  microns, which is in reasonable agreement with the 60 micron depth estimated above.

To conclude, LSP was demonstrated to be able to create two-way indent recovery or reversible extend-to-flat transition by coupling a planarization step in NiTi SMAs. This is due to the subsurface slip deformation zone induced by large peak load, high intensity, and ultra high strain rate of LSP. The two-way effect of the indent made by LSP is more than twice the maximum effect made by quasi-static indent in low strain rate condition, which maybe due to the strain rate sensitivity effect induced by ultra high strain rate LSP. Further experiments can be designed to ascertain deformation strain, residual stress and the size of the subsurface deformation zone, either by experimentation or by finite element modeling.

Thermally-reversible surface topographical transitions have potential application to micro-electrical-mechanical systems (MEMS), variable friction surfaces, information storage media, controllable optical devices, tribological surfaces, and mechanical joining.

### 3.7 Modeling Indent Recovery and SFM

#### 3.7.1 Finite Element Modeling of the Deformation Zone

Finite element analysis was carried out using a commercial program ABAQUS (SIMULIA, Providence, RI). The mesh used has 15,000 nodes with mesh refinement in the contact deformation region as shown in Figure 3.57. The mechanical properties of NiTi used in the model were measured in a tensile test. The Young's modulus was measured to be 28GPa, the yield stress was 180 MPa. The work hardening rate was 6.5 GPa and the poisson's ratio was 0.3.

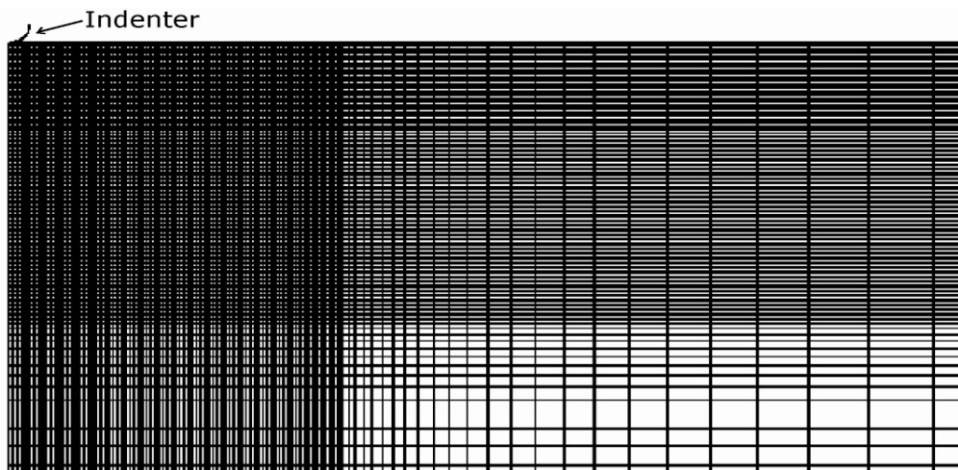


Figure 3.57 Finite element mesh with 15,000 nodes and a refined area as the contact region and 4 mm spherical indenter.

##### 3.7.1.1 Spherical Indentation and the Deformation Zone

Spherical indentation was modeled by indenting a half-space shape memory alloy using a 4 mm radius indenter. The mechanical properties of the shape memory alloy were defined above. The indentation depth was varied in order to achieve a

range of  $a/r$  ratios. Figure 3.58 shows the development of plastic strains inside the shape memory alloy upon indentation. As we can see, the maximum plastic strain almost stays at a constant distance below the indent, while the plastic strains progress downwards as the indenter goes into the material progressively.

For the spherical indent with an  $a/r$  of 0.4, the maximum plastic strain is about 16.6%. The deformation zone at a depth of  $D^*$  which was measured to be about  $1.1-1.35a$  has a minimum plastic strain of about 8-9%, as shown in Figure 3.59(a). For the spherical indent with an  $a/r$  ratio of 0.65, the plastic strain can be as high as about 30%, as shown in Figure 3.59(b). The deformation zone at a depth of  $D^*$ , measured by the front and back thinning experiments to be about  $1.5-1.7a$  for such indent, has a minimum plastic strain of about 7-9%. For the spherical indent with an  $a/r$  of 0.95 has a maximum plastic strain about 80%. The deformation zone at a depth of  $D^*$  which was measured to be about  $1.9-2.0a$  has a minimum plastic strain of about 9-10%, as shown in Figure 3.59(c).

Therefore, the finite element model consistently shows a deformation zone at a depth of  $D^*$  has a plastic strain larger than 7%, which is beyond the strain that can be accommodated by the martensite deformation twinning. Thus slip plastic deformation takes control and dislocations generated in the detwinned martensite variants achieve the lowest free energy and favor the formation of certain martensite variant in the subsequent cooling, enabling a two-way response.

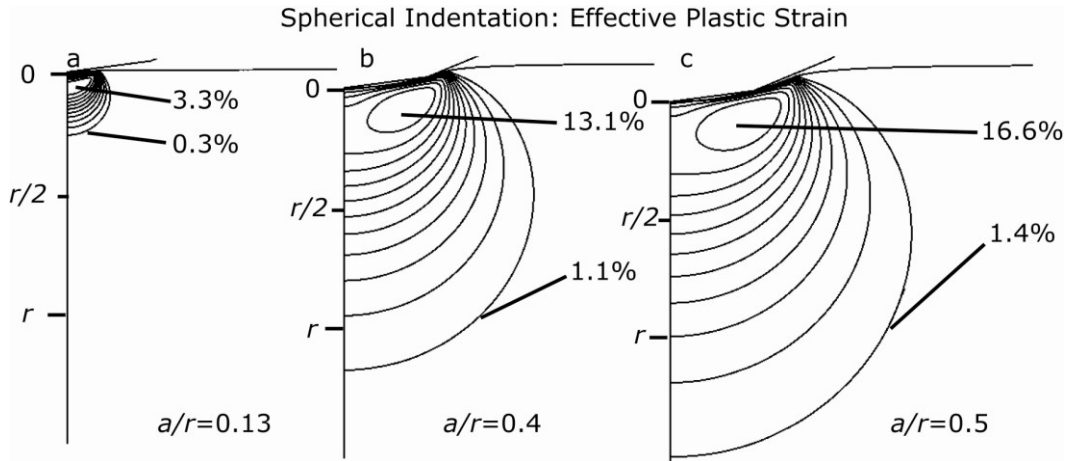


Figure 3.58 Finite element model of the spherical indentation process: a) 10% of the indentation steps; b) 60% of the indentation steps; c) 100% of the indentation steps (Indentation step finished).

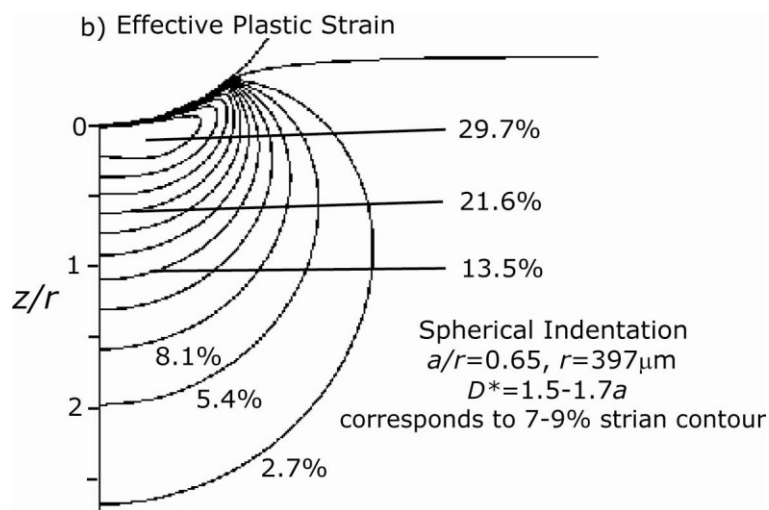
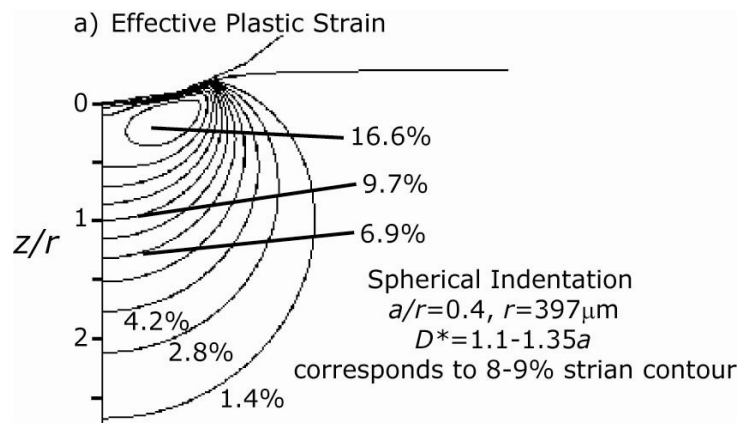


Figure 3.59 Effective plastic strain developed after spherical indentation with an  $a/r$  of a) 0.4, b) 0.65, and c) 0.95 simulated by ABAQUS finite element model.

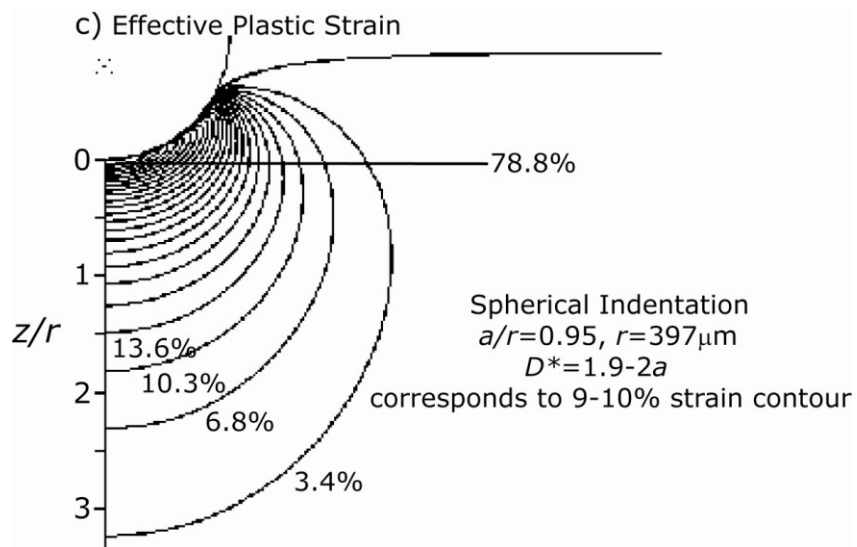


Figure 3.59 cont'd.

### 3.7.1.2 Cylindrical Indentation and the Deformation Zone

The difference between spherical and cylindrical indentation lies in the indenter geometry. As spherical indentation involves an axisymmetric problem, cylindrical indentation relates to a plane strain problem. Thus, the cylindrical indentation experiment was modeled by indenting a half-space shape memory alloy using a 4 mm radius cylindrical rod.

Figure 3.60(a) shows that for the cylindrical indent with an  $a/r$  ratio of 0.41, the plastic strain can be as high as about 10%. The deformation zone at a depth of  $D^*$ , measured by the front thinning experiment to be about  $1.8a$  for such cylindrical indent, has a minimum plastic strain of about 7%.

Figure 3.60(b) shows that for the cylindrical indent with an  $a/r$  ratio of 0.65, the plastic strain can be as high as about 17%. The deformation zone at a depth of  $D^*$ , measured by the front thinning experiment to be about  $2.3a$ , has a minimum plastic strain of about 8%.

Figure 3.60(c) shows that for the cylindrical indent with an  $a/r$  ratio of 0.95, the plastic strain can be as high as about 31%. The deformation zone at a depth of  $D^*$ , measured by the front thinning experiment to be about  $4.15a$ , has a minimum plastic strain of about 7.5%.

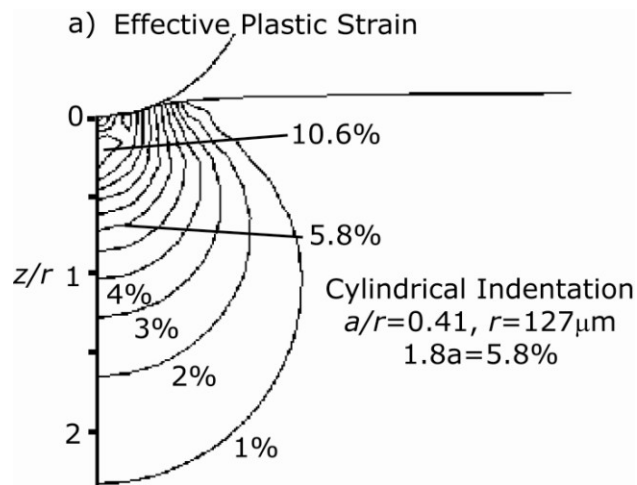


Figure 3.60 Effective plastic strain developed after cylindrical indentation with an  $a/r$  of a) 0.41, b) 0.65, and c) 0.95 simulated by ABAQUS finite element model.

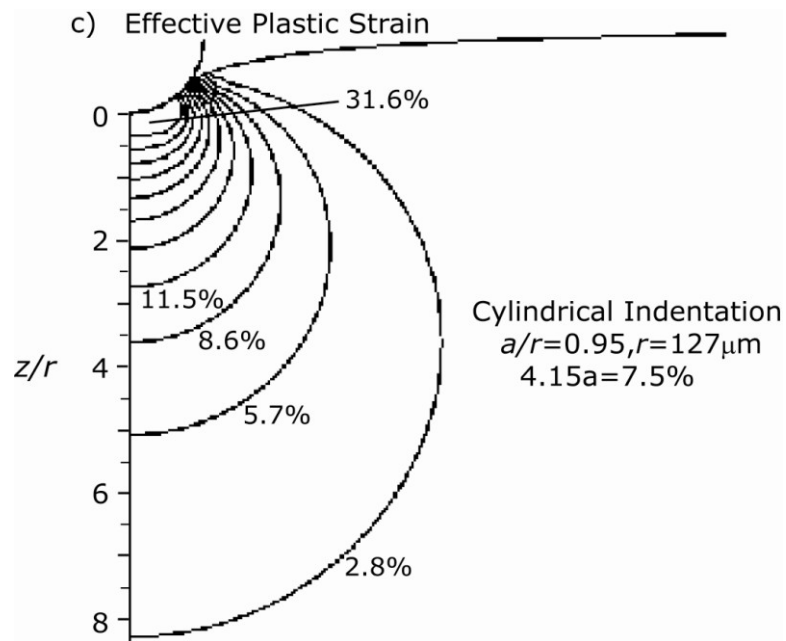
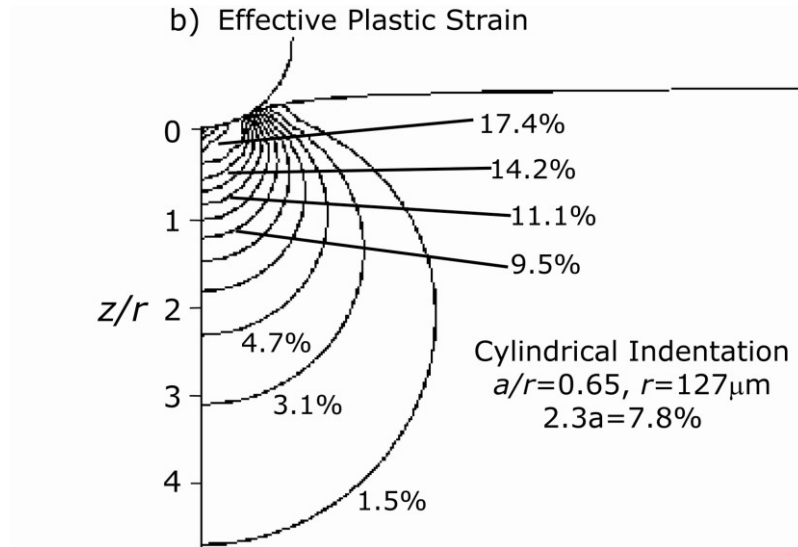


Figure 3.60 cont'd.

As we can see, the sizes of the spherical deformation zones are around 50% smaller than those of the cylindrical deformation zones. The difference in the size of the deformation zone accounts for the difference in the observed two-way response (cylindrical indents have about twice as large two-way response as spherical indents).

However, both spherical and cylindrical deformation zones correspond to strains around 7-9%, which can induce slip deformation. This again supports the conclusion that TWSME induced by indentation is due to the dislocations in the subsurface deformation zone. Dislocations in this zone are retained in the austenite after warming and, on cooling, encourage the formation of the same variants in which dislocations were originally formed and presumed minimal free energy, thus stabilizing the original martensite variants, and resulting in a degree of 'memory' of both the warm and cool shapes.

## CHAPTER 4 CONCLUSIONS AND FUTURE WORK

### 4.1 Conclusions

1. An indentation-planarization method has been demonstrated not only to induce two-way cyclic depth change but also to create thermally-driven reversible surface form transitions in NiTi alloys. These surface features can be easily modified by various indenter geometries, such as spheres, cylinders, punches, pyramids and many others.

2. Indentation-induced two-way response increases with increasing  $a/r$  ratio for both spherical and cylindrical indents. Thermal cycling after indentation can increase two-way response by about 40% due to the completion of phase transformation.

3. Reducing indent spacing can also increase two-way response due to the interplay of the deformation zone of each indent. Zero indent spacing or double indentation maximizes the two-way response. Further increase of indentation repetitions does not have much effect on increasing two-way response. Indentation at temperature below  $A_s$  could decrease the two-way response because the material flow stress increases below  $A_s$ , causing the material work harden faster and reducing plastic deformation.

4. This indentation-induced two-way shape memory effect is thought to be enabled by a deformation zone under the indent in which the martensite has been plastically

strained beyond the detwinning plateau strain of  $\sim 5\%$ , causing production of defects associated with slip deformation. The depth of this active zone,  $D^*$ , has been experimentally determined by successive grinding experiments and shown that, for both spherical and cylindrical indents and over a range of  $a/r$  ratios between 0.4 and 0.95, the maximum cyclic extent height amplitude is approximately 2.4% of the magnitude of  $D^*$ .

5. Cylindrical indentation is shown to produce substantially larger cyclic extent response than spherical indentations with similar  $a/r$  ratios. This increased response can be directly related to the depth of the active zone for these indents.  $D^*$  for cylindrical indent is greater than that for spherical indent. This is due to different local constraint conditions, with cylindrical indentation leading to plane-strain deformation and larger hydrostatic stress components in the deformation zone.

6. Finite element modeling shows the deformation zone at a depth of  $D^*$  has a minimum plastic strain of 7% for spherical and cylindrical indents at various  $a/r$  ratios. This confirms the conclusion that slip deformation is a necessary condition for indentation-induced TWSME. It is due to the preferential formation of certain martensite variants, where the dislocations were developed by slip deformation, that lead to a selective shape change in martensitic transformation. The driving force for the selection of martensite variants is the system's tendency to achieve lowest free

energy in martensitic transformation. Only in the martensite variants in which the dislocations initially generated can they find the lowest free energy.

7. Surface Form Memory has been demonstrated to exert large specific work output.

The energy density of the spherical indent in constrained recovery can be close to  $10^7$   $J/m^3$ , the magnitude which is close to the maximum of energy density of conventional NiTi actuators.

8. Dynamically made indents by the Laser Shock Peening process were found to have larger two-way response at smaller indentation depth or smaller  $a/r$  ratio level than the quasi-static indent made by conventional indenters. This was due to the larger plastic depth, thus larger deformation zone under the LSP indent. High efficiency, large two-way response, and high energy density of SFM indents make the material an ideal candidate for miniature actuators for MEMS.

## **4.2 Future Development**

1. *Mechanisms of the indentation-induced shape memory, super-elasticity and two-way shape memory effect.* New experimental tools such as synchrotron X-ray diffraction, Neutron Diffraction, Electron Back Scattering Diffraction and in-situ TEM indentation may be used to assess the critical information like the one-to-one correspondence between austenite and martensite variants in the indentation deformation zone in NiTi alloys.

2. *Tribological applications of the surface form memory.* Surfaces with indent-to-flat surface transition or flat surface-to-indent transition can be made to vary friction coefficients with differences on the order of a magnitude. Special interest can be placed in the wheel-roll contact in the high speed railway system.

3) Developing finite element modeling of shape memory effect is the next step after current modeling of the indentation deformation zone. FEA of shape memory effect can provide stress-strain distributions beneath indents in NiTi before and after phase transformations, which can be used to explain indentation-induced shape memory and two-way shape memory effect. Coupling the thermal field with the current model is essential in developing shape memory model.

## APPENDIX

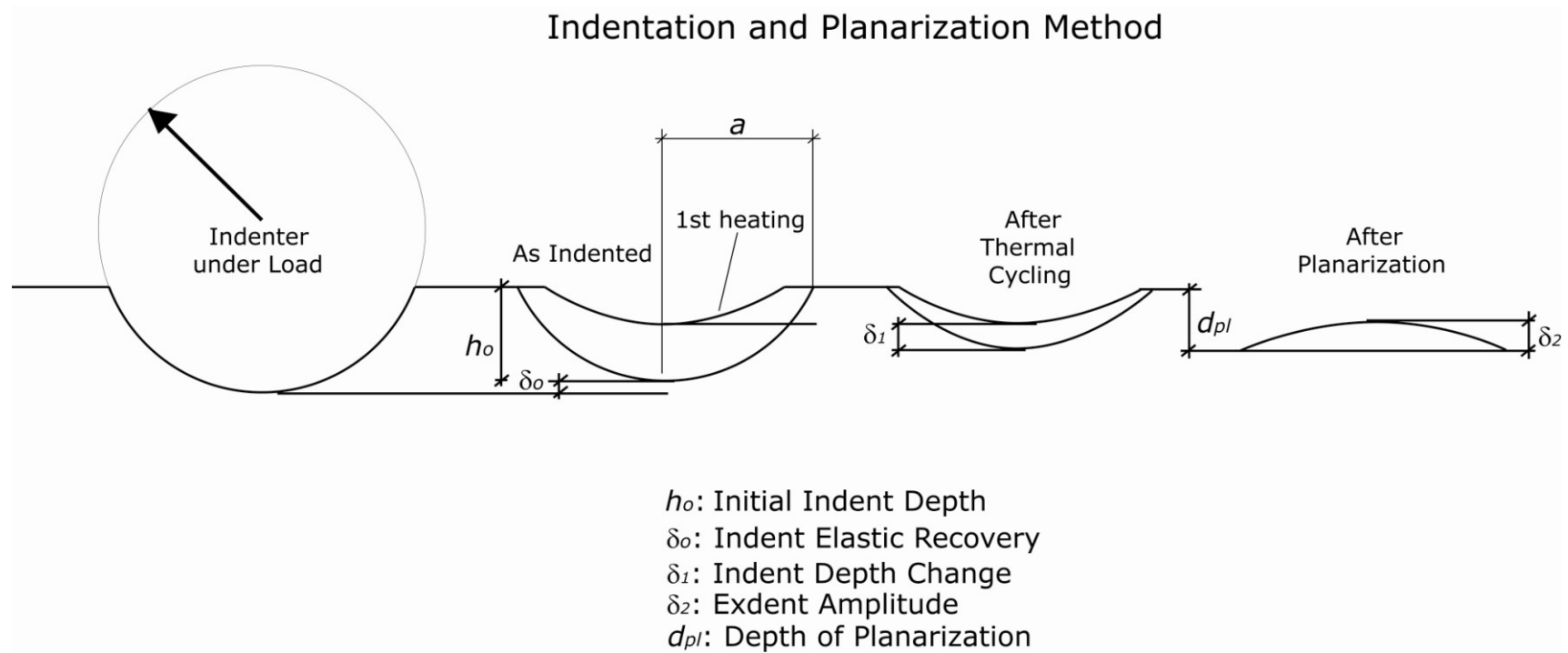


Figure a. Schematic illustration of the indentation-planarization process.

## **Bibliography**

## Bibliography

- Adharapurapu R. R., Jiang F. C., Vecchio K. S., Gary III G. T., *Acta Materialia*, **54**, 4609 (2006)
- Arciniegas M., Manero J.M., Pena J., Gil F.J., Planell J.A., *Metallurgical Materials Transactions A*, **39**, 742 (2008).
- Bonavolonta C., Valentino M., Adamo M., Sarnelli E., *Measurement Science Technology*, **18**, 2116 (2007)
- Brinson L. C., Huang M. S., *Journal of Intelligent Material Systems and Structures*, **7**, 108 (1996).
- Buehler W.J., Wiley R.C., Gilfrich J.V., *Journal of Applied Physics*, **34**, 1475 (1962)
- Cheng F.T., Shi P., Man H.C., *Scripta Materialia*, **45**, 1083 (2001).
- Crone W.C., Brock H., Creuziger A., *Experimental Mechanics*, **47**, 133 (2007).
- Delaey L and Thienel J: Shape Memory Effects in Alloys, J. Perkins, ed., Plenum, New York, NY, 341 (1975)
- Fabbro R., Fournier J., Ballard P., Devoux D., Virmont J., *Journal of Applied Physics*, **68**, 775 (1990)
- Fei X.L., Zhang Y.J., Grummon D.S., Cheng Y.T., *Journal of Materials Research*, **24**, 823 (2009).
- Fei X.L., O'Connell C.J., Cheng Y.T., Grummon D.S., *Journal of Engineering Materials and Performance*, **18**, 538 (2009)
- Fernandez J., Zhang X.M., Guilemany J.M., *Journal Materials Processing Technology*, **139**, 117 (2003).
- Frick C.P et al., *Acta Materialia*, **54**, 2223 (2006)
- Frick C.P., Ortega A.M., Tyber J., Maksound A.E.M., *Materials Science & Engineering A*, **405**, 34 (2005).
- Fukuda T et al., *Materials Transactions Jim*, **42**,323 (2001)

- Fukuda T., Kakeshita T., Saburi T., *Materials Transactions JIM*, **38**, 514 (1997)
- Gall K., Juntunen K., Maier H.J., Sehitoglu H., Chumlyakov Y.I., *Acta Materialia*, **49**, 3205 (2001).
- Goo B. C., LExcellent C., *Acta Materialia*, **45**, 727 (1997).
- Guenin G., Gobin P. F., *Metallurgical Transactions A*, **13**, 1127 (1982).
- Hardy C., Tordion G. V., Baronet C. N., *Journal of Basic Engineering*, **94**, 251 (1972).
- Huang W.M., Su J.F., Hong M.H., Yang B., *Scripta Materialia*, **53**, 1055 (2005).
- Huang M., Brinson L.C., *Journal of the Mechanics and Physics of Solids*, **46**, 1379 (1998).
- Humbeeck J.V., *Materials Science & Engineering A*, **273**, 134 (1999).
- Hunter I.W., Lafontaine S., Technical Digest of the IEEE Solid-State Sensor and Actuator Workshop, Hilton Head, South Carolina, 178-185, 1992.
- Ivshin Y., Pence T. J., *International Journal of Engineering Science*, **32**, 681 (1994).
- Johnson J. N., Rhode R. W., *Journal of Applied Physics*, **42**, 4171 (1971).
- Johnson K.L, "Contact mechanics" (Cambridge University Press, Cambridge [Cambridgeshire]; New York, 1985)
- Kainuma R., Matsumoto M., Honma T., *Proceedings of International Conference on Martensitic Transformations (ICOMAT-86)*. Sendai: Japan Institute of Metals; 1987. p. 717
- Kim H.C., Yoo Y.I., and Lee J.J., *Smart Materials and Structure*, **18**, 095042 (2009)
- Komvopoulos K., Ma X.G., *Applied Physics Letters*, **87**, 263108 (2005).
- Lahoz R., Gracia-Villa L., Puertolas J.A., *Journal of Engineering Materials Technology-Transaction of the Asme*, **124**, 397 (2002).
- Lee Y., Kim B., Lee M., Park J., *IEEE International Conference on Robotics and Automation*, 2004, p 5007

- Lieberman D.S., Wechsler M.S., Read T.A., *Journal of Applied Physics*, **26**, 473 (1955)
- Liu C., Zhao Y.P., Yu T.X., *Materials & Design*, **26**, 465 (2005).
- Liu C., Zhao Y.P., Sun Q.P., Yu T.X., Cao Z.X., *Journal of Material Science*, **40**, 1501 (2005).
- Liu R., Li D.Y., Xie Y.S., Llewellyn R., Hawthorne H.M., *Scripta Materialia*, **41**, 691 (1999).
- Liu Y., Humbeeck J.V., *Acta Materialia*, **47**, 199 (1998).
- Liu Y., McCormic P.G., *Acta Metallurgica*, **38**, 1321 (1990)
- Liu Y., Li Y. L., Ramesh K. T., Humbeeck J. V., *Scripta Materialia*, **41**, 89 (1999)
- Liu Y., Liu Y., Humbeeck J. V., *Scripta Materialia*, **39**, 1047 (1998)
- Liu Y., Xie Z., Humbeeck J.V., Delaey L., *Acta Materialia*, **46**, 4325 (1998)
- Loloee R., Pence T.J., Grummon D.S., *Journal De Physique IV*, **5**, C8-545 (1995)
- Lublinter J., Auricchio F., *International Journal of Solids and Structures*, **33**, 991 (1996)
- Ma X.G., Komvopoulos K., *Applied Physics Letters*, **83**, 3773 (2003)
- Ma X.G., Komvopoulos K., *Applied Physics Letters*, **84**, 4274 (2004).
- Mackerle J., *Engineering Computations*, **21**, 23 (2004).
- Madangopal K., *Acta Materialia*, **45**, 5347 (1997).
- Maeda S., Abe K., Yamamoto K., Tohyama O., Ito H., *Proceedings of the IEEE Micro Electro Mechanical Systems*, 1996, p290
- Manach P.Y., Favier D., *Scripta Metallurgical Materialia*, **28**, 1417 (1993).
- Mata M., Anglada M., Alcalá J., *Journal of Materials Research*, **17**, 964 (2002)
- Mata M., Casals O., Alcalá J., *International Journal of Solids and Structures*, **43**, 5994 (2006)

- Meng X. L., Zheng Y. F., Cai W., Zhao L. C., *Journal of Alloys and Compounds*, **372**, 180 (2004).
- Michaud V., Schrooten J., Parlinska M., Gotthardt R., Bidaux J., *The International Society for Optical Engineering*, **336**, 4698 (2002)
- Miller D.A., Lagoudas D.C., *Materials Science and Engineering a-Structural Materials Properties Microstructure and Processing*, **308**, 161 (2001).
- Millett J. C. F., Bourne N. K., Gary III G. T., *Journal of Applied Physics*, **92**, 3107 (2002)
- Morgon N. B., *Materials Science and Engineering A*, **378**, 16 (2004)
- Muir Wood A.J., Clyne T.W., *Acta Materialia*, **54**, 5607 (2006)
- Ni W.Y., Cheng Y.T., Grummon D.S., *Applied Physics Letters*, **82**, 2811 (2003).
- Ni W.Y., Cheng Y.T., Grummon D.S., *Applied Physics Letters*, **80**, 3310 (2002).
- Nishida M., Honma T, *Scripta Metallurgica*, **18**, 1293 (1984)
- Omori T., Sutou Y., Wang J.J., Kainuma R., Ishida K., *Journal De Physique IV*, **112**, 507 (2003).
- Otsuka K., Ren X., *Progress in Materials Science*, **50**, 511 (2005)
- Otsuka K., *International Metals Review*, **31**, 93 (1986)
- Otsuka K., Wayman C.M., "Shape memory materials" (Cambridge University Press, New York, 1998).
- Park S., ShROUT T., *Journal of Applied Physics*, **82**, 1804 (1997)
- Patoor E., *Journal De Physique IV*, **5**, C2-495 (1995)
- Patoor E., Bensalah M. O., Eberhardt A., Berveiller M., *Revue De Metallurgie-Cahiers D Informations Techniques*, **90**, 1587 (1993).
- Perkins J., Hodgson D., "The Two-Way Shape Memory Effect", *Engineering Aspects of Shape Memory Alloys*, Butterworth-Heinemann, 195 (1990).
- Perkins J., Sponholz R.O., *Metallurgical Transactions*, **15A**, 313 (1984)

- Pelrine, R., R Kornbluh., SRI International, 1999
- Peyre P., Fabbro R., Merrien P., Lieurade H.P., *Materials Science and Engineering A*, **210**, 102 (1996).
- Qian L.M., Xiao X.D., Sun Q.P., Yu T.X., *Applied Physics Letters*, **84**, 1076 (2004).
- Rios-Jara D., Guenin G., *Acta metallurgica*, **35**, 109 (1987)
- Saburi T., Nenno S., *Script Metallurgica*, **8**, 1363 (1974).
- Saburi T., Wayman C.M., *Acta Metallurgica*, **27**, 979 (1979).
- Samuels L.E., Mulhearn T.O., *Journal of Mechanics and Physics of Solids*, **5**, 125 (1957)
- Scherngell H., Kneissl A.C., *Acta Materialia*, **50**, 327 (2002).
- Shaw G.A., *Applied Physics Letters*, **83**, 257 (2003)
- Shaw G.A., Trethewey J.S., Johnson A.D., Drugan W.J., Crone W.C., *Advanced Materials*, **17**, 1123 (2005).
- Schroeder T. A., Wayman C. M., *Scripta Metallurgica*, **11**, 225 (1977)
- Sinclair G.B., Follansbee P.S., Johnson K.L., *International Journal of Solids and Structures*, **21**, 865 (1985).
- Stalmans R., Humbeeck J.V., Delaey L., *Acta Metallurgica Materialia*. **40**, 2921 (1992)
- Stalmans R., Humbeeck J.V., Delaey L., *Acta Metallurgica Materialia*, **40**, 501 (1992).
- Su J.F., Huang W.M., Hong H.M., *Smart Materials and Structures*, **16**, S137 (2007).
- Tabor D., *Proceedings of the Royal Society of London Series A-Mathematical and Physical Sciences*, **192**, 247 (1948).
- Tabor D., *Philosophical Magazine a-Physics of Condensed Matter Structure Defects and Mechanical Properties*, **74**, 1207 (1996).
- Tanaka K., Nagaki S., "A Thermomechanical Description of Materials with Internal Variables in the Process of Phase-Transitions", *Ingenieur Archive*, 51, 287

(1982).

Wang J.J., *Scripta Materialia*, **52**, 311 (2005).

Wang Z.G., *Materials Science and Engineering a-Structural Materials Properties Microstructure and Processing*, **360**, 126 (2003).

Xie Z.L., Liu Y., Humbeeck J.V., *Acta Metallurgica*, **46**, 1989 (1998)

Yan W.Y., Sun Q.P., Feng X.Q., Qian L.M., *International Journal of Solids and Structure*, **44**, 1 (2007)

Yu H.J., *Journal of Materials Science*, **41**, 3435 (2006)

Xie Z.L., Liu Y., Humbeeck J. V., *Acta Metallurgica*, **46**, 1989 (1998)

Zhang H.S. Komvopoulos K., *Journal of Materials Science*, **41**, 5021 (2006).

Zhang X.M., Fernandez J., Guilemany J.M., *Journal De Physique IV*, **112**, 487 (2003)

Zhang Y.J., Cheng Y.T., Grummon D.S., *Applied Physics Letters*, **89**, 1912 (2006).

Zhang Y.J., Cheng Y.T., Grummon D.S., *Applied Physics Letters*, **88**, 1904 (2006).

Zhang Y.J., Cheng Y.T., Grummon D.S., *Journal of Material Research*, **22**, 2851 (2007).

Zhang Y.J., Cheng Y.T., Grummon D.S., *Journal of Applied Physics*, **101**, 053507 (2007).